

Journal of Healthcare Engineering

Advancements of Image Processing and Vision in Healthcare

Lead Guest Editor: Md. A. R. Ahad

Guest Editors: Syoji Kobashi and João M. R. S. Tavares





Advancements of Image Processing and Vision in Healthcare

Journal of Healthcare Engineering

Advancements of Image Processing and Vision in Healthcare

Lead Guest Editor: Md. A. R. Ahad

Guest Editors: Syoji Kobashi and João M. R. S. Tavares



Copyright © 2018 Hindawi. All rights reserved.

This is a special issue published in “Journal of Healthcare Engineering.” All articles are open access articles distributed under the Creative Commons Attribution License, which permits unrestricted use, distribution, and reproduction in any medium, provided the original work is properly cited.

Editorial Board

Saverio Affatato, Italy
William Bertucci, France
Olivier Beuf, France
Daniel H.K. Chow, Hong Kong
Tiago H. Falk, Canada
Mostafa Fatemi, USA
Jesus Favela, Mexico
Joseph Finkelstein, USA
Antonio Gloria, Italy
Philippe Gorce, France
Valentina Hartwig, Italy
Andreas H. Hielscher, USA
Norio Iriguchi, Japan

Zhongwei Jiang, Japan
John S. Katsanis, Greece
Terry K.K. Koo, USA
Panagiotis Kosmas, UK
Michel Labrosse, Canada
Jui-Yang Lai, Taiwan
Feng-Huei Lin, Taiwan
Maria Lindén, Sweden
Francisco Lopez-Valdes, Spain
Andreas Maier, Germany
Mehran Moazen, UK
Rafael Morales, Spain
David Moratal, Spain

Vincenzo Positano, Italy
Alessandro Reali, Italy
Jose Joaquin Rieta, Spain
Sébastien Roth, France
Hélder A. Santos, Finland
Emiliano Schena, Italy
Maurizio Schmid, Italy
Jiann-Shing Shieh, Taiwan
Jinshan Tang, USA
Vinoy Thomas, USA
Ioannis G. Tollis, Greece

Contents

Advancements of Image Processing and Vision in Healthcare

Md Atiqur Rahman Ahad , Syoji Kobashi , and João Manuel R. S. Tavares 
Volume 2018, Article ID 8458024, 3 pages

A Subband-Specific Deconvolution Model for MTF Improvement in CT

Seokmin Han, Kihwan Choi, and Sang Wook Yoo
Volume 2017, Article ID 2193635, 8 pages

Gaussian Elimination-Based Novel Canonical Correlation Analysis Method for EEG Motion Artifact Removal

Vandana Roy, Shailja Shukla, Piyush Kumar Shukla, and Paresh Rawat
Volume 2017, Article ID 9674712, 11 pages

Novel Variants of a Histogram Shift-Based Reversible Watermarking Technique for Medical Images to Improve Hiding Capacity

Vishakha Kelkar, Kushal Tuckley, and Hitesh Nemade
Volume 2017, Article ID 3538979, 7 pages

Intraoral Scanner Technologies: A Review to Make a Successful Impression

Raphaël Richert, Alexis Goujat, Laurent Venet, Gilbert Viguie, Stéphane Viennot, Philip Robinson, Jean-Christophe Farges, Michel Fages, and Maxime Ducret
Volume 2017, Article ID 8427595, 9 pages

Recent Development of Augmented Reality in Surgery: A Review

P. Vávra, J. Roman, P. Zonča, P. Ihnát, M. Němec, J. Kumar, N. Habib, and A. El-Gendi
Volume 2017, Article ID 4574172, 9 pages

Model of Murine Ventricular Cardiac Tissue for *In Vitro* Kinematic-Dynamic Studies of Electromagnetic and β -Adrenergic Stimulation

Lorenzo Fassina, Marisa Cornacchione, Manuela Pellegrini, Maria Evelina Mognaschi, Roberto Gimmelli, Andrea Maria Isidori, Andrea Lenzi, Giovanni Magenes, and Fabio Naro
Volume 2017, Article ID 4204085, 7 pages

Quantitative Analysis of Intracellular Motility Based on Optical Flow Model

Yali Huang, Lei Hao, Heng Li, Zhiwen Liu, and Peiguang Wang
Volume 2017, Article ID 1848314, 10 pages

A Kalman Filtering and Nonlinear Penalty Regression Approach for Noninvasive Anemia Detection with Palpebral Conjunctiva Images

Yi-Ming Chen and Shaou-Gang Miaou
Volume 2017, Article ID 9580385, 11 pages

The Use of Optical Coherence Tomography in Dental Diagnostics: A State-of-the-Art Review

Monika Machoy, Julia Seeliger, Liliana Szyszka-Sommerfeld, Robert Koprowski, Tomasz Gedrange, and Krzysztof Woźniak
Volume 2017, Article ID 7560645, 31 pages

Editorial

Advancements of Image Processing and Vision in Healthcare

Md Atiqur Rahman Ahad ¹, Syoji Kobashi ², and João Manuel R. S. Tavares ³

¹*Department of Electrical and Electronic Engineering, University of Dhaka, Dhaka, Bangladesh*

²*Graduate School of Engineering, University of Hyogo, Himeji, Japan*

³*Instituto de Ciência e Inovação em Engenharia Mecânica e Engenharia Industrial, Departamento de Engenharia Mecânica, Faculdade de Engenharia, Universidade do Porto, Porto, Portugal*

Correspondence should be addressed to Md Atiqur Rahman Ahad; atiqahad@du.ac.bd

Received 21 November 2017; Accepted 23 November 2017; Published 15 January 2018

Copyright © 2018 Md Atiqur Rahman Ahad et al. This is an open access article distributed under the Creative Commons Attribution License, which permits unrestricted use, distribution, and reproduction in any medium, provided the original work is properly cited.

1. Introduction

Advancements of image processing and computer vision in healthcare sectors are required to be explored. Though this arena has been expanded a lot in the last few decades, still the progresses are not satisfactory. Hence, we have endeavored to delve into the healthcare using image processing and computer vision, though sensor-based activity is also a very important area [1, 2]. Integration of various cues and modalities can enhance the performance of image- or vision-based analysis. This special issue demanded to cover the broad spectrum that benefits from the automatic understanding of medical healthcare image analysis and related topics. This special issue accepted high-quality research papers as well as review articles covering both the challenges and applications of image processing and vision in healthcare, for the betterment of human life.

Various important areas are covered here, broadly medical imaging for healthcare, vision systems in healthcare applications, pattern recognition related to healthcare, big data and data mining in healthcare, multimodal integration for healthcare, affective computing, biometrics issues related to healthcare, and action or emotion or behavior analysis/recognition [2, 3] for healthcare applications, and so forth. For example, in order to develop smart homes for elderly people, comprehending various activities based on image or video or sensor are very crucial. Though we concentrated mainly on video-based analysis from a digital camera or similar image sensors, normal and abnormal daily activity

understandings/recognition [4] based on other sensors are widely explored in the last several years. This special issue was approachable in other related areas too, for example, related databases, special system or instrumentations related to healthcare, nurse robot, big data, assistive technologies, and applications.

2. Various Approaches

We have received thirty-two manuscripts for this special issue under the umbrella of various advancements of imaging and vision in healthcare. Core topics of the submissions are brain detection, prediction in hypertension-nondiabetic patients, patient position on the goniometric assessment task, deconvolution model for MTF improvement in CT, knee arthroplasty, radiomics for cerebral aneurysm occurrence in MR angiography images, OCT retinal image segmentation, knee joint kinematics recognition, shape change analysis of human brain, classification of microscopic colonic images, 3D macrophage tracking, deep neural network-based medical image compression, reconstruction quality in digital breast tomosynthesis, phase-contrast X-ray imaging, medical image restoration, brain tumor growth investigation, eye-pointer interaction device, brain abnormality detection, quality index of medical images, brain MRI segmentation, assessment of bulged disk cervical vertebral, blue-white structure detection in dermoscopy images, and so forth.

Among 32 different submissions from various countries, we finally accepted 9 quality papers. None of these papers are

from guest editors. For the final acceptance of these papers, the average processing period was 4.5 months, after 2 or 3 revisions.

Y. Huang et al. presented intracellular mobility based on adaptive total variation optical flow model. They extracted the histograms of oriented optical flow (HOOF) [5] after the optical flow of intracellular mobility was calculated. Then, distances of different HOOFs were computed as the motion features. These are covered in “Quantitative Analysis of Intracellular Motility Based on Optical Flow Model.”

S. Han et al. proposed a deconvolution-based model for modulation transfer function (MTF) improvement in CT to achieve uniform spatial resolution. They considered eleven subband regions that can reduce noise as well as enhance spatial resolution. By exploiting approximate blurring point spread function (PSF) kernel, they proposed the work as “A Subband-Specific Deconvolution Model for MTF Improvement in CT.” It can perform well even in the soft tissue region.

The paper by V. Kelkar et al. shows variants of histogram shift method to enhance the hiding capacity for telemedicine application. In their reversible watermarking method for medical images, they achieved high peak signal-to-noise ratio (PSNR). The higher the PSNR value, the better the imperceptibility of the watermarking. They demonstrated better performance than classical histogram shifting-based algorithms [6] for this purpose.

Y.-M. Chen and S.-G. Miaou offered a new idea for non-invasive anemia detection in their paper titled “A Kalman Filtering and Nonlinear Penalty Regression Approach for Noninvasive Anemia Detection with Palpebral Conjunctiva Images.” In their anemia examining method, they considered a modified Kalman filter [7] along with a regression method with a penalty function. Their results were good compared with other similar methods.

V. Roy et al. proposed a method to remove motion artifacts from EEG signals. In the paper “Gaussian Elimination-Based Novel Canonical Correlation Analysis method for EEG Motion Artifact Removal,” they improved the canonical correlation analysis (CCA) [8] based approach by introducing Gaussian elimination method, called GECCA. Their approach is found to be better than similar few other CCA-based methods for removing EEG motion artifacts.

The paper by L. Fassina et al. evaluated the dynamics and kinematics of beating cardiac syncytia and studied the inotropic effects of electromagnetic simulation and so forth. In their work “Model of Murine Ventricular Cardiac Tissue for *In Vitro* Kinematic-Dynamic Studies of Electromagnetic and β -Adrenergic Stimulation,” they designed an *in vitro* model of murine ventricular cardiac tissue so that they can study various related parameters, for example, the contraction movement.

In this special issue, we could accept a few excellent review papers as well. Augmented reality (AR) becomes very crucial in various vision-based applications, including medical surgery. In this special issue, one of the papers, written by P. Vávra et al. under the title of “Recent Development of Augmented Reality in Surgery: A Review,” demonstrated the reality of the augmented reality in surgical procedures.

In this paper, we can get an in-depth summary and evaluation of recent works (from 2010 till 2016), published in PubMed and SCOPUS on AR and surgery. From several hundred research papers, they finally covered about one hundred important and related works to demonstrate the state of the art on AR-based surgery. Various application areas and future challenges are also profoundly addressed in this work.

Another review work is also published in this volume by R. Richert et al. In the paper “Intraoral Scanner Technologies: A Review to Make a Successful Impression,” R. Richert et al. reviewed intraoral scanner (IOS) technologies for dental and clinical applications. They highlighted the current technologies on IOS and their respective clinical approaches and impacts. Finally, they addressed a very important aspect, that is, the accuracy of IOS technologies, precision and trueness of IOS files, and the intermaxillary relationship to perform prosthetic rehabilitation for patients.

M. Machoy et al. comprehensively presented a review of the applications of optical coherence tomography (OCT) in dental diagnostics. At the basic level, various types of OCT and its operating principle are addressed. OCT can be used in various applications, but this survey addressed the involvement of OCT in the arena of dentistry. A number of tables illustrated the OCT facilities, OCT in cardiology and restorative dentistry, in endodontics, in prosthetics, in diagnostics of oral tissues and implantology, in orthodontics, and so on in the last five years. These can be very useful for researchers.

3. Conclusion

In this short note, we presented the background and papers that are covered in the special issue on the advancements of image processing and computer vision for healthcare. From 32 submissions, 9 papers are finally selected with the rigorous review process. These works will contribute to the community. We wish to have more research works on healthcare.

Acknowledgments

We sincerely acknowledge the enormous contributions from authors and supports from many expert reviewers.

Md Atiqur Rahman Ahad
Syoji Kobashi
João Manuel R. S. Tavares

References

- [1] L. Chen, J. Hoey, C. D. Nugent, D. J. Cook, and Z. Yu, “Sensor-based activity recognition,” *IEEE Transactions on Systems, Man, and Cybernetics, Part C (Applications and Reviews)*, vol. 42, no. 6, pp. 790–808, 2012.
- [2] M. A. R. Ahad, *Computer Vision and Action Recognition*, Atlantis Press, The Netherlands, 2011, available in Springer, Germany.
- [3] M. A. R. Ahad, *Motion History Images for Action Recognition and Understanding*, Springer, Germany, 2013.

- [4] Z. Z. Islam, S. M. Tazwar, M. Z. Islam, S. Serikawa, and M. A. R. Ahad, "Automatic fall detection system of unsupervised elderly people using smartphone," in *5th IIAE International Conference on Intelligent Systems and Image Processing*, Hawaii, USA, 2017.
- [5] R. Chaudhry, A. Ravichandran, G. Hager, and R. Vidal, "Histograms of oriented optical flow and Binet-Cauchy kernels on nonlinear dynamical systems for the recognition of human actions," in *2009 IEEE Conference on Computer Vision and Pattern Recognition*, pp. 1932–1939, Miami, FL, USA, June 2009.
- [6] Z. Ni, Y.-Q. Shi, N. Ansari, and W. Su, "Reversible data hiding," *IEEE Transactions on Circuits and Systems for Video Technology*, vol. 16, no. 3, pp. 354–362, 2006.
- [7] R. E. Kalman, "A new approach to linear filtering and prediction problems," *Journal of Basic Engineering*, vol. 82, no. 1, pp. 35–45, 1960.
- [8] J. Gao, C. Zheng, and P. Wang, "Online removal of muscle artifact from electroencephalogram signals based on canonical correlation analysis," *Clinical EEG and Neuroscience*, vol. 41, no. 1, pp. 53–59, 2010.

Research Article

A Subband-Specific Deconvolution Model for MTF Improvement in CT

Seokmin Han,¹ Kihwan Choi,² and Sang Wook Yoo²

¹Korea National University of Transportation, Chungju, Republic of Korea

²Samsung Electronics, Suwon-si, Kyunggi-do 443-742, Republic of Korea

Correspondence should be addressed to Kihwan Choi; kihwan@gmail.com and Sang Wook Yoo; sangwook.yoo@gmail.com

Received 17 February 2017; Revised 2 June 2017; Accepted 8 June 2017; Published 25 October 2017

Academic Editor: João Manuel R. S. Tavares

Copyright © 2017 Seokmin Han et al. This is an open access article distributed under the Creative Commons Attribution License, which permits unrestricted use, distribution, and reproduction in any medium, provided the original work is properly cited.

The purpose of this research is to achieve uniform spatial resolution in CT (computed tomography) images without hardware modification. The main idea of this study is to consider geometry optics model, which can provide the approximate blurring PSF (point spread function) kernel, which varies according to the distance from X-ray tube to each pixel. The FOV (field of view) was divided into several band regions based on the distance from X-ray source, and each region was deconvolved with different deconvolution kernels. Though more precise calculation for the PSF for deconvolution is possible as the number of subbands increases, we set the number of subbands to 11. 11 subband settings seem to be a balancing point to reduce noise boost, while MTF (modulation transfer function) increase still remains. As the results show, subband-wise deconvolution makes image resolution (in terms of MTF) relatively uniform across the FOV. The results show that spatial resolution in CT images can be uniform across the FOV without using additional equipment. The beauty of this method is that it can be applied to any CT system as long as we know the specific system parameters and determine the appropriate PSF for deconvolution maps of the system. The proposed algorithm shows promising result in improving spatial resolution uniformity while avoiding the excessive noise boost.

1. Introduction

Image quality is of primary concern in diagnostic and screening imaging. Among many elements that affect the image quality, resolution is one of the most concerned. For the early detection of diseases, high spatial resolution imaging is very important. The goal of high spatial resolution is to look into small structures such as airways, arteries, and lesions as well as to detect small changes, so that prevention and intervention can be made earlier. The spatial resolution of a CT image is affected by a number of factors including the focal spot size of X-ray tube, detector size, scattering, magnification, the number of projections per rotation, and the reconstruction process [1]. The contribution of each factor is hard to determine separately; however, they can be lumped into PSF which determines the final measured resolution in the images. It is also known that the resolution in the FOV decreases as the distance from isocenter increases, which results in spatial variation of resolution. The spatial

variation of resolution can be also considered as spatial variation of PSF. This variation affects the image quality, which sometimes can cause mistakes in inspection, such as overlooking a calcification at the periphery region. Because of the spatial variation of resolution, the patient table is steered so that the heart of the imaged patient should be located at the isocenter. If the problem of the spatial variation of resolution is alleviated, it can be beneficial for improving the imaging workflow.

Different techniques have been used to overcome this problem. They can be divided into two categories. One category is to employ specially designed hardware such as high-resolution detector [2], focal-spot wobbling on the X-ray tube [3, 4], or aperture collimator to refine the focus of X-ray source [5]. The other category is to apply model-based computation such as optics model [6–10] or system model [11–15]. Each method has its own advantage. However, the idea of recovering the inherent spatial resolution of CT images using the knowledge of the system blurring

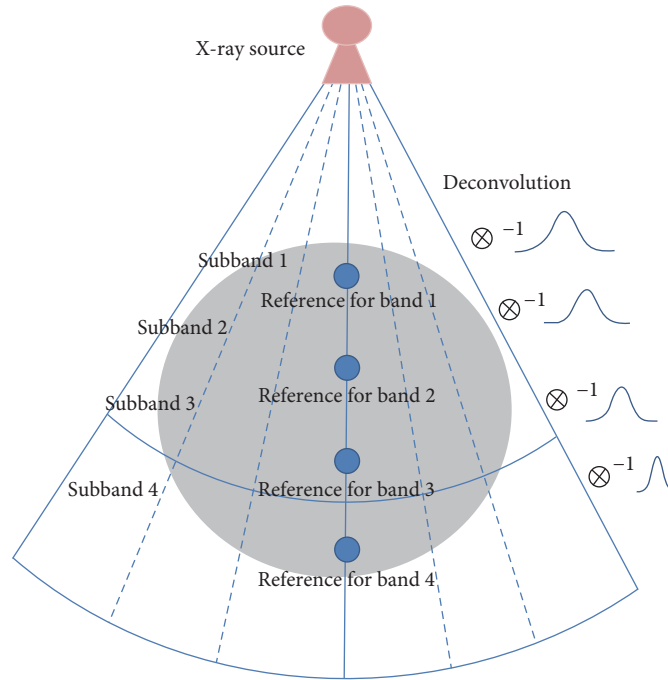


FIGURE 1: If the distance from X-ray source to ROI is close, the divergence of beam becomes wide.

PSF and its deconvolution can be practical in that it does not require any additional hardware modification. The main idea of this study is to consider geometrical optics model, which can provide the approximation of the blurring PSF kernel dependent on the distance from X-ray tube to each pixel. Based on the approximation, we can deconvolve each pixel to recover the inherent spatial resolution of CT images.

While previous methods generally employ iterative reconstruction or forward projection to combine PSF with reconstruction, the authors' method is an analytical method like FBP (filtered backprojection). In the authors' previous method [16], we had to increase the number of measurements to precisely estimate the variation of the blurring PSF. In the proposed method, we estimate the variation of the blurring PSF based on the fixed number of measurements. And it should be also noted that the purpose of the previous method was to enhance MTF at the isocenter, not to make MTF uniform across the FOV. The proposed method is an extended method of the previous method [16] in that it does not require PSF measurement in every subband and can be applied to alleviate the problem of spatial variation of reconstructed image resolution in CT.

2. Methods and Materials

To improve the resolution of reconstructed CT image, deconvolution procedure was employed. Backprojection is calculating the contribution of each voxel of the imaged structure to the measured data. For the calculation, the images of all views are backprojected and accumulated. The backprojection of each view was separated into several band

regions according to the distance from the X-ray source, and each of the band regions was deconvolved with a corresponding deconvolution kernel. Because X-ray source moves along a scanning trajectory, the distance from the source to an arbitrary point in the FOV varies. Therefore, each point in the FOV goes through plural band regions. As a result, each point in the reconstructed image is deconvolved with plural corresponding deconvolution kernels, which can be regarded as a function dependent on the distance from isocenter.

2.1. The Concept of Subband Deconvolution of FOV. In fanbeam case, X-ray beam diverges as it propagates. The divergence depends on the distance from X-ray source to the measurement point, which is the ROI (region of interest). If it is far from the source, and close to the detector, the beam divergence becomes relatively narrow. We measured PSF bandwidth at five locations using 1 mm cylindrical rods of aluminium, and the Gaussian fit to each PSF was used as the deconvolution kernel. Thus, the kernel width was experimentally determined to approximate the PSF of the center of each subband. The precise measurement procedure is explained in the next section. For deconvolution, MATLAB built-in *deconvreg* function was applied. This concept is shown in Figure 1.

In Figure 1, we separated the FOV into three subbands. Each kernel corresponding to each subband was used to deconvolve the backprojection for each view. As illustrated in Figure 1, relatively wide kernel width corresponds to the subband close to the X-ray source, while relatively narrow kernel width corresponds to the subband far from the X-ray source.

2.2. The Calculation of Deconvolution Kernel Width. We deconvolved each subband in backprojected image for each view. To determine the kernel width values for each subband, we put cylindrical rods of aluminium in the FOV to measure the amount of blur, as can be seen in Figure 2. We measured the blur at five locations (0 cm, 7 cm, 14 cm, -7 cm, and -14 cm from isocenter). The rods were scanned at 120 kV, 100 mAs, and 60 rpm (rotations per minute), which provides 1440 views per rotation. The detector cell size was 1.09 mm, and each detector row has 912 cells. Ram-Lak filter was used for filtering the acquired sinogram, and slice thickness was 6 mm. Each location of the rods was on the line which connects the X-ray source and isocenter. The metal rod was scanned one by one at each location and produced five sinograms. Because we have five sinograms, we could have five acquisitions of data at each view. With the five acquisitions of data, we could estimate the amount of blur and the kernel width according to the distance from X-ray tube to each rod, based on the knowledge about the shape of the aluminium rod. From the estimated blur and kernel width, we obtained PSF. The PSFs were fitted to Gaussian functions, and we estimated the kernel width of the Gaussian functions. The estimated kernel width values were 0.1, 0.4, 0.95, 1.0, and 1.1. After the estimation of the kernel width at each location, we calculate the rational function expressed in (1) to approximate the relation between the kernel width and the distance from the X-ray source to the rod.

$$\sigma = \frac{ax^2 + bx + c}{dx + e}, \quad (1)$$

where x is the distance from the X-ray source, σ is the kernel width, and $a, b, c, d,$ and e are coefficients. To solve (1), at least five pairs of kernel width and distance from X-ray source are required. From (1), we could estimate deconvolution kernel width at any location in FOV. Different from the previous research of the authors [16], we applied model fit to the measurement in this research for comfortability in experiments and practical use, rather than measuring the blur at many locations across the FOV.

2.3. Subband Deconvolution-Based Backprojection. The subband that corresponds to a specific ROI varies, because X-ray source rotates along a scanning trajectory. Figure 3 shows the concept of the distance-divergence relation as the X-ray source rotates.

In case 1 of Figure 3, ROI is apart from isocenter, which makes the corresponding PSF varies in width as the distance from X-ray source varies. In case 2, ROI is at the isocenter, and the corresponding PSF does not vary. If we divide the FOV into several subbands, a specific ROI moves through plural subbands as X-ray source rotates along a scanning trajectory. This process is repeated until all views are backprojected and accumulated. In this way, each point in the FOV is assigned with a corresponding superposed kernel. In this research, we set the number of subbands to 11, which was found experimentally to give the balance between the overshoot and MTF improvement.

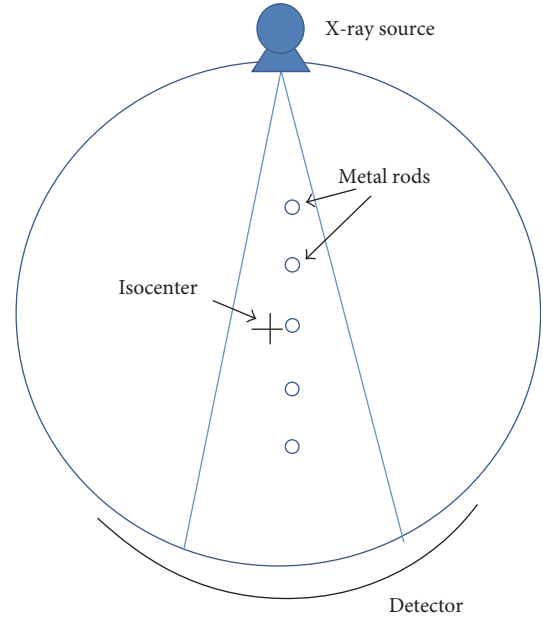


FIGURE 2: Locations to measure the kernel width in FOV.

This process can be summarized by the following:

$$f(x, y) = \int_0^{2\pi} \left[\sum_{i=1}^n d_i \left[L^{-2} \int_{-\gamma_m}^{\gamma_m} q(\gamma, \beta) h(\gamma' - \gamma) D \cos(\gamma) d\gamma \right] \right] d\beta, \quad (2)$$

where $f(x, y)$ is the image, n is the number of subbands (in this research, we set this number to 11), d_i is the deconvolution function for i th subband, L is the distance from the X-ray source to the point of reconstruction (x, y) , β is the projection angle, γ is the detector angle, γ_m is the maximum detector angle from the centerline of the detector, $q(\gamma, \beta)$ is the projection sample, γ' is the detector angle of the ray that passes through (x, y) , $h(\gamma' - \gamma)$ is the filter, and D is the distance between X-ray source and isocenter. Except the deconvolution function d_i and the summation of the deconvolved subbands, the equation equals to the ordinary FBP [17].

3. Experiments and Results

We acquired the sinogram data of Helios QA phantom using BodyTom CT scanner (NeuroLogica Inc., Danvers, MA), moving the phantom 6 mm, 47 mm, 79 mm, 127 mm, and 171 mm from the isocenter. The scanning parameters used for the CT scanner were 120 kV and 100 mAs with 1440 views per rotation (acquired over 360°) at 60 rpm (rotation per minute). The detector cell size was 1.09 mm, and each detector row has 912 cells. By default, Ram-Lak filter was used for filtering the acquired sinogram, and slice thickness was 6 mm. In addition, the filtered sinogram was deconvolved with appropriate Gaussian kernels. For the deconvolution, we divided FOV to 11 subbands and applied MATLAB built-in *deconvreg* function to each subband, to which appropriate Gaussian filter was assigned.

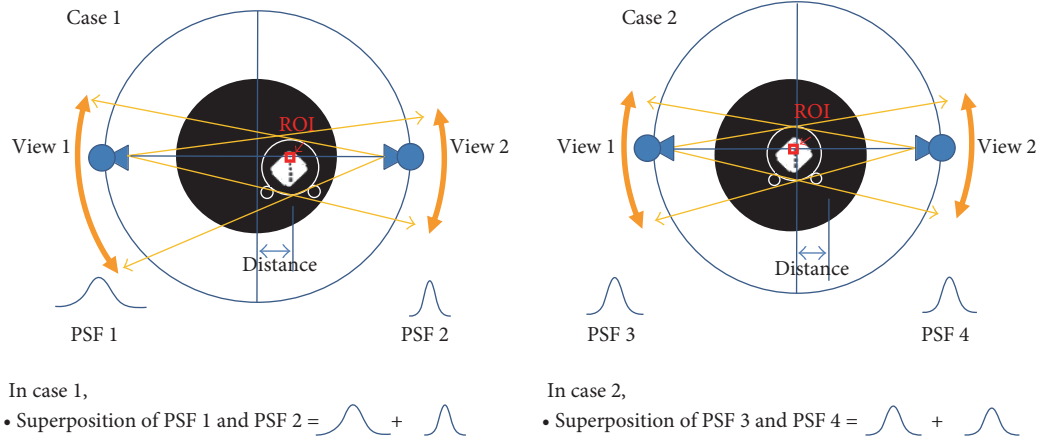


FIGURE 3: The closer is the distance from the X-ray source to ROI, the wider is the divergence of beam.

The subband deconvolution was applied to each Helios QA phantom sinogram. To test the feasibility of the proposed method, about 25 images have been reconstructed. In Figure 4, the region for MTF measurement is described. The region pointed by red arrow corresponds to 10 lp/cm.

In Figure 5, the reconstructed Helios QA phantom images at 6 mm, 47 mm, and 127 mm from the isocenter are shown. For comparison, normal FBP images, sharpened FBP images, and 11 subband-reconstructed images are presented.

The performance was measured in terms of MTF of the reconstructed image. In Figure 6, the MTF values measured at 10 lp/cm are shown as MTF curves. In Figure 6(a), the MTF values of each method are drawn for comparison. Absolute values of them have different ranges. Absolute value of the proposed method has a range of almost 20, which is much higher than the other methods. Thus, we also present the MTF values normalized by each of the MTF values at 6 mm from isocenter in Figure 6(b). Seeing the result in Figure 6, it seems that MTF of the proposed method remains relatively stable at each position.

In Figure 7, the proposed method is compared with the previous method of the author [16]. In the previous method, the subband-specific kernel width is not estimated using a model, but measured at each subband. And it should be also noted that the purpose of the previous method was to enhance MTF at isocenter, not to make MTF uniform across the FOV. As can be seen in Figure 7, the proposed method shows much more uniform and stable MTF.

In Figure 8, the reconstructed lung phantom images are shown for a simulation of clinical image. For comparison, normal FBP image, sharp reconstructed image, and 11 subband-reconstructed images are shown. As can be seen in Figure 8, the proposed method does not show much overshoot while maintaining relatively sharp edge.

Though the material of lung phantom is close to soft tissue in human body and it is not used for MTF measurement, we tried to measure MTF values at several positions of the lung phantom image to show the effect of the proposed method. MTF curves measured at several points are

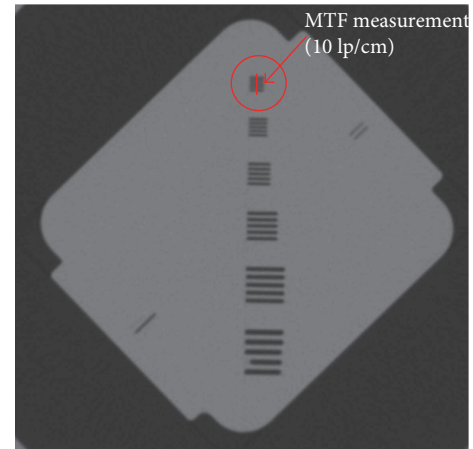


FIGURE 4: Helios image for describing MTF measurement region.

presented in Figure 9. As can be seen in Figure 9, MTF curves of the proposed method show higher MTF values than normal MTF or sharpened MTF at relatively high-frequency region. Particularly, the location of the intersect between MTF curves of the proposed method and 0.1 MTF seems to remain relatively stable, near 0.05 cycles/pixel. This shows that the proposed method seems to work even in soft tissue region.

4. Discussion

The proposed method shows a promising result in that the reconstructed image can have relatively uniform resolution across the FOV, in terms of MTF. Another advantage of the proposed method is that it is an analytical method, without thresholding or regularization. The proposed method implicitly assigns appropriate kernels to each pixel. Because we know that X-ray beam diverges as it propagates, we apply wide width PSF to the subband region close to X-ray tube for deconvolution and narrow width PSF to the far subband region. This process is done view by view, and the resultant

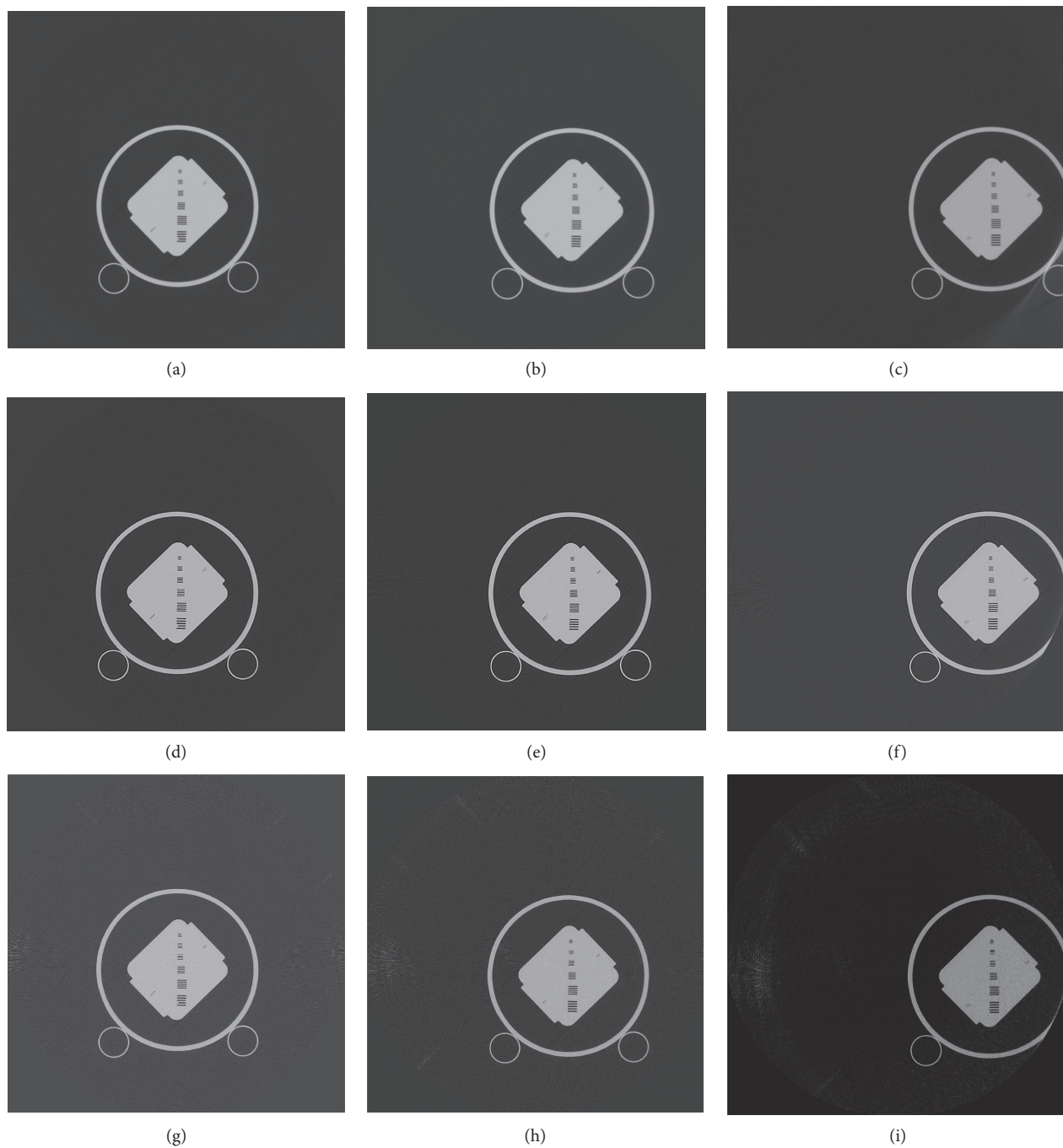


FIGURE 5: Helios images. (a) 6 mm from isocenter (FBP), (b) 47 mm from isocenter (FBP), (c) 127 mm from isocenter (FBP), (d) 6 mm from isocenter (sharp FBP), (e) 47 mm from isocenter (sharp FBP), (f) 127 mm from isocenter (sharp FBP), (g) 6 mm from isocenter (11 subbands), (h) 47 mm from isocenter (11 subbands), (i) 127 mm from isocenter (11 subbands).

effect of deconvolution kernel width for each pixel is the summation of the deconvolution PSF kernels for that pixel. Thus, we can provide different deconvolution PSF with different location in the FOV. The resultant image can be considered as deconvolved by location-dependent filters. Therefore, we can guess that it may be better to have many subbands to restore the signal. Though more precise calculation for the PSF for deconvolution is possible

as the number of subbands increases, we set the number of subbands to 11 experimentally. 11 subband settings seem to be the balancing point to reduce noise boost, while MTF increase still remains.

As the results show, subband-wise deconvolution makes image resolution (in terms of MTF) relatively uniform across the FOV. MTF values were kept around 20% from 6 mm to 127 mm apart from the isocenter. This can be

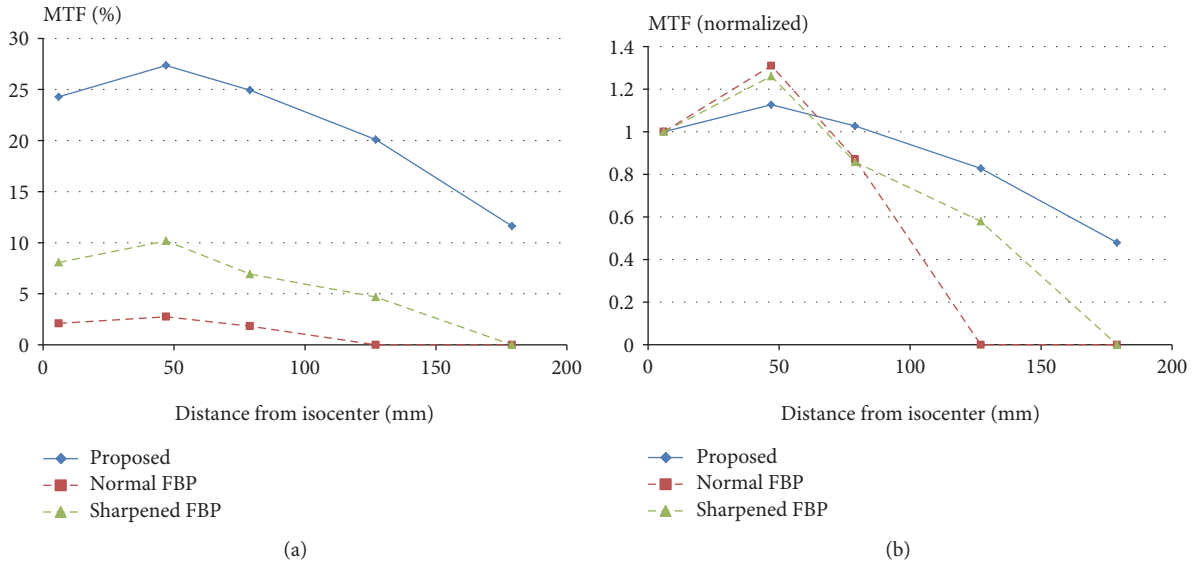


FIGURE 6: (a) MTF curves at 10 lp/cm as the phantom moves from isocenter. (b) MTF curves normalized by each of the MTF values at 6 mm from isocenter.

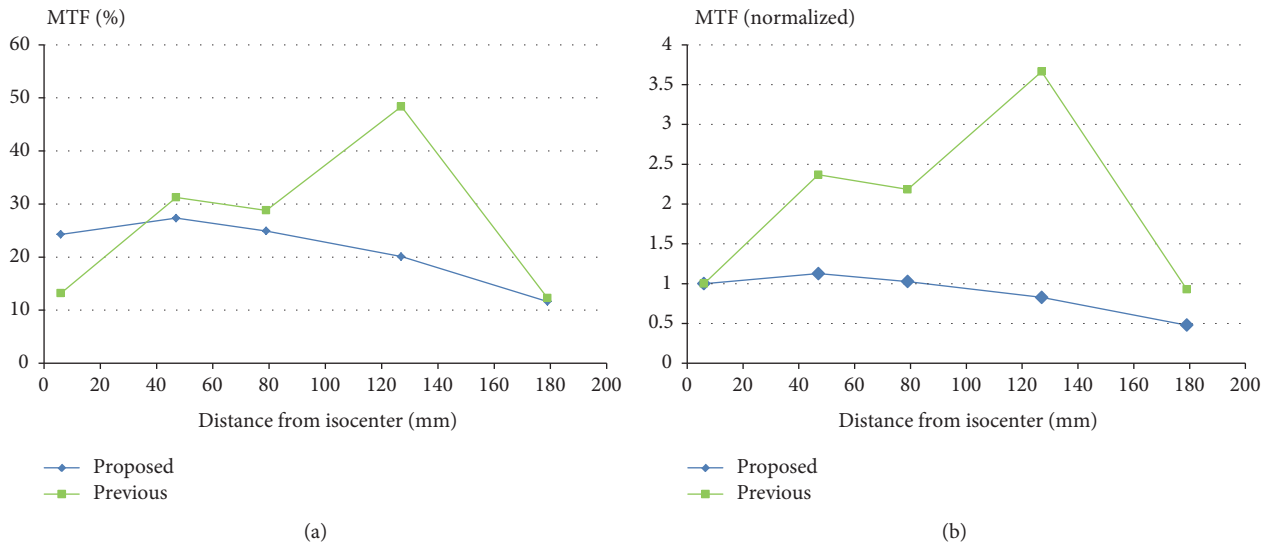


FIGURE 7: The previous method of the author [16] is compared with the proposed method. (a) MTF curves at 10 lp/cm as the phantom moves from isocenter. (b) MTF curves normalized by each of the MTF values at 6 mm from isocenter.

very beneficial in clinical situation, because relatively uniform resolution alleviates the necessity to move the patient table so that the imaging region should be near the isocenter. If the location-dependent filter completely restores the signal, MTF values may be equal across the FOV. For complete restoration of the signal, denser PSF measurements across the FOV may be requisite. Currently, we assumed that the same PSF width can be applied in a sub-band region. However, the subband can be also divided in angular direction to make the location-dependent filter more accurate.

5. Conclusion

The results show that spatial resolution in CT images can be uniform across the FOV without using additional equipment. The beauty of this method is that it can be applied to any CT system as long as we know the specific system parameters and determine the appropriate deconvolution PSF maps of the system. The proposed algorithm shows promising result in improving spatial resolution uniformity while avoiding the excessive noise boost. This technique can possibly improve the detection and quantification of small structures

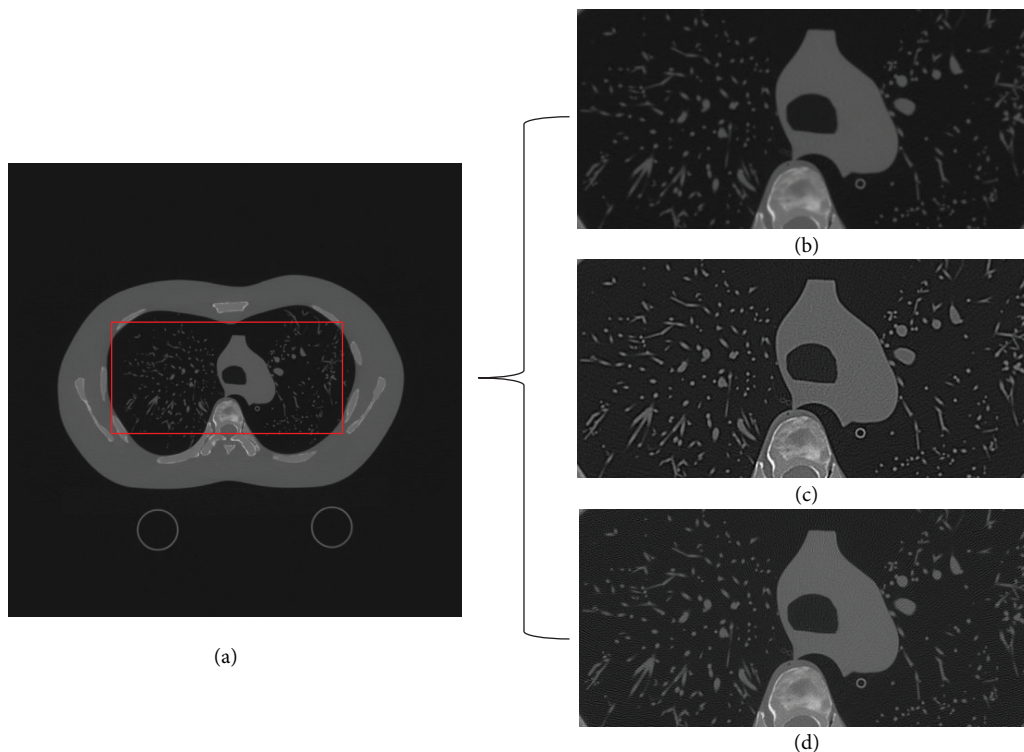


FIGURE 8: Lung phantom images. (a) The region to be compared. (b) FBP, (c) sharp FBP, and (d) 11 subband-reconstructed images.

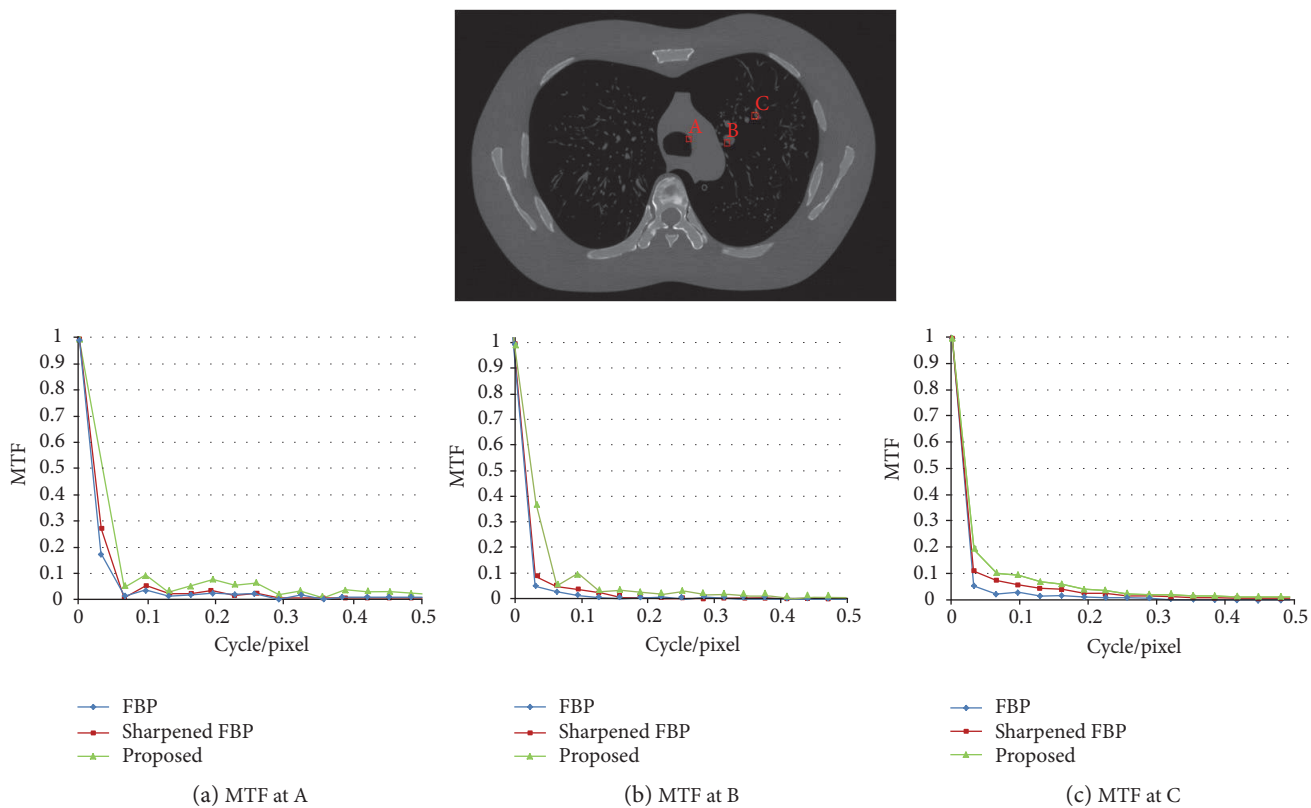


FIGURE 9: (a) MTF curve at A, (b) MTF curve at B, and (c) MTF curve at C.

in the heart, lung, and brain images and improve workflow efficiency by alleviating the necessity to move the patient table so that the imaging region should be near the isocenter.

Disclosure

When the study was performed, the authors Kihwan Choi and Sang Wook Yoo were employees of Samsung Electronics, Suwon-si, Kyunggi-do 443-742, Republic of Korea; this study was done independently of their employment.

Conflicts of Interest

The authors declare that there is no conflict of interest regarding the publication of this paper.

References

- [1] A. Staude and J. Goebbels, "Determining the spatial resolution in computed tomography - comparison of MTF and line-pair structures," in *International Symposium on Digital Industrial Radiology and Computed Tomography*, pp. 20–22, 2011.
- [2] P. J. L. Riviere and X. Pan, "Sampling and aliasing consequences of quarter-detector offset use in helical CT," *IEEE Transactions on Medical Imaging*, vol. 23, no. 6, pp. 738–749, 2004.
- [3] X. Tang, S. Narayanan, J. Hsieh et al., "Enhancement of in-plane spatial resolution in volumetric computed tomography with focal spot wobbling-overcoming the constraint on number of projection views per gantry rotation," *Journal of X-Ray Science and Technology*, vol. 18, no. 3, pp. 251–265, 2010.
- [4] T. G. Flohr, K. Stierstorfer, S. Ulzheimer, H. Bruder, A. N. Primak, and C. H. McCollough, "Image reconstruction and image quality evaluation for a 64-slice CT scanner with z-flying focal spot," *Medical Physics*, vol. 32, no. 8, pp. 2536–2547, 2005.
- [5] Y. Zhu, D. Chen, Y. Zhao, H. Li, and P. Zhang, "An approach to increasing the resolution of industrial CT images based on an aperture collimator," *Optics Express*, vol. 21, no. 23, pp. 27946–27963, 2013.
- [6] M. Chang, Y. Xiao, and Z. Chen, "Improve spatial resolution by modeling finite focal spot (MFFS) for industrial CT reconstruction," *Optics Express*, vol. 22, no. 25, pp. 30641–30656, 2014.
- [7] M. Balda, J. Hornegger, and B. Heismann, "Ray contribution masks for structure adaptive sinogram filtering," *IEEE Transactions on Medical Imaging*, vol. 31, no. 6, pp. 1228–1239, 2012.
- [8] E. P. Visser, J. A. Disselhorst, M. Brom et al., "Spatial resolution and sensitivity of the Inveon small-animal PET scanner," *Journal of Nuclear Medicine*, vol. 50, no. 1, pp. 139–147, 2009.
- [9] V. Y. Panin, F. Kehren, C. Michel, and M. Casey, "Fully 3-D PET reconstruction with system matrix derived from point source measurements," *IEEE Transactions on Medical Imaging*, vol. 25, no. 7, pp. 907–921, 2006.
- [10] A. M. Alessio, C. W. Stearns, S. Tong et al., "Application and evaluation of a measured spatially variant system model for PET image reconstruction," *IEEE Transactions on Medical Imaging*, vol. 29, no. 3, pp. 938–949, 2010.
- [11] C. Hofmann, M. Knaup, and M. Kachelriess, "Effects of ray profile modeling on resolution recovery in clinical CT," *Medical Physics*, vol. 41, no. 2, article 021907, 2014.
- [12] H. Yu and G. Wang, "Finite detector based projection model for high spatial resolution," *Journal of X-Ray Science and Technology*, vol. 20, no. 2, pp. 229–238, 2012.
- [13] J. Nuyts, B. D. Man, J. A. Fessler, W. Zbijewski, and F. J. Beekman, "Modelling the physics in the iterative reconstruction for transmission computed tomography," *Physics in Medicine and Biology*, vol. 58, no. 12, pp. R63–R96, 2013.
- [14] L. Fu, K. Choi, and B. D. Man, "Enhancement of spatial resolution in model-based iterative CT reconstruction by using sinogram preprocessing filters," in *2012 IEEE Nuclear Science Symposium and Medical Imaging Conference Record (NSS/MIC)*, pp. 2278–2281, Anaheim, CA, 2012.
- [15] K. Li, J. Garrett, Y. Ge, and G. H. Chen, "Statistical model based iterative reconstruction (MBIR) in clinical CT systems. Part II. Experimental assessment of spatial resolution performance," *Medical Physics*, vol. 41, no. 7, article 071911, 2014.
- [16] S. Han, K. Choi, S. W. Yoo, and J. Yi, "A distance driven deconvolution method for CT image resolution improvement," *Journal of the Korean Physical Society*, vol. 69, no. 12, pp. 1830–1833, 2016.
- [17] J. Hsieh, *Computed Tomography: Principles, Design, Artifacts, and Recent Advances*, SPIE Press, 2nd edition, 2009.

Research Article

Gaussian Elimination-Based Novel Canonical Correlation Analysis Method for EEG Motion Artifact Removal

Vandana Roy,¹ Shailja Shukla,² Piyush Kumar Shukla,³ and Paresh Rawat⁴

¹Department of Electronics and Communication, Jabalpur Engineering College, Jabalpur 482011, India

²Department of Computer Sciences and Engineering, Jabalpur Engineering College, Jabalpur 482011, India

³Department of Computer Sciences and Engineering, University Institute of Technology, Bhopal 462023, India

⁴Department of Electronics and Communication, Truba Group of Institute, Bhopal 462023, India

Correspondence should be addressed to Piyush Kumar Shukla; pphdwss@gmail.com

Received 7 December 2016; Accepted 7 June 2017; Published 8 October 2017

Academic Editor: João Manuel R. S. Tavares

Copyright © 2017 Vandana Roy et al. This is an open access article distributed under the Creative Commons Attribution License, which permits unrestricted use, distribution, and reproduction in any medium, provided the original work is properly cited.

The motion generated at the capturing time of electro-encephalography (EEG) signal leads to the artifacts, which may reduce the quality of obtained information. Existing artifact removal methods use canonical correlation analysis (CCA) for removing artifacts along with ensemble empirical mode decomposition (EEMD) and wavelet transform (WT). A new approach is proposed to further analyse and improve the filtering performance and reduce the filter computation time under highly noisy environment. This new approach of CCA is based on Gaussian elimination method which is used for calculating the correlation coefficients using backslash operation and is designed for EEG signal motion artifact removal. Gaussian elimination is used for solving linear equation to calculate Eigen values which reduces the computation cost of the CCA method. This novel proposed method is tested against currently available artifact removal techniques using EEMD-CCA and wavelet transform. The performance is tested on synthetic and real EEG signal data. The proposed artifact removal technique is evaluated using efficiency matrices such as del signal to noise ratio (DSNR), lambda (λ), root mean square error (RMSE), elapsed time, and ROC parameters. The results indicate suitability of the proposed algorithm for use as a supplement to algorithms currently in use.

1. Introduction

EEG signal is widely used for exploring the human brain activity and is preferred over other physiological signals because they can be used to detect directly brain electrical activity changes over spans of millisecond time, whereas functional magnetic resonance imaging (fMRI) has time resolutions in seconds or minutes. Usually, EEG signal suffers from various motion artifacts generated at the capturing time. There are two main sources of artifact in neural signals other than the machine and environment. These are the muscular and ocular activities of the individual which generate low-amplitude, low-frequency electrical pulses that fall in filter range of sensors and recording equipment.

The EEG signal is contaminated by various artifacts as electrocardiogram (ECG), electrooculogram (EOG), and electromyogram (EMG). The EMG artifact is of more interest as it is having higher amplitude, broad spectrum, and variable topographical distribution than EEG signal [1]. The EMG artifacts have lower autocorrelation than EEG signal due to its wide frequency spectrum. Moreover, these artifacts resemble as temporal white noise. Therefore, artifact rejection is a fundamental research topic and is well researched in [2]. The EEMD is a data-driven and noise-assisted approach which is applied to remove motion artifacts from single-channel EEG signal [3].

A component-based automated separator of artifacts is required to linearly decompose the signals into source components. The components give the individual nature of

information, where artifact information combines into separate sources and reconstruction of signals without these sources are claimed as artifact-free information. The performance of blind source separation (BSS) methods as independent component analysis (ICA) and CCA for EEG signal eye blink artifact removal is compared in [4] and concluded that CCA is more accurate and faster than ICA. The CCA algorithm performs better than ICA for muscle artifact removal because these artifacts are generated due to movement of body muscle group. Moreover, these artifacts do not represent stereotyped topography [5]. Anastasiadou et al. [6] applied CCA algorithm to remove muscle artifact from EEG signal. Moreover, artifact removal approach is improved by applying WT after CCA algorithm for automatic detection and removal of muscle artifact from EEG signal [7]. The cascaded combination of EEMD and CCA techniques is applied for single-channel EEG artifact removal in [8, 9]. The single-channel EEG signal is converted into the multidimensional signal by EEMD technique. In CCA, a second-order statistics is applied to segregate the artifact components from the input signal and its performance is compared and presented better in comparison of existing wavelet denoising and EEMD-ICA cascaded algorithms. Chen et al. [10] have improved the filtering approach by applying EEMD and MCCA (multiset CCA) to remove EMG with more computational time. To remove ocular artifacts automatically, the cascaded combination of CCA and WT algorithms is proposed in [11] and demonstrated that the proposed method removes artifacts significantly with preserving neural activity of the original signal. Safieddine et al. [12] suggested that EEMD algorithm outperforms over other stochastic and deterministic artifact removal approaches and WT algorithm performs well in the case of less noisy data.

An efficient cascaded approach EEMD-CCA-SWT is found successful for EEG motion artifact removal [13]. The combination of EEMD, CCA, and SWT approaches has been applied for effective suppression of the motion artifact from EEG signal. This three-stage cascaded approach removes the artifacts effectively with increased computational cost. This computational complexity is reduced in this research paper by developing an existing correlation-based algorithm with Gaussian elimination (GE) and inserted at the cascade of EEMD-SWT, leading to EEMD-GECCA-SWT which is the combination of EEMD and an improved approach GECCA (Gaussian elimination canonical correlation analysis) with SWT. This increased computational cost is effectively reduced due to applying GECCA approach in place of CCA. The left matrix division applied in GECCA allows better estimates for the matrix inversion; therefore, it improves the SWT filtering efficiency and thus improves the overall efficiency of the EEG motion artifact removal.

The paper organization is as the following. The artifact removal methods are recalled in Section 2, and then the proposed algorithm is discussed in Section 3. Details of applied EEG dataset is given in Section 4; results obtained by methods are presented, compared in tabular form, and detailed discussed in Section 5. Finally, conclusion is in Section 6.

2. Artifact Removal Methods

2.1. Ensemble Empirical Mode Decomposition. The EEMD algorithm decomposes a signal into a number of intrinsic mode functions (IMFs) through an iterative method termed as sifting [12]. At first level, the IMF1 is the mean of upper and lower envelop of original EEG signal $X(t)$. Then residual signal is obtained by subtracting IMF1 from $X(t)$. This process is iterated till stopping criterion is fulfilled (residual signal energy content is close to zero). The remaining residual signal is

$$P_n(t) = P_{n-1}(t) - \text{IMF}_n(t), \quad (1)$$

where $P_n(t) = X(t)$.

Finally, the signal is reconstructed by adding all IMFs and residual signal as

$$X(t) = P_n(t) + \sum_{i=1}^N \text{IMF}_i(t). \quad (2)$$

2.2. Gaussian Elimination Canonical Correlation Analysis (GECCA). The standard existing CCA algorithm starts with an assumption that $X[n]$ and $Y[n]$ are two sets of random variables [4]. $X[n]$ is the input vector of matrix and $Y[n]$ is defined as temporally correlated by 2-D valid convolution operator from $X[n]$ vectors using the linear convolution mask $[1 \ 0 \ 1]$ as

$$Y[n] = \text{conv2}(X, [1 \ 0 \ 1]). \quad (3)$$

Merging both input vectors as

$$Z = [X; Y]. \quad (4)$$

If ρ is the maximum canonical correlation, C_{xx} , C_{yy} are auto covariances of vectors X and Y , respectively, and C_{xy} and C_{yx} are the cross covariance between vectors X and Y . The various possible correlation matrixes are

$$C_{xx} = C(1 : sx, 1 : sx) + \beta * \text{eye}(sx), \quad (5)$$

where sx is the size of the X , sy is the size of the Y , β is the predefined small residual constant which is set to 10^{-8} in this paper which is used by standard CCA method [2], and eye is the identity matrix with diagonal terms as 1 and all other terms are zero. The term $\beta * \text{eye}(sx)$ is used in order to set and maintain the initial nonzero value of the covariance matrix C_{xx} . The small value of β does not affect the covariance matrix values much.

$$C_{xy} = C(1 : sx, sx + 1 : sx + sy),$$

$$C_{yx} = C_{xy}',$$

$$C_{yy} = C(sx + 1 : sx + sy, sx + 1 : sx + sy) + \zeta * \text{eye}(sy),$$

$$C_{yy}^{-1} = \text{inv}(C_{yy}).$$

(6)

Two different canonical solutions are obtained from Z by calculating the covariance as

$$C = \text{cov}(Z.^'). \quad (7)$$

This is equivalent to two linear equations in X and Y vector directions, respectively, as

$$\begin{aligned} p[n] &= a * X[n], \\ q[n] &= b * Y[n], \end{aligned} \quad (8)$$

where a and b are weight vectors and $p[n]$ and $q[n]$ are canonical variates correspondent to $X[n]$ and $Y[n]$, respectively.

The maximum correlation between variables a and b are calculated as [8]

$$\max(\rho) = \frac{a^T C_{xy} b}{\sqrt{a^T C_{xx} a} \sqrt{b^T C_{yy} b}}. \quad (9)$$

Now, the demixing matrix W is calculated by simplifying (9) as

$$\rho^2 a = \text{inv}(C_{xx}) * C_{xy} * \text{inv}(C_{yy}) * C_{yx} * a, \quad (10)$$

$$\rho^2 b = \text{inv}(C_{xx}) * (C_{xy}) * \text{inv}(C_{yy}) * C_{yx} * b, \quad (11)$$

where ρ^2 is calculated by obtaining Eigen values (k) of (10) and (11) and further, a and b variables are equal to Eigen vectors for the greatest value of k (Eigen value).

These weight vectors a and b are replaced in (8) to calculate canonical variates $p[n]$ and $q[n]$. Moreover, the demixing matrix W can be calculated by inverse of estimated weight vector ($W = a^{-1}$). Finally, the source $S[n]$ is estimated by applying W and $p[n]$ or $q[n]$ as

$$S[n] = W^T p[n]. \quad (12)$$

Thus, it is observed that standard CCA algorithm uses the matrix inverse operation to solve the linear equations by obtaining the maximum value of ρ^2 for determining the demixing matrix W .

In this research paper, a fast and efficient modified CCA algorithm is proposed which uses the backslash or left matrix division operator for solving the linear (10) and (11) to calculate Eigen values. This backslash operator is fast and efficient than the inverse operator. The remaining algorithm is similar to the CCA approach. Let us define the linear (10) as

$$G = \rho^2 = \text{inv}(C_{xx}) * C_{xy} * \text{inv}(C_{yy}) * C_{yx}, \quad (13)$$

$$G = \rho^2 = A * B, \quad (14)$$

where

$$A = \text{inv}(C_{xx}) * C_{xy} = C_{xx}^{-1} * C_{xy}, \quad (15)$$

$$B = \text{inv}(C_{yy}) * C_{yx} = C_{yy}^{-1} * C_{yx}. \quad (16)$$

The parameters A and B from linear (15) and (16) are defined as

$$\begin{aligned} A * C_{xx} &= C_{xy}, \\ B * C_{yy} &= C_{yx}. \end{aligned} \quad (17)$$

Standard CCA method uses matrix inverse to obtain the value of A and B . In this paper, the left matrix division is proposed to solve these linear (15) and (16).

The left division operator as $C_{xx} \setminus C_{xy}$ can be defined as a matrix division of C_{xx} into C_{xy} , which is equal to the solution of $\text{inv}(C_{xx}) * C_{xy}$. If C_{xx} is an N -by- N matrix and C_{xy} is a column vector with N components or a matrix containing several such columns, then $A * C_{xx} = C_{xy}$ equation can be defined in terms of left division operator as $A = C_{xx} \setminus C_{xy}$.

The similar solution can be defined for the matrix B . The solution of (15) and (16) can be written as

$$A = C_{xx} \setminus C_{xy}, \quad (18)$$

$$B = C_{yy} \setminus C_{yx}. \quad (19)$$

Equations (18) and (19) suggest that the role of inverse operation is avoided to obtain the value of parameters A and B . This will simplify the equation and thus computation time too.

2.2.1. The Justification of Left Division Operator Employed in GECCA. In order to prove left division operator, the numerator and denominator are multiplied by numerator transposed as

$$\begin{aligned} A &= C_{xx}^T * C_{xx} \setminus C_{xx}^T * C_{xy}, \\ B &= C_{yy}^T * C_{yy} \setminus C_{yy}^T * C_{yx}. \end{aligned} \quad (20)$$

By shuffling the order of operator by using Gaussian elimination concept,

$$A = C_{xx}^T * (C_{xx} * C_{xx}^T) \setminus C_{xy}, \quad (21)$$

$$B = C_{yy}^T * (C_{yy} * C_{yy}^T) \setminus C_{yx}, \quad (22)$$

since C_{xx} and C_{yy} are N -by- N symmetric matrix and C_{xy} and C_{yx} are column vectors with N components or a matrix with several such columns.

Since $C_{xx} * C_{xx}^T = C_{yy} * C_{yy}^T = 1$, therefore, (21) and (22) can be written as

$$A = C_{xx}^T * (1) \setminus C_{xy}, \quad (23)$$

$$B = C_{yy}^T * (1) \setminus C_{yx}. \quad (24)$$

For symmetric and square matrix, $C_{xx}^T = C_{xx}$ and $C_{yy}^T = C_{yy}$.

Then (23) and (24) are simplified as

$$A = C_{xx} \setminus C_{xy}, \quad (25)$$

$$B = C_{yy} \setminus C_{yx}. \quad (26)$$

Replacing the values of A and B from (25) and (26) to (14), the solution of G is obtained as

$$G = (C_{xx} \setminus C_{xy}) * (C_{yy} \setminus C_{yx}). \quad (27)$$

The value of G is obtained without inverse operation by just applying left division operator. This solution not only saves the computation time but also increases the efficiency of the CCA method with minimizing the error. The obtained

$G = \rho^2$ is the Eigen value with k in descending order, that is, $k_1 > k_2 > k_n$; a and b are the Eigen vector for the greatest value of k .

Then the CCA component $p[n] = [p_1, p_2, \dots, p_n]$ are obtained by placing the vector $X[n]$ in (8), and sources are expected by using the weighted demixing matrix from X by using (12).

If A is a $M \times N$ matrix with $M \leq N$ and B is a column vector with M components, or a matrix with several such columns, then $X = A \setminus B$ is the solution in the least squares sense to the under or over determined system of equations $A * X = B$. The effective rank K of A is determined from the QR decomposition with pivoting. The solution X is computed which has at most K nonzero components per column.

2.2.2. Benefits of GECCA over CCA Algorithm. The advantage of GECCA Algorithm over CCA are as follows:

- (1) The operation of CCA algorithm depends on the inverse operation to find the demixing matrix. If the input matrix is not a square matrix, then this CCA algorithm fails. However, left division operator-based GECCA algorithm provides a solution if input matrix is not square.
- (2) The CCA algorithm involves the inverse of the matrix for their operation. The inverse operation is computationally complex and time-consuming. However, proposed GECCA algorithm is faster than CCA for obtaining the correlation-based source separation by employing left division operator in place of inverse operation.
- (3) The proposed GECCA algorithm employs left division operator. This operator allows better estimates of the matrix inversion. These efficiently estimated coefficients once applied to SWT filter improve the SWT filtering efficiency thus improving the overall efficiency of the motion artifact removal algorithm.
- (4) The CCA algorithm operation is not consistent in each situation. This issue can be overcome by the proposed GECCA algorithm.

The above discussed efficient and fast correlation-based algorithm applied with WT algorithm is discussed in the subsequent section.

2.3. Wavelet Transform (WT). The artifacts available in the EEG signal are suppressed with cascaded approach of EEMD and GECCA. Although, some brain actions may be disturbed due to high-frequency sensor noise and low-pass and high-pass filter components. As these noise signal frequencies will get overlap with the brain signals, then conventional filtering technique cannot be utilized and thus this WT is applied to take away unwanted noises from EEG signal [12].

The most frequently applied wavelet transform is discrete wavelet transform (DWT). In the case of EEG artifact removal, preserving neural information of the signal is determinant. Thus, some latest research shows that stationary

wavelet transform (SWT) is a powerful tool to remove artifacts of the signal with preserving the neural information of original EEG signal [14].

SWT algorithm is translation invariant, so no down-sampling of the data is involved. Translation-invariance is achieved by removing the down- and upsamplers as in the DWT and upsampling the filter coefficients by a factor of $2^{(j-1)}$ at the j th level of the algorithm. SWT is preferred as it removes unpredictable behavior and noise randomness in the EEG signal due to the motion artifacts remaining after two-stage filtering of EEG signals. Therefore, EEG signal gets smoothed over the length with containing all their fundamental properties. Finally, proposed algorithm based on discussed algorithm is discussed in the next section.

3. Proposed Algorithm

The proposed artifact removal algorithm is as follows:

- (1) Define the reference EEG data from the multichannel data set for correlation match.
- (2) The input artifact EEG channel is passed through EEMD to decompose with 3 ensembles to convert single-channel EEG into multichannel EEG data.
- (3) Generated IMFs are passed to GECCA algorithm for source separation.
- (4) The GECCA output contains traces of artifacts in the form of randomness and noise. Thus, the output of GECCA is applied further to SWT algorithm for effective artifact removal. The decomposition through SWT is performed on the frequency domain of the signal with Rigrsure thresholding.
- (5) Pearson's correlation coefficient is used for artifact recognition and their suppression and finally reconstructed to find the artifact-free signal.
- (6) Parametric evolution is carried out based on SNR and correlation improvement. The correlation is carried out with respect to reference original EEG data initially defined.
- (7) The parametric evaluation of the proposed method is done with existing motion artifact removal methods.

4. EEG Signal Data Set

The EEG data is a multichannel data considered from standard MIT scalp data set with 24 channels recorded with different electrodes. This dataset is available on PhysioNet. The data is taken for 10 seconds and with 2560 samples/signals. Sampling frequency is taken as 256 Hz, and sampling interval is of 0.00390625 sec. These data samples are reduced to 16 channels to satisfy the international standard of 10–20 channels. Figure 1 shows the first 16 channels of EEG data set available online with chb01_01_edfm.mat available at PhysioNet provided by Shoeb [15]. It is observed from Figure 1

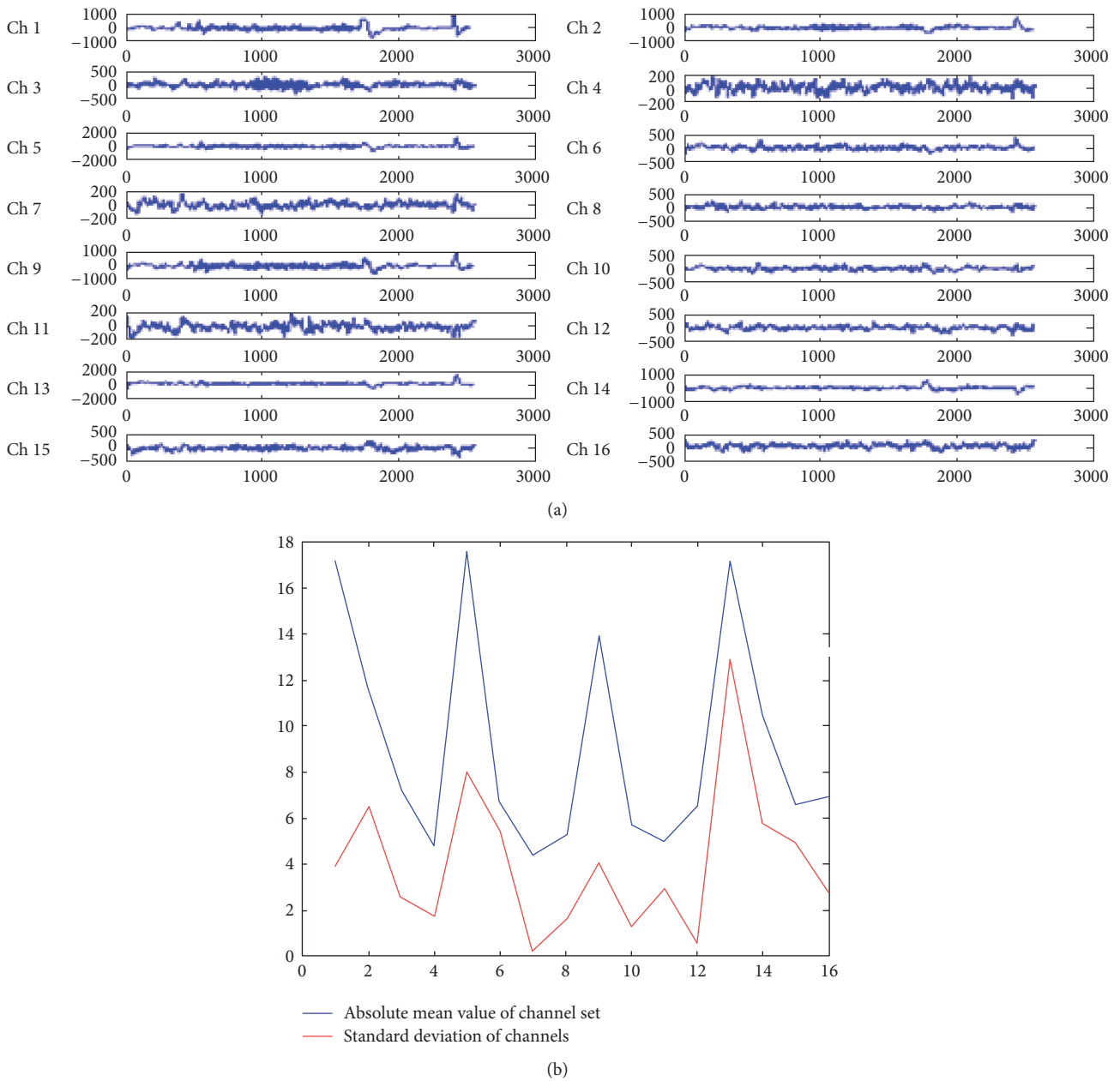


FIGURE 1: (a) Multichannel EEG data set containing the muscular and eye blink motions. (b) Statistical properties of EEG channels.

that each channel is recorded with different electrode having different motion characteristics.

In Figure 1(a), the channels 1, 5, 9, and 13 correspond to the eye blinks as shown by negative high peaks (scale of 1000 and 2000). This was displayed and referenced by Shoeb [15]. These channels (1, 5, 9, and 13) have maximum motion or artifacts since they have higher standard deviation 172.0907, 175.417, 136.129, and 170.467, respectively. In this paper, channel numbers 4, 7, and 11 have the least artifact effects (only with scale of 200) out of the 16 channel EEG signal, this can be quantitatively justified by their lowest mean value and standard deviation (on division by 10 scale) as shown in Figure 1(b). The channel 7 in Figure 1(a) has the smallest standard deviation ($=4,364,903$) and the smallest

absolute mean value ($=0.228125$) as shown in Figure 1(b) which justifies the minimum motion artifacts. Thus, the channel number 7 is used as a reference signal for correlation-based artifact removal. This reference signal is termed as original signal in the paper.

Figure 2 compares the original or reference EEG data (channel number 7) with blue color and artifactual signals (channel number 5) with red color. The channel 5 is shown here for the comparison because it has maximum standard deviation of 175.417 with maximum peak variations with eye blink. It is observed from Figure 2 that raw EEG data may suffer from either muscular motion artifact (shown under green rectangle) or eye blink artifact (shown under yellow rectangle) or both of them. The eye blink artifact

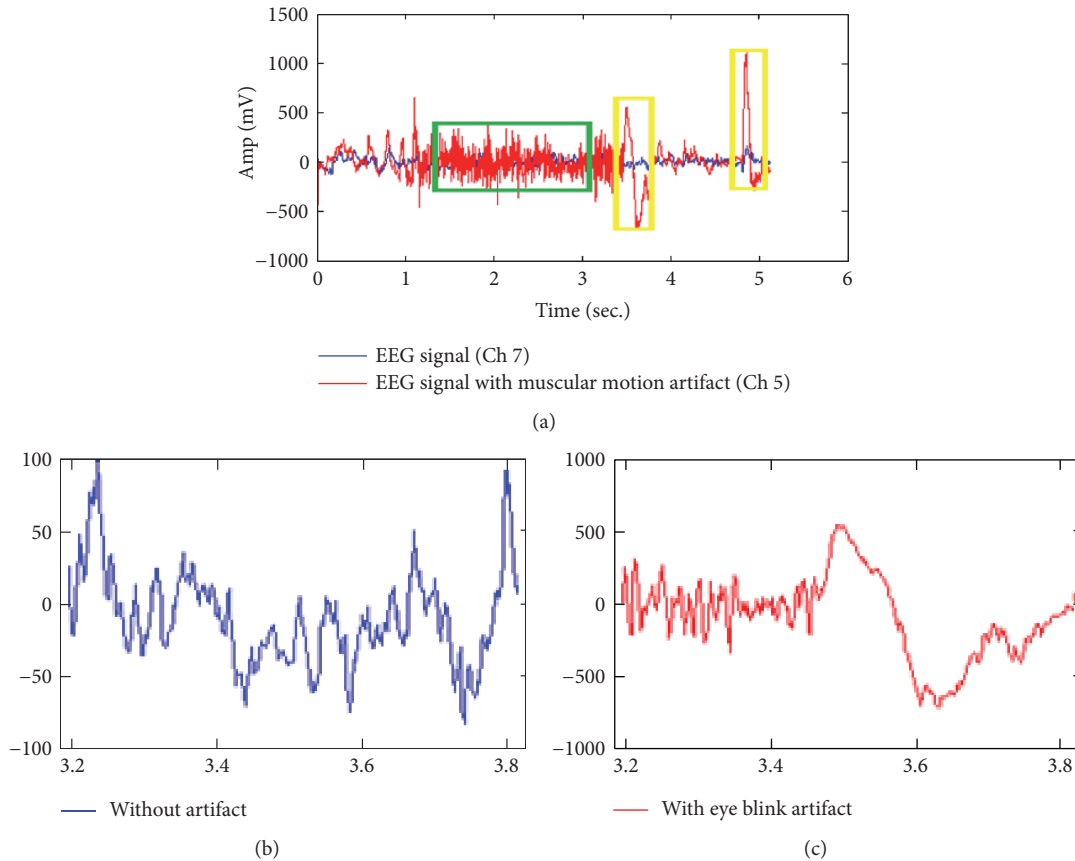


FIGURE 2: (a) Comparison of referenced channel 7 and artifact channel 5 for first 10 seconds. (b) Enhanced reference data channel 7. (c) Artifact channel 5 for 3-4 seconds respective to yellow rectangle.

may cause amplitude increase about 10 times greater than the original EEG data. The EOG artifact overlaps with EEG signal in impulsive form, while muscular motions cause random broad spectrum amplitude variations. Nature of the reference EEG data with and without artifacts is clearly shown in Figures 2(b) and 2(c).

The eye blink artifact may cause amplitude increase about 10 times greater than the original EEG data. The EOG artifact overlaps with EEG signal in impulsive form, while muscular motions cause random broad spectrum amplitude variations. In this paper, the muscular motion artifact signals (as in channel 5) are naturally generated at the time of EEG data capturing with electrodes. Therefore, for the sake of clarity, the enhanced version of reference and artifact signal is shown in Figures 2(b) and 2(c).

5. Result and Discussion

The novel GECCA artifact removal approach is evaluated on artifactual EEG channel number 5 and compared with CCA algorithm. Comparison of the EEG artifact removal methods for channel number 5 using CCA and GECCA along with DWT is shown in Figure 3. The EEG signal channel number 7 is considered as pure EEG signal. The comparison of the green and yellow boxes in Figures 3(a)

and 3(b) suggests that blind source separation- (BSS-) based proposed GECCA method removes the motion artifacts significantly better than the existing CCA-based method. Green rectangles are correspondent to CCA, and yellow rectangles are correspondent to GECCA. It is observed that the eye blink peaks with GECCA-DWT are minimized to half that of the eye blink peaks with CCA-DWT (of the order of ± 200 is reduced to around ± 100) as mentioned in fourth row of Figure 3. Moreover, the pattern of the second blink is also much similar to the reference EEG signal after GECCA-DWT.

The SWT algorithm is more proficient for artifact removal of neural EEG signal in comparison to DWT algorithm; consequently, the efficacy of proposed BSS approach (GECCA) is also evaluated with SWT and compared with CCA-based approaches. Figure 4 provides the comparison of the EEG artifact removal methods using CCA and GECCA along with SWT filtering. The artifact removal approaches are applied on channel number 5, and performance is compared with reference channel 7 EEG signal. The comparison of the respective green and yellow boxes in Figures 4(a) and 4(b) suggests that the proposed GECCA method removes the motion artifacts significantly better than the existing CCA-based method. In addition, the vigilant observation and comparison of the respective green rectangles in Figure 4(a) and yellow rectangles in Figure 4(b) suggests that

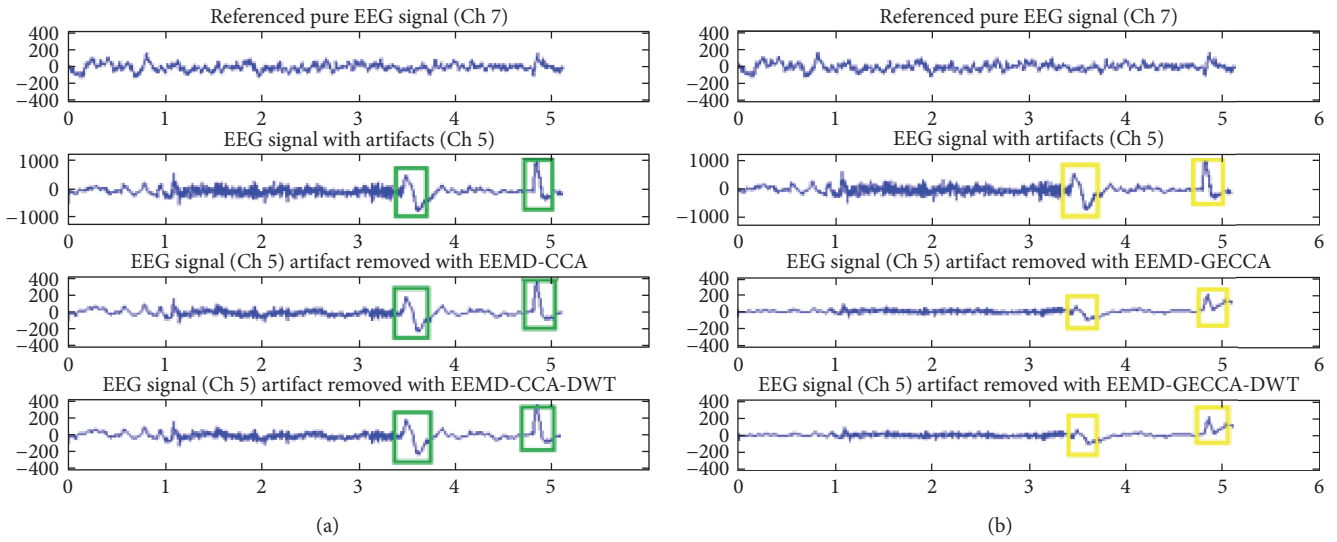


FIGURE 3: Comparisons of EEG artifact removal methods (a) with CCA and DWT and (b) with GECCA and DWT.

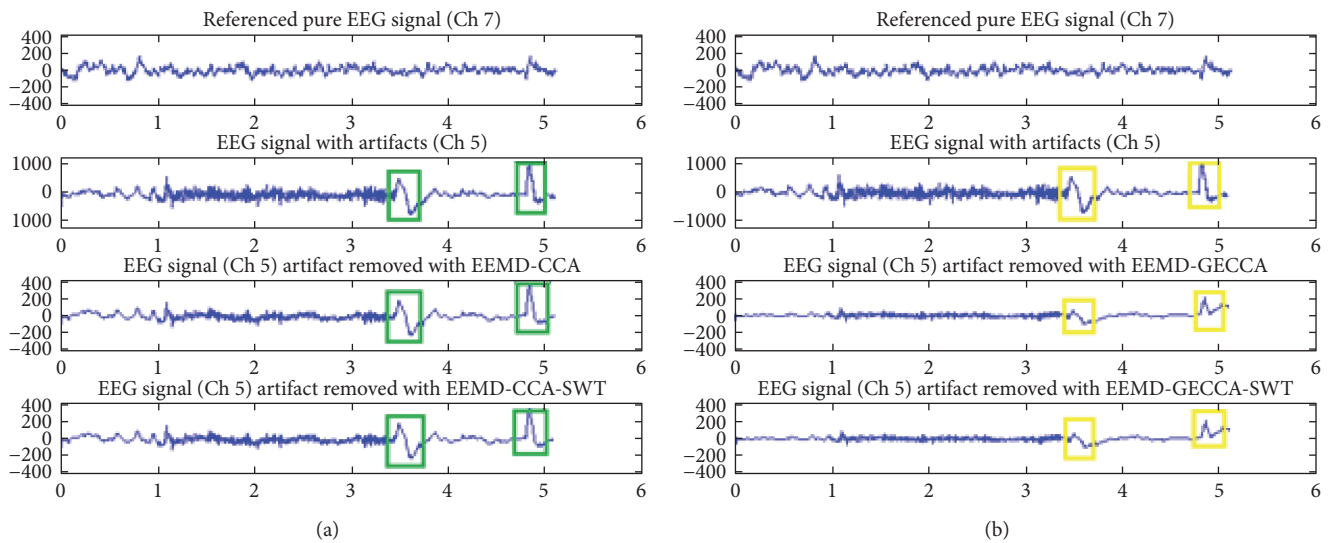


FIGURE 4: Comparisons of EEG artifact removal methods (a) with CCA and SWT and (b) with GECCA and SWT.

GECCA with SWT removes the eye blink effect better than CCA-SWT. It is observed that the eye blink peaks with GECCA-SWT are minimized to half that of the eye blink peaks with CCA-SWT (of the order of ± 200 is reduced to around ± 100) as mentioned in the fourth row of Figure 4. This could be quantitatively even better clear in the next sections with evaluation parametric comparison encapsulated in Table 1.

The 8 reconstructed signals after SWT-smoothed approach are compared for CCA and GECCA as shown in Figure 5. It is observed that GECCA method not only preserves the information but also provides better and fast estimates. This is concluded by comparing the 2nd and 4th frequency bands as shown in Figures 5(c) and 5(d).

Moreover, the proposed artifact removal method (EEMD-GECCA-SWT) outputs are compared for three

TABLE 1: Parametric comparison of the artifact removal methods with CCA and GECCA.

Algorithm Parameters	With DWT filtering		With SWT filtering	
	EEMD-CCA	EEMD-GECCA	EEMD-CCA	EEMD-GECCA
MSE	69.3283	51.2272	70.2484	50.1366
Correlation improvement	0.0019	0.0666	0.0103	0.0654
Lambda	66.8838	86.0016	66.2544	87.2759
DSNR	17.7248	29.0387	17.2621	30.2080

distinct EEG channel data, namely, Ch 9, Ch 4, and Ch 14, as presented in Figure 6. In Figure 6, blue color presents the original artifactual signal, whereas red color signal represents the filtered output by the proposed approach. It is demonstrated

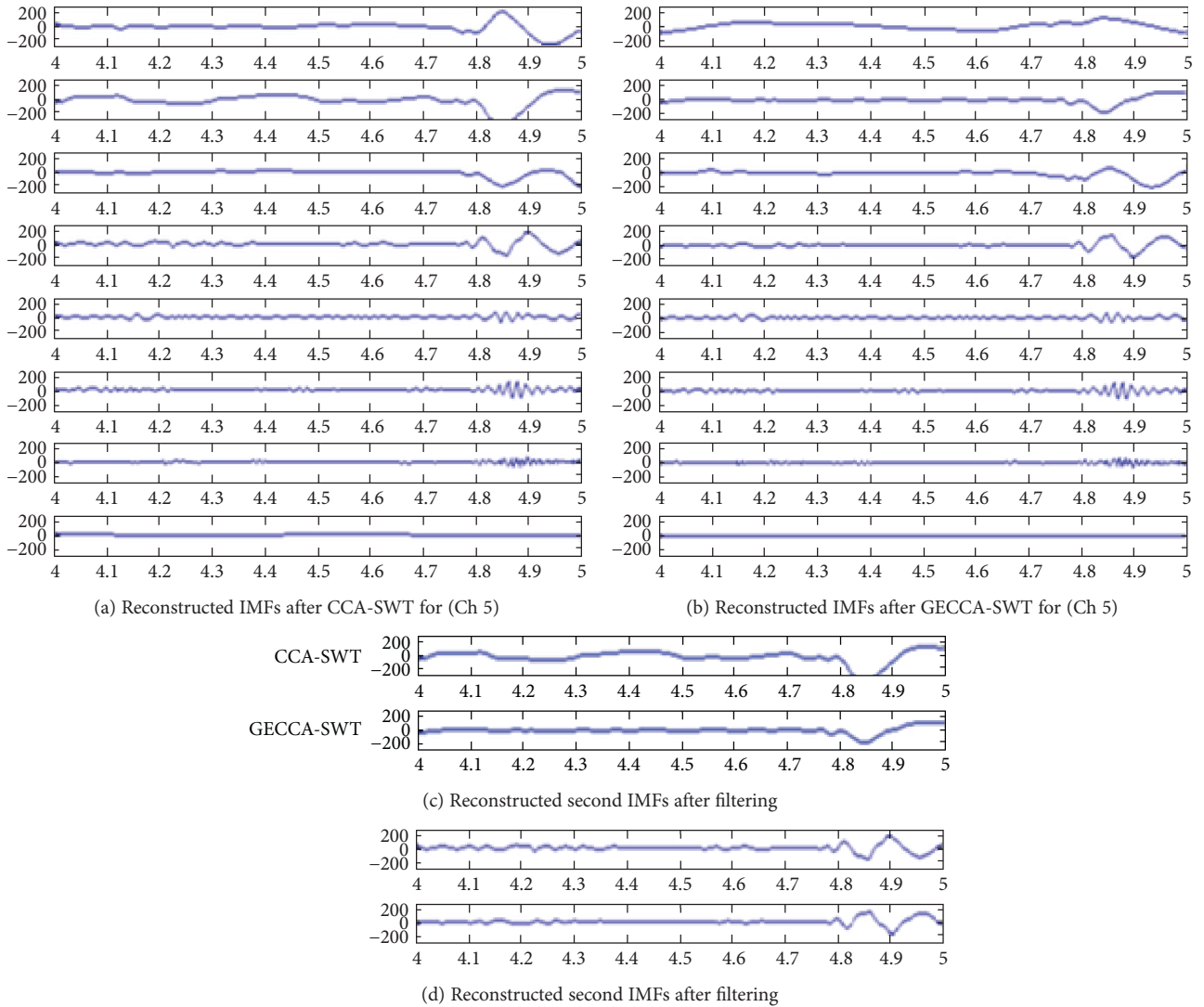


FIGURE 5: Reconstructed IMFs after (a) CCA-SWT, (b) GECCA-SWT, and (c) comparison of CCA and GECCA for the 2nd and 4th reconstructed EEMD (IMFs).

that proposed method of GECCA removes the eye blink artifacts and motion artifacts significantly.

In order to evaluate the performance of the proposed method, parametric evaluation is carried out as shown in Table 1. The performance of artifact removal methods is carried out for CCA and GECCA methods along with DWT and SWT filtering methods. It is observed that proposed method EEMD-GECCA-SWT reduces the mean square error (MSE) by around 15.81% and improves the DSNR performance significantly. Moreover, the higher lambda (λ) value indicates the improved filtering performance [8]. Table 1 shows that GECCA-based artifact removal methods attain improved lambda (λ) value. The vigilant observation of results on Table 1 also presents better correlation improvement of GECCA when compared to CCA, both for DWT and SWT. The backslash operator provides better estimation efficiency. Thus, Gaussian elimination-based approach provides improved correlation by using backslash operation which is more efficient than the matrix inverse method.

The proposed method evaluation is also carried out with the receiver operation characteristic (ROC) curve parameters as shown in Table 2. The positive predictive value (PPV), negative predictive value (NPV), sensitivity (Sen), and specificity (Spe) are calculated by true positive (TP), true negative (TN), false positive (FP), and false negative (FN) [16] as follows:

$$\text{Sen} = \frac{\text{TP}}{\text{TP} + \text{FN}}, \quad (28)$$

$$\text{Spe} = \frac{\text{TN}}{\text{TN} + \text{FP}}, \quad (29)$$

$$\text{PPV} = \frac{\text{TP}}{\text{TP} + \text{FP}}, \quad (30)$$

$$\text{NPV} = \frac{\text{TN}}{\text{TN} + \text{FN}}. \quad (31)$$

The true positive (TP) indicates that the sample is identified as an artifact when it was actually an artifact.

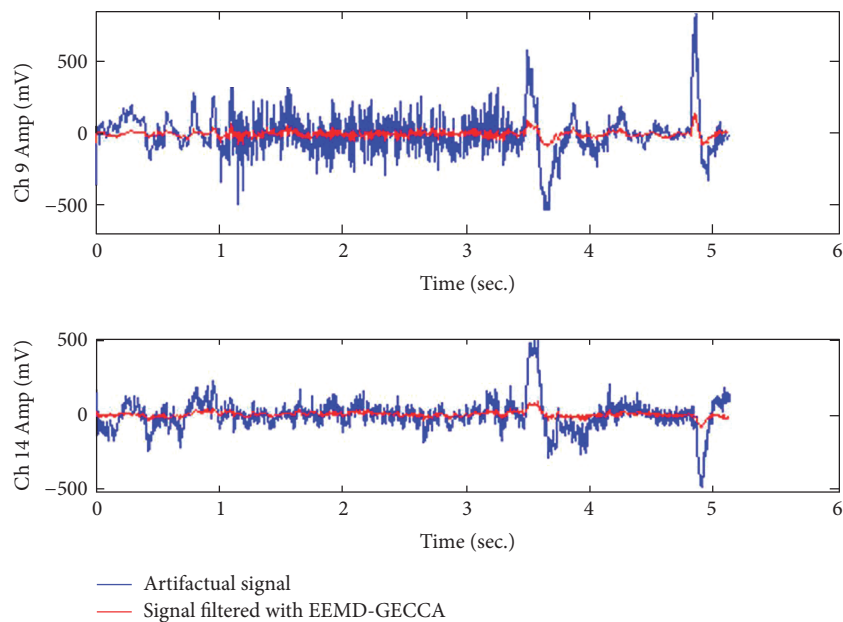


FIGURE 6: Artifact removal consequences with the proposed (EEMD-GECCA-SWT) method.

TABLE 2: Comparison of the ROC parameters with CCA and GECCA for channel 5.

Algorithm Parameters	DWT filtering with		SWT filtering with	
	EEMD_CCA	EEMD_GECCA	EEMD_CCA	EEMD_GECCA
Sensitivity	0.39961	0.45156	0.43438	0.43789
Specificity	0.74062	0.78477	0.65469	0.82656
Accuracy	57.0117%	61.8164%	54.4531%	63.2227%
PPV	60.6402%	67.7211%	55.7114%	71.6294%
NPV	55.2287%	58.8632%	53.6492%	59.5218%

False positive (FP) presents that the sample is identified as an artifact but actually it was not. The false negative (FN) is an indicator for the absence of artifact; however, the artifact was present in the sample. Moreover, true negative (TN) indicates the absence of the artifact when the artifact was actually not present.

This ROC curve is a comparison plot between true positive rate or sensitivity and false positive rate ($1 - \text{specificity}$) [16] for accurate detection of artifact from EEG signal as shown in Figure 7.

Figure 7(a) shows comparison of CCA and GECCA approaches based on DWT. Blue and red color horizontal line indicates the sensitivity of EEMD-CCA-DWT and EEMD-GECCA-DWT artifact removal methods, respectively. The sensitivity or true artifact detection rate for CCA-based approach is 0.39961, whereas GECCA-based approach presents improved and fast response with increased value of 0.45156. However, Figure 7(b) shows SWT-based approach comparison for CCA and GECCA algorithm with the same blue and red color code. Both approaches present almost similar sensitivity 0.43438 and 0.43789, respectively, as shown in Table 2. Although, GECCA-based approach performs better than CCA artifact removal algorithm. Moreover, the sensitivity is associated

with accuracy of the algorithm too. All the ROC parameters as sensitivity, specificity, PPV, and NPV as mentioned above in (28), (29), (30), and (31) are calculated for EEG signal channel number 5 and tabulated for effective comparison of CCA and GECCA-based approaches as shown in Table 2. It is observed that GECCA-based approach shows improved sensitivity and thus better accuracy than CCA-based approaches with both DWT and SWT filtering. Moreover, specificity, PPV, and NPV also improve by GECCA-based methods.

In addition, the efficiency of GECCA-based artifact removal approach is also evaluated by considering ROC parameters for most artifact contaminated channel numbers (1, 3, 5, 6, 9, and 14) from Figure 1. Table 3 encapsulates all the ROC parameters for filtering approach based on CCA and GECCA. It is observed from Table 3 that GECCA-based methods show improved accuracy in comparison to CCA-based method except channel 1. Similarly, specificity, PPV, and NPV parameters are also improved for most of the channel which presents the success of GECCA-based artifact removal approach.

The use of the left matrix division operator in the GECCA algorithms executes faster than the inverse matrix method used in CCA algorithm. Therefore, the proposed GECCA

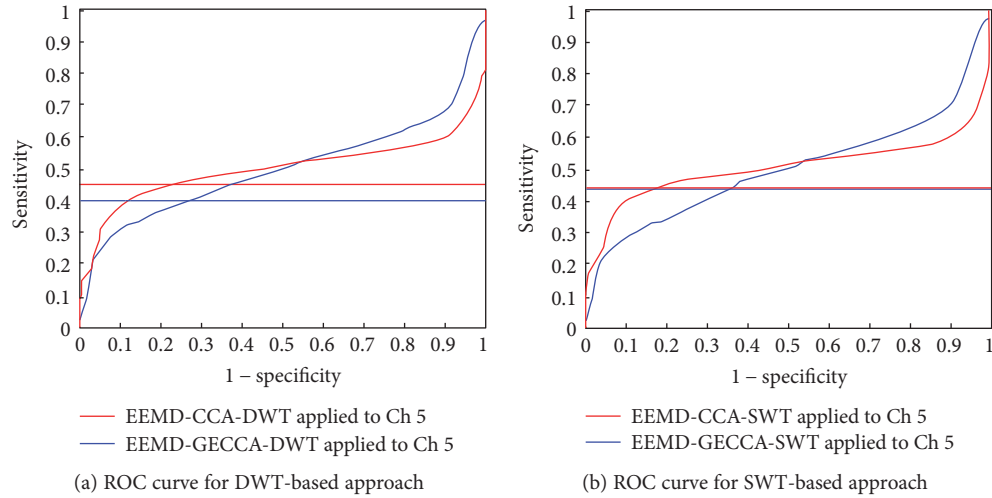


FIGURE 7: ROC plot comparison for CCA and GECCA (a) based on DWT and (b) based on SWT.

TABLE 3: Comparison of ROC parameters for 6 different EEG channels for proposed method.

Method ↓	Parameters in %	Ch 1	Ch 3	Ch 5	Ch 6	Ch 9	Ch 14
With GECCA	Accuracy	57.3047	59.4141	63.2227	65.3125	63.0859	63.5352
	PPV	57.18	57.0674	71.6294	75.0319	71.9241	59.802
	NPV	55.3368	64.0936	59.5218	61.0298	59.3263	71.8612
With CCA	Accuracy	57.6953	58.8672	54.4531	60.2734	62.2461	61.2109
	PPV	56.0578	62.6251	55.7114	64.7422	69.3399	58.2566
	NPV	60.546	56.8332	53.6492	57.8837	58.9597	67.4574

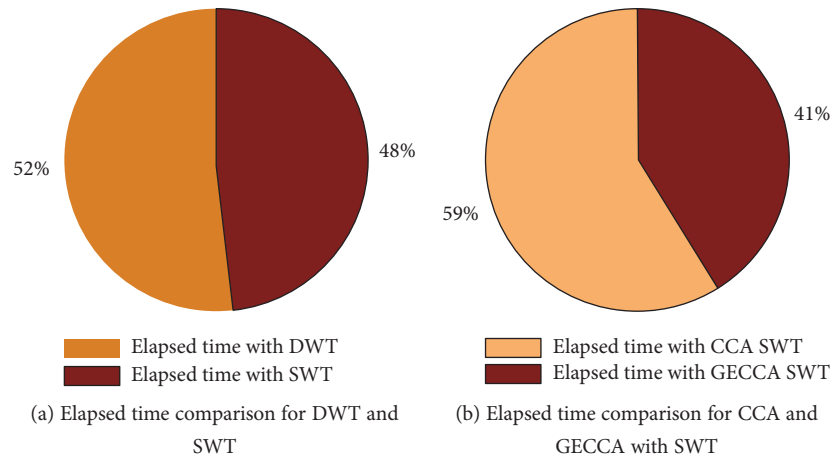


FIGURE 8: (a) Elapsed time comparison for DWT and SWT approach and (b) elapsed time comparison for proposed GECCA method with CCA method.

method is faster than the CCA. Moreover, left matrix division allows better estimates of the matrix inversion which improves the SWT filtering efficiency thus improves the overall efficiency of the Pearson's correlation-based artifact removal.

This execution or computation speed is evaluated by elapsed time. The elapsed time comparison of DWT and SWT is shown in Figure 8(a) suggesting that SWT is faster than DWT. Figure 8(b) compares the elapsed time for

GECCA and CCA with SWT. This presents that GECCA with SWT algorithm computation time is faster than CCA with SWT approach.

Figure 8(a) suggests that SWT is faster than DWT approach for artifact removal. Thus, SWT elapsed time is evaluated with CCA and GECCA approaches and concluded that GECCA approach with SWT is faster and efficient for EEG artifact removal.

6. Conclusion

The measurement and processing of EEG signal result in the probability of signal contamination prominently through motion artifacts which can obstruct the important features and information quality existing in the original EEG signal. To diagnose the human neurological diseases like epilepsy, tumors, and problems associated with trauma [15], these artifacts must be properly pruned assuring that there is no loss of the main attributes of EEG signals. Thus, a novel algorithm GECCA is introduced in cascade with EEMD and SWT for fast and effective suppression of motion artifacts from single-channel EEG signal. The proposed GECCA method uses backslash operation to solve the linear equations. This improves the computation efficiency of the methods. The application of SWT instead of DWT improves the SNR performance of the method and faster than the DWT method too. However, the proposed algorithm may give over smoothing if not properly designed. The proposed method based on GECCA is 18% faster than the conventional CCA. The various evaluation parameters as del signal to noise ratio (DSNR), lambda (λ), root mean square error (RMSE), and ROC parameters are employed to compare the performance of the proposed artifact removal algorithm. The ROC parameter comparison suggested that the improved accuracy is attained with GECCA algorithm except for Ch 1. The optimum evaluation result shows the success of proposed motion artifact removal method.

Conflicts of Interest

The authors declare that they have no conflicts of interest.

References

- [1] B. W. McMenamin, A. J. Shackman, L. L. Greischar, and R. J. Davidson, "Electromyogenic artifacts and electroencephalographic inferences revisited," *NeuroImage*, vol. 54, no. 1, pp. 4–9, 2011.
- [2] K. T. Sweeney, T. E. Ward, and S. F. McLoone, "Artifact removal in physiological signals—practices and possibilities," *IEEE Transactions on Information Technology in Biomedicine*, vol. 16, no. 3, pp. 488–500, 2012.
- [3] H. Zeng, A. Song, R. Yan, and H. Quin, "EOG artifact correction from EEG recording using stationary subspace analysis and empirical mode decomposition," *Sensors*, vol. 13, no. 11, pp. 14839–14859, 2013.
- [4] M. H. Soomro, N. Badruddin, and M. Z. Yusoff, "Comparison of blind source separation methods for removal of eye blink artifacts from EEG," in *2014 5th International Conference on Intelligent and Advanced Systems (ICIAS)*, pp. 1–6, Kuala Lumpur, 2014.
- [5] J. Gao, C. Zheng, and P. Wang, "Online removal of muscles artefact from electroencephalogram signal based on canonical correlation analysis," *Clinical EEG and Neuroscience*, vol. 41, no. 1, pp. 53–59, 2010.
- [6] M. Anastasiadou, A. Hadjipapas, M. Christodoulakis, E. S. Papathanasiou, S. S. Papacostas, and G. D. Mitsis, "Detection and removal of muscle artifacts from scalp EEG recordings in patients with epilepsy," in *2014 IEEE International Conference on Bioinformatics and Bioengineering*, pp. 291–296, Boca Raton, FL, 2014.
- [7] M. Anastasiadou, M. Christodoulakis, E. S. Papathanasiou, S. S. Papacostas, and G. D. Mitsis, "Automatic detection and removal of muscle artifacts from scalp EEG recordings in patients with epilepsy," in *2015 37th Annual International Conference of the IEEE Engineering in Medicine and Biology Society (EMBC)*, pp. 1946–1950, Milan, 2015.
- [8] K. T. Sweeney, S. F. McLoone, and T. E. Ward, "The use of ensemble empirical mode decomposition with canonical correlation analysis as a novel artifact removal technique," *IEEE Transactions Biomedical Engineering*, vol. 60, no. 1, pp. 97–105, 2013.
- [9] M. H. Soomro, N. Badruddin, M. Z. Yusoff, and M. A. Jatoi, "Automatic eye-blink artifact removal method based on EMD-CCA," in *2013 ICME International Conference on Complex Medical Engineering*, pp. 186–190, Beijing, 2013.
- [10] X. Chen, C. He, and H. Peng, "Removal of muscle artifacts from single-channel EEG based on ensemble empirical mode decomposition and multi-set canonical correlation analysis," *Journal of Applied Mathematics*, vol. 2014, Article ID 261347, 10 pages, 2014.
- [11] C. Zhao and T. Qiu, "An automatic ocular artifacts removal method based on wavelet-enhanced canonical correlation analysis," in *2011 Annual International Conference of the IEEE Engineering in Medicine and Biology Society*, pp. 4191–4194, Boston, MA, 2011.
- [12] D. Safieddine, A. Kachenoura, L. Albera et al., "Removal of muscle artifact from EEG data: comparison between stochastic (ICA and CCA) and deterministic (EMD and wavelet-based) approaches," *EURASIP Journal on Advances in Signal Processing*, vol. 127, pp. 1–15, 2012.
- [13] V. Roy and S. Shukla, "A methodical health-care model to eliminate motion artifacts from big EEG data," *JOEUC, Big Data Analytics in Business, Healthcare & Governance*, vol. 29, 2016.
- [14] S. Khatun, R. Mahajan, and B. I. Morshed, "Comparative analysis of wavelet based approaches for reliable removal of ocular artifacts from single channel EEG," in *2015 IEEE International Conference on Electro/Information Technology (EIT)*, pp. 335–340, Dekalb, IL, 2015.
- [15] A. H. Shoeb, *Application of Machine Learning to Epileptic Seizure Onset Detection and Treatment*, [Ph.D. thesis], Massachusetts Institute of Technology, 2009.
- [16] R. Mahajan and B. I. Morshed, "Unsupervised eye blink artifact denoising of EEG data with modified multi-scale sample entropy, kurtosis and wavelet-ICA," *Biomedical and Health Informatics*, vol. 19, no. 1, pp. 158–165, 2015.

Research Article

Novel Variants of a Histogram Shift-Based Reversible Watermarking Technique for Medical Images to Improve Hiding Capacity

Vishakha Kelkar,¹ Kushal Tuckley,² and Hitesh Nemade³

¹UMIT, SNDT University, Mumbai, Maharashtra, India

²AGV Systems Pvt. Ltd. India, Mumbai, Maharashtra, India

³D.J. Sanghvi Engineering College, Mumbai, Maharashtra, India

Correspondence should be addressed to Vishakha Kelkar; kelkar.vishakha@gmail.com

Received 17 February 2017; Revised 16 June 2017; Accepted 20 August 2017; Published 26 September 2017

Academic Editor: Syoji Kobashi

Copyright © 2017 Vishakha Kelkar et al. This is an open access article distributed under the Creative Commons Attribution License, which permits unrestricted use, distribution, and reproduction in any medium, provided the original work is properly cited.

In telemedicine systems, critical medical data is shared on a public communication channel. This increases the risk of unauthorised access to patient's information. This underlines the importance of secrecy and authentication for the medical data. This paper presents two innovative variations of classical histogram shift methods to increase the hiding capacity. The first technique divides the image into nonoverlapping blocks and embeds the watermark individually using the histogram method. The second method separates the region of interest and embeds the watermark only in the region of noninterest. This approach preserves the medical information intact. This method finds its use in critical medical cases. The high PSNR (above 45 dB) obtained for both techniques indicates imperceptibility of the approaches. Experimental results illustrate superiority of the proposed approaches when compared with other methods based on histogram shifting techniques. These techniques improve embedding capacity by 5–15% depending on the image type, without affecting the quality of the watermarked image. Both techniques also enable lossless reconstruction of the watermark and the host medical image. A higher embedding capacity makes the proposed approaches attractive for medical image watermarking applications without compromising the quality of the image.

1. Introduction

Rapid growth in the internet and multimedia technology in the recent times poses threat to the authentication and secured transmission of multimedia data. In telemedicine applications, the medical images are exchanged to facilitate improved patient's clinical status [1]. As the communication channel is shared between multiple users, poor security services may have adverse effect on the quality of care provided. The quality of biomedical images needs to be strictly maintained. The presence of an artefact and other impurities in the medical data may cause diagnostic errors [2]. Patient's information security is crucial to support the trust relationship. So, watermarking techniques are used for authentication. However, watermarking can cause harm to the sensitive information present in the cover image. In medical imagery, a small change in the cover image may affect

interpretation significantly. Consequently, the watermarking methods used for medical applications must be reversible, in which the original medical image must be recovered pixel by pixel accurately. Most reversible watermarking methods impose limitation on the hiding capacity. Another approach for using watermarking for medical images could be to keep intact the region of interest and to embed the watermark in the region of noninterest [3].

Various algorithms have been proposed by various researchers for reversible watermarking. These techniques can be categorised into five classes, namely, (i) integer transform based, (ii) data compression based, (iii) based on histogram bin shifting, (iv) prediction of pixel values based, and (v) based on modification of frequency domain characteristics [4].

The histogram bin shifting-based methods are popular because of the ease of implementation and the overhead

generated is lesser. It makes use of the histogram of the original image, modifies selected portion of the histogram near the peak point, and then embeds the secret data into the image. The scheme was initially proposed by Ni et al. [5]. In this technique, each pixel value is altered at most by 1, so this assures imperceptibility in the watermarked image. It is further observed that the embedding capacity of the histogram-based method is limited and is image dependent. Instead, if the difference value between adjacent pixels is chosen to represent the histogram, it can effectively increase the peak value and more amount of information can be embedded into the image without sacrificing the quality of the output image. There are many modifications suggested in the literature in the basic approach primarily to increase the hiding capacity. One method by Jung and Ko [6] suggests an improved histogram modification-based reversible data hiding technique. In this algorithm, human visual system characteristics are exploited to decide the data embedding level for each pixel. Another variation by Arabzadeh et al. [7] suggests generalization of the well-known histogram shifting method for reversible watermarking. A new reversible image authentication technique [8] based on watermarking utilizes histogram characteristics of the difference image and modifies pixel values slightly to embed more data than other lossless data hiding algorithms. Another work [9] proposes a blind reversible watermarking approach for medical images based on histogram shifting in a wavelet domain. Recent work by Cao and Zhou [10] proposes rhombus prediction model and difference histogram shifting idea for images. Various other researchers have tried to improve the embedding capacity of the basic histogram shift technique [11–14]. All the methods mentioned before increase computational complexity of the histogram shift method. Two of the most important requirements for a reversible watermark are the imperceptibility of the watermark and the hiding capacity. Both should be achieved with as less complexity as possible. Therefore, to design a reversible watermarking technique with increased hiding capacity and to produce output image with acceptable imperceptibility with minimal increase in complexity are the contributions of this paper. All the methods mentioned before increase computational complexity of the histogram shift method. In this paper, two new techniques are proposed which modify the histogram shift method to improve the hiding capacity. The first technique divides the image into nonoverlapping blocks and considers the histogram of each block. In each block, the watermark is embedded. This technique is a simple extension of the classic histogram shift method, but it provides an almost 10% increase in the embedding capacity. This technique takes full advantage of the pixel correlation in a small block of image. Not just that but by changing the size of the block, the required values of the embedding capacity and PSNR can be achieved. A large block size will improve PSNR while reducing capacity. It should be noted that the histogram shift technique discussed here affects all the pixels in the watermarked medical image. Medical professionals remain sceptical about allowing possible alteration of all pixels in the medical image irrespective of the watermarking technique used. This scepticism motivates researchers to

consider RONI (region of noninterest) that are of no or little interest to doctors or medical professionals. In the second technique, first, the RONI is separated from the medical image and the watermark is embedded in this region. This region can have irregular shape. The algorithm will embed the watermark in this region of noninterest. Degradation caused with this type of embedding affects the only RONI by keeping intact the region of interest. The PSNR values achieved with this technique are also comparable to the existing methods.

The next section gives the details about the implemented methods. Section 3 demonstrates the results for the proposed methods and Section 4 is the conclusion.

2. Methodology

In this section, the novel approaches for reversible watermarking are discussed. Firstly, the classical histogram shift method is revisited. Then, the block-wise embedding technique for the watermarking is explained. While embedding watermark in the medical image, care needs to be taken in order that the region of interest in the image is not tempered. To achieve this, the third method is proposed where the region of noninterest is separated from the image and the watermark is embedded only in the region of noninterest. The performance evaluation parameters used for determining the imperceptibility and the quality are the peak signal-to-noise ratio (PSNR), the mean square error (MSE) [15], and MSSIM [16]. Another parameter for performance measurement is the size of the watermark that can be embedded in the original medical image. This is the watermarking capacity. Let I denote the original medical image; whereas I_w denotes the watermarked image then MSE is calculated according to the following:

$$\text{MSE}(I, I_w) = \frac{1}{M \times N} \sum_{i=1}^M \sum_{j=1}^N (I(i, j) - I_w(i, j))^2. \quad (1)$$

Mean square error estimates the average of the square of the errors. The lower the value of MSE, the lower the errors and the higher the imperceptibility. $M \times N$ is the size of the image. PSNR is calculated based on the following:

$$\text{PSNR}(I, I_w) = 10 * \log \left(\frac{2^8 - 1}{\text{MSE}} \right). \quad (2)$$

Higher PSNR indicates higher imperceptibility of the watermark in the image.

In the last three decades, a great deal of effort has gone into the development of quality assessment methods that take advantage of known characteristics of the human visual system (HVS). Here, a measure of structural similarity (SSIM) that compares local patterns of pixel intensities that have been normalized for luminance and contrast is used to access the similarity between the original and the watermarked image. The structural similarity (SSIM) index [16] is based on the computation of three terms, namely, the luminance term, the contrast term, and the structural term. The



FIGURE 1: Original medical image.

overall index is a multiplicative combination of the three terms. For two images x and y ,

$$\text{SSIM}(x, y) = [l(x, y)]^\alpha \cdot [c(x, y)]^\beta \cdot [s(x, y)]^\gamma, \quad (3)$$

where

$$\begin{aligned} l(x, y) &= \frac{2\mu_x\mu_y + C_1}{\mu_x^2 + \mu_y^2 + C_1}, \\ c(x, y) &= \frac{2\sigma_x\sigma_y + C_2}{\sigma_x^2 + \sigma_y^2 + C_2}, \\ s(x, y) &= \frac{2\sigma_{xy} + C_3}{\sigma_x\sigma_y + C_3}, \end{aligned} \quad (4)$$

where μ_x , μ_y , σ_x , σ_y , and σ_{xy} are the local means, standard deviations, and cross-covariance for images x, y . If $\alpha = \beta = \gamma = 1$ (the default for exponents) and $C_3 = C_2/2$ (default selection of C_3), the index simplifies to the following:

$$\text{SSIM}(x, y) = \frac{(2\mu_x\mu_y + C_1)(2\sigma_{xy} + C_2)}{(\mu_x^2 + \mu_y^2 + C_1)(\sigma_x^2 + \sigma_y^2 + C_2)}. \quad (5)$$

Generally, SSIM is calculated for blocks of the image and then mean SSIM (MSSIM) is used as the performance parameter.

2.1. The Classical Histogram Shift Method and Its Limitations. In the general histogram shift method proposed by Ni et al. [5], data embedding is performed by shifting the one-dimensional histogram of the image. Consider image I with gray scale values ranging from 0 to 255. Consider p the gray scale value in image I which is the most frequently occurring gray value and c be the maximum count of the grayscale value p . The histogram is shifted to the right by one bin each according to the following rules and shifted image I_{shift} is formed:

$$\begin{aligned} I_{\text{shift}} &= I_{i,j} & \text{if } I_{i,j} = <p \text{ or if } I_{i,j} = 253, \\ I_{\text{shift}} &= I_{i,j} + 1 & \text{if } I_{i,j} > p \text{ and } I_{i,j} < 253. \end{aligned} \quad (6)$$

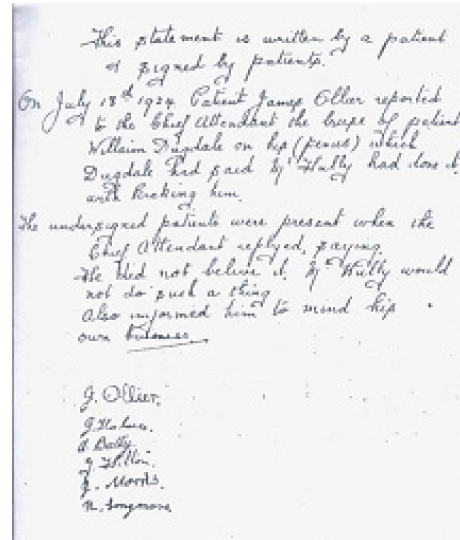


FIGURE 2: Watermark image.



FIGURE 3: Watermarked image.

Consider m the pixel value of the watermark image which is either "1" or "0." The watermarked image \tilde{I} is formed according to following conditions:

$$\begin{aligned} \tilde{I} &= I_{\text{shift}} & \text{if } I_{\text{shift}} = p \text{ and } m = 0, \\ \tilde{I} &= I_{\text{shift}} + 1 & \text{if } I_{\text{shift}} = p \text{ and } m = 1. \end{aligned} \quad (7)$$

To demonstrate the various techniques, different modality medical images are considered here. The image sizes ranged from 544×304 to 1002×1132 . Figure 1 shows the medical image, X-ray image used which is of size 900×854 . Figure 2 shows the watermark image used which is of size 256×256 . This research considers the patient's medical report in the form of an image which is a generalized consideration. So, it is evident that all the discussed algorithms can be performed for text data as well. The watermark has the patient's information and is a black and white image.

The results were obtained with the help of MATLAB. The image in Figure 3 is a watermarked image using the classical

histogram shift technique. The capacity with this method for this image is 44,417 bits. This is around 6% of the total no of pixels. The watermarked image confirms that the watermark is imperceptible. Moreover, the MSE is 0.9831 and the PSNR is 47.92 which are much better than the accepted values. The most important advantage of the histogram shift technique is its simplicity in implementation. The computations required are only the calculations of the histogram which are very simple and fast. It needs to be noted that the capacity changes from image to image. The capacity of the watermark is dependent on the type of the image and the image pixel distribution. Overall, it can be observed that the capacity using the histogram shift technique is limited for medical images. To address this shortcoming of the histogram shift technique, two modifications are suggested in this paper. These proposed techniques increase the embedding capacity but at the same time, they keep the calculations simple. These two novel techniques are discussed in the following subsections.

2.2. Block-Wise Watermark Embedding [17]. To improve the limited watermarking capacity provided by the classical histogram shift technique, here, a new method is proposed. In this technique, the first cover medical image is divided into nonoverlapping blocks of equal size. The blocks are chosen to be nonoverlapping so a pixel will not be embedded with multiple bits. The histogram is calculated for each block and the maximum count greyscale value is noted along with the maximum count. Then, the watermark is embedded in each block. Each block can accommodate watermark bits equal to the maximum count in that block. For the image shown in Figure 1, the embedding capacity increases from 44,417 bits for the classical histogram shift method to 48,164 bits with this technique using the block size 4×4 . This is almost a 10% increase in the hiding capacity. Still, the PSNR is fairly high. Similar results are observed for other medical images also. This technique exploits the correlation between the image pixels. As the histogram is plotted for smaller blocks of the image, the histogram is peakier. This increases the overall embedding capacity for the cover image. The watermark as well as the cover image can be retrieved completely.

Further, the algorithm is tested for varied block sizes like 4×4 , 8×8 , and 16×16 . It is observed that as the block size increases, the embedding capacity decreases as expected. In this technique, though the histogram needs to be calculated for each block, the overall complexity of the algorithm is still simpler compared to that in other reversible watermarking algorithms. Figure 4 shows the watermarked image using a 4×4 block for the cover image in Figure 1.

2.3. Embedding in the Region of Noninterest (RONI). While hiding the watermark in a medical image, it is very important that the region of interest in the image should be kept unaltered. This is very important for the medical conclusions [18]. If the region of interest (ROI) in the medical image is modified, this may cause wrong diagnosis and could be fatal. When the histogram shift algorithm is used for embedding data in medical images, it is bound to change the contents



FIGURE 4: Watermarked image for block size 4×4 .

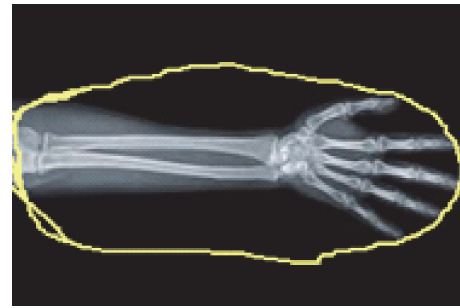


FIGURE 5: Image with the region of interest (ROI).

of the region of interest. To prevail over this flaw, here, a novel idea is proposed where the watermark is embedded in only in region of noninterest (RONI). Hence, this technique completely preserves the region of interest and the medical conclusions are unaffected. In this technique, first, the region of noninterest is separated from the medical image. In Figure 5, the circled region is the region of interest for this medical image which is the hand X-ray.

This ROI is separated using Otsu's method [19]. There are various techniques documented for separating the region of interest for medical images. Here, we have chosen Otsu's method which uses adaptive thresholding to separate the ROI from the RONI. This method is tested for various medical image modalities and gives satisfactory results. The method is implemented using MATLAB command which chooses a proper threshold for the image and converts it to a binary image. Using this binary image, the region of noninterest can be identified and the watermark is selectively embedded in this RONI. This RONI will have irregular shape. Once the region of interest is separated, the histogram of the RONI is plotted and the classical histogram shift technique is used to embed the watermark. After separation of the ROI, the remaining image is more correlated and hence has peakier histogram. Hence, in this technique, the embedding capacity is increased. Not only as the capacity improves but also as the watermark is embedded only in the RONI, the medical information in the cover image is kept intact.

Moreover, the histogram shift method alters the pixel values closer to the peak. So, at the receiver end, again, the RONI can be obtained using Otsu's method. So, no extra information needs to be transmitted with the payload. For the image shown in Figure 1, the embedding capacity using this technique is 44,494 bits which is improved over the classical histogram technique. MSE and PSNR values obtained are 0.6013 and 49.99, respectively, which are fairly satisfactory. The MSSIM is 0.9386 which is closer to 1. Figure 6 shows the watermarked image where the watermark is embedded in the RONI for the cover image in Figure 1.

3. Results and Discussion

All the reversible watermarking techniques explained in the previous section are tried on various types of medical images. The algorithms are implemented using MATLAB.

The first implemented method performs the watermark embedding based on the classical histogram shift technique. Table 1 compiles the results for this method for three medical images. Cover1 image is the image shown in Figure 1. The table contains the image sizes and the embedding capacity in bits for each image. Also, it records the MSE and PSNR values for the watermarked images for the three considered medical images. The watermark image used for embedding is a black and white image of size 256×256 . The hiding capacity of each image is different.

For a given image, the watermark image is resized to the maximum hiding capacity for that image and the watermark is embedded using the histogram shift method. It can be concluded that with this technique, the PSNR value achieved is very high. So, the method is imperceptible. The calculations are very simple—only those required for plotting histogram of the image. So, the method is easy to implement.

The classical histogram shift technique has limited hiding capacity which changes from image to image. To improve the embedding capacity, a novel variant of the classical histogram shift technique is proposed in Section 2.2. In this technique, the cover image is divided into nonoverlapping blocks of the same size. While implementing this technique, the block size is varied from 4×4 , 8×8 and 16×16 . In each block, the maximum occurring gray level is noted and the pixel count is also noted. Each block has a hiding capacity same as the maximum count for that block. The watermark is embedded in each block. The results are found for the three images; Cover1, Cover2, and Cover3. It can be seen that the hiding capacity is increased when the watermark is embedded block wise. Also, as the block size is increased, the hiding capacity decreases. Table 2 indicates these results. Columns 3, 4, and 5 show the hiding capacity for different block sizes for the three images. The capacity reduces with an increasing block size. Table 3 records the MSE, PSNR, and MSSIM values for the three images for different block sizes. High PSNR value and MSSIM value confirm the imperceptibility of this algorithm which are important criteria for watermarking medical images. The algorithm is simple to implement so the advantage of simplicity is still maintained.

In the new technique discussed in Section 2.3, the RONI of the image is separated first. Then, histogram for this

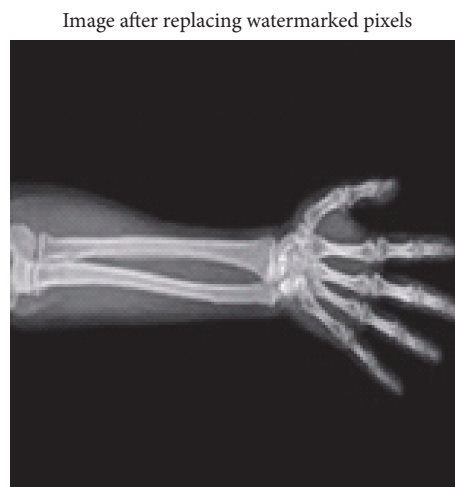


FIGURE 6: Watermark embedded in the RONI.

TABLE 1: Results of the classical histogram shift technique.

Images	Image size	Hiding capacity	MSE	PSNR
Cover1	900×854	44,417	0.9831	47.92
Cover2	1002×1132	36,947	1.086	47.49
Cover3	544×304	37,651	1.076	47.53

separated region is plotted and the watermark is embedded in this region. This technique has an important advantage over the previous two methods. It keeps the ROI of the medical image intact. So, the watermark embedding does not disturb the medical implications. Referring Table 2, the last column indicates the hiding capacity with this technique for the three images. There is an improvement in the capacity compared to classical histogram shift method. Table 4 lists the MSE, PSNR, and MSSIM values for this technique. Here, though the capacity is improved, MSE is low whereas PSNR and MSSIM are higher. Also, the distortion in this method is only in the RONI. The following discussion brings out the significance of the techniques presented in the foregone text.

Most of the watermarking techniques modify the host image and thereby distort it while embedding the watermark. In many applications, these distortions or loss of fidelity is acceptable if the original image and the watermarked image are perceptually equivalent. On the contrary, images in some typical applications have stringent constraints on the image fidelity and thus, distortions during watermarking are not acceptable. Some of the application areas wherein images have stringent constraints on the image fidelity are medical images, military surveillance images, spy-satellite images, and legal document images. The reversible watermarking techniques, as discussed in this paper, are recommended for such applications mainly due to the lossless property of watermarking. It may be noted that the techniques presented in this paper give special emphasis on the reversibility property. In principle, these techniques can be applied to all types of images; however,

TABLE 2: Comparison of the hiding capacity for novel variants with the classical histogram shift technique.

Image	Image size	Hiding capacity in bits (histogram shift)	Block-wise histogram shift in bits (4 × 4)	Block-wise histogram shift in bits (8 × 8)	Block-wise histogram shift in bits (16 × 16)	Embedding in non-ROI in bits
Cover1	900 × 854	44,417	48,164	46,201	45,367	44,494
Cover2	1002 × 1132	36,947	42,258	39,567	38,253	37,103
Cover3	544 × 304	37,651	43,784	41,211	39,499	37,862

TABLE 3: MSE, PSNR, and MSSIM values for the block-wise embedding technique.

Images	Block size 4 × 4			Block size 8 × 8			Block size 16 × 16		
	MSE	PSNR	SSIM	MSE	PSNR	SSIM	MSE	PSNR	SSIM
Cover1	0.8266	48.68	0.9149	0.8481	48.56	0.9146	0.8831	48.39	0.9148
Cover2	0.7822	49.02	0.9273	0.7962	48.96	0.9297	0.8187	48.82	0.9271
Cover3	0.7668	49.28	0.9325	0.7766	49.23	0.9321	0.8022	49.08	0.9317

TABLE 4: MSE, PSNR, and MSSIM values for the technique using non-ROI.

Image name	MSE	PSNR	MSSIM
Cover1	0.6013	49.99	0.9386
Cover2	0.3431	52.63	0.9659
Cover3	0.5292	50.72	0.9476

its effectiveness gets highlighted in the applications where reversibility of the image is imperative.

Both the novel techniques proposed are reversible, so they can extract the watermark as well as the original medical image accurately.

4. Conclusion

Medical data exchange on the communication channel needs to be secured and authenticated. This can be achieved by means of watermarking the patient's data in the medical image itself. These watermarking techniques have to be carefully chosen as the data embedded should not hinder the vital medical information. Also, the techniques chosen should be reversible, that is, the cover medical image as well as the watermark should be extracted accurately. In this research work, the classical histogram technique is discussed with its application for medical images. To overcome the limited available watermarking capacity of this algorithm, two innovative techniques are suggested. For the block-wise embedding technique, it is observed that with a smaller block size like 4 × 4, higher embedding capacity is accomplished compared to larger block sizes like 8 × 8 or 16 × 16. The quantitative results indicate high imperceptibility with this technique. The second technique embeds watermark only in the region of noninterest. This technique provides lesser improvement in the hiding capacity compared to the block-wise technique. But in case of critical medical images where small distortion in the region of interest cannot be tolerated, this technique changes only the region of noninterest. Moreover, both the techniques preserve the simplicity of the

original method. These innovative variants are well-suited techniques for medical image watermarking with higher capacity and better imperceptibility. These techniques are more suitable and beneficial for the applications that put stringent restriction on the image distortion.

Conflicts of Interest

The authors declare that there is no conflict of interest regarding the publication of this paper to the best of their knowledge.

References

- [1] V. Garg and J. Brewer, "Telemedicine security: a systematic review," *Journal of Diabetes Science and Technology*, vol. 5, no. 3, pp. 768–777, 2011.
- [2] G. Coatrieux, L. Lecornu, B. Sankur, and C. Roux, "A review of image watermarking applications in healthcare," in *28th Annual International Conference of the IEEE Engineering in Medicine and Biology Society, 2006. EMBS'06*, pp. 4691–4694, New York, NY, USA, 2006.
- [3] J. Zain and M. Clarke, "Security in telemedicine: issues in watermarking medical images," in *3rd International Conference: Science of Electronic, Technologies of Information and Telecommunications*, Tunisia, 2005.
- [4] C. Rey and J.-L. Dugelay, "A survey of watermarking algorithms for image authentication," *EURASIP Journal on Applied Signal Processing*, vol. 2002, no. 6, pp. 613–621, 2002.
- [5] Z. Ni, Y.-Q. Shi, N. Ansari, and W. Su, "Reversible data hiding," *IEEE Transactions on Circuits and Systems for Video Technology*, vol. 16, no. 3, pp. 354–362, 2006.
- [6] S.-W. Jung and S.-J. Ko, "A new histogram modification based reversible data hiding algorithm considering the human visual system," *IEEE Signal Processing Letters*, vol. 18, no. 2, pp. 95–98, 2011.
- [7] M. Arabzadeh, M. S. Helfroush, H. Danyali, and K. Kasiri, "Reversible watermarking based on generalized histogram shifting," in *2011 18th IEEE International Conference on Image Processing (ICIP)*, pp. 2741–2744, Brussels, Belgium, 2011.

- [8] X. Gui, X. Li, and B. Yang, "Efficient reversible data hiding based on two-dimensional pixel-intensity-histogram modification," in *2014 IEEE International Conference on Acoustics, Speech and Signal Processing (ICASSP)*, pp. 7420–7424, Florence, Italy, 2014.
- [9] H. Golpîra and H. Danyali, "Reversible blind watermarking for medical images based on wavelet histogram shifting," in *2009 IEEE International Symposium on IEEE Signal Processing and Information Technology (ISSPIT)*, pp. 31–36, Ajman, United Arab Emirates, 2009.
- [10] L. Cao and H. Zhou, "A new reversible data-hiding algorithm for encrypted images," *Mathematical Problems in Engineering*, vol. 2016, Article ID 4313580, 11 pages, 2016.
- [11] C. Vinoth Kumar, V. Natarajan, and D. Bhogadi, "High capacity reversible data hiding based on histogram shifting for medical images," in *2013 International Conference on Communications and Signal Processing (ICCSP)*, Melmaruvathur, India, 2013.
- [12] K. Hazarathiah, "Reversible data hiding using histogram shifting technique," *International Journal of Computer Science and Mobile Computing*, vol. 3, no. 6, pp. 735–740, 2014.
- [13] T. H. Nguyen and D. M. Duong, "Reversible medical image watermarking technique based on choosing threshold values in histogram shifting," in *2015 Seventh International Conference on Knowledge and Systems Engineering (KSE)*, pp. 204–209, Ho Chi Minh City, Vietnam, 2015.
- [14] H. S. Nemade and V. Kelkar, "Reversible watermarking for colored medical images using histogram shifting method," in *2016 3rd International Conference on Computing for Sustainable Global Development (INDIACom)*, New Delhi, India, 2016.
- [15] M. Fallahpour, D. Megias, and M. Ghanbari, "High capacity, reversible data hiding in medical images," in *2009 16th IEEE International Conference on Image Processing (ICIP)*, pp. 4241–4244, Cairo, Egypt, 2009.
- [16] Z. Wang, A. C. Bovik, H. R. Sheikh, and E. P. Simoncelli, "Image quality assessment: from error visibility to structural similarity," *IEEE Transactions on Image Processing*, vol. 13, no. 4, pp. 600–612, 2004.
- [17] V. Kelkar and H. Nemade, "Reversible watermarking in medical images using histogram shifting method with improved security and embedding capacity," in *2016 IEEE International Conference on Recent Trends in Electronics, Information & Communication Technology (RTEICT)*, Bangalore, India, 2016.
- [18] N. A. Memon and S. A. M. Gilani, "NROI watermarking of medical images for content authentication," in *2008 IEEE International Multitopic Conference. INMIC 2008*, Karachi, Pakistan, 2008.
- [19] N. Otsu, "A threshold selection method from gray-level histograms," *IEEE Transactions on Systems, Man, and Cybernetics*, vol. 9, no. 1, pp. 62–66, 1979.

Review Article

Intraoral Scanner Technologies: A Review to Make a Successful Impression

**Raphaël Richert,^{1,2} Alexis Goujat,^{1,2} Laurent Venet,^{1,2} Gilbert Viguié,^{1,2}
Stéphane Viennot,^{1,2,3} Philip Robinson,⁴ Jean-Christophe Farges,^{1,2,5}
Michel Fages,⁶ and Maxime Ducret^{1,2,5}**

¹Faculté d'Odontologie, Université Lyon 1, Université de Lyon, Lyon, France

²Service de Consultations et Traitements Dentaires, Hospices Civils de Lyon, Lyon, France

³Laboratoire P2S, Parcours Santé Systémique, Université Lyon 1, Université de Lyon, Lyon, France

⁴DRCI, Hospices Civils de Lyon, Lyon, France

⁵Laboratoire de Biologie Tissulaire et Ingénierie Thérapeutique, UMR5305 CNRS/Université Lyon 1, UMS3444 BioSciences Gerland, Lyon Sud, Lyon, France

⁶Laboratoire de Bioingénierie et Nanosciences, EA 4203, UFR d'Odontologie, Université Montpellier 1, Montpellier, France

Correspondence should be addressed to Maxime Ducret; ducret.maxime@gmail.com

Received 24 January 2017; Accepted 19 June 2017; Published 5 September 2017

Academic Editor: Md. A. R. Ahad

Copyright © 2017 Raphaël Richert et al. This is an open access article distributed under the Creative Commons Attribution License, which permits unrestricted use, distribution, and reproduction in any medium, provided the original work is properly cited.

To overcome difficulties associated with conventional techniques, impressions with IOS (intraoral scanner) and CAD/CAM (computer-aided design and manufacturing) technologies were developed for dental practice. The last decade has seen an increasing number of optical IOS devices, and these are based on different technologies; the choice of which may impact on clinical use. To allow informed choice before purchasing or renewing an IOS, this article summarizes first the technologies currently used (light projection, distance object determination, and reconstruction). In the second section, the clinical considerations of each strategy such as handling, learning curve, powdering, scanning paths, tracking, and mesh quality are discussed. The last section is dedicated to the accuracy of files and of the intermaxillary relationship registered with IOS as the rendering of files in the graphical user interface is often misleading. This overview leads to the conclusion that the current IOS is adapted for a common practice, although differences exist between the technologies employed. An important aspect highlighted in this review is the reduction in the volume of hardware which has led to an increase in the importance of software-based technologies.

1. Introduction

Since the eighteenth century, conventional impression techniques have been used to register the three-dimensional geometry of dental tissues. Nevertheless, volumetric changes of impression materials and expansion of dental stone seem error-prone, and thus the process requires the services of an excellent dental laboratory [1–3]. To overcome these difficulties, impression with IOS (intraoral scanner) was developed for dental practice [4]. The implementation of the IOS device in dental practices coincided with the development of CAD/CAM (computer-aided design and manufacturing) technology

in dentistry, with numerous advantages for practitioners. Nowadays, IOS and CAD/CAM provide easier planning of treatment, case acceptance, communication with laboratories, reduced operative time, storage requirements, and reduced treatment times [5–7]. The last decade has seen an increasing number of optical IOS, and these are based on different technologies; the choice of which may impact on clinical use [6].

To allow the practitioner to make an informed choice before purchasing or renewing an IOS, this article is divided in three distinct parts. The first presents the different technologies employed by the current IOS for the capture of image and the generation of a digital file by the software, the second

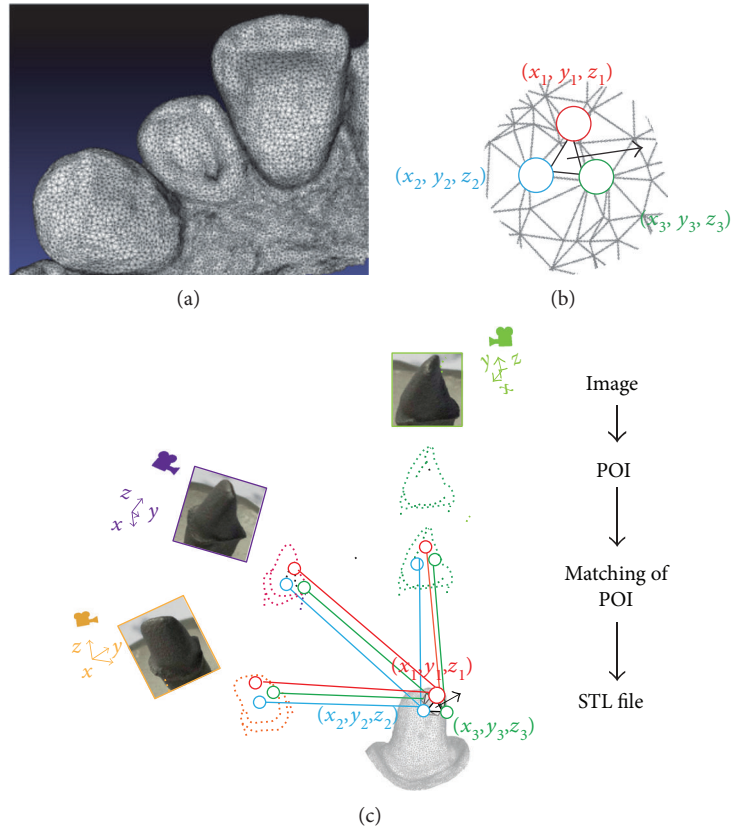


FIGURE 1: Generation of a STL file by intraoral scanner. (a) An example of a STL file. (b) Each triangle of a STL file is composed by three points with cartesian coordinates $(x, y, \text{ and } z)$ and a normal surface. (c) Schematic representation of the reconstruction technology: each picture is analyzed, and POI (points of interest) are selected by the software. After similarity calculation between different images, a matching of coinciding POI is defined and triangles with coordinates are generated by projection matrix.

is dedicated to the clinical pitfalls associated with these technologies during IOS use, and the last part reports on the accuracy of these current technologies.

2. IOS Technologies

IOS is a medical device composed of a handheld camera (hardware), a computer, and a software. The goal of IOS is to record with precision the three-dimensional geometry of an object. The most widely used digital format is the open STL (Standard Tessellation Language) or locked STL-like (Figure 1(a)). This format is already used in many industrial fields and describes a succession of triangulated surfaces where each triangle is defined by three points and a normal surface (Figure 1(b)). However, other file formats have been developed to record color, transparency, or texture of dental tissues (such as Polygon File Format, PLY files). Irrespective of the type of imaging technology employed by IOS, all cameras require the projection of light that is then recorded as individual images or video and compiled by the software after recognition of the POI (points of interest). The first two coordinates (x and y) of each point are evaluated on the image, and the third coordinate (z) is then calculated depending on the distance to object technologies of each camera, as explained below (Figure 1(c)).

2.1. Light Projection and Capture. Within the 3D reconstruction field, there is a clear distinction between passive and active techniques. Passive techniques use only ambient lighting to illuminate intraoral tissues and are reliant on a certain level of texture of an object. Active techniques use white, red, or blue structured lights projected from the camera onto the object that is less reliant on the real texture and color of tissues for reconstruction [8, 9]. In active techniques, a luminous point is projected onto an object and the distance to the object is calculated by triangulation (process explained later) (Figure 2(a)). An alternative is light pattern projection, such as line or mesh projections (Figures 2(b) and 2(c)) [10]. The surface reconstruction can be achieved with a compilation of images, a video that can take several images per second in a continuous data flow, or per wave analysis [11, 12].

2.2. Distance to Object Technologies

2.2.1. Triangulation. Triangulation is based on a principle that the position of a point of a triangle (the object) can be calculated knowing the positions and angles of two points of view (Figure 3(a)). These two points of view may be produced by two detectors, a single detector using a prism, or captured at two different points in time.

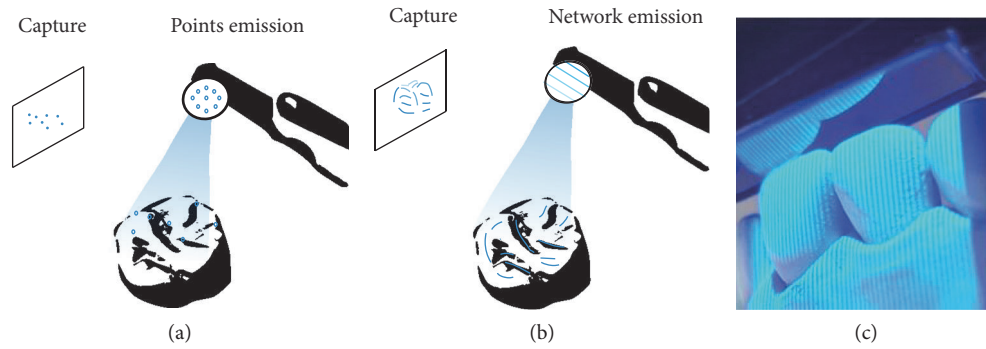


FIGURE 2: Nature of light. (a) Projection of points. (b) Projection of a mesh. (c) Projection of a mesh by an intraoral scanner.

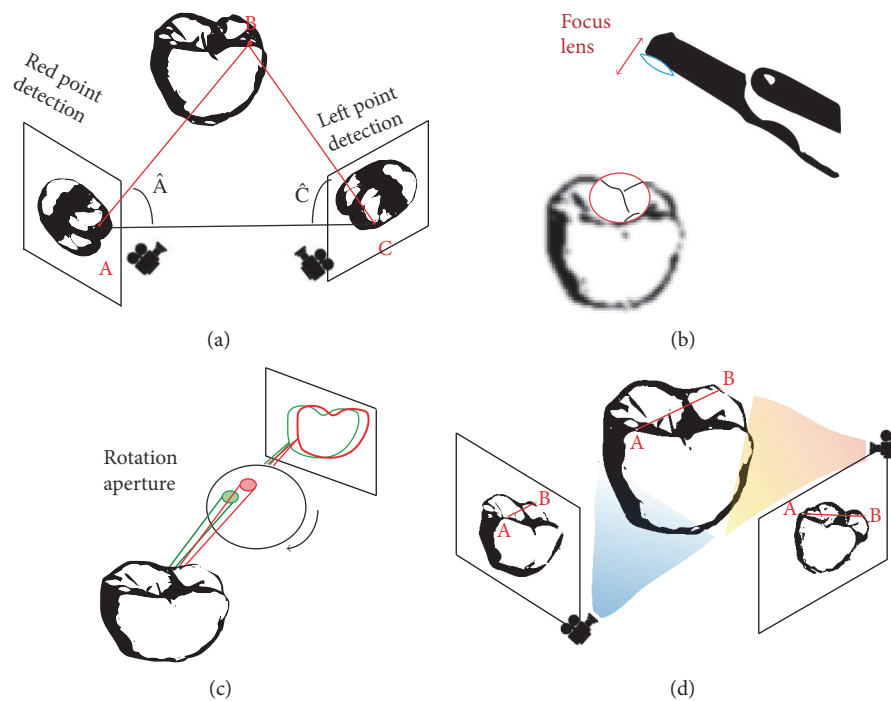


FIGURE 3: Determining distance to the object. (a) Triangulation: distance BC could be determined according to the formula $BC = AC \times \sin(\hat{A}) / \sin(\hat{A} + \hat{C})$. (b) Confocal: distance to the object is determined according to the focal distance. (c) AWS requiring a camera and an off-axis that moves on a circular path around the optical axis and produces a rotation of interest points. (d) Stereophotogrammetry is a technology that generates files by algorithm analyzing numerous pictures.

2.2.2. Confocal. Confocal imaging is a technique based on acquisition of focused and defocused images from selected depths (Figure 3(b)). This technology can detect the sharpness area of the image to infer distance to the object that is correlated to the focal length of the lens. A tooth can then be reconstructed by successive images taken at different focuses and aperture values and from different angles around the object [12]. The sharpness area is directly related to the dexterity of the operator who can generate motion blur [13], and this technique also requires large optics that may lead to difficulties in clinical practice.

2.2.3. AWS (Active Wavefront Sampling). AWS is a surface imaging technique, requiring a camera and an off-axis aperture module. The module moves on a circular path around

the optical axis and produces a rotation of POI (Figure 3(c)). Distance and depth information are then derived and calculated from the pattern produced by each point [8].

2.2.4. Stereophotogrammetry. Stereophotogrammetry estimates all coordinates (x , y , and z) only through an algorithmic analysis of images [14] (Figure 3(d)). As this approach relies on passive light projection and software rather than active projection and hardware, the camera is relatively small, its handling is easier, and its production is cheaper.

2.3. Reconstruction Technologies. One of the major challenges of generating a 3D numerical model is the matching of POI taken under different angles. Distances between different pictures may be calculated using an accelerometer integrated in

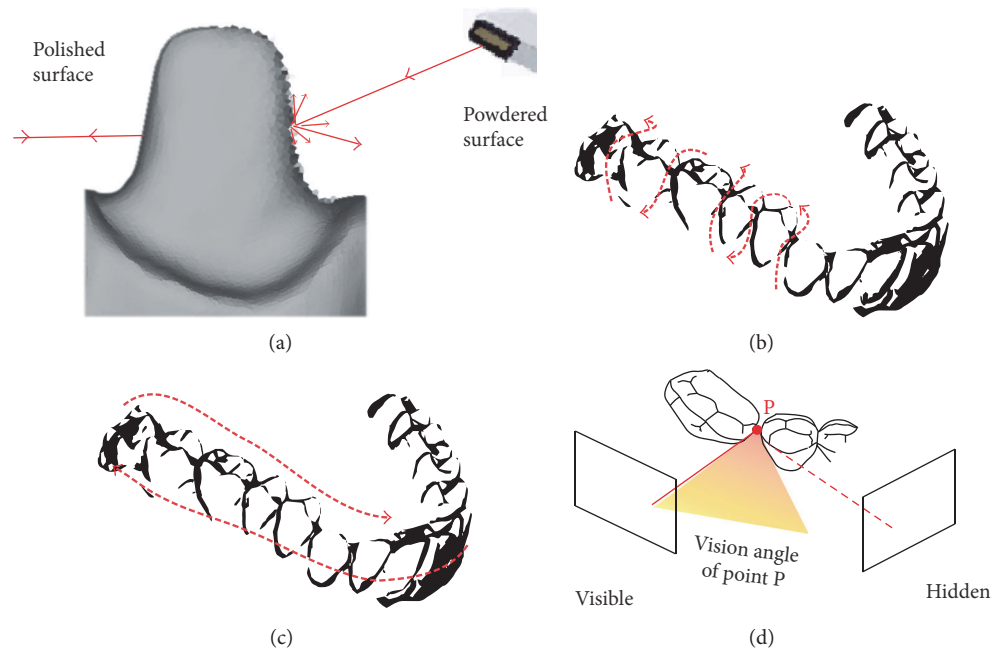


FIGURE 4: Scanning strategies. (a) Prepared teeth have reflective surfaces due to enamel or polished surface. Powdering can increase diffuse light that diminish this phenomenon. (b) A one-way scan (S sweep on vestibular, occlusal, and lingual surfaces). (c) A linear movement on occlusal-palatal surfaces followed by buccal surface. (d) Proximal faces are hidden if the scanning strategy is not adapted.

the camera, but a similarity calculation is more often used to determine the point of view of the image. Using algorithms, similarity calculation defines POI coincident on different images [2]. These POI can be found by detection of transition areas, such as strong curvatures, physical limits, or differences of grey intensity (“Shape from Silhouette”) [15]. A transformation matrix is then calculated to evaluate similarity between all images such as rotation or homothety. Extreme points can also be statistically eliminated to reduce noise. Each coordinate (x , y , and z) is extracted from the projection matrix, and a file is then generated.

3. Clinical Impact of IOS Technologies

3.1. Handling and Learning. Recent studies have indicated that the digital impression technique was more comfortable and faster than the current impression technique [16–19]. Lee and Gallucci have reported that implant impression with IOS using confocal technology was a more efficient technique with shorter preparation and retake time than conventional implant impressions for inexperienced second year dental students [20]. In two other clinical studies, IOS using confocal or AWS was significantly preferred over conventional impression; it was more time efficient, comfortable, and patient friendly for implant impression [19, 21].

Each scanner also includes specific technology and captors that impact size and weight of the scan head [6]. For instance, technologies such as confocal or AWS are mainly based on hardware that requires voluminous components. However, among the IOS that employ the same technology, clinical differences are reported; it is reported that participants preferred the use of Trios over iTero although these are both based on confocal technology [17]. This is related

to the time for operators to familiarize themselves with the ergonomics and software of each IOS, and the learning curve can be initially slow. Indeed, a study compared experience curves between initial scan and after repeated scans using two IOS with confocal technology. It was found that, although scanning time decreased with training for both scanner, the average scanning time for Trios was always shorter than that for iTero [22]. In addition, the software, the technology employed, and the scanning path all seem to affect handling time during digital impression that has been reported to be between 4 and 15 minutes with no clear determining factor [12].

3.2. Powdering. Dental tissues present many reflective surfaces, such as enamel crystals or polished surfaces, that could disrupt the matching of POI by the software due to overexposure. To prevent this, practitioners could change the orientation of the camera to increase diffuse light (Figure 4(a)). Another strategy to overcome this difficulty employed by some systems is to use cameras with a polarizing filter [23]. For other scanners, a 20–40 μm powder coating is required during the digitizing process to reduce reflectivity (Figure 4(a)). Theoretically, the powder thickness could vary between operators and reduce file accuracy, but the software of the IOS is capable of taking an average thickness into account [24].

Powder-based digital impression has been previously shown to be very accurate for partial impressions [25, 26]. However, powder could be relatively uncomfortable for patients, and additional scanning time has been reported when powder is contaminated with saliva during impression as this requires cleaning and reapplication of powder [21]. Moreover, concerning full-jaw scans, IOS using powder-

free technologies appears to be recommended due to the difficulty to maintain powder coating on all the teeth for the duration of the scan [6]. In conclusion, although powder is not very comfortable for patients, no clear difference was found in articles concerning the effect of powdering on scan accuracy.

3.3. Scanning Paths. Scan path means that the intraoral scanner must be used according to a specific movement to increase accuracy of the virtual model [6]. Recent studies have shown the influence of the scan path on the accuracy of data captured using confocal scanners, both *in vitro* and *in vivo* [27]. The scanned object should be positioned at the center of an acquisition area to describe an optimal sphere around the object. Practitioners also have to maintain a fluid movement, always preserving a steady distance and the tooth centered during recording. The camera should be held in a range of between 5 and 30 mm of the scanned surface depending on the scanners and technologies [6, 8, 28]. This handling is particularly difficult during the change of axis, such as the passage from posterior to anterior tooth or in case of malposition. Some manufacturers propose guides to avoid practitioners to maintain distance and keep the surrounding tissue out of the field of view of the camera.

For IOS using confocal technology, when a scan of the entire arcade is required, different strategies are described by manufacturers. One is a linear movement on all occlusal-palatal surfaces followed by buccal surface (Figure 4(b)). Another procedure consists of making an S sweep on vestibular, occlusal, and lingual faces of each tooth successively [27, 29] (Figure 4(c)). The first strategy seems to limit spatial distortion by finishing the capture at the initial position, and so avoiding an overall one-way error, but linear or rough movement of vestibular scans could be imprecise on interproximal areas. This technical observation leads practitioners to adapt their clinical protocol in difficult areas such as interproximal zones, tooth preparation, high curvatures of central incisors, and change of axis around canines. However, the capture of areas with a steep downward slope, such as the anterior mandibular area, is often associated with difficulties in the treatment of the image [6]. This limitation underlines the increasing significance of IOS tracking and software that is described below.

3.4. Tracking and Software. Sometimes during impression, tracking could be lost which may destabilize the software when distance to the object or scan path is not respected; movement is too fast or too jerky. A scan strategy must be followed beginning, for example, with easy parts (occlusal faces of posterior teeth) so that the software has enough information if tracking is lost. Manufacturers are currently developing different strategies and software algorithms to continue scanning when tracking is lost mainly by recognizing saved geometry of the object. For this, practitioners need to rescan a meaningful area without being stationary to give enough information to the camera and software. The second scan will allow matching the previous POI, and the software will complete this missed area [30]. This rematching of POI is directly influenced by a complex geometry of the object such

as high curvatures or many hidden faces that reduce the number of POI and complicates the process for the software [31, 32] (Figure 4(d)).

3.5. Mesh Quality. The IOS software can generate files of varying mesh densities (Figures 5(a), 5(b), and 5(c)). However, a high mesh density for the whole tooth is not relevant due to high computing time involved. Some files incorporate a routine mesh on flat zones (vestibular face of incisors) and a more dense mesh for high curvatures (incisal edge or gingival sulcus, for example; Figures 5(d) and 5(e)). Indeed, a large number of triangles are sufficient to follow precisely the emergence profile whereas a low number could lead to smoothing of margins (Figures 5(f) and 5(g)). During intraoral scanning, a major difficulty is to control patient mobility that can lead to scanning by mistake peripheral soft tissues such as the tongue or jaws [12]. Similarly, the presence of blood, saliva, or gingival fluid can also falsify the picture acquired [15]. For example, a tight film of water can lead to an error to the order of millimeters on margin impression (Figure 5(h)). The latest IOS also provide color and texture that greatly increase the perception of clinical situations and dental volume.

Nevertheless, the rendering of file in the graphical user interface is often misleading on the accuracy of a scan due to the use of shaders and of smoothing algorithms. A thorough analysis of trueness and precision appears to be more relevant factors to evaluate the scanner accuracy of the current IOS, and these aspects are discussed below.

4. Accuracy of IOS Technologies

4.1. Definition of IOS Accuracy. According to ISO 5725, the accuracy is described by two measurement methods: trueness and precision [33, 34]. Trueness refers to the closeness of agreement between the arithmetic mean of a large number of test results and the true or accepted reference value. Precision refers to the closeness of agreement between test results. The method of measurement contributes to the variability of trueness and precision reported for IOS, as this depends on aspects such as the operator, equipment used and calibration, the time elapsed between measurements, and the environment (temperature, humidity, etc.). However, the methods to calculate precision and trueness for IOS are limited due to the quality of references used and the measurement technique employed. For instance, *in vitro*, a plaster model scan using extra oral technology is currently defined as the reference, but it is difficult to compare these results with *in vivo* files as for the latter a plaster scan obtained from indirect physicochemical impression (i.e., likely to contain inaccuracies) is the reference [34, 35]. Moreover, some studies have compared distances between STL generated from a plaster model and those generated with IOS manually, whereas other studies have used an algorithm to align two different files and calculate the distance between them [36, 37]. However, the process of measurement in the first strategy is highly operator dependent whereas the alignment algorithm requires subjective manual operator suppression of inaccurate areas, such as the tongue or soft tissues, to prevent falsified alignment.

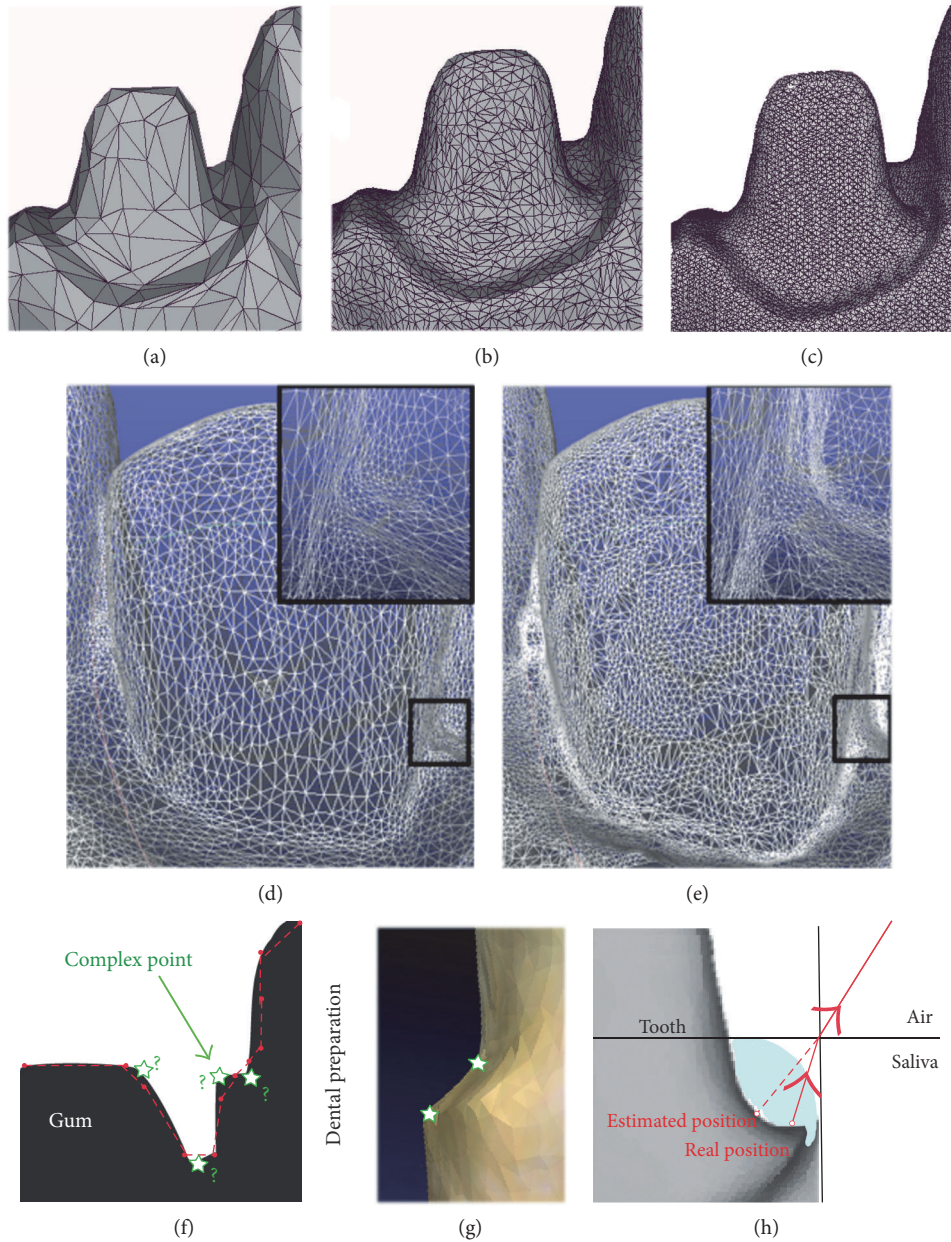


FIGURE 5: Management of mesh quality. Comparison of STL files depending on mesh density. (a) Low density. (b) Medium density. (c) High density. (d) Large number of triangles over the whole tooth. (e) Routine mesh on flat zones and denser mesh for gingival sulcus. (f) Prepared teeth present various points that are complex to scan. (g) Complex points can appear smoothed on CAD-CAM software. (h) Saliva or water film can generate errors during margin impression that could reduce mesh quality.

Then, further investigations are required to develop standardized and comparable strategies for the measurement of IOS accuracy [34].

4.2. Precision and Trueness of IOS Files. Many papers have reported clinically valuable precision and trueness of current IOS, both in vitro and in vivo [16, 38–42]. For example, Ender et al. have reported that the mean trueness of various IOS technologies is between 20 and 48 μm and the precision is between 4 and 16 μm , when the impression is partial and compared to conventional impression [40]. The conclusion of these reports is that current IOS devices are clinically

adapted for common practice, with at least similar accuracy to conventional impression taking [6, 41, 42]. However, in vivo full-arch impression is reported to be associated with a phenomenon of distortion, in particular for triangulation, confocal, or AWS technologies [40, 43, 44].

Concerning implantology, various in vitro studies concluded that triangulation, confocal and AWS technologies can be feasible alternatives to high-accuracy scans currently used for scanning conventional impressions or plaster models [29, 45–47]. Nevertheless, both in vitro and in vivo studies have reported that distance and angulation errors were currently too large to make multiple implant-based

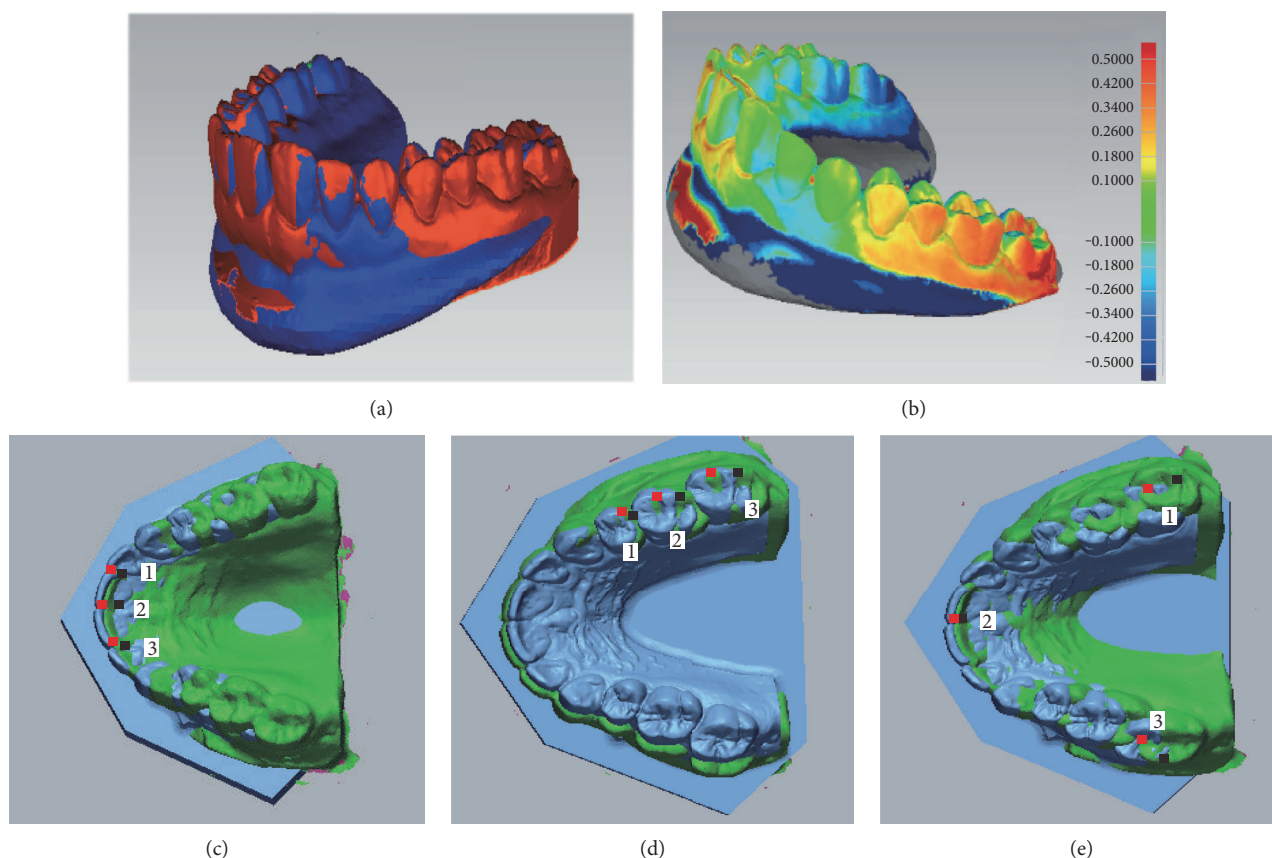


FIGURE 6: Accuracy of full arch impression and matching process. (a) Full-arch files generated with IOS and laboratory scanner were matched (with Geomagic software). (b) Three-dimensional deviations between IOS and reference files revealed posterior distortion. Impact of selected points (1, 2, and 3) to the matching process (with CloudCompare). (c) Anterior points. (d) Lateral-located points. (e) Scattered points.

prosthesis (Figures 6(a) and 6(b)), such as for edentulous mandibles, due to the lack of anatomical landmarks for scanning, irrespective of the technology employed. Indeed, compared to teeth, absence of a periodontal ligament limits implant adaptations in case of microscopic error that can lead to implant complications [45, 48, 49].

4.3. Intermaxillary Relationship Registration. Dentists always require to take the intermaxillary relationship to perform prosthetic rehabilitation for patients. This complex clinical step is a common source of error due to cumbersome and imprecision of bite registration materials. By contrast, impressions using IOS only require a new acquisition of vestibular faces when the patient is in occlusion [50]. Maxillary and mandibular arches are then aligned with a matching process. Even if this complex algorithm requires coincident areas positioned under different planes (Figures 6(c), 6(d), and 6(e)), a recent study reported that only one left and one right lateral occlusal records are required for software alignment, with a minimum dimension of 12×15 mm [50, 51].

5. Conclusion

After an objective overview of the literature, IOS seems clinically adapted for common practice, irrespective of the technology used. Each technology has to be considered

in the context of individual activity, requirements, and expectations of practitioners. An understanding of the IOS technology is necessary for any practitioner to have a successful clinical strategy during the scanning of prepared teeth. However, there is no scanning technique, scanner, or technology that can currently be unanimously considered more accurate due to the lack of standardized procedures or comparable *in vivo* studies. Although IOS is currently mainly based on confocal technology, the requirement of voluminous hardware means that alternatives are sought such as software-based technologies, especially for ergonomic reasons, patient comfort, and manufacturing price (20–25 k€ for software based instead of 35–40 k€ for hardware based).

Conflicts of Interest

The authors declare that there are no competing interests.

References

- [1] L. C. Chen and Z. Q. Xu, "Innovative 3D dental measurement for tooth model restoration," *Key Engineering Materials*, vol. 295–296, no. 12, pp. 145–150, 2005.
- [2] P. Hong-Seok and S. Chintal, "Development of high speed and high accuracy 3D dental intra oral scanner," *Procedia Engineering*, vol. 100, pp. 1174–1181, 2015.

- [3] A. O. Ali, "Accuracy of digital impressions achieved from five different digital impression systems," *Dentistry*, vol. 5, p. 5, 2015.
- [4] F. Duret, "Toward a new symbolism in the fabrication of prosthetic design," *Les Cahiers de Prothèse*, vol. 13, no. 50, pp. 65–71, 1985.
- [5] M. J. Baheti, U. N. Soni, N. V. Gharat, P. Mahagaonkar, R. Khokhani, and S. Dash, "Intra-oral scanners: a new eye in dentistry," *Austin Journal of Orthopedics & Rheumatology*, vol. 2, no. 3, 2015.
- [6] M. Zimmermann, A. Mehl, W. H. Mörmann, and S. Reich, "Intraoral scanning systems - a current overview," *International Journal of Computerized Dentistry*, vol. 18, no. 2, pp. 101–129, 2015.
- [7] T. F. Alghazzawi, "Advancements in CAD/CAM technology: options for practical implementation," *Journal of Prosthodontic Research*, vol. 60, no. 2, pp. 72–84, 2016.
- [8] S. Logozzo, E. M. Zanetti, G. Franceschini, A. Kilpelä, and A. Mäkynen, "Recent advances in dental optics - part I: 3D intraoral scanners for restorative dentistry," *Optics and Lasers in Engineering*, vol. 54, pp. 203–221, 2014.
- [9] F. Duret and B. Péliissier, "Différentes méthodes d'empreinte en CFAO dentaire," *EMC (Elsevier Masson SAS, Paris), Médecine Buccale*, pp. 1–16, 2010.
- [10] J. Geng, "Structured-light 3D surface imaging: a tutorial," *Advances in Optics and Photonics*, vol. 3, pp. 128–160, 2011.
- [11] A. J. Ireland, C. McNamara, M. J. Clover et al., "3D surface imaging in dentistry - what we are looking at," *British Dental Journal*, vol. 205, no. 7, pp. 387–392, 2008.
- [12] E. Taneva, B. Kusnoto, and C. A. Evans, "3D scanning, imaging, and printing in orthodontics," *Chapter 9 Issues in Contemporary Orthodontics*, pp. 147–188, 2015.
- [13] B. Giménez, M. Özcan, F. Martínez-Rus, and G. Pradies, "Accuracy of a digital impression system based on active wavefront sampling technology for implants considering operator experience, implant angulation, and depth," *Clinical Implant Dentistry and Related Research*, Supplement 1, pp. e54–e64, 2015.
- [14] G. Pradies, A. Ferreiroa, M. Özcan, B. Giménez, and F. Martínez-Rus, "Using stereophotogrammetric technology for obtaining intraoral digital impressions of implants," *Journal of the American Dental Association (1939)*, vol. 145, no. 4, pp. 338–344, 2014.
- [15] O. Aubreton, A. Bajard, B. Verney, and F. Truchetet, "Infrared system for 3D scanning of metallic surfaces," *Machine Vision and Applications*, vol. 24, no. 7, pp. 1513–1524, 2013.
- [16] B. Gjølvd, B. R. Chrcanovic, E. K. Korduner, I. Collin-Bagewitz, and J. Kisch, "Intraoral digital impression technique compared to conventional impression technique. A randomized clinical trial," *Journal of Prosthodontics*, vol. 25, no. 4, pp. 282–287, 2016.
- [17] E. Yuzbasioglu, H. Kurt, R. Turunc, and H. Bilir, "Comparison of digital and conventional impression techniques: evaluation of patients' perception, treatment comfort, effectiveness and clinical outcomes," *BMC Oral Health*, vol. 14, no. 1, pp. 1–10, 2014.
- [18] S. B. M. Patzelt, A. Emmanouilidi, S. Stampf, J. R. Strub, and W. Att, "Accuracy of full-arch scans using intraoral scanners," *Clinical Oral Investigations*, vol. 18, no. 6, pp. 1687–1694, 2014.
- [19] L. Burhardt, C. Livas, W. Kerdijk, W. J. v. d. Meer, and Y. Ren, "Treatment comfort, time perception, and preference for conventional and digital impression techniques: a comparative study in young patients," *American Journal of Orthodontics and Dentofacial Orthopedics*, vol. 150, no. 2, pp. 261–267, 2016.
- [20] S. J. Lee and G. O. Gallucci, "Digital vs. conventional implant impressions: efficiency outcomes," *Clinical Oral Implants Research*, vol. 24, no. 1, pp. 111–115, 2013.
- [21] T. Joda and U. Brägger, "Patient-centered outcomes comparing digital and conventional implant impression procedures: a randomized crossover trial," *Clinical Oral Implants Research*, vol. 27, no. 12, pp. e185–e189, 2016.
- [22] J. Kim, J.-M. Park, M. Kim, S.-J. Heo, I. H. Shin, and M. Kim, "Comparison of experience curves between two 3-dimensional intraoral scanners," *The Journal of Prosthetic Dentistry*, vol. 116, no. 2, pp. 221–230, 2016.
- [23] J. Burgner, A. L. Simpson, J. M. Fitzpatrick et al., "A study on the theoretical and practical accuracy of conoscopic holography-based surface measurements: toward image registration in minimally invasive surgery," *International Journal of Medical Robotics and Computer Assisted Surgery*, vol. 9, no. 2, pp. 190–203, 2013.
- [24] J. B. da Costa, F. Pelogia, B. Hagedorn, and J. L. Ferracane, "Evaluation of different methods of optical impression making on the marginal gap of onlays created with CEREC 3D," *Operative Dentistry*, vol. 35, no. 3, pp. 324–329, 2010.
- [25] S. B. M. Patzelt, C. Lamprinos, S. Stampf, and W. Att, "The time efficiency of intraoral scanners: an in vitro comparative study," *Journal of the American Dental Association (1939)*, vol. 145, no. 6, pp. 542–551, 2014.
- [26] G. D. Hack and S. B. M. Patzelt, "Evaluation of the accuracy of six intraoral scanning," *Journal of the American Dental Association (1939)*, vol. 10, no. 4, pp. 1–5, 2015.
- [27] P. Müller, A. Ender, T. Joda, and J. Katsoulis, "Impact of digital intraoral scan strategies on the impression accuracy using the TRIOS pod scanner," *Quintessence International*, vol. 47, no. 4, pp. 343–349, 2016.
- [28] S. Logozzo, A. Kilpelä, A. Mäkynen, E. M. Zanetti, and G. Franceschini, "Recent advances in dental optics - part II: experimental tests for a new intraoral scanner," *Optics and Lasers in Engineering*, vol. 54, pp. 187–196, 2014.
- [29] W. J. V. Van der Meer, F. S. Andriessen, D. Wismeijer, and Y. Ren, "Application of intra-oral dental scanners in the digital workflow of implantology," *PLoS One*, vol. 7, no. 8, pp. 1–8, 2012.
- [30] Z. Mao, K. Park, K. Lee, and X. Li, "Robust surface reconstruction of teeth from raw pointsets," *International Journal of Numerical Methods in Biomedical Engineering*, vol. 30, no. 3, pp. 382–396, 2014.
- [31] T. Yuan, W. Liao, N. Dai, X. Cheng, and Q. Yu, "Single-tooth modeling for 3D dental model," *International Journal of Biomedical Imaging*, vol. 2010, Article ID 535329, 14 pages, 2010.
- [32] C. H. J. Tzou, N. M. Artner, I. Pona et al., "Comparison of three-dimensional surface-imaging systems," *Journal of Plastic, Reconstructive & Aesthetic Surgery*, vol. 67, no. 4, pp. 489–497, 2014.
- [33] A. Menditto, M. Patriarca, and B. Magnusson, "Understanding the meaning of accuracy, trueness and precision," *Accreditation and Quality Assurance*, vol. 12, no. 1, pp. 45–47, 2007.
- [34] A. Ender and A. Mehl, "Accuracy of complete-arch dental impressions: a new method of measuring trueness and

- precision,” *The Journal of Prosthetic Dentistry*, vol. 109, no. 2, pp. 121–128, 2013.
- [35] I.-D. Jeong, J.-J. Lee, J.-H. Jeon, J.-H. Kim, H.-Y. Kim, and W.-C. Kim, “Accuracy of complete-arch model using an intraoral video scanner: an in vitro study,” *The Journal of Prosthetic Dentistry*, vol. 115, no. 6, pp. 755–759, 2016.
- [36] T. V. Flügge, W. Att, M. C. Metzger, and K. Nelson, “Precision of dental implant digitization using intraoral scanners,” *The International Journal of Prosthodontics*, vol. 29, no. 3, pp. 277–283, 2016.
- [37] A. Ender and A. Mehl, “Accuracy in dental medicine, a new way to measure trueness and precision,” *Journal of Visualized Experiments*, no. 86, article e51374, 2014.
- [38] B. Vecsei, G. Joós-Kovács, J. Borbély, and P. Hermann, “Comparison of the accuracy of direct and indirect three-dimensional digitizing processes for CAD/CAM systems – an in vitro study,” *Journal of Prosthodontic Research*, vol. S1883-1958, no. 16, pp. 30062–30067, 2016.
- [39] H. B. Jacob, G. D. Wyatt, and P. H. Buschang, “Reliability and validity of intraoral and extraoral scanners,” *Progress in Orthodontics*, vol. 16, p. 38, 2015.
- [40] A. Ender, T. Attin, and A. Mehl, “In vivo precision of conventional and digital methods of obtaining complete-arch dental impressions,” *The Journal of Prosthetic Dentistry*, vol. 115, no. 3, pp. 313–320, 2016.
- [41] P. Ahlholm, K. Sipilä, P. Vallittu, M. Jakonen, and U. Kotiranta, “Digital versus conventional impressions in fixed prosthodontics: a review,” *Journal of Prosthodontics*, pp. 1–7, 2016.
- [42] S. Ting-Shu and S. Jian, “Intraoral digital impression technique: a review,” *Journal of Prosthodontics*, vol. 24, no. 4, pp. 313–321, 2015.
- [43] Y.-K. Rhee, Y.-H. Huh, L.-R. Cho, and C.-J. Park, “Comparison of intraoral scanning and conventional impression techniques using 3-dimensional superimposition,” *The Journal of Advanced Prosthodontics*, vol. 7, no. 6, pp. 460–467, 2015.
- [44] N. Gan, Y. Xiong, and T. Jiao, “Accuracy of intraoral digital impressions for whole upper jaws, including full dentitions and palatal soft tissues,” *PLoS One*, vol. 11, no. 7, article e0158800, 2016.
- [45] B. Giménez, M. Özcan, F. Martínez-Rus, and G. Pradies, “Accuracy of a digital impression system based on active triangulation technology with blue light for implants: effect of clinically relevant parameters,” *Implant Dentistry*, vol. 24, no. 5, pp. 498–504, 2015.
- [46] B. Giménez, G. Pradies, F. Martínez-Rus, and M. Özcan, “Accuracy of two digital implant impression systems based on confocal microscopy with variations in customized software and clinical parameters,” *The International Journal of Oral & Maxillofacial Implants*, vol. 30, no. 1, pp. 56–64, 2015.
- [47] B. Gimenez-Gonzalez, B. Hassan, M. Özcan, and G. Pradies, “An in vitro study of factors influencing the performance of digital intraoral impressions operating on active wavefront sampling technology with multiple implants in the edentulous maxilla,” *Journal of Prosthodontics*, 2016.
- [48] F. G. Mangano, G. Veronesi, U. Hauschild, E. Mijiritsky, and C. Mangano, “Trueness and precision of four intraoral scanners in oral implantology: a comparative in vitro study,” *PLoS One*, vol. 11, no. 9, article e0163107, 2016.
- [49] F. S. Andriessen, D. R. Rijkens, W. J. V. D. Meer, and D. W. Wismeijer, “Applicability and accuracy of an intraoral scanner for scanning multiple implants in edentulous mandibles: a pilot study,” *The Journal of Prosthetic Dentistry*, vol. 111, no. 3, pp. 186–194, 2014.
- [50] E. Solaberrieta, A. Garmendia, A. Brizuela, J. R. Otegi, G. Pradies, and A. Szentpétery, “Intraoral digital impressions for virtual occlusal records: section quantity and dimensions,” *BioMed Research International*, vol. 2016, Article ID 7173824, 7 pages, 2016.
- [51] E. Solaberrieta, A. Arias, A. Brizuela, X. Garikano, and G. Pradies, “Determining the requirements, section quantity, and dimension of the virtual occlusal record,” *The Journal of Prosthetic Dentistry*, vol. 115, no. 1, pp. 52–56, 2016.

Review Article

Recent Development of Augmented Reality in Surgery: A Review

P. Vávra,¹ J. Roman,² P. Zonča,¹ P. Ihnát,^{1,2} M. Němec,³ J. Kumar,⁴ N. Habib,⁴ and A. El-Gendi⁵

¹Department of Surgery, University Hospital Ostrava, 17. Listopadu 1790, 708 52 Ostrava, Czech Republic

²Faculty of Medicine, University of Ostrava, Syllabova 19, 703 00 Ostrava, Czech Republic

³Faculty of Electrical Engineering and Computer Science, Technical University of Ostrava, 17. Listopadu 15/2172, 708 33 Ostrava, Czech Republic

⁴Department of Surgery & Cancer, Faculty of Medicine, Imperial College London, South Kensington Campus, London SW7 2AZ, UK

⁵Department of Surgery, Faculty of Medicine, Alexandria University, Chamblion Street, El Azareeta, Alexandria Governorate, Egypt

Correspondence should be addressed to J. Roman; mail@janroman.cz

Received 12 February 2017; Accepted 3 July 2017; Published 21 August 2017

Academic Editor: Md. A. R. Ahad

Copyright © 2017 P. Vávra et al. This is an open access article distributed under the Creative Commons Attribution License, which permits unrestricted use, distribution, and reproduction in any medium, provided the original work is properly cited.

Introduction. The development augmented reality devices allow physicians to incorporate data visualization into diagnostic and treatment procedures to improve work efficiency, safety, and cost and to enhance surgical training. However, the awareness of possibilities of augmented reality is generally low. This review evaluates whether augmented reality can presently improve the results of surgical procedures. **Methods.** We performed a review of available literature dating from 2010 to November 2016 by searching *PubMed* and *Scopus* using the terms “augmented reality” and “surgery.” **Results.** The initial search yielded 808 studies. After removing duplicates and including only journal articles, a total of 417 studies were identified. By reading of abstracts, 91 relevant studies were chosen to be included. 11 references were gathered by cross-referencing. A total of 102 studies were included in this review. **Conclusions.** The present literature suggest an increasing interest of surgeons regarding employing augmented reality into surgery leading to improved safety and efficacy of surgical procedures. Many studies showed that the performance of newly devised augmented reality systems is comparable to traditional techniques. However, several problems need to be addressed before augmented reality is implemented into the routine practice.

1. Introduction

The first experiments with medical images date back to the year 1895, when W. C. Röntgen discovered the existence of X-ray. This marks the starting point of using medical images in the clinical practice. The development of ultrasound (USG), computed tomography (CT), magnetic resonance imaging (MRI), and other imaging techniques allows physicians to use two-dimensional (2D) medical images and three-dimensional (3D) reconstructions in diagnosis and treatment of various health problems. Further development of medical technology has given an opportunity to combine anatomical and functional (or physiological) imaging in advanced diagnostic procedures, that is, functional MRI (fMRI) or single photon emission computed tomography (SPECT/CT). These methods allowed physicians to better

understand both the anatomical and the functional aspects of a target area.

The latest development in medical imaging technology focuses on the acquisition of real-time information and data visualization. Improved accessibility of real-time data is becoming increasingly important as their usage often makes the diagnosis and treatment faster and more reliable. This is especially true in surgery, where the real-time access to 2D or 3D reconstructed images during an ongoing surgery can prove to be crucial. This access is further enhanced by the introduction of augmented reality (AR)—a fusion of projected computer-generated (CG) images and real environment.

The ability to work in symbiosis with a computer broadens horizons of what is possible in surgery, as AR can alter the reality we experience in many ways. The wide range of possibilities it offers to surgeons challenges us to develop

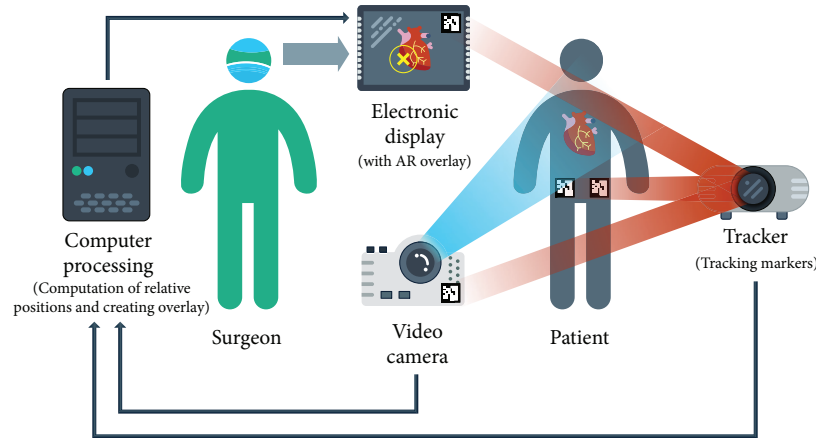


FIGURE 1: A scheme showing the basic principles of augmented reality.

new techniques based on AR. In the future, AR may fully replace many items required to perform a successful surgery today, that is, navigation, displays, microscopes, and much more, all in a small wearable piece of equipment. However, the awareness of AR implementation and what it may offer is generally low, as at current state, it cannot fully replace most of long established surgical methods. The main aim of this work is to focus on the latest trends of the rapidly developing connection between augmented reality and surgery.

2. Methods

We performed a review of available literature dating from 2010 to November 2016 by searching *PubMed* and *Scopus* using the terms “augmented reality” and “surgery.”

The initial search yielded 808 studies. After removing duplicates and including only journal articles, a total of 417 studies were identified. By reading of abstracts, 91 relevant studies were chosen to be included. 11 references were gathered by cross-referencing. A total of 102 studies were included in this review.

3. Results and Discussion

3.1. Basic Principles of Augmented Reality. An augmented reality system provides the surgeon with computer-processed imaging data in real-time via dedicated hardware and software. The projection of AR is made possible by using displays, projectors, cameras, trackers, or other specialized equipment. The main principle of a basic AR system is presented in Figure 1. The most basic method is to superimpose a CG image on a real-world imagery captured by a camera and displaying the combination of these on a computer, tablet PC, or a video projector [1–7]. In case it is impossible to mount a video projector in the operating room, a portable video projection device has been designed [3, 4]. The main advantage of AR is that the surgeon is not forced to look away from the surgical site as opposed to common visualization techniques.

Another possibility is to use a special head-mounted display (HMD, sometimes referred to as “smart glasses”) which resembles eyeglasses. They use special projectors, head

tracking, and depth cameras to display CG images on the glass, effectively creating the illusion of augmented reality. Several AR systems with a HMD have already been developed with success [1, 8]. Using a HMD is beneficial as there is almost no obstruction in the surgeon’s view compared to a traditional display; it is not necessary to move the display, and the need of a proper line-of-sight alignment between the display and the surgeon is not as accented [9].

At present, the applications of AR are limited by the essential requisite of preoperative 3D reconstructions of medical images. It is possible to create these reconstructions by using commercial or self-made software from the Digital Imaging and Communications in Medicine (DICOM) format [7, 10–12]. The quality of a reconstruction depends on the quality of input data and the accuracy of the reconstruction system. Such reconstructions can be used for virtual exploration of target areas, planning an effective surgical approach in advance, and for better orientation and navigation in the operative field.

The type and amount of displayed data rely on the requirements of the procedure and personal preferences of the surgical team. AR is especially useful in visualizing critical structures such as major vessels, nerves, or other vital tissues. By projecting these structures directly onto the patient, AR increases safety and reduces the time required to complete the procedure. Another useful feature of AR is the ability to control the opacity of displayed objects [13, 14]. Most HMDs allow the wearer to turn off all displayed images, becoming fully opaque, thus removing any possible distractions in an emergency. Furthermore, it is possible to utilize voice recognition to create voice commands, enabling hands-free control of the device. This is especially important in surgery as it allows surgeons to control the device without the need of assistance or break aseptic protocols. Another interesting option is to use gesture recognition, allowing the team to interact with the hardware even on sterile surfaces or in the air through body movements [6].

3.2. Monitoring the Operative Field. Most surgeries target deformable structures, which change significantly during a procedure (i.e., a removal of tissue during a resection). This problem needs to be addressed by constantly monitoring

the operative field and making real-time changes to the displayed 3D model. It is possible to use perioperative ultrasound [15, 16], CT, or MRI to update the surgical site model. However, the amount of time required to capture and reconstruct medical images is significant. Using CT [17] or its modifications (i.e., C-arm cone-beam CT [18]) expose the patient to radiation and therefore can only be performed in a limited number of times. An open MRI is a feasible option for perioperative imaging; however, a single surgery requires 40 ± 9.4 minutes of scanning in average and the use of specialized MRI-compatible instruments [19]. Automatic medical reconstructions tend to include many different structures, which make the orientation difficult, especially in abdominal surgery. In some cases, this can be overcome by a method proposed by Sugimoto et al. [2]. In this technique, carbon dioxide is introduced into the gastrointestinal tract and pancreatico-biliary duct in conjunction with an intravenous contrast agent, which allows better display of these individual structures [2]. The quality of reconstructions may be improved in the future due to the development of imaging techniques, which allow making more detailed and refined images. Medical imaging may be replaced by depth-sensing cameras or video cameras in some cases; however, this method cannot detect structures beneath the surface that might be negated by developing a software to predict tissue behaviour by measuring forces applied to the target tissue. However, all currently proposed solutions need further improvement [7, 12, 17, 20, 21].

3.3. Augmented Reality for Education and Cooperation. Augmented reality proved to be an effective tool for training and skill assessment of surgery residents, other medical staff, or students [22–26]. Specialized training simulators can be created and used to improve surgeons' skills in various scenarios, as well as to objectively measure their technical skills. This will be especially beneficial for trainee residents and students in developing intuition and proper decision-making abilities, which can otherwise be only gained through long clinical practice. It allows simulation of very unlikely scenarios, which can be solved with the assistance of an experienced surgeon. Compared to virtual reality (VR) simulators, where the whole simulation takes part in a CG environment, the main advantage of AR simulators is the ability to combine real life objects with CG images, resulting in satisfactory tactile feedback as opposed to VR. AR has also been reported to increase the enjoyment of basic surgical training [27].

AR enables experienced surgeons to remotely assist residents by using Internet connection and therefore opens the way of excellent distant teaching. Shenai et al. [28] created virtual interactive presence and augmented reality (VIPAR) system. By continually monitoring and transmitting the image of a surgical site between two distant stations, it enables remote virtual collaboration between two surgeons [28]. This concept is sometimes referred to as “telepresence.” Davis et al. [29] used VIPAR system in an effort to allow communication between Vietnam and the USA. Thanks are due to the high resolution of the transmitted image, submillimetre achieved precision, and average latency of 237 milliseconds; the interaction between both surgeons was described as effective [29].

3.4. Methods of Image Alignment. The exact alignment of a real environment and CG images is an extremely important aspect to consider. The simplest method is to manually align both images [30]. Such a method is slow and may be imprecise, and therefore the registration process (the alignment of preoperative images with the currently treated patient) needs to be continuous to compensate for the changes in organ layout, that is, during breathing. The accurate alignment of both images is achieved by a set of trackers, which are used to determine the exact position of the camera and patient's body. These trackers usually track fiducial markers placed on the surface of specific structures, which remain still during the surgery (i.e., iliac crest, clavicles, etc.) and thus providing the system with points of reference.

There are several types of markers described in the literature. Many authors used a set of optical markers and a dedicated camera to detect them for navigation [15, 31–36]. The positions of the camera and the patient are determined by measuring distances between individual trackers and markers. Several studies reported using a set of infrared markers [4, 10, 13, 33, 37–40]. A newer approach suggested by Wild et al. [41] involved using fluorescent markers during laparoscopic procedures. The main advantage of such markers is the clear visibility even in difficult conditions and the ability to remain in the patient after the surgery. However, this requires an endoscopic system capable of detecting the emitted light [41]. Konishi et al. proposed an electromagnetic tracking system paired with an infrared sensor for laparoscopic surgery [42]. The main problem of magnetic tracking is the distortion caused by metal tools and equipment, which can however be minimized by using a special calibration technique [43]. The passive coordinate measurement arm (PCMA) method promises very high precision and the possibility to navigate without a direct line of sight by using a robotic arm for distance measurement [44]. Another method of registration is tracking of a laparoscopic camera and consequent automatic alignment of captured video with a 3D reconstruction [45]. Inoue et al. proved that using simple and affordable equipment, for instance a set of regular web cameras and freeware 3D reconstruction software, can be used to create a registration system thus depicting the purchase of such systems as possibility for all medical institutions [10]. The necessity of a direct line of sight may reduce the maximum possible organ deformation and rotation as well as the maximum range of tracked tools, depending on the exact configuration of the tracking system. It is possible to employ an increased number of tracker markers to minimize the chance of tracking failure due to a line of sight obstruction. Several commercially available tracking systems for medical AR are available, relying mostly on infrared or electromagnetic tracking [46].

With advancement in technology in the future, it may be possible to track organ position in real-time without the use of dedicated markers, using various methods for analysis of the operative field. Hostettler et al. used a real-time predictive simulation of abdominal organs [47], and Haouchine et al. designed a physics-based deformation model of registration [48]. These approaches are based on the usage of computing power to predict and visualize organ movement

and deformation. It is also possible to use an RGB (red-green-blue) or range camera to perform registration without the use of markers [49, 50]. On the other hand, Hayashi et al. described natural points of reference as tracking points in the patient's body for progressive registration of cut vessels as markers [50]. Kowalczyk et al. created a system for real-time 3D modelling of the surgical site, with accuracy within 1.5 mm by using a high definition stereoscopic camera and a live reconstruction of the captured image [51].

Another possibility is to use a laser surface scanning technique, aligning images by scanning a high number of surface points without the use of fiducial markers. While Krishnan et al. found the accuracy of laser scanning to be sufficient [52], another study by Schicho et al. [53] suggests lower accuracy compared to using fiducial markers, with the overall deviation of 3.0 mm and 1.4 mm, respectively. Authors suggest that the accuracy may be improved by using an increased number of tracked surface points [53]. An additional marker-less registration method has been described by Lee et al., where authors combined a cone-beam CT image with a 3D RGB image with a sufficient accuracy of 2.58 mm; the absence of real-time image alignment is however still an issue [54]. All camera-based techniques are severely limited by the necessity of a direct line of sight. A novel method designed by Nosrati et al. [55] estimated organ movement by combining preoperative data, intraoperative colour, and visual cues with a vascular pulsation detection (also described by Amir-Khalili et al. [56]), resulting in a robust system not affected by common obstructions (light reflection, light smoke). This method increased the accuracy by 45% compared to traditional techniques. The proposed method, however, is not capable of real-time computation, as every registration requires approximately 10 seconds to be completed [55].

It needs to be noted that the amount of time required to prepare and calibrate an AR system needs to be considered for routine implementation. Pessaux et al. [12] reported a delay of a few seconds for each marker registration. The total time for AR-related registrations was 8 (6–10) minutes [7, 16]. The registration process of a marker-less system used by Sugimoto et al. [2] was completed within 5 minutes. The latency of displaying movement is important as lower latency generally means a better experience.

3.5. Precision. The accuracy and complexity of 3D reconstructed imaging are crucial in providing the correct data to the surgical team. An exact comparison of accuracy between specific studies is impossible due to variable conditions and different approaches for measuring accuracy. Optical systems feature precision within 5 mm in several studies [8, 10, 15, 18, 35, 37, 44, 57–59], which is considered sufficient for clinical application. The required precision differs greatly among various procedures and should be determined individually. The PCMA method of registering relative positions represents the best precision of all mentioned techniques, with an overall precision of <1 mm [44]. Yoshino et al. used a high-resolution MRI image for the reconstruction and an optical tracking system, with reported accuracy of 2.9 ± 1.9 mm while using an operative microscope during an experiment in a phantom model [31]. Two

studies reported using a video projector during phantom experiments or an actual surgery, with results comparable to using an electronic display, featuring accuracy of 0.8–1.86 mm [1, 5]. Gavaghan et al. proposed a portable projection device with accuracy of 1.3 mm [3]. A few authors achieved a deviation of <2.7 mm while using a head-mounted display [8, 40, 60]. Although the difference in precision between a computer monitor and an HMD is not statistically significant [40]. It has been noted that the accuracy is not dependent on the surgeon's experience [8]. The maximum achievable precision is further diminished due to the difficulties in giving the projected image 3D appearance [1, 31] or giving a correct depth perception [8, 32, 34]. One of the possible solutions is to display objects with different opacity [61] or increasingly dark colour. This could be further minimized by taking advantage of motion parallax, which can be created by tracking surgeons head and modifying the projection accordingly [62].

3.6. Uses in Clinical Practice. Augmented reality can be used effectively for preoperative planning and completion of the actual surgery in timely fashion. The preoperative 3D reconstructed images can be modified and prepared for display in AR systems. Commonly, AR is used for tailoring individually preferred incisions and cutting planes [1, 36, 58], optimal placement of trocars, [63] or to generally improve safety by displaying positions of major organ components [7]. Another benefit of AR is the ability to aid surgeons in difficult terrain after a neoadjuvant chemotherapy or radiotherapy [64]. AR may be used to envisage and optimize the surgical volume of resection [16]. In many procedures, the AR-assisted surgery is comparable to other methods of assistance and the usage of such devices depends on surgeon's preference [58].

Augmented reality systems are the most useful during a surgery of organs with little movement and deformation (i.e., skull, brain, and pancreas) as the least amount of tracking and processing power is required whereas mobile organs, like the bowel, are significantly more complicated track and display. Considering these facts, the most frequently targeted areas in AR research are the head and brain [1, 8, 9, 11, 22, 31, 34, 36, 59, 61, 65–69], orthopaedic surgery [4, 37, 60, 70–77], hepato-biliary system [2, 3, 7, 13, 18, 32], and pancreas [13, 14, 35]. On top of that, AR may compensate the lack of tactile feedback usually experienced during laparoscopic surgery by presenting the surgeon with visual clues, thus improving hand-eye coordination and orientation, even in robotic surgery [78, 79]. Many studies proposed using augmented reality in laparoscopic procedures with success [7, 33, 38, 51, 64, 69].

Neurosurgical procedures have employed AR systems successfully, because of the inherent limitation of head and brain movement. It has been reported that AR had a major impact in 16.7% of neurovascular surgeries [34], allowing a higher rate of precise localization of lesions and shorter operative time compared to a traditional 2D approach [66]. Neurosurgeons benefit mainly from precise localization of individual gyri, blood vessels, important neuronal tracts,

and the possibility to plan the operation corridor, for instance, in a removal of superficial tumours [10, 66], epilepsy surgery [65], or in neurovascular surgery [80].

AR has also proved to be useful during orthopaedic surgeries and reconstructions, especially because it allows to view reconstructions directly on top of the patient's body, which reduces the number of distractions caused by looking at an external display [37]. The list of procedures successfully utilizing AR ranges from minimally invasive percutaneous surgeries to trauma reconstructions [74], bone resections, osteotomies [73, 77, 81], arthroscopic surgery, Kirschner wire placement [82], joint replacement, or tumour removal [75, 76]. Percutaneous interventions only require a surface indicator of the insertion point, which can be displayed by AR [4]. A fluoroscopic dual-laser-based system was used by Liang et al. [37] for insertion guidance with satisfactory accuracy. However, the inability to perceive the depth of insertion forces the use of additional techniques [37]. In spite of that, the use of AR limits the radiation exposure during fluoroscopy and the amount of time required to perform the task [71, 72] while minimizing the risk of unnecessary haemorrhage. Rodas and Padoy used AR to create a user friendly visualization of scattered radiation during a minimally invasive surgery [70], enabling to measure and visualize the amount of radiation received. AR can change the workflow of creating orthopaedic implants, replacing 3D printing of a patient-specific model [60]. It is also possible to employ AR in orthopaedic robot-assisted surgeries [81].

It is more difficult to use AR in abdominal surgery, as the amount of organ movement is significant; nevertheless, it is currently used during liver and pancreatic surgeries as it allows better projection of large vessels [39] or tumour sites owing to comparative static nature of these organs. By comparing the reconstructed data with intraoperative ultrasound, AR can be used for intraoperative guidance during liver resections [83]. It can also assist the surgeon with the establishment of laparoscopic ports [13] or phrenotomy sites [84]. Similarly, the kidneys appear to be suitable for the usage of AR, as demonstrated by Muller et al. during a nephrolithotomy, where the AR was used to establish the percutaneous renal access [58]. An AR system has been proposed to accurately detect a sentinel node using a preoperative SPECT/CT scan of the surrounding lymph nodes. This allows to precisely navigate to the sentinel node and perform a resection even in difficult terrain [85]. Using a freehand SPECT to scan radiation distribution, reconstruction of the data and its implementation into AR in real time can extend the concept [27]. AR has also been successfully employed during splenectomies in children [33] and urological procedures [86]. With the increasing precision of AR systems, they can be safely used even in endocrine surgeries [87–89], otorhinolaryngologic surgery [90], eye surgery [91], vascular surgery [92, 93], or dental implantology too [60]; however, their exact usefulness in such surgeries is not exactly quantified owing to the complicated structures [61]. An AR system for transcatheter aortic valve implantation was designed and successfully used by Currie et al., showing comparable accuracy to traditional fluoroscopic guidance technique, hence avoiding impending complications of contrast agent administration [93].

The use of AR in robotic surgery is expanding rapidly, due to its ability to easily incorporate AR directly into the operators' console, which allows the surgeon to navigate more quickly and better identify important structures [7, 94]. The CG projection can be displayed separately or as an overlay of real-time video as needed by the surgeon. A few authors successfully applied AR during a robotic surgery with satisfactory results, showing a possible role of AR as a future trend in robotic surgery [12, 79, 95].

3.7. Advanced Image in Fusion Using Augmented Reality. Augmented reality cannot only display CG images but can also display images which are not normally visible. A handful of studies successfully combined optical images with near-infrared fluorescence images [96–99]. This technique can be used to increase precision by providing additional data for a surgeon to consider. Using this technique, surgeons could be able to detect blood vessels under the organ surface or detect other tissue abnormalities. Koreeda et al. [100] proposed another interesting concept. Here, AR has been used to visualize areas obscured by surgical instruments in laparoscopic procedures, making the tools appear invisible. This system also helped in effectively reducing the needle exit point errors during suturing, while achieving average accuracy of 1.4mm and acceptable latency of 62.4 milliseconds [100].

3.8. Problems of Augmented Reality. Augmented reality introduces many new possibilities and adds new dimensions to surgical science. Surgeons can use additional data for decision making and improving safety and efficacy. Advances in technology allow AR devices to display information with increasing accuracy and lower latency. Despite of constant improvement, there are several difficulties which need to be addressed. Currently, all reconstructed images need to be prepared in advance using complex algorithms requiring powerful computers. However, thanks to an expected advancement in technology, a real-time acquisition of high-resolution medical scans and 3D reconstructions may be possible. Such reconstructions of the operative field would significantly improve overall accuracy. Even though AR can speed up a surgical procedure, the necessity to prepare the whole system and make required registrations and measurements generally increases the time necessary to complete the surgery, with the amount of time depending on the type of the procedure and the complexity of the AR system. The introduction of fully automatic systems would eliminate this problem and reduce the total time required for completion.

The time required for completing a procedure has been reduced while using any form of AR; however, there are certain limitations. One of them is inattentive blindness (an event where the surgeon does not see an unexpected object which suddenly appears in his field of view), which is a concerning issue that needs to be addressed while using 3D overlays [101]. The amount of information a surgeon has presented through AR during a surgery is increasing and may be distracting [60]. Therefore, it is necessary to display only important data or provide a method to switch between different sets of information on demand. A method for the

reduction of cognitive demands was proposed by Hansen et al. [102]. By optimizing the spatial relationship of individual structures, reducing the occlusion caused by AR to minimum, and maximizing contrast, surgeons were able to reduce visual clutter in some cases [102]. Reaching an adequate image contrast during a projection directly onto organs is also necessary [13]. Difficulties in creating a correct 3D and depth perception also persist. The latency of the whole system is also of concern because excessive latency may lower precision and reduce comfort of the surgeon. Kang et al. measured the latency of their optical system for laparoscopic procedures to be 144 ± 19 milliseconds [15].

Currently used head-mounted displays usually weigh several hundred grams and produce plenty of heat; therefore, long-term wear comfort is an issue. These need to be addressed in future to better fit the ergonomics and allow continuous usage for a long period. It is known that virtual and augmented reality projections in HMDs produce simulator sickness, which is presented by nausea, headache, and vertigo or vomiting in the worst scenario. The exact causes behind the simulator sickness are unknown; however, a discrepancy between visual, proprioceptive, and vestibular inputs is probably the case.

4. Conclusions

Studies suggest that AR systems are becoming comparable to traditional navigation techniques, with precision and safety sufficient for routine clinical practice. Most problems faced presently will be solved by further medical and technological research. Augmented reality appears to be a powerful tool possibly capable of revolutionising the field of surgery through a rational use. In the future, AR will likely serve as an advanced human-computer interface, working in symbiosis with surgeons, allowing them to achieve even better results. Nevertheless, further advancement is much needed to achieve maximum potential and cost-effectiveness of augmented reality.

Conflicts of Interest

The authors declare that there is no conflict of interest regarding the publication of this paper.

References

- [1] L. B. Tabrizi and M. Mahvash, "Augmented reality-guided neurosurgery: accuracy and intraoperative application of an image projection technique," *Journal of Neurosurgery*, vol. 123, pp. 206–211, 2015.
- [2] M. Sugimoto, H. Yasuda, K. Koda et al., "Image overlay navigation by markerless surface registration in gastrointestinal, hepatobiliary and pancreatic surgery," *Journal Hepato-Biliary-Pancreatic Sciences*, vol. 17, pp. 629–636, 2010.
- [3] K. A. Gavaghan, M. Peterhans, T. Oliveira-Santos, and S. Weber, "A portable image overlay projection device for computer-aided open liver surgery," *IEEE Transactions on Biomedical Engineering*, vol. 58, pp. 1855–1864, 2011.
- [4] K. Gavaghan, T. Oliveira-Santos, M. Peterhans et al., "Evaluation of a portable image overlay projector for the visualisation of surgical navigation data: phantom studies," *International Journal of Computer Assisted Radiology and Surgery*, vol. 7, pp. 547–556, 2012.
- [5] R. Wen, C. K. Chui, S. H. Ong, K. B. Lim, and S. K. Y. Chang, "Projection-based visual guidance for robot-aided RF needle insertion," *International Journal of Computer Assisted Radiology and Surgery*, vol. 8, pp. 1015–1025, 2013.
- [6] B. Kocev, F. Ritter, and L. Linsen, "Projector-based surgeon-computer interaction on deformable surfaces," *International Journal of Computer Assisted Radiology and Surgery*, vol. 9, pp. 301–312, 2014.
- [7] P. Pessaux, M. Diana, L. Soler, T. Piardi, D. Mutter, and J. Marescaux, "Towards cybernetic surgery: robotic and augmented reality-assisted liver segmentectomy," *Langenbeck's Archives of Surgery*, vol. 400, pp. 381–385, 2015.
- [8] G. Badiali, V. Ferrari, F. Cutolo et al., "Augmented reality as an aid in maxillofacial surgery: validation of a wearable system allowing maxillary repositioning," *Journal of Cranio-Maxillofacial Surgery*, vol. 42, pp. 1970–1976, 2014.
- [9] E. Watanabe, M. Satoh, T. Konno, M. Hirai, and T. Yamaguchi, "The trans-visible navigator: a see-through neuronavigation system using augmented reality," *World Neurosurgery*, vol. 87, pp. 399–405, 2016.
- [10] D. Inoue, B. Cho, M. Mori et al., "Preliminary study on the clinical application of augmented reality neuronavigation," *Journal of Neurological Surgery Part A*, vol. 74, pp. 71–76, 2013.
- [11] G. Callovin, S. Sherkat, G. Callovin, and R. Gazzeri, "Frameless nonstereotactic image-guided surgery of supratentorial lesions: introduction to a safe and inexpensive technique," *Journal of Neurological Surgery Part A*, vol. 75, pp. 365–370, 2014.
- [12] P. Pessaux, M. Diana, L. Soler, T. Piardi, D. Mutter, and J. Marescaux, "Robotic duodenopancreatectomy assisted with augmented reality and real-time fluorescence guidance," *Surgical Endoscopy*, vol. 28, pp. 2493–2498, 2014.
- [13] T. Okamoto, S. Onda, K. Yanaga, N. Suzuki, and A. Hattori, "Clinical application of navigation surgery using augmented reality in the abdominal field," *Surgery Today*, vol. 45, pp. 397–406, 2015.
- [14] J. Marescaux and M. Diana, "Inventing the future of surgery," *World Journal of Surgery*, vol. 39, pp. 615–622, 2015.
- [15] X. Kang, M. Azizian, E. Wilson et al., "Stereoscopic augmented reality for laparoscopic surgery," *Surgical Endoscopy*, vol. 28, pp. 2227–2235, 2014.
- [16] S. J. Gonzalez, Y. H. Guo, and M. C. Lee, "Feasibility of augmented reality glasses for real-time, 3-dimensional (3D) intraoperative guidance," *Journal of the American College of Surgeons*, vol. 219, pp. S64–S64, 2014.
- [17] R. Shekhar, O. Dandekar, V. Bhat et al., "Live augmented reality: a new visualization method for laparoscopic surgery using continuous volumetric computed tomography," *Surgical Endoscopy*, vol. 24, pp. 1976–1985, 2010.
- [18] H. G. Kenngott, M. Wagner, M. Gondan et al., "Real-time image guidance in laparoscopic liver surgery: first clinical experience with a guidance system based on intraoperative CT imaging," *Surgical Endoscopy*, vol. 28, pp. 933–940, 2014.
- [19] N. Tsutsumi, M. Tomikawa, M. Uemura et al., "Image-guided laparoscopic surgery in an open MRI operating theater," *Surgical Endoscopy*, vol. 27, pp. 2178–2184, 2013.

- [20] M. Kranzfelder, M. Bauer, M. Magg et al., "Image guided surgery," *Endoskopie Heute*, vol. 27, pp. 154–158, 2014.
- [21] W. H. Nam, D. G. Kang, D. Lee, J. Y. Lee, and J. B. Ra, "Automatic registration between 3D intra-operative ultrasound and pre-operative CT images of the liver based on robust edge matching," *Physics in Medicine and Biology*, vol. 57, pp. 69–91, 2012.
- [22] S. F. Shakur, C. J. Luciano, P. Kania et al., "Usefulness of a virtual reality percutaneous trigeminal rhizotomy simulator in neurosurgical training," *Operative Neurosurgery*, vol. 11, pp. 420–425, 2015.
- [23] F. Leblanc, B. J. Champagne, K. M. Augestad et al., "Colorectal Surg Training Group: a comparison of human cadaver and augmented reality simulator models for straight laparoscopic colorectal skills acquisition training," *Journal of the American College of Surgeons*, vol. 211, pp. 250–255, 2010.
- [24] N. Lelos, P. Campos, K. Sugand, C. Bailey, and K. Mirza, "Augmented reality dynamic holography for neurology," *Journal of Neurology, Neurosurgery, and Psychiatry*, vol. 85, p. 1, 2014.
- [25] A. M. Vera, M. Russo, A. Mohsin, and S. Tsuda, "Augmented reality telementoring (ART) platform: a randomized controlled trial to assess the efficacy of a new surgical education technology," *Surgical Endoscopy*, vol. 28, pp. 3467–3472, 2014.
- [26] V. Lahanas, C. Loukas, N. Smailis, and E. Georgiou, "A novel augmented reality simulator for skills assessment in minimal invasive surgery," *Surgical Endoscopy*, vol. 29, pp. 2224–2234, 2015.
- [27] A. C. Profeta, C. Schilling, and M. McGurk, "Augmented reality visualization in head and neck surgery: an overview of recent findings in sentinel node biopsy and future perspectives," *The British Journal of Oral & Maxillofacial Surgery*, vol. 54, pp. 694–696, 2016.
- [28] M. B. Shenai, M. Dillavou, C. Shum et al., "Virtual interactive presence and augmented reality (VIPAR) for remote surgical assistance," *Neurosurgery*, vol. 68, p. 8, 2011.
- [29] M. C. Davis, D. D. Can, J. Pindrik, B. G. Rocque, and J. M. Johnston, "Virtual interactive presence in global surgical education: international collaboration through augmented reality," *World Neurosurgery*, vol. 86, pp. 103–111, 2016.
- [30] A. S. Vemuri, J. C. H. Wu, K. C. Liu, and H. S. Wu, "Deformable three-dimensional model architecture for interactive augmented reality in minimally invasive surgery," *Surgical Endoscopy*, vol. 26, pp. 3655–3662, 2012.
- [31] M. Yoshino, T. Saito, T. Kin et al., "A microscopic optically tracking navigation system that uses high-resolution 3D computer graphics," *Neurologia Medico-Chirurgica*, vol. 55, pp. 674–679, 2015.
- [32] T. Okamoto, S. Onda, M. Matsumoto et al., "Utility of augmented reality system in hepatobiliary surgery," *Journal Hepato-Biliary-Pancreatic Sciences*, vol. 20, pp. 249–253, 2013.
- [33] S. Ieiri, M. Uemura, K. Konishi et al., "Augmented reality navigation system for laparoscopic splenectomy in children based on preoperative CT image using optical tracking device," *Pediatric Surgery International*, vol. 28, pp. 341–346, 2012.
- [34] M. Kersten-Oertel, I. Gerard, S. Drouin et al., "Augmented reality in neurovascular surgery: feasibility and first uses in the operating room," *International Journal of Computer Assisted Radiology and Surgery*, vol. 10, pp. 1823–1836, 2015.
- [35] T. Okamoto, S. Onda, J. Yasuda, K. Yanaga, N. Suzuki, and A. Hattori, "Navigation surgery using an augmented reality for pancreatectomy," *Digestive Surgery*, vol. 32, pp. 117–123, 2015.
- [36] M. Qu, Y. K. Hou, Y. R. Xu et al., "Precise positioning of an intraoral distractor using augmented reality in patients with hemifacial microsomia," *Journal of Cranio-Maxillofacial Surgery*, vol. 43, pp. 106–112, 2015.
- [37] J. T. Liang, T. Doke, S. Onogi et al., "A fluorolaser navigation system to guide linear surgical tool insertion," *International Journal of Computer Assisted Radiology and Surgery*, vol. 7, pp. 931–939, 2012.
- [38] S. Onda, T. Okamoto, M. Kanehira et al., "Short rigid scope and stereo-scope designed specifically for open abdominal navigation surgery: clinical application for hepatobiliary and pancreatic surgery," *Journal Hepato-Biliary-Pancreatic Sciences*, vol. 20, pp. 448–453, 2013.
- [39] S. Onda, T. Okamoto, M. Kanehira et al., "Identification of inferior pancreaticoduodenal artery during pancreaticoduodenectomy using augmented reality-based navigation system," *Journal Hepato-Biliary-Pancreatic Sciences*, vol. 21, pp. 281–287, 2014.
- [40] B. Vigh, S. Muller, O. Ristow et al., "The use of a head-mounted display in oral implantology: a feasibility study," *International Journal of Computer Assisted Radiology and Surgery*, vol. 9, pp. 71–78, 2014.
- [41] E. Wild, D. Teber, D. Schmid et al., "Robust augmented reality guidance with fluorescent markers in laparoscopic surgery," *International Journal of Computer Assisted Radiology and Surgery*, vol. 11, pp. 899–907, 2016.
- [42] K. Konishi, M. Hashizume, M. Nakamoto et al., "Augmented reality navigation system for endoscopic surgery based on three-dimensional ultrasound and computed tomography: application to 20 clinical cases," in *CARS 2005: Computer Assisted Radiology and Surgery*, H. U. Lemke, K. Inamura, K. Doi, M. W. Vannier and A. G. Farman, Eds., vol. 1281, pp. 537–542, Elsevier Science Bv, Amsterdam, 2005.
- [43] M. Nakamoto, K. Nakada, Y. Sato, K. Konishi, M. Hashizume, and S. Tamura, "Intraoperative magnetic tracker calibration using a magneto-optic hybrid tracker for 3-D ultrasound-based navigation in laparoscopic surgery," *IEEE Transactions on Medical Imaging*, vol. 27, pp. 255–270, 2008.
- [44] R. J. Lapeer, S. J. Jeffrey, J. T. Dao et al., "Using a passive coordinate measurement arm for motion tracking of a rigid endoscope for augmented-reality image-guided surgery," *International Journal of Medical Robotics and Computer Assisted Surgery*, vol. 10, pp. 65–77, 2014.
- [45] C. Conrad, M. Fusaglia, M. Peterhans, H. X. Lu, S. Weber, and B. Gayet, "Augmented reality navigation surgery facilitates laparoscopic rescue of failed portal vein embolization," *Journal of the American College of Surgeons*, vol. 223, pp. E31–E34, 2016.
- [46] S. Nicolau, L. Soler, D. Mutter, and J. Marescaux, "Augmented reality in laparoscopic surgical oncology," *Surgical Oncology-Oxford*, vol. 20, pp. 189–201, 2011.
- [47] A. Hostettler, S. A. Nicolau, Y. Remond, J. Marescaux, and L. Soler, "A real-time predictive simulation of abdominal viscera positions during quiet free breathing," *Progress in Biophysics and Molecular Biology*, vol. 103, pp. 169–184, 2010.
- [48] N. Haouchine, J. Dequidt, M. O. Berger, and S. Cotin, "Deformation-based augmented reality for hepatic surgery,"

- Studies in Health Technology and Informatics*, vol. 184, pp. 182–188, 2013.
- [49] T. Kilgus, E. Heim, S. Haase et al., “Mobile markerless augmented reality and its application in forensic medicine,” *International Journal of Computer Assisted Radiology and Surgery*, vol. 10, pp. 573–586, 2015.
- [50] Y. Hayashi, K. Misawa, D. J. Hawkes, and K. Mori, “Progressive internal landmark registration for surgical navigation in laparoscopic gastrectomy for gastric cancer,” *International Journal of Computer Assisted Radiology and Surgery*, vol. 11, pp. 837–845, 2016.
- [51] J. Kowalczyk, A. Meyer, J. Carlson et al., “Real-time three-dimensional soft tissue reconstruction for laparoscopic surgery,” *Surgical Endoscopy*, vol. 26, pp. 3413–3417, 2012.
- [52] R. Krishnan, A. Raabe, and V. Seifert, “Accuracy and applicability of laser surface scanning as new registration technique in image-guided neurosurgery,” in *Cars 2004: Computer Assisted Radiology and Surgery*, H. U. Lemke, K. Inamura, K. Doi, M. W. Vannier, A. G. Farman and R. JHC, Eds., vol. 1268, pp. 678–683, Elsevier Science Bv, Amsterdam, 2004.
- [53] K. Schicho, M. Figl, R. Seemann et al., “Comparison of laser surface scanning and fiducial marker-based registration in frameless stereotaxy - technical note,” *Journal of Neurosurgery*, vol. 106, pp. 704–709, 2007.
- [54] S. C. Lee, B. Fuerst, J. Fotouhi, M. Fischer, G. Osgood, and N. Navab, “Calibration of RGBD camera and cone-beam CT for 3D intra-operative mixed reality visualization,” *International Journal of Computer Assisted Radiology and Surgery*, vol. 11, pp. 967–975, 2016.
- [55] M. S. Nosrati, A. Amir-Khalili, J. M. Peyrat et al., “Endoscopic scene labelling and augmentation using intraoperative pulsatile motion and colour appearance cues with preoperative anatomical priors,” *International Journal of Computer Assisted Radiology and Surgery*, vol. 11, pp. 1409–1418, 2016.
- [56] A. Amir-Khalili, G. Hamarneh, J. M. Peyrat et al., “Automatic segmentation of occluded vasculature via pulsatile motion analysis in endoscopic robot-assisted partial nephrectomy video,” *Medical Image Analysis*, vol. 25, pp. 103–110, 2015.
- [57] L. Li, J. Yang, Y. K. Chu et al., “A novel augmented reality navigation system for endoscopic sinus and skull base surgery: a feasibility study,” *PLoS One*, vol. 11, p. 17, 2016.
- [58] M. Muller, M. C. Rassweiler, J. Klein et al., “Mobile augmented reality for computer-assisted percutaneous nephrolithotomy,” *International Journal of Computer Assisted Radiology and Surgery*, vol. 8, pp. 663–675, 2013.
- [59] W. W. Deng, F. Li, M. N. Wang, and Z. J. Song, “Easy-to-use augmented reality neuronavigation using a wireless tablet PC,” *Stereotactic and Functional Neurosurgery*, vol. 92, pp. 17–24, 2014.
- [60] D. Katic, P. Spengler, S. Bodenstedt et al., “A system for context-aware intraoperative augmented reality in dental implant surgery,” *International Journal of Computer Assisted Radiology and Surgery*, vol. 10, pp. 101–108, 2015.
- [61] I. Cabrilo, P. Bijlenga, and K. Schaller, “Augmented reality in the surgery of cerebral arteriovenous malformations: technique assessment and considerations,” *Acta Neurochirurgica*, vol. 156, pp. 1769–1774, 2014.
- [62] M. Riechmann, L. Kahrs, C. Ulmer, J. Raczowsky, W. Lamadé, and H. Wörn, “Visualisierungskonzept für die projektorbasierte Erweiterte Realität in der Leberchirurgie,” *Proceeding of BMT*, vol. 209, pp. 1-2, 2006.
- [63] F. Volonte, F. Pugin, P. Bucher, M. Sugimoto, O. Ratib, and P. Morel, “Augmented reality and image overlay navigation with OsiriX in laparoscopic and robotic surgery: not only a matter of fashion,” *Journal Hepato-Biliary-Pancreatic Sciences*, vol. 18, pp. 506–509, 2011.
- [64] R. Souzaki, S. Ieiri, M. Uemura et al., “An augmented reality navigation system for pediatric oncologic surgery based on preoperative CT and MRI images,” *Journal of Pediatric Surgery*, vol. 48, pp. 2479–2483, 2013.
- [65] A. Wang, S. M. Mirsattari, A. G. Parrent, and T. M. Peters, “Fusion and visualization of intraoperative cortical images with preoperative models for epilepsy surgical planning and guidance,” *Computer Aided Surgery*, vol. 16, pp. 149–160, 2011.
- [66] A. Mert, K. Buehler, G. R. Sutherland et al., “Brain tumor surgery with 3-dimensional surface navigation,” *Neurosurgery*, vol. 71, pp. 286–294, 2012.
- [67] I. Cabrilo, P. Bijlenga, and K. Schaller, “Augmented reality in the surgery of cerebral aneurysms: a technical report,” *Neurosurgery*, vol. 10, pp. 252–260, 2014.
- [68] I. Cabrilo, A. Sarrafzadeh, P. Bijlenga, B. N. Landis, and K. Schaller, “Augmented reality-assisted skull base surgery,” *Neurochirurgie*, vol. 60, pp. 304–306, 2014.
- [69] A. Schoob, D. Kundrat, L. Kleingrothe, L. A. Kahrs, N. Andreff, and T. Ortmaier, “Tissue surface information for intraoperative incision planning and focus adjustment in laser surgery,” *International Journal of Computer Assisted Radiology and Surgery*, vol. 10, pp. 171–181, 2015.
- [70] N. L. Rodas and N. Padoy, “Seeing is believing: increasing intraoperative awareness to scattered radiation in interventional procedures by combining augmented reality, Monte Carlo simulations and wireless dosimeters,” *International Journal of Computer Assisted Radiology and Surgery*, vol. 10, pp. 1181–1191, 2015.
- [71] R. Londei, M. Eposito, B. Diotte et al., “Intra-operative augmented reality in distal locking,” *International Journal of Computer Assisted Radiology and Surgery*, vol. 10, pp. 1395–1403, 2015.
- [72] F. Y. Shen, B. L. Chen, Q. S. Guo, Y. Qi, and Y. Shen, “Augmented reality patient-specific reconstruction plate design for pelvic and acetabular fracture surgery,” *International Journal of Computer Assisted Radiology and Surgery*, vol. 8, pp. 169–179, 2013.
- [73] M. Zhu, G. Chai, Y. Zhang, X. F. Ma, and J. L. Gan, “Registration strategy using occlusal splint based on augmented reality for mandibular angle oblique split osteotomy,” *The Journal of Craniofacial Surgery*, vol. 22, pp. 1806–1809, 2011.
- [74] S. Weber, M. Klein, A. Hein, T. Krueger, T. C. Lueth, and J. Bier, “The navigated image viewer - evaluation in maxillofacial surgery,” in *Medical Image Computing and Computer-Assisted Intervention - Miccai 2003, Pt 1*, R. E. Ellis and T. M. Peters, Eds., vol. 2878, pp. 762–769, Springer-Verlag Berlin, Berlin, 2003.
- [75] C. Nikou, A. M. Digioia, M. Blackwell, B. Jaramaz, and T. Kanade, “Augmented reality imaging technology for orthopaedic surgery,” *Operative Techniques in Orthopaedics*, vol. 10, pp. 82–86, 2000.
- [76] M. Blackwell, F. Morgan, and A. M. DiGioia, “Augmented reality and its future in orthopaedics,” *Clinical Orthopaedics and Related Research*, vol. 354, pp. 111–122, 1998.

- [77] A. Wagner, M. Rasse, W. Millesi, and R. Ewers, "Virtual reality for orthognathic surgery: the augmented reality environment concept," *Journal of Oral and Maxillofacial Surgery*, vol. 55, pp. 456–462, 1997.
- [78] A. Hughes-Hallett, E. K. Mayer, P. Pratt, A. Mottrie, A. Darzi, and J. Vale, "The current and future use of imaging in urological robotic surgery: a survey of the European Association of Robotic Urological Surgeons," *International Journal of Medical Robotics and Computer Assisted Surgery*, vol. 11, pp. 8–14, 2015.
- [79] F. Volonte, F. Pugin, N. C. Buchs et al., "Console-integrated stereoscopic OsiriX 3D volume-rendered images for da Vinci colorectal robotic surgery," *Surgical Innovation*, vol. 20, pp. 158–163, 2013.
- [80] I. Cabrilo, K. Schaller, and P. Bijlenga, "Augmented reality-assisted bypass surgery: embracing minimal invasiveness," *World Neurosurgery*, vol. 83, pp. 596–602, 2015.
- [81] L. Lin, Y. Y. Shi, A. Tan et al., "Mandibular angle split osteotomy based on a novel augmented reality navigation using specialized robot-assisted arms—a feasibility study," *Journal of Cranio-Maxillofacial Surgery*, vol. 44, pp. 215–223, 2016.
- [82] M. Fischer, B. Fuerst, S. C. Lee et al., "Preclinical usability study of multiple augmented reality concepts for K-wire placement," *International Journal of Computer Assisted Radiology and Surgery*, vol. 11, pp. 1007–1014, 2016.
- [83] D. Ntourakis, R. Memeo, L. Soler, J. Marescaux, D. Mutter, and P. Pessaux, "Augmented reality guidance for the resection of missing colorectal liver metastases: an initial experience," *World Journal of Surgery*, vol. 40, pp. 419–426, 2016.
- [84] J. Hallett, L. Soler, M. Diana et al., "Trans-thoracic minimally invasive liver resection guided by augmented reality," *Journal of the American College of Surgeons*, vol. 220, pp. E55–E60, 2015.
- [85] O. R. Brouwer, N. Van den Berg, H. Matheron et al., "Feasibility of image guided sentinel node biopsy using augmented reality and SPECT/CT-based 3D navigation," *Annals of Surgical Oncology*, vol. 20, pp. S103–S103, 2013.
- [86] O. Ukimura and I. S. Gill, "Imaging-assisted endoscopic surgery: Cleveland clinic experience," *Journal of Endourology*, vol. 22, pp. 803–809, 2008.
- [87] J. D'Agostino, J. Wall, L. Soler, M. Vix, Q. Y. Duh, and J. Marescaux, "Virtual neck exploration for parathyroid adenomas a first step toward minimally invasive image-guided surgery," *JAMA Surgery*, vol. 148, pp. 232–238, 2013.
- [88] J. D'Agostino, M. Diana, M. Vix et al., "Three-dimensional metabolic and radiologic gathered evaluation using VR-RENDER fusion: a novel tool to enhance accuracy in the localization of parathyroid adenomas," *World Journal of Surgery*, vol. 37, pp. 1618–1625, 2013.
- [89] J. Marescaux, F. Rubino, M. Arenas, D. Mutter, and L. Soler, "Augmented-reality-assisted laparoscopic adrenalectomy," *JAMA: The Journal of the American Medical Association*, vol. 292, pp. 2214–2215, 2004.
- [90] C. Winne, M. Khan, F. Stopp, E. Jank, and E. Keeve, "Overlay visualization in endoscopic ENT surgery," *International Journal of Computer Assisted Radiology and Surgery*, vol. 6, pp. 401–406, 2011.
- [91] P. Mezzana, F. Scarinci, and N. Marabottini, "Augmented reality in oculoplastic surgery: first iPhone application," *Plastic and Reconstructive Surgery*, vol. 127, pp. 57E–58E, 2011.
- [92] Y. Mochizuki, A. Hosaka, H. Kamiuchi et al., "New simple image overlay system using a tablet PC for pinpoint identification of the appropriate site for anastomosis in peripheral arterial reconstruction," *Surgery Today*, vol. 46, pp. 1387–1393, 2016.
- [93] M. E. Currie, A. J. McLeod, J. T. Moore et al., "Augmented reality system for ultrasound guidance of transcatheter aortic valve implantation," *Innovations*, vol. 11, pp. 31–39, 2016.
- [94] A. Balaphas, N. C. Buchs, J. Meyer, M. E. Hagen, and P. Morel, "Partial splenectomy in the era of minimally invasive surgery: the current laparoscopic and robotic experiences," *Surgical Endoscopy*, vol. 29, pp. 3618–3627, 2015.
- [95] F. Volonte, N. C. Buchs, F. Pugin et al., "Augmented reality to the rescue of the minimally invasive surgeon. The usefulness of the interposition of stereoscopic images in the da Vinci (TM) robotic console," *International Journal of Medical Robotics and Computer Assisted Surgery*, vol. 9, pp. E34–E38, 2013.
- [96] J. R. Watson, N. Martirosyan, J. Skoch, G. M. Lemole, R. Anton, and M. Romanowski, "Augmented microscopy with near-infrared fluorescence detection," in *Molecular-Guided Surgery: Molecules, Devices, and Applications*, B. W. Pogue and S. Gioux, Eds., vol. 9311, Spie-Int Soc Optical Engineering, Bellingham, 2015.
- [97] M. Diana, P. Halvax, B. Dallemagne et al., "Real-time navigation by fluorescence-based enhanced reality for precise estimation of future anastomotic site in digestive surgery," *Surgical Endoscopy*, vol. 28, pp. 3108–3118, 2014.
- [98] M. Diana, E. Noll, P. Diemunsch et al., "Enhanced-reality video fluorescence a real-time assessment of intestinal viability," *Annals of Surgery*, vol. 259, pp. 700–707, 2014.
- [99] N. L. Martirosyan, J. Skoch, J. R. Watson, G. M. Lemole, and M. Romanowski, "Integration of indocyanine green videoangiography with operative microscope: augmented reality for interactive assessment of vascular structures and blood flow," *Operative Neurosurgery*, vol. 11, pp. 252–257, 2015.
- [100] Y. Koreeda, Y. Kobayashi, S. Ieiri et al., "Virtually transparent surgical instruments in endoscopic surgery with augmentation of obscured regions," *International Journal of Computer Assisted Radiology and Surgery*, vol. 11, pp. 1927–1936, 2016.
- [101] H. J. Marcus, P. Pratt, A. Hughes-Hallett et al., "Comparative effectiveness and safety of image guidance systems in neurosurgery: a preclinical randomized study," *Journal of Neurosurgery*, vol. 123, pp. 307–313, 2015.
- [102] C. Hansen, J. Wieferrich, F. Ritter, C. Rieder, and H. O. Peitgen, "Illustrative visualization of 3D planning models for augmented reality in liver surgery," *International Journal of Computer Assisted Radiology and Surgery*, vol. 5, pp. 133–141, 2010.

Research Article

Model of Murine Ventricular Cardiac Tissue for *In Vitro* Kinematic-Dynamic Studies of Electromagnetic and β -Adrenergic Stimulation

Lorenzo Fassina,^{1,2} Marisa Cornacchione,³ Manuela Pellegrini,^{4,5} Maria Evelina Mognaschi,¹ Roberto Gimmelli,⁶ Andrea Maria Isidori,⁴ Andrea Lenzi,⁴ Giovanni Magenes,^{1,2} and Fabio Naro⁶

¹Department of Electrical, Computer and Biomedical Engineering, University of Pavia, Pavia, Italy

²Centre for Health Technologies (CHT), University of Pavia, Pavia, Italy

³IRCCS SDN, Naples, Italy

⁴Department of Experimental Medicine, Sapienza University of Rome, Rome, Italy

⁵Institute of Cell Biology and Neurobiology (IBCN), National Research Council (CNR), Rome, Italy

⁶Department of Anatomical, Histological, Forensic and Orthopaedic Sciences, Sapienza University of Rome, Rome, Italy

Correspondence should be addressed to Lorenzo Fassina; lorenzo.fassina@unipv.it

Received 13 February 2017; Accepted 17 July 2017; Published 8 August 2017

Academic Editor: Syoji Kobashi

Copyright © 2017 Lorenzo Fassina et al. This is an open access article distributed under the Creative Commons Attribution License, which permits unrestricted use, distribution, and reproduction in any medium, provided the original work is properly cited.

In a model of murine ventricular cardiac tissue *in vitro*, we have studied the inotropic effects of electromagnetic stimulation (frequency, 75 Hz), isoproterenol administration (10 μ M), and their combination. In particular, we have performed an image processing analysis to evaluate the kinematics and the dynamics of beating cardiac syncytia starting from the video registration of their contraction movement. We have found that the electromagnetic stimulation is able to counteract the β -adrenergic effect of isoproterenol and to elicit an antihypertrophic response.

1. Introduction

A core concept of tissue engineering is to understand the relationships between structures and functions in mammalian cells, tissues, and organs.

This knowledge is of fundamental importance during the growth and the development of tissue substitutes *in vitro*; in other words, the “morphogenesis” of tissue engineering constructs needs to be based not only on the use of molecules (e.g., growth factors) but also on the stimuli provided by the structural context (e.g., the natural/synthetic biomaterials with specific surface/volume properties, biocompatibility features, and mechanical properties) and provided by the biophysical context (e.g., the concentrated/distributed, perpendicular/tangential forces and stresses acting onto the

plasma membrane, transmitted to the cytoskeleton and biochemically transduced; the deformations applied to the cell shape and transferred, via cytoskeleton, to the nuclear membrane and, as a consequence, to the DNA macromolecules in the form of heterochromatin and euchromatin; and the mechanical forces that influence, through cytoskeleton, the porosity of the nuclear envelop and, as a consequence, the trafficking of biochemical signals of mRNAs and microRNAs across the nuclear pores).

For example, a fluid shear stress [1–3] or ultrasounds [4] or biomaterial features [5] lead to the remodeling of bone matrix *in vitro*. In addition, the mechanical forces may also change the transcription more rapidly when they are transmitted directly into the nucleus via the cytoskeleton linked to nuclear envelop proteins [6].

The previous examples of structure/function relationship are comprehensible via the “tensegrity” theory [7–10]: during the *in vitro* morphogenesis inside bioreactors and biomaterials, the biophysical forces establish an equilibrium, the “tensegrity,” suitable to alter the transcription [11, 12].

Specifically, a modulation of the cell behavior is well proved by the cardiomyocytes subjected to the mechanical forces induced by an electromagnetic field [13, 14]. However, the effects of the electromagnetic fields are controversial. A work showed no main effects on heart function [15], whereas others suggested unfavorable consequences, such as arrhythmias and tachycardia [16, 17]. In addition, some studies showed that basal heart rate was either decreased and coupled with arrhythmias or increased with occurrence of tachycardia [18, 19].

In the heart, the β -adrenergic receptors (β ARs), associated to G proteins, play a crucial role in the regulation of the cardiac function [20, 21]; the stimulation of β_1 ARs and β_2 ARs increases the cardiac rate via cAMP production [20].

In this work, we have designed an *in vitro* model of murine ventricular cardiac tissue in order to study the contraction movement under electromagnetic and/or β -adrenergic stimulation, addressing, in particular, the inotropic and trophic effects.

2. Materials and Methods

2.1. Beating Mouse Cardiac Syncytia. Spontaneously beating cardiac syncytia were obtained from the hearts of 1- to 2-day-old CD-1[®] mouse pups (Charles River Laboratories Italia, Calco, Italy), as previously described [22–24] with some modifications. Briefly, beating primary cultures of murine cardiomyocytes were prepared *in vitro* as follows: the hearts were quickly excised, the atria were cut off, and the ventricles were minced and digested by incubation with 100 μ g/ml type II collagenase (Invitrogen, Carlsbad, CA) and with 900 μ g/ml pancreatin (Sigma-Aldrich, Milan, Italy) in ADS buffer (0.1 M HEPES, 0.1 M D-glucose, 0.5 M NaCl, 0.1 M KCl, 0.1 M NaH₂PO₄•H₂O, 0.1 M MgSO₄) for 15 min at 37°C. The resulting cell suspension was preplated for 2 h at 37°C to reduce the contribution of nonmyocardial cells. The unattached, cardiomyocyte-enriched cells remaining in suspension were collected, plated onto collagen-coated 35 mm Petri dishes, and covered by DMEM containing 10% horse serum, 5% fetal bovine serum, and 1 \times gentamicin (Roche Molecular Biochemicals, Indianapolis, IN). About 3×10^5 cardiomyocytes were cultured in each Petri dish at 37°C and 5% CO₂ to form a spontaneously beating cardiac syncytium (i.e., a cardiac cell culture made by multilayers of contracting cardiomyocytes as in our previous works [25, 26]).

2.2. Experimental Conditions. On day 3 of culture, at a constant temperature of 37°C and 5% CO₂, each syncytium was observed via a movie capture system (ProgRes C5, Jenoptik, Germany) in four different conditions: untreated control (CTRL); stimulus via β -adrenergic isoproterenol (ISO, 10 μ M; Sigma-Aldrich, Milan, Italy); stimulus via an electromagnetic field (EMF; see below for details); and stimulus via both isoproterenol and electromagnetic field (ISO + EMF). In particular, for each condition, AVI videos

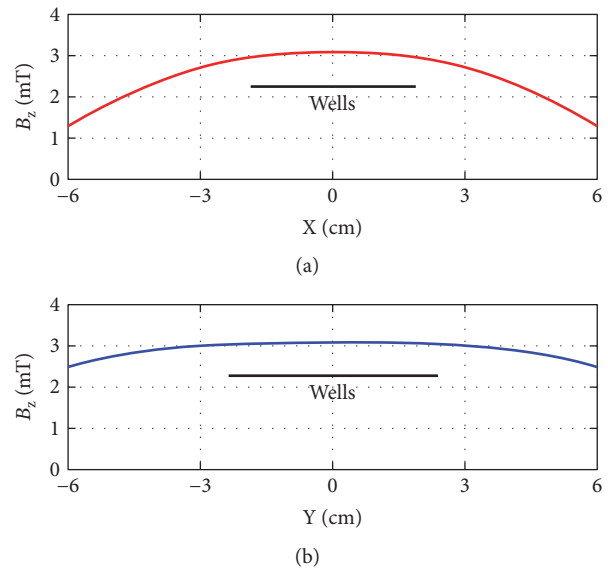


FIGURE 1: Magnetic induction field. Vertical component B_z (in the Z direction) of the magnetic induction field B inside the electromagnetic bioreactor versus the X and the Y directions (panels (a) and (b), resp.). B_x and B_y were negligible. The wells used for cell culture were in the region of field’s quasihomogeneity (black horizontal lines in the center of the bioreactor).

(duration, 20 s) of 20 beating syncytia were collected every 3 min, permitting us to specifically study the average contraction pattern during the time interval 27–39 min.

2.3. Electromagnetic Bioreactor. The electromagnetic bioreactor used here has been previously investigated in terms of biological effects [27–31] and in terms of numerical dosimetry and physical parameters (induced electric field, induced electric current, and induced forces) [13]. The setup was based on two air-cored solenoids (see Figure 1 in [13]) connected in series, placed inside a cell incubator, and powered by a pulse generator (Biostim SPT from Igea, Carpi, Italy). The magnetic induction field (module, circa 3 mT; frequency, 75 Hz) was perpendicular to the seeded cells. In particular, in our experimental setup

- (i) the electric current in the solenoids’ wire ranged from 0 to 319 mA in 1.36 ms;
- (ii) in order to optimize the spatial homogeneity of the magnetic induction field, especially in the central region where the cells were stimulated, the two solenoids were supplied by the same electric current and their dimensions and distance were comparable; the spatial homogeneity was calculated *in silico* [13] and verified inside the cell incubator by means of a Hall effect gaussmeter (Figure 1);
- (iii) the maximum electromagnetic energy density applied to the cells was about 3.18 joule/m³ and, using a thermocouple, we observed no EMF-induced heating;
- (iv) during the same time interval of the electromagnetic stimulation, control cells were placed into another but identical incubator with no EMF.

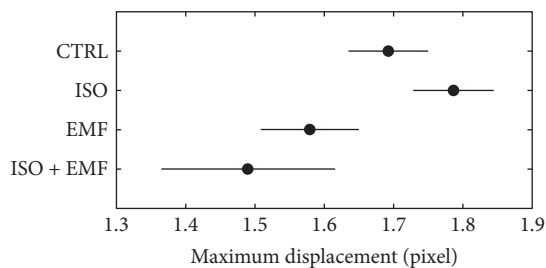


FIGURE 2: Mean maximum contraction displacement (during the time interval 27–39 min). In terms of kinematics, in comparison with control (CTRL), the isoproterenol (ISO) showed a nonsignificant positive inotropic effect ($p > 0.05$) and the electromagnetic stimulation (EMF) caused a nonsignificant negative inotropic action ($p > 0.05$). The simultaneous use of pharmacological and physical stimulation (ISO + EMF) significantly reduced the positive inotropic effect of ISO ($p < 0.05$), giving an overall significant negative inotropic action in comparison with CTRL ($p < 0.05$). The horizontal bars are the 95% confidence intervals for the differences between means according to LSD (least significant difference) statistical test: there is a statistically significant difference between the means with nonoverlapping bars ($n = 20$ syncytia for each condition).

2.4. Registration of the Syncytium Movement via the Apposition of Software Markers. By the Video Spot Tracker (VST) program, which is used to track the motion of one or more spots in an AVI video file (<http://cismm.web.unc.edu/software/>), in each video, we have systematically selected 30 spots or markers onto the first video frame, according to the same orthogonal grid [32, 33]. By starting the videos in VST, frame by frame, the program followed and registered the spatial-temporal coordinates x , y , and t for each marker, as previously described [25]. The coordinates x and y are expressed in pixel, whereas the coordinate t is in s.

2.5. Kinematics and Dynamics of the Beating Syncytium. By an algorithm based on the Matlab programming language (The MathWorks Inc., Natick, MA), frame by frame and for each marker, we have studied the kinematics and the dynamics of the beating cardiac syncytia, as previously described [25, 26, 34] (see Appendix below for the mathematical details). In particular, in this work, we have evaluated the syncytium contraction in terms of maximum contraction displacement [pixel], contractility (maximum contraction velocity) [pixel/s], and contraction acceleration [pixel/s²].

2.6. Immunofluorescence Analysis. Isolated cardiomyocytes were cultured in monolayer in a humidified atmosphere of 5% CO₂ at 37°C for 48 h in the four preceding conditions. The cardiomyocytes were then fixed with 4% w/v paraformaldehyde (Sigma-Aldrich) in PBS (EuroClone, Pero, Italy) for 10 min at 4°C. The cells were washed with PBS and permeabilized with a solution of 0.2% v/v Triton X-100 (Sigma-Aldrich) in PBS for 10 min at 4°C and for further 30 min at room temperature.

The cells were blocked and incubated overnight with the murine monoclonal antibody MHC obtained from hybridoma (MF20, 1:5 v/v; Developmental Studies Hybridoma Bank, University of Iowa), which is able to recognize the

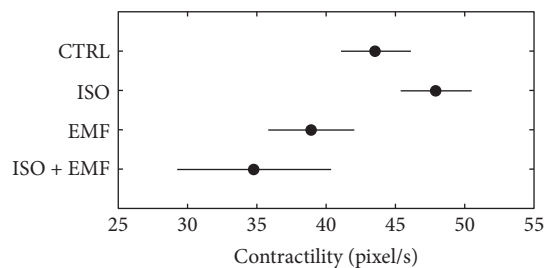


FIGURE 3: Mean contractility (during the time interval 27–39 min). In terms of kinematics, in comparison with control (CTRL), the isoproterenol (ISO) showed a nonsignificant positive inotropic effect ($p > 0.05$) and the electromagnetic stimulation (EMF) caused a nonsignificant negative inotropic action ($p > 0.05$). The simultaneous use of pharmacological and physical stimulation (ISO + EMF) significantly reduced the positive inotropic effect of ISO ($p < 0.05$), giving an overall significant negative inotropic action in comparison with CTRL ($p < 0.05$). The horizontal bars are the 95% confidence intervals for the differences between means according to LSD (least significant difference) statistical test: there is a statistically significant difference between the means with nonoverlapping bars ($n = 20$ syncytia for each condition).

sarcomeric myosin expressed by differentiated cardiomyocytes. Subsequently, the cells were incubated for 45 min at room temperature with a secondary antibody (anti-mouse Cy3, 1:50 v/v; Jackson ImmunoResearch, Newmarket, UK) conjugated to a fluorescent probe.

The cells were then observed with a Nikon Eclipse Ti microscope. The immunofluorescence was quantified by ImageJ software (<https://imagej.nih.gov/ij/index.html>).

2.7. Statistics. In order to compare the results between the different conditions, one-way analysis of variance (ANOVA) with post hoc least significant difference (LSD) test was applied, electing a significance level of 0.05. The results are expressed as mean \pm 95% confidence interval for the differences between means.

3. Results

In terms of kinematics (Figures 2 and 3), in comparison with the control, the isoproterenol showed a nonsignificant positive inotropic effect ($p > 0.05$) and the electromagnetic stimulation caused a nonsignificant negative inotropic action ($p > 0.05$). The pharmacological-physical stimulation significantly reduced the positive inotropic effect of isoproterenol ($p < 0.05$), giving an overall significant negative inotropic action in comparison with the control ($p < 0.05$).

In terms of dynamics (Figure 4), in comparison with the control, the isoproterenol showed a significant positive inotropic effect ($p < 0.05$) and the electromagnetic stimulation caused a significant negative inotropic action ($p < 0.05$). The pharmacological-physical stimulation significantly reduced the positive inotropic effect of isoproterenol ($p < 0.05$), giving an overall significant negative inotropic action in comparison with the control ($p < 0.05$).

In addition, in isolated cardiomyocytes after 48 h of culture (Figures 5 and 6), in comparison with the control,

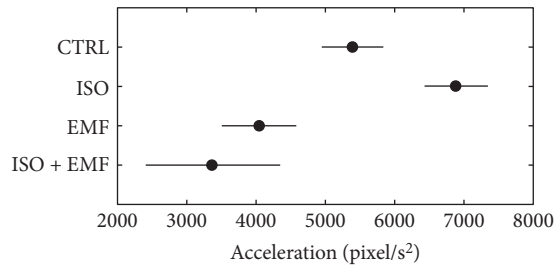


FIGURE 4: Mean contraction acceleration (during the time interval 27–39 min). In terms of dynamics, in comparison with control (CTRL), the isoproterenol (ISO) showed a significant positive inotropic effect ($p < 0.05$) and the electromagnetic stimulation (EMF) caused a significant negative inotropic action ($p < 0.05$). The simultaneous use of pharmacological and physical stimulation (ISO + EMF) significantly reduced the positive inotropic effect of ISO ($p < 0.05$), giving an overall significant negative inotropic action in comparison with CTRL ($p < 0.05$). The horizontal bars are the 95% confidence intervals for the differences between means according to LSD (least significant difference) statistical test: there is a statistically significant difference between the means with nonoverlapping bars ($n = 20$ syncytia for each condition).

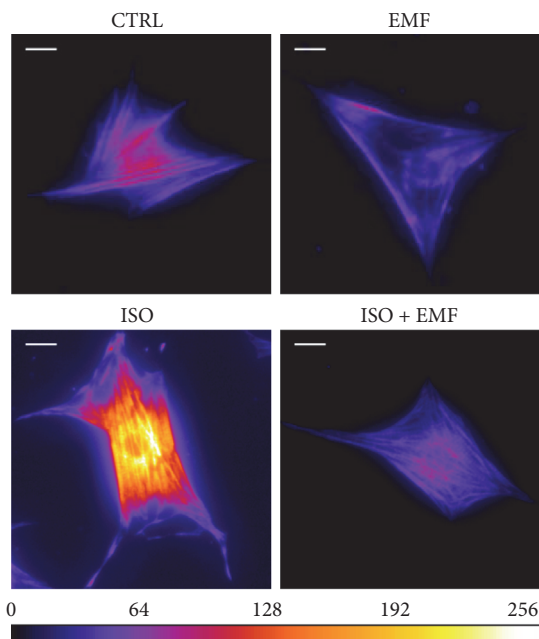


FIGURE 5: Immunofluorescence. A Fire LUT was applied using ImageJ in order to show the levels of MF20 immunofluorescence after 48 h of culture (white scale bar, $10 \mu\text{m}$; color scale in the range of 0–256 [arbitrary unit]). In comparison with control (CTRL), the isoproterenol (ISO) showed an enhancement of the fluorescence, whereas the electromagnetic stimulation (EMF) caused a reduction. The simultaneous use of pharmacological and physical stimulation (ISO + EMF) weakened the effect of ISO, giving an impairment in comparison with CTRL. The physically stimulated cultures showed an antisarcomeric effect of the electromagnetic field in the long term.

the isoproterenol showed a significant prosarcomeric effect ($p < 0.05$) and the electromagnetic stimulation caused a significant antisarcomeric action ($p < 0.05$). The simultaneous

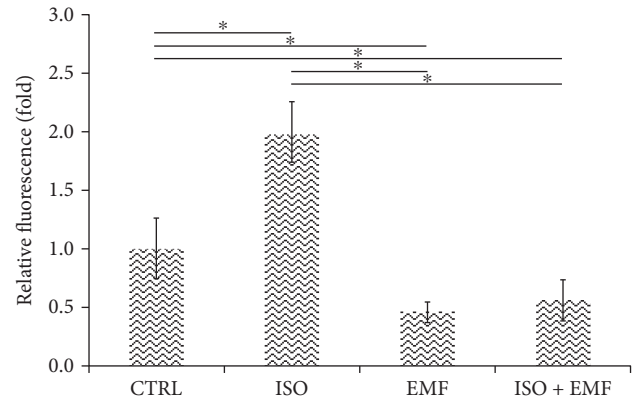


FIGURE 6: Quantitative immunofluorescence. After 48 h of culture, in comparison with control (CTRL), the isoproterenol (ISO) showed a significant prosarcomeric effect ($*p < 0.05$) and the electromagnetic stimulation (EMF) caused a significant antisarcomeric action ($*p < 0.05$). The simultaneous use of pharmacological and physical stimulation (ISO + EMF) significantly reduced the effect of ISO ($*p < 0.05$), giving an overall significant antisarcomeric action in comparison with CTRL ($*p < 0.05$). The normalized data are expressed as mean fold \pm 95% confidence interval ($n = 20$ cells for each condition).

use of pharmacological and physical stimulation significantly reduced the effect of isoproterenol ($p < 0.05$), giving an overall significant antisarcomeric action in comparison with the control ($p < 0.05$).

4. Discussion

The mouse is in the center of the research due to the high potential in manipulating its genome and the consequent availability of models of cardiovascular diseases. Using *in vitro* beating primary murine ventricular cardiomyocytes, we have studied the alteration of their contraction following the mechanical forces induced by an electromagnetic field and/or a β -adrenergic stimulation ($10 \mu\text{M}$ isoproterenol) [13, 14].

Studies about the action of electromagnetic fields on the heart function are of interest due to the high rate of cardiac diseases and the everyday environmental electromagnetic exposure [35]. However, the epidemiological studies have been indecisive [18, 36].

By means of an electromagnetic bioreactor, previously described [27–29, 37–45], our preceding study showed that an exposure to a low-frequency EMF decreases the beat frequency of neonatal murine cardiomyocytes, frequency and amplitude of the intracellular calcium transients, the contraction force, the kinetic energy, and also the effects of the β -adrenergic stimulation [14].

In the present study, we have showed that a low-frequency electromagnetic stimulus was able to counteract both the basal inotropism and the β -adrenergically enhanced inotropism, probably due to the internalization of $\beta_2\text{ARs}$ [14] and/or the inhibition of T-type calcium channels via AA/LTE4 signaling pathway [46].

In addition, the anti- β -adrenergic response after short exposure (27–39 min) to EMF preempted an antisarcomeric/antihypertrophic effect due to a longer exposure (48 h); in other words, a prolonged underuse of the sarcomeric apparatus caused a down remodeling of it.

5. Conclusion

Although some epidemiological studies raise concerns about the low-frequency electromagnetic exposure [18, 36], this work suggests a potential application of that biophysical stimulus in the treatment of arrhythmias and hypertrophy. In particular, a weakening of the β -adrenergic sensibility can be significant in the ischemia-reperfusion injuries, where an abnormal depolarization could arise outside the normal conduction tissue causing life-threatening arrhythmias.

Appendix

Being both contraction and relaxation active phases of the syncytium movement, we have defined E as the mean kinetic energy of a beating syncytium in a discrete video:

$$E = \frac{1}{2} A \frac{B}{NM} \sum_{i=1}^N \sum_{j=1}^M |\underline{v}_{i,j}|^2 \quad \text{in joule,} \quad (\text{A.1})$$

where $\underline{v}_{i,j}$ is the velocity of the marker i in the frame j , M is the total number of video frames, N is the total number of markers ($N = 30$), A is the constant related to the tissue mass, and B is the constant derived from the linear relation between the units meter and pixel in a bitmap AVI video at a given magnification. In (A.1), for each syncytium, in order to compare the four different experimental conditions [untreated control (CTRL), stimulus via β -adrenergic isoproterenol (ISO), stimulus via an electromagnetic field (EMF), and stimulus via both isoproterenol and electromagnetic field (ISO + EMF)], there was no need to know the mass of the beating tissue or the A constant, because that mass and constant were the same in the four different conditions and the spot markers were juxtaposed in the same grid positions. In addition, there was no need to know the video metrics or the B constant, because that metrics and constant and the video magnification were the same at all conditions.

According to Sonnenblick et al. [47, 48], the maximum contraction velocity is an indicator of contractility. As a consequence, in order to study a possible inotropic effect under a kinematic point of view, for each marker during its beating, we have identified both the maximum contraction velocity and the maximum contraction displacement; then, we have calculated the mean contractility [pixel/s] (Figure 3) and the mean maximum contraction displacement [pixel] (Figure 2), respectively.

In order to study a possible inotropic effect under a dynamic point of view, we have evaluated the syncytium contraction by the Hamiltonian mechanics. The so-called Hamiltonian function H is the sum of the kinetic and potential energy. Assuming that, during the whole video observation, there was a plentiful source of available glucose from the culture medium and that the subsequent ATP production

and distribution were isotropic, P_{ATP} , the ATP-related potential energy for the contraction movement, could be supposed constant in time and in space. As a consequence, the Hamilton differential equations to describe the syncytium movement were

$$\begin{aligned} F_x &= -\frac{\partial H}{\partial x} = -\frac{\partial}{\partial x} (E_{\text{ATP}} + P_{\text{ATP}}) = -\frac{\partial E_{\text{ATP}}}{\partial x} \quad \text{in newton,} \\ F_y &= -\frac{\partial H}{\partial y} = -\frac{\partial}{\partial y} (E_{\text{ATP}} + P_{\text{ATP}}) = -\frac{\partial E_{\text{ATP}}}{\partial y} \quad \text{in newton,} \end{aligned} \quad (\text{A.2})$$

where F_x and F_y are the orthogonal components of the contraction force \underline{F} and $E_{\text{ATP}} = E_{\text{ATP}}(x, y, t)$ is the kinetic energy function of the beating syncytium.

Then, we have defined F_{mean} as the normalized mean contraction force, that is, as the mean contraction acceleration (Figure 4) of a beating syncytium in a discrete video:

$$F_{\text{mean}} = \frac{1}{ABNM} \sum_{i=1}^N \sum_{j=1}^M |E_{i,j}| \quad \text{in } \frac{\text{pixel}}{\text{s}^2}. \quad (\text{A.3})$$

Ethical Approval

All procedures involving mice were completed in accordance with the policy of the Italian National Institute of Health (Protocol no. 118/99-A) and with the ethical guidelines for animal care of the European Community Council (Directive no. 86/609/ECC). CD-1 mice were obtained from Charles River Laboratories Italia (Calco, Italy) and were housed under 12 h light/dark cycles, at constant temperature, and with food and water ad libitum. The mice were sacrificed by cervical dislocation.

Conflicts of Interest

The authors declare that there is no conflict of interest regarding the publication of this paper.

Acknowledgments

This work was supported by Research Grants from INAIL [INAIL 2010 to Andrea Lenzi and Fabio Naro], from Sapienza University of Rome [Ateneo 2009 to Fabio Naro], and from the Italian Ministry of University [FIRB 2010 RBAP109BLT and FIRB 2010 RBFR10URHP to Andrea Lenzi and Fabio Naro; PRIN 2010 KL2Y73-006 to Fabio Naro].

References

- [1] F. M. Pavalko, S. M. Norvell, D. B. Burr, C. H. Turner, R. L. Duncan, and J. P. Bidwell, "A model for mechanotransduction in bone cells: the load-bearing mechanosomes," *Journal of Cellular Biochemistry*, vol. 88, no. 1, pp. 104–112, 2003.
- [2] L. Fassina, L. Visai, L. Asti et al., "Calcified matrix production by SAOS-2 cells inside a polyurethane porous scaffold, using a perfusion bioreactor," *Tissue Engineering*, vol. 11, no. 5-6, pp. 685–700, 2005.

- [3] S. R. Young, R. Gerard-O'Riley, J. B. Kim, and F. M. Pavalko, "Focal adhesion kinase is important for fluid shear stress-induced mechanotransduction in osteoblasts," *Journal of Bone and Mineral Research*, vol. 24, no. 3, pp. 411–424, 2009.
- [4] L. Fassina, E. Saino, M. G. Cusella De Angelis, G. Magenes, F. Benazzo, and L. Visai, "Low-power ultrasounds as a tool to culture human osteoblasts inside cancellous hydroxyapatite," *Bioinorganic Chemistry and Applications*, vol. 2010, Article ID 456240, 8 pages, 2010.
- [5] E. Saino, V. Maliardi, E. Quartarone et al., "In vitro enhancement of SAOS-2 cell calcified matrix deposition onto radio frequency magnetron sputtered bioglass-coated titanium scaffolds," *Tissue Engineering Part A*, vol. 16, no. 3, pp. 995–1008, 2010.
- [6] D. H. Kim, S. B. Khatau, Y. Feng et al., "Actin cap associated focal adhesions and their distinct role in cellular mechanosensing," *Scientific Reports*, vol. 2, article 555, 2012.
- [7] D. E. Ingber, "Tensegrity I. Cell structure and hierarchical systems biology," *Journal of Cell Science*, vol. 116, Part 7, pp. 1157–1173, 2003.
- [8] D. E. Ingber, "Tensegrity II. How structural networks influence cellular information processing networks," *Journal of Cell Science*, vol. 116, Part 8, pp. 1397–1408, 2003.
- [9] D. E. Ingber, "Mechanical control of tissue morphogenesis during embryological development," *The International Journal of Developmental Biology*, vol. 50, no. 2-3, pp. 255–266, 2006.
- [10] T. Mammoto and D. E. Ingber, "Mechanical control of tissue and organ development," *Development*, vol. 137, no. 9, pp. 1407–1420, 2010.
- [11] J. Hansmann, F. Groeber, A. Kahlig, C. Kleinhans, and H. Walles, "Bioreactors in tissue engineering - principles, applications and commercial constraints," *Biotechnology Journal*, vol. 8, no. 3, pp. 298–307, 2013.
- [12] S. V. Murphy and A. Atala, "Organ engineering—combining stem cells, biomaterials, and bioreactors to produce bioengineered organs for transplantation," *BioEssays*, vol. 35, no. 3, pp. 163–172, 2013.
- [13] M. E. Mognaschi, P. Di Barba, G. Magenes, A. Lenzi, F. Naro, and L. Fassina, "Field models and numerical dosimetry inside an extremely-low-frequency electromagnetic bioreactor: the theoretical link between the electromagnetically induced mechanical forces and the biological mechanisms of the cell tensegrity," *Spring*, vol. 3, p. 473, 2014.
- [14] M. Cornacchione, M. Pellegrini, L. Fassina et al., " β -Adrenergic response is counteracted by extremely-low-frequency pulsed electromagnetic fields in beating cardiomyocytes," *Journal of Molecular and Cellular Cardiology*, vol. 98, pp. 146–158, 2016.
- [15] L. Hardell and C. Sage, "Biological effects from electromagnetic field exposure and public exposure standards," *Biomedicine & Pharmacotherapy*, vol. 62, no. 2, pp. 104–109, 2008.
- [16] C. M. Maresh, M. R. Cook, H. D. Cohen, C. Graham, and W. S. Gunn, "Exercise testing in the evaluation of human responses to powerline frequency fields," *Aviation, Space, and Environmental Medicine*, vol. 59, no. 12, pp. 1139–1145, 1988.
- [17] C. Graham, M. R. Cook, H. D. Cohen, and M. M. Gerkovich, "Dose response study of human exposure to 60 Hz electric and magnetic fields," *Bioelectromagnetics*, vol. 15, no. 5, pp. 447–463, 1994.
- [18] D. A. Savitz, D. Liao, A. Sastre, R. C. Kleckner, and R. Kavet, "Magnetic field exposure and cardiovascular disease mortality among electric utility workers," *American Journal of Epidemiology*, vol. 149, no. 2, pp. 135–142, 1999.
- [19] L. Korpinen, J. Partanen, and A. Uusitalo, "Influence of 50 Hz electric and magnetic fields on the human heart," *Bioelectromagnetics*, vol. 14, no. 4, pp. 329–340, 1993.
- [20] M. J. Lohse, S. Engelhardt, and T. Eschenhagen, "What is the role of β -adrenergic signaling in heart failure?," *Circulation Research*, vol. 93, no. 10, pp. 896–906, 2003.
- [21] D. K. Rohrer, A. Chruscinski, E. H. Schauble, D. Bernstein, and B. K. Kobilka, "Cardiovascular and metabolic alterations in mice lacking both β_1 - and β_2 -adrenergic receptors," *The Journal of Biological Chemistry*, vol. 274, no. 24, pp. 16701–16708, 1999.
- [22] E. Devic, Y. Xiang, D. Gould, and B. Kobilka, " β -Adrenergic receptor subtype-specific signaling in cardiac myocytes from β_1 and β_2 adrenoceptor knockout mice," *Molecular Pharmacology*, vol. 60, no. 3, pp. 577–583, 2001.
- [23] Y. Xiang, V. O. Rybin, S. F. Steinberg, and B. Kobilka, "Caveolar localization dictates physiologic signaling of β_2 -adrenoceptors in neonatal cardiac myocytes," *The Journal of Biological Chemistry*, vol. 277, no. 37, pp. 34280–34286, 2002.
- [24] Y. Xiang, F. Naro, M. Zoudilova, S. L. Jin, M. Conti, and B. Kobilka, "Phosphodiesterase 4D is required for β_2 adrenoceptor subtype-specific signaling in cardiac myocytes," *Proceedings of the National Academy of Sciences of the United States of America*, vol. 102, no. 3, pp. 909–914, 2005.
- [25] L. Fassina, A. Di Grazia, F. Naro, L. Monaco, M. G. Cusella De Angelis, and G. Magenes, "Video evaluation of the kinematics and dynamics of the beating cardiac syncytium: an alternative to the Langendorff method," *The International Journal of Artificial Organs*, vol. 34, no. 7, pp. 546–558, 2011.
- [26] L. Fassina, G. Magenes, R. Gimmelli, and F. Naro, "Modulation of the cardiomyocyte contraction inside a hydrostatic pressure bioreactor: in vitro verification of the Frank-Starling law," *BioMed Research International*, vol. 2015, Article ID 542105, 7 pages, 2015.
- [27] L. Fassina, L. Visai, F. Benazzo et al., "Effects of electromagnetic stimulation on calcified matrix production by SAOS-2 cells over a polyurethane porous scaffold," *Tissue Engineering*, vol. 12, no. 7, pp. 1985–1999, 2006.
- [28] L. Fassina, E. Saino, L. Visai et al., "Electromagnetic enhancement of a culture of human SAOS-2 osteoblasts seeded onto titanium fiber-mesh scaffolds," *Journal of Biomedical Materials Research Part A*, vol. 87, no. 3, pp. 750–759, 2008.
- [29] L. Fassina, E. Saino, M. S. Sbarra et al., "In vitro electromagnetically stimulated SAOS-2 osteoblasts inside porous hydroxyapatite," *Journal of Biomedical Materials Research Part A*, vol. 93, no. 4, pp. 1272–1279, 2010.
- [30] C. Osera, L. Fassina, M. Amadio et al., "Cytoprotective response induced by electromagnetic stimulation on SH-SY5Y human neuroblastoma cell line," *Tissue Engineering Part A*, vol. 17, no. 19-20, pp. 2573–2582, 2011.
- [31] N. Marchesi, C. Osera, L. Fassina et al., "Autophagy is modulated in human neuroblastoma cells through direct exposition to low frequency electromagnetic fields," *Journal of Cellular Physiology*, vol. 229, no. 11, pp. 1776–1786, 2014.
- [32] C. A. Mandarim-de-Lacerda, "Stereological tools in biomedical research," *Anais da Academia Brasileira de Ciências*, vol. 75, no. 4, pp. 469–486, 2003.

- [33] C. Mühlfeld, J. R. Nyengaard, and T. M. Mayhew, "A review of state-of-the-art stereology for better quantitative 3D morphology in cardiac research," *Cardiovascular Pathology*, vol. 19, no. 2, pp. 65–82, 2010.
- [34] V. Meraviglia, J. Wen, L. Piacentini et al., "Higher cardiogenic potential of iPSCs derived from cardiac versus skin stromal cells," *Frontiers in Bioscience (Landmark Edition)*, vol. 21, pp. 719–743, 2016.
- [35] L. Kheifets, A. Ahlbom, C. Johansen, M. Feychting, J. Sahl, and D. Savitz, "Extremely low-frequency magnetic fields and heart disease," *Scandinavian Journal of Work, Environment & Health*, vol. 33, no. 1, pp. 5–12, 2007.
- [36] O. Elmas, S. Comlekci, and H. Koylu, "Effects of short-term exposure to powerline-frequency electromagnetic field on the electrical activity of the heart," *Archives of Environmental & Occupational Health*, vol. 67, no. 2, pp. 65–71, 2012.
- [37] A. Icaro Cornaglia, M. Casasco, F. Riva et al., "Stimulation of osteoblast growth by an electromagnetic field in a model of bone-like construct," *European Journal of Histochemistry*, vol. 50, no. 3, pp. 199–204, 2006.
- [38] E. Saino, L. Fassina, S. Van Vlierberghe et al., "Effects of electromagnetic stimulation on osteogenic differentiation of human mesenchymal stromal cells seeded onto gelatin cryogel," *International Journal of Immunopathology and Pharmacology*, vol. 24, no. 1, Supplement 2, pp. 1–6, 2011.
- [39] L. Fassina, E. Saino, L. Visai et al., "Electromagnetic stimulation to optimize the bone regeneration capacity of gelatin-based cryogels," *International Journal of Immunopathology and Pharmacology*, vol. 25, no. 1, pp. 165–174, 2012.
- [40] G. Ceccarelli, N. Bloise, M. Mantelli et al., "A comparative analysis of the *in vitro* effects of pulsed electromagnetic field treatment on osteogenic differentiation of two different mesenchymal cell lineages," *BioResearch Open Access*, vol. 2, no. 4, pp. 283–294, 2013.
- [41] C. Osera, M. Amadio, S. Falone et al., "Pre-exposure of neuroblastoma cell line to pulsed electromagnetic field prevents H₂O₂-induced ROS production by increasing MnSOD activity," *Bioelectromagnetics*, vol. 36, no. 3, pp. 219–232, 2015.
- [42] S. Falone, N. Marchesi, C. Osera et al., "Pulsed electromagnetic field (PEMF) prevents pro-oxidant effects of H₂O₂ in SK-N-BE(2) human neuroblastoma cells," *International Journal of Radiation Biology*, vol. 92, no. 5, pp. 281–286, 2016.
- [43] F. Pasi, L. Fassina, M. E. Mognaschi et al., "Pulsed electromagnetic field with temozolomide can elicit an epigenetic pro-apoptotic effect on glioblastoma T98G cells," *Anticancer Research*, vol. 36, no. 11, pp. 5821–5826, 2016.
- [44] E. Capelli, F. Torrisi, L. Venturini et al., "Low-frequency pulsed electromagnetic field is able to modulate miRNAs in an experimental cell model of Alzheimer's disease," *Journal of Healthcare Engineering*, vol. 2017, Article ID 2530270, 10 pages, 2017.
- [45] P. Di Barba, L. Fassina, G. Magenes, and M. E. Mognaschi, "Shape synthesis of a well-plate for electromagnetic stimulation of cells," *International Journal of Numerical Modelling: Electronic Networks, Devices and Fields*, vol. 30, 2017.
- [46] Y. Cui, X. Liu, T. Yang, Y. A. Mei, and C. Hu, "Exposure to extremely low-frequency electromagnetic fields inhibits T-type calcium channels via AA/LTE4 signaling pathway," *Cell Calcium*, vol. 55, no. 1, pp. 48–58, 2014.
- [47] E. H. Sonnenblick, J. F. Williams Jr., G. Glick, D. T. Mason, and E. Braunwald, "Studies on digitalis. XV. Effects of cardiac glycosides on myocardial force-velocity relations in the non-failing human heart," *Circulation*, vol. 34, no. 3, pp. 532–539, 1966.
- [48] J. W. Covell, J. Ross Jr., E. H. Sonnenblick, and E. Braunwald, "Comparison of the force-velocity relation and the ventricular function curve as measures of the contractile state of the intact heart," *Circulation Research*, vol. 19, no. 2, pp. 364–372, 1966.

Research Article

Quantitative Analysis of Intracellular Motility Based on Optical Flow Model

Yali Huang,¹ Lei Hao,¹ Heng Li,² Zhiwen Liu,² and Peiguang Wang¹

¹College of Electronics and Information Engineering, Hebei University, Baoding 071002, China

²School of Information and Electronics, Beijing Institute of Technology, Beijing 100081, China

Correspondence should be addressed to Zhiwen Liu; zwliu@bit.edu.cn and Peiguang Wang; pgwang@hbu.edu.cn

Received 17 February 2017; Accepted 21 May 2017; Published 30 July 2017

Academic Editor: Md. A. R. Ahad

Copyright © 2017 Yali Huang et al. This is an open access article distributed under the Creative Commons Attribution License, which permits unrestricted use, distribution, and reproduction in any medium, provided the original work is properly cited.

Analysis of cell mobility is a key issue for abnormality identification and classification in cell biology research. However, since cell deformation induced by various biological processes is random and cell protrusion is irregular, it is difficult to measure cell morphology and motility in microscopic images. To address this dilemma, we propose an improved variation optical flow model for quantitative analysis of intracellular motility, which not only extracts intracellular motion fields effectively but also deals with optical flow computation problem at the border by taking advantages of the formulation based on L_1 and L_2 norm, respectively. In the energy functional of our proposed optical flow model, the data term is in the form of L_2 norm; the smoothness of the data changes with regional features through an adaptive parameter, using L_1 norm near the edge of the cell and L_2 norm away from the edge. We further extract histograms of oriented optical flow (HOOF) after optical flow field of intracellular motion is computed. Then distances of different HOOFs are extracted as the intracellular motion features to grade the intracellular motion. Experimental results show that the features extracted from HOOFs provide new insights into the relationship between the cell motility and the special pathological conditions.

1. Introduction

Cell morphology and mobility indicate physiological and pathological characters of the organism [1]. It has been demonstrated that quantitative analysis of cell morphology and mobility offers the possibility to improve our understanding of the biological processes at the cellular level [2]. Estimation of live cell mobility for analyzing dynamic properties of biological and pathological phenomena has been extensively used in clinical diagnosis and biological research, including inflammation research, drug test, wound healing, tumor genesis, and immune response [3–7]. Life information under special condition is to be uncovered by quantitative analysis of intracellular motility. However, it is difficult to measure intracellular motility due to irregular complicated cell deformation. Here, we proposed a novel approach for quantitative analysis of intracellular motility based on optical flow model.

Starting from the original work of Horn and Schunck (HS) model as well as Lucas and Kanade (LK) model [8, 9],

optical flow method has been widely used in the computer vision applications for estimating the motion of the object, which is also a primary method applied in quantitative motion estimation of biological structures in light microscopy [10–12]. Vig et al. reviewed the main methods for measuring cell-scale flows, including single-particle tracking (SPT), particle image velocimetry (PIV), and optical flow [13]. Moreover, they found that although SPT and PIV techniques have been the principal means for analyzing bioflows in the cellular biophysics, optical flow technique outperforms than the formers for its relatively simple implementation and providing additional biophysical information such as local velocity [13]. Boric et al. applied optical flow method to quantify the movements of populations of cells and detect subtle cell changes in quantitative analysis of cell migration [14]. Guo et al. applied optical flow methods to track red blood cell [15]. Optical flow technique was also used in measurement of blood flow velocity in vivo [16]. All the abovementioned research work mainly regarded the cell as a whole and focus

their attention on the movement of the whole cell. Little attention has been to the intracellular motion.

In this paper, we propose an improved optical flow method-based variation model for analyzing intracellular mobility in phase contrast microscopic cell images. The data term in the energy functional of the optical flow model adopts a L_2 norm, which is beneficial to extract the smooth velocity field of the intracellular movement. While the smoothness term in the energy functional changes with the regional feature of the image, using L_2 norm in the intracellular area and L_1 norm nears the edge of the cell according to local features of the image, which is helpful to address the optical flow computation near the edge of the object. Furthermore, histograms of oriented optical flow are used to quantify the intracellular mobility.

The rest of the article is organized as follows. Section 2 reviews related work on optical flow models. Section 3 proposes our scheme: the improved optical flow based on variation model and characterization of intracellular motion based on HOOFs. In Section 4, we present the visualization of intracellular motion based on optical flow and apply the proposed scheme to the synthesized data and the actual data; experimental results are provided. Discussion and conclusions are given in Section 5.

2. The Variation Model of Optical Flow

Optical flow is defined as the vector field expressing 2-dimensional apparent motion pattern of moving object projected on the screen, and this vector field is also viewed as the velocity field of the moving object, which comprises motion and structure information of the observed object. Optical flow computation is based on the correlation in respect with time and space between the two subsequent images of a video. Although many new concepts have been proposed for dealing with different problems in optical flow models, today's optical flow is still similar to HS model or LK model [8, 9]. This kind of variation optical flow normally can be expressed as follows:

$$E(u, v) = E_{\text{data}}(u, v) + \alpha E_{\text{smooth}}(u, v), \quad (1)$$

where (u, v) is the flow vector of a pixel in the 2-dimensional optical flow field; $E_{\text{data}}(u, v)$ is a data term and $E_{\text{smooth}}(u, v)$ is a smooth term, with α being a weight between the two terms. Normally, the data terms are composed of some constancy assumptions, such as gray value, gradient constancy assumption, Hessian conservation equations, and Laplacian conservation equations. These constancy assumptions form constraints for the solution of the variation optical flow model. Different constraints of data term have been used in different motion patterns. The smoothness term, which guarantees the existence of a unique of the optical flow model, adopts different smooth strategies in different applications. The optical flow computation based on the variation method is realized by minimizing an energy functional constituted by some data constraints and a smoothness constraint. For example, in the classical HS model, the data term adopts gray value constancy assumption and the smoothness constraint

is the square of the magnitude of the gradient of the optical flow velocity. Therefore, the energy functional of HS optical flow model is expressed as follows:

$$E_{\text{HS}}(u, v) = \int_{\Omega} \{ [I_{t+1}(x+u) - I_t(x)]^2 + \alpha (|\nabla u|^2 + |\nabla v|^2) \} d\Omega, \quad (2)$$

where $I_t(x)$ and $I_{t+1}(x)$ denote the successive images used to compute optical flow field; $x = (x, y)$ denotes the pixel coordinate and $u = (u, v)$ is the flow vector of a pixel (u and v denote the displacement of a pixel at the horizontal direction and the vertical direction, resp.); Ω indicates the image region. The optical flow field is computed by optimizing the energy functional. That is to say, $u = (u, v)$ is obtained by the minimization of $E_{\text{HS}}(u, v)$.

In the HS optical flow model, both the data term and smooth term are in the form of L_2 norm, and the implementation based on L_2 norm to the image is equivalent to the isotropic diffusion. This kind of method can avoid piecewise constant in the image but lead to blurry edge and details lost. Thus, Papenberg et al. proposed a novel energy functional, in which the data term and the smooth term were expressed as $\Psi(s^2) = \sqrt{s^2 + \varepsilon^2}$ (ε is a small positive number) [17]. To some extent, the minimization of $\Psi(s^2)$ results in approximate implementation based on the L_1 norm. Moreover, Pock et al. proposed a total variation energy functional model, named TV-L1, expressed as follows [18]:

$$E_{\text{TV-L1}}(u, v) = \int_{\Omega} \{ |I_{t+1}(x+u) - I_t(x)| + \alpha (|\nabla u| + |\nabla v|) \} d\Omega, \quad (3)$$

where the data term is based on L_1 norm and the smooth term adopts total variation (TV). From this energy functional, it is found that the minimization of $E_{\text{TV-L1}}$ is equivalent to the optimization based on L_1 norm. The formulation based on L_1 norm to the image is equivalent to the anisotropic diffusion. This kind of implementation can preserve discontinuities near the edge in the optical flow field but result in piecewise constant in the optical flow field. In order to obtain accurate optical flow field both in the edge and in the intracellular area, we propose a flexible optical flow model functional based on the variation model, and the details are described as follows.

3. Methods

3.1. Adaptive Total Variation Optical Flow Model (Adaptive TV Optical Flow Model). In order to compute accurately the optical flow field of the single intracellular motion both near the edge and in the intracellular area, we proposed an energy functional of optical flow model as follows:

$$E_{\text{aTV}}(u, v) = \int_{\Omega} \left\{ \frac{1}{2} [I_{t+1}(x+u) - I_t(x)]^2 + \frac{\alpha}{p} (|\nabla u|^p + |\nabla v|^p) \right\} d\Omega, \quad (4)$$

where $I_t(x)$ is the intensity of the pixel located at $x = (x, y)$ in the frame corresponding to time t ; α is a weight between the data term and the smooth term. The vector $u = (u, v)$ denotes the vector of a pixel in the 2-dimension optical flow field; $u(x, y)$ and $v(x, y)$ are the horizontal and vertical components of the flow field. It can be concluded that $I_{t+1}(x+u) - I_t(x) = I_x u + I_y v + I_t$ based on the gray value constancy assumptions and Taylor's formula [8], so we have another expression of (4).

$$E_{aTV}(u, v) = \int_{\Omega} \left\{ \frac{1}{2} (I_x u + I_y v + I_t)^2 + \frac{\alpha}{p} (|\nabla u|^p + |\nabla v|^p) \right\} d\Omega, \quad (4-1)$$

where $1 < p < 2$ is an adaptive parameter varying with the features of the image.

Our proposed adaptive TV optical flow model is to minimize the above energy functional in (4-1). That is to say, the solution of optical flow field $(u, v) = \arg \min \{E_{aTV}(u, v)\}$ is obtained by minimizing the energy functional (4-1). Using the calculus of the variations, the Euler-Lagrange equation for this energy functional is obtained as follows [19] (the details of solution are shown in Appendix A):

$$\begin{aligned} (I_x u + I_y v + I_t) I_x - \alpha \cdot \nabla \cdot \frac{\nabla u}{|\nabla u|^{2-p}} &= 0 \\ (I_x u + I_y v + I_t) I_y - \alpha \cdot \nabla \cdot \frac{\nabla v}{|\nabla v|^{2-p}} &= 0, \end{aligned} \quad (5)$$

where I_x, I_y, I_t denote the partial derivatives of image brightness with respect to x, y, t . We choose p according to the local feature of the image, using the following equation:

$$p(x, y) = 1 + \frac{1}{1 + |\nabla G_{\sigma} * I(x, y)|^2}, \quad (6)$$

where $G_{\sigma} * I(x, y)$ is the convolution of the image $I(x, y)$ with the Gaussian filter G_{σ} , obtaining smoother image. It is obvious that the value of $|\nabla G_{\sigma} * I(x, y)|$ is high near the edge of the cell. Particularly, if $|\nabla G_{\sigma} * I(x, y)|^2 \rightarrow \infty$, then $p(x, y) \rightarrow 1$. On the contrary, at the intracellular region where far away from the edge, there is $|\nabla G_{\sigma} * I(x, y)|^2 \rightarrow 0$, so we obtain $p(x, y) \rightarrow 2$. In brief, the adaptive parameter $p(x, y)$ is chosen so that it is smaller near a likely edge and larger away from possible edges, varying with the characteristic of the image. Therefore, the proposed adaptive TV optical flow model is equivalent to the image implementation based on L_1 norm near a likely edge when $p(x, y) \approx 1$ and based on L_2 norm far away from possible edges when $p(x, y) \approx 2$, which is helpful to deal with the problem of optical flow computation at the border.

In this study, the numerical implementation of the proposed adaptive TV optical flow model is obtained based on $p = 1$ and $p = 2$, respectively. First, if $p = 1$, we have

$$\begin{aligned} (I_x u + I_y v + I_t) I_x - \alpha \cdot \nabla \cdot \frac{\nabla u}{|\nabla u|} &= 0 \\ (I_x u + I_y v + I_t) I_y - \alpha \cdot \nabla \cdot \frac{\nabla v}{|\nabla v|} &= 0. \end{aligned} \quad (7)$$

Note that $|\nabla u|$ is in the denominator, in order to avoid the singularity. It is common to use a slightly perturbed norm $|\nabla u|_{\varepsilon} = \sqrt{|\nabla u|^2 + \varepsilon}$ to replace $|\nabla u|$, where ε is a small positive number. In the same way, we used $|\nabla v|_{\varepsilon} = \sqrt{|\nabla v|^2 + \varepsilon}$ to replace $|\nabla v|$. Then the gradient decent flow of (7) is

$$\begin{aligned} u_t &= (I_x u + I_y v + I_t) I_x - \alpha \cdot \nabla \cdot \frac{\nabla u}{\sqrt{|\nabla u|^2 + \varepsilon}} \\ v_t &= (I_x u + I_y v + I_t) I_y - \alpha \cdot \nabla \cdot \frac{\nabla v}{\sqrt{|\nabla v|^2 + \varepsilon}}, \end{aligned} \quad (8)$$

where $\nabla u = (u_x, u_y)$; $\nabla v = (v_x, v_y)$; $|\nabla u| = \sqrt{u_x^2 + u_y^2}$; $|\nabla v| = \sqrt{v_x^2 + v_y^2}$; $\nabla^2 u = (\partial^2 u / \partial x^2) + (\partial^2 u / \partial y^2)$; and $\nabla^2 v = (\partial^2 v / \partial x^2) + (\partial^2 v / \partial y^2)$.

To set up discrete iterative solution, using a finite difference approach on a discrete grid, our iterative solution to (8) is as follows:

$$\begin{aligned} u^{n+1} &= u^n + \gamma \left[(I_x u^n + I_y v^n + I_t) I_x - \alpha \cdot \nabla \cdot \frac{\nabla u^n}{\sqrt{|\nabla u^n|^2 + \varepsilon}} \right] \\ v^{n+1} &= v^n + \gamma \left[(I_x u^n + I_y v^n + I_t) I_y - \alpha \cdot \nabla \cdot \frac{\nabla v^n}{\sqrt{|\nabla v^n|^2 + \varepsilon}} \right], \end{aligned} \quad (9)$$

where n corresponds to discrete time and γ denotes the time step for each interaction. Let the indices i, j , and k correspond to x, y , and t . Here, we define some equations as follows:

$$\begin{aligned} I_x &\approx \frac{1}{4} \left\{ I_{ij+1,k} - I_{i,j,k} + I_{i+1,j+1,k} - I_{i+1,j,k} \right. \\ &\quad \left. + I_{i,j+1,k+1} - I_{i,j,k+1} + I_{i+1,j+1,k+1} - I_{i+1,j,k+1} \right\} \\ I_y &\approx \frac{1}{4} \left\{ I_{i+1,j,k} - I_{i,j,k} + I_{i+1,j+1,k} - I_{i,j+1,k} \right. \\ &\quad \left. + I_{i+1,j,k+1} - I_{i,j,k+1} + I_{i+1,j+1,k+1} - I_{i,j+1,k+1} \right\} \\ I_t &\approx \frac{1}{4} \left\{ I_{i,j,k+1} - I_{i,j,k} + I_{i+1,j,k+1} - I_{i+1,j,k} \right. \\ &\quad \left. + I_{i,j+1,k+1} - I_{i,j+1,k} + I_{i+1,j+1,k+1} - I_{i+1,j+1,k} \right\}, \end{aligned} \quad (10)$$

$$\begin{aligned} \nabla^2 u &= \bar{u}_{i,j,k} - u_{i,j,k} \\ \nabla^2 v &= \bar{v}_{i,j,k} - v_{i,j,k}, \end{aligned} \quad (11)$$

$$\begin{aligned} \bar{u}_{i,j,k} &= \frac{1}{6} \{ u_{i-1,j,k} + u_{i,j+1,k} + u_{i+1,j,k} + u_{i,j-1,k} \} \\ &\quad + \frac{1}{12} \{ u_{i-1,j-1,k} + u_{i+1,j-1,k} + u_{i+1,j+1,k} + u_{i-1,j+1,k} \} \\ \bar{v}_{i,j,k} &= \frac{1}{6} \{ v_{i-1,j,k} + v_{i,j+1,k} + v_{i+1,j,k} + v_{i,j-1,k} \} \\ &\quad + \frac{1}{12} \{ v_{i-1,j-1,k} + v_{i+1,j-1,k} + v_{i+1,j+1,k} + v_{i-1,j+1,k} \}. \end{aligned} \quad (12)$$

Substituting (10), (11), and (12) into (9), then we can obtain optical flow (u, v) by the iteration procedure. Second, if $p = 2$, we have

$$\begin{aligned} (I_x u + I_y v + I_t) I_x - \alpha \cdot \nabla^2 u &= 0 \\ (I_x u + I_y v + I_t) I_y - \alpha \cdot \nabla^2 v &= 0, \end{aligned} \quad (13)$$

which is the same as the Euler-Lagrange equation in HS model [8]. Similarly, the iterative solution of (13) is as follows:

$$\begin{aligned} u^{n+1} &= u^n + \gamma [(I_x u^n + I_y v^n + I_t) I_x - \alpha \cdot \nabla^2 u^n] \\ v^{n+1} &= v^n + \gamma [(I_x u^n + I_y v^n + I_t) I_y - \alpha \cdot \nabla^2 v^n]. \end{aligned} \quad (14)$$

3.2. Characterization of Intracellular Motion Based on HOOF. Details on the direction and the magnitude of each pixel's velocity of intracellular motion are expressed in the optical flow field $u = (u, v)$, which is a 2-dimensional vector field. However, the raw optical flow data may be of no use, as it is composed of huge volumes of data. How to obtain quantitative information from the optical flow field is always haunting researchers. A variety of techniques have been devised to address this problem. Chaudhry et al. proposed HOOF for the recognition of human actions [20]. In our study, the HOOF technique is developed to quantify intracellular motion. We perform statistical analysis to the distribution of velocity in the optical flow field. That is to say, the distribution of each pixel's velocity in the optical flow field is analyzed on the basis of statistics theory.

The feature vector of intracellular motion is extracted as follows. First, our proposed optical flow model is applied to compute optical flow fields from the successive frames of the video. Second, each flow vector in the optical flow field is binned according to its primary angle from the horizontal axis and weighed according to its magnitude. Then, we obtain the histogram of all flow vectors in the optical flow field. The function of the histogram is expressed as follows.

$$h(\theta_k) = s_k, \quad k = 1, 2, \dots, L, \quad (15)$$

where $\theta_k = 2\pi(k-1)/L$ denotes different directions (bins); L denotes the number of bins; and s_k is the sum of all velocities of each flow vector in the interval of directions $[\theta_k, \theta_{k+1}]$. The direction of each flow vector is computed as $\theta = \arctan(v/u)$, and the velocity of flow vector is obtained by $\sqrt{u^2 + v^2}$. In our research, in order to extract the quantitative features based on the intracellular motion, the directions of flow vectors are quantified into 16, that is, $L = 16$. So the number of bins in the histogram is 16, and the height of every bin is the sum of all velocities whose angles are in the interval $[\theta_k, \theta_{k+1}]$. Lastly, the histogram is normalized. In brief, HOOFs express the features of the distribution of flow vectors in the optical flow field. Furthermore, we compute the distances of the successive HOOFs and then use these series distances as the feature vector of the intracellular mobility.

4. Experiments and Results

Cell microscopic images were acquired through optical phase contrast microscope at a magnification of 16,000x from the

peripheral blood samples of clean healthy mice. The animal experiments were conducted by the trained staff in Beijing You'an Hospital, which is affiliated to the Capital Medical University. All the disposals are in accordance with the guideline of animal ethics. Each video lasts for 22–24 seconds, and the frame rate is 25 frames per second (every video includes 550–600 frames). It should be noted that the details of segmentation and tracking of the single cell are presented in our early work [21]. In this article, it is assumed that the cell has been segmented and tracked from microscopic images, so we analyze the intracellular motion directly.

4.1. Visualization of Intracellular Motion Based on Optical Flow. We compute optical flow field from the segmented lymphocyte in video directly, and one frame of optical flow field, which is extracted from two successive images, is shown in Figure 1. The direction of the arrow in the optical flow field denotes the direction of the intracellular motion, and the length of the arrow denotes the magnitude of the intracellular motion. In order to compare the effectiveness of the smooth term with different $p(x, y)$, we compute three kinds of optical flows according to $p(x, y) \approx 1$, $p(x, y) \approx 2$, and adaptive $p(x, y)$, as shown in Figures 1(b), 1(c), and 1(d). The results show that the formulation can preserve discontinuities by applying the robust L_1 norm in the smooth term but leads to piecewise constant in the image. On the other side, using L_2 norm in the smooth term can extract more details of motion but causes blurry edge. Applying the adaptive $p(x, y)$ changing with the local features of the image can obtain a good balance between preserving discontinuities and optical flow details.

In addition, we randomly chose two videos, one from the slight intracellular motion of the data group (normal group, NG), and the other is from the dramatic motion group (abnormal group, AG). Then, we computed the optical flow field of the intracellular motion and extracted the magnitude of the optical flow, as is shown by color coding in Figure 2. Based on Figure 2, it is found that the amplitude of the AG is larger than that of NG, which agrees with clinical observation.

4.2. HOOFs Extracted from Intracellular Motion Fields. After the optical flow fields of the intracellular motion are computed, HOOF is extracted from optical flow fields. The characterization of the distribution of all vectors in the optical flow field is counted and expressed in HOOF, as shown in Figure 3.

From Figure 3, it is quite clear that the velocities of pixels in normal group are small and equal in each direction, while the intracellular motion in the abnormal group is more intense and the speed is large at specific direction. These HOOF results agree with the clinicians' observation: the activity of cell is enhanced in the abnormal group (when the disease occurs), that is, the cells in the abnormal group have dramatic deformation, while those in the normal group are more stable.

4.3. Instantaneous Velocity Extraction of Intracellular Motion Fields. To verify our proposed approach, we first verify it to the synthesized data then apply it to the actual data in Section 4.4. Four kinds of synthesized data were obtained by

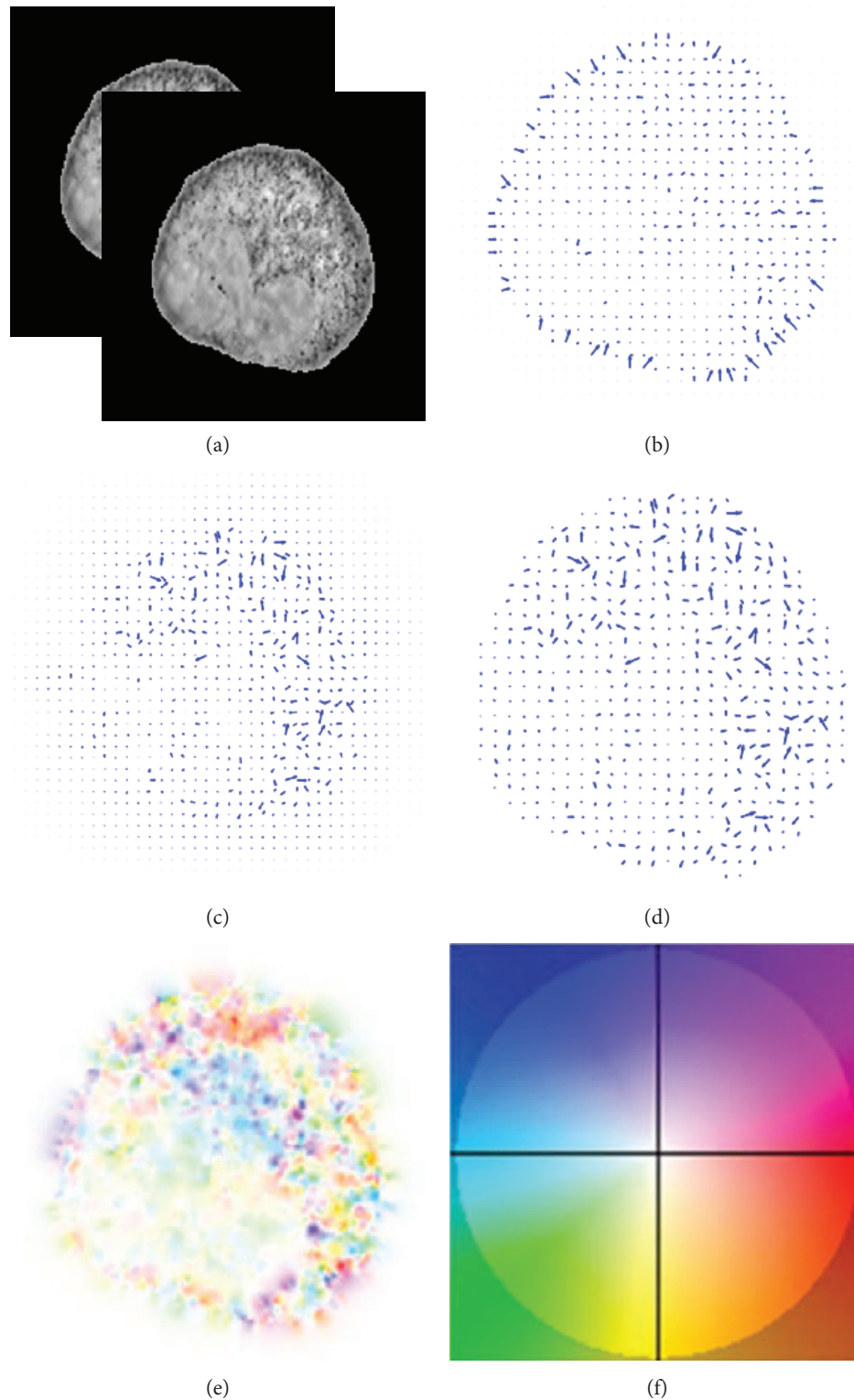


FIGURE 1: (a) The successive images from one video. (b) The optical flow field computed based on $p(x, y) \approx 1$. (c) The optical flow field computed based on $p(x, y) \approx 2$. (d) The optical flow field computed based on adaptive $p(x, y)$ as (6). (e) Optical flow of (d) by color coding. (f) Color coding of the flow [22].

sampling with different frame intervals, as the following steps. Step 1: choose a frame from the cell microscopic images as the reference frame. Step 2: choose a float frame, and the interval between the float and the reference frame

is 20. Step 3: a new video is obtained by sampling with the 20 frame intervals. And we name this sampled video as Celldata_20. The last step: using the similar sampling method, we obtain other three kinds of cell videos (Celldata_40,

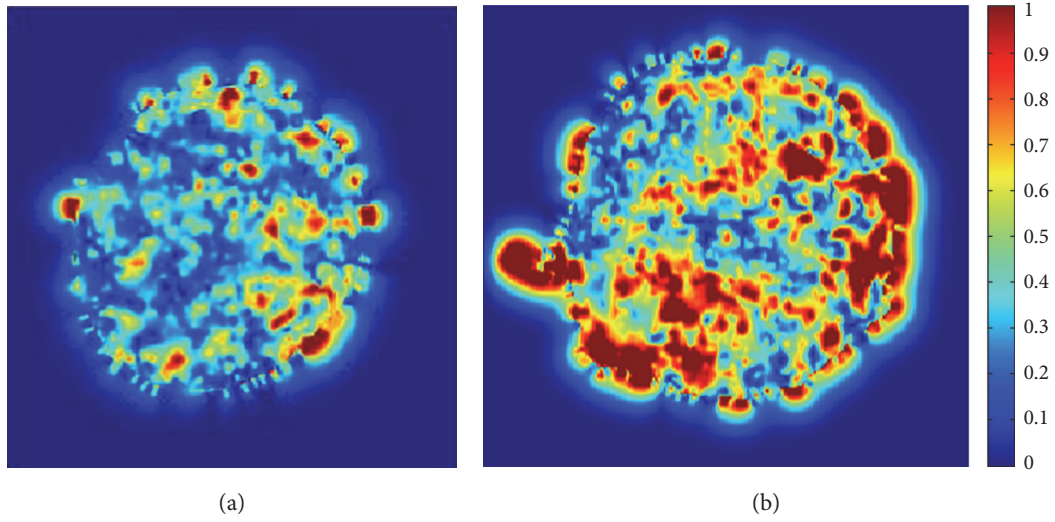


FIGURE 2: Examples of intracellular motion by color coding: red represents high velocity, while blue represents slow velocity. (a) From the NG. (b) From the AG.

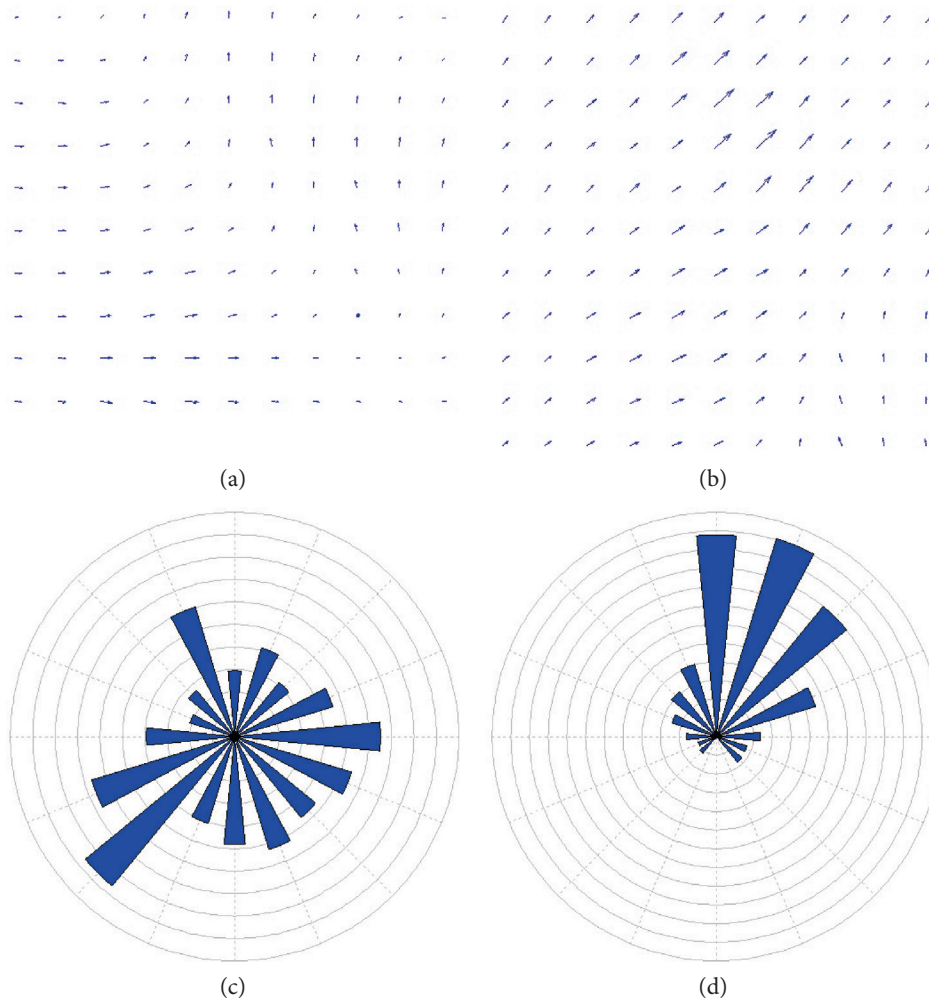


FIGURE 3: (a) The optical flow field of cell video with slight intracellular motion from NG; (b) the optical flow field of cell video with dramatic intracellular motion from AG; (c) the HOOF according to (a); and (d) the HOOF according to (b).

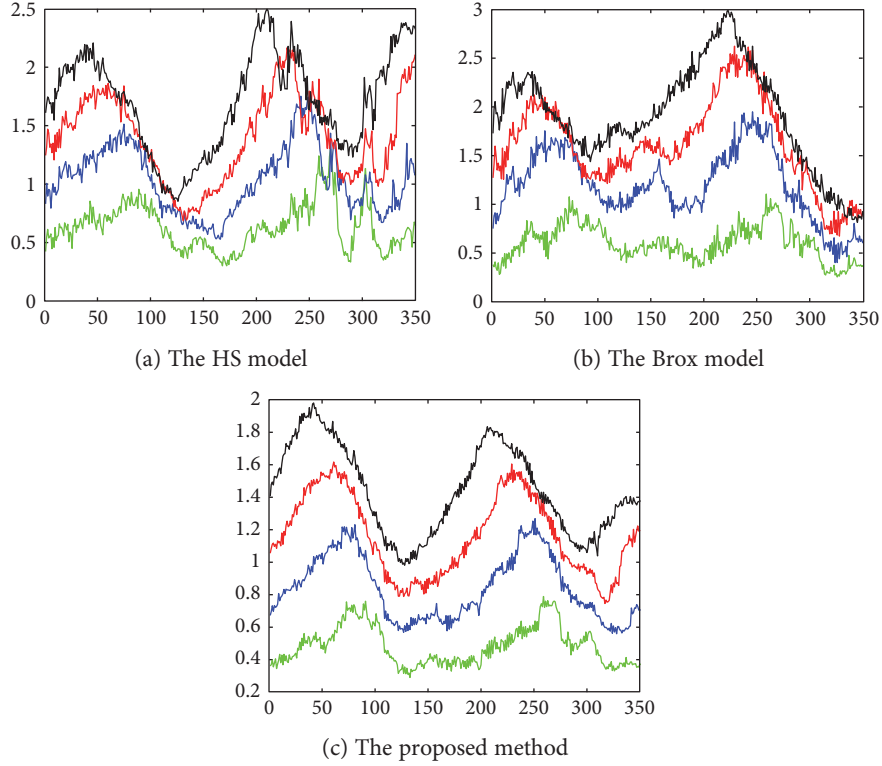


FIGURE 4: The instantaneous velocity extracted from 4 kinds of data (Celldata_20, Celldata_40, Celldata_60, and Celldata_80), by three kinds of optical flow approaches (the HS model, the Brox model, and the proposed method).

Celldata_60, and Celldata_80) with the frame interval 40, 60, and 80, respectively. In theory, the motion velocity in Celldata_20 is slower, and those in Celldata_40 and Celldata_60 are higher. Obviously, the intracellular motion in Celldata_80 is the most violent.

After four kinds of synthesized data were obtained, first, we computed the optical flow fields based on the proposed variation optical flow model of every data. Second, we calculated the mean velocity of each optical flow field as the instantaneous velocity, defined as follows:

$$V_{\text{MeanVeloField}} = \frac{1}{A_{\Omega_1}} \sum_{(x,y) \in \Omega_1} \sqrt{u^2(x,y) + v^2(x,y)}, \quad (16)$$

where $u(x,y)$ and $v(x,y)$ are the horizontal and vertical components of the velocity at the point (x,y) . A_{Ω_1} is the area of the region Ω_1 , which is a closed 2-dimensional optical flow field domain, defined as follows:

$$\Omega_1 = \left\{ (x,y) : \sqrt{u^2(x,y) + v^2(x,y)} \geq \text{thresholds} \right\}, \quad (17)$$

where $\text{thresholds} = 0.0001$ (fixed by experiments), which is used to restrict the region of the optical flow fields and restrict the optical flow data to the intracellular area.

In order to evaluate the performance of the proposed optical flow model, instantaneous velocities of four kinds of data computed based on the proposed variation optical flow model were compared with those extracted based on other two methods: the traditional HS [8] method and the Brox

method [17]. All experimental parameters are set as follows. The weight parameter α in the energy functional is set as $\alpha = 15$. In the Brox model, the gradient constancy assumption is removed, that is, the optimization of the data term and the smoothness term are based on L_1 norm constraint approximately. In the traditional HS model, the optimization of the data term and the smoothness term is based on L_2 norm constraint. In our proposed approach, the data term is based on the L_2 norm constraint, while the smoothness term depends on the local region features: adopting the L_2 norm in smooth area of cell and L_1 norm near the edge of cell automatically. In addition, the size of Gaussian mask is 5×5 .

The experimental results of the abovementioned approaches (the traditional HS model, the Brox model, and our proposed model) applied to the data (four kinds of cell video: Celldata_20, Celldata_40, Celldata_60, and Celldata_80) are shown in Figure 4. The horizontal axis shows the number of frame in the image sequences; the green, blue, red, and black lines represent the instantaneous velocity calculated from the Celldata_20, Celldata_40, Celldata_60, and Celldata_80, respectively. The black lines denote the instantaneous velocity from Celldata_80, which have the highest velocity. Based on Figure 4, it is found that instantaneous velocity in the intracellular area is proportional to the frame interval. That is to say, the larger the frame interval between the float frame and the reference frame, the higher the instantaneous velocity, which agrees with the theoretical analysis. Experimental results show that our proposed adaptive optical flow model based on variation model can deal with the problems of optical flow computation at the border region to

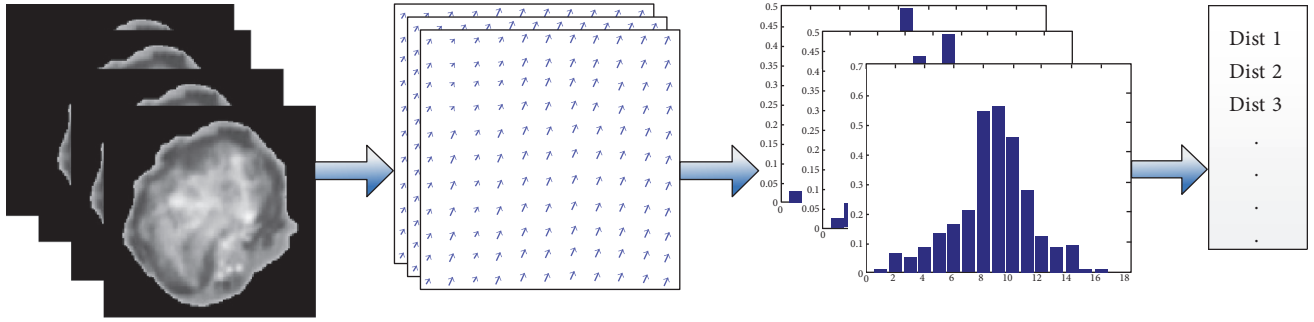


FIGURE 5: Extraction of feature vector based on intracellular motion; (a) segmented cell images; (b) successive optical flow fields; (c) histograms of optical flow (HOOFs); and (d) the Euclidean distances of HOOF (feature vector).

some extent and obtain optical flow values which are close to the true.

4.4. Feature Vector Extraction of Intracellular Motion Fields.

Based on the above analysis, it can be seen that our proposed adaptive optical flow model can extract the instantaneous velocity of the synthesized data effectively. Next, we apply it to study the intracellular motion of the actual microscopic images. 120 microscopic images of cell data acquired from clean mice were used in our experiments. These data were acquired from mice with three kinds of physical state, and their corresponding intracellular motion is different: the slight motion, the moderate motion, and the dramatic motion. Every video contains more than 500 frames, which lasts for 20 seconds or so. That is to say, we analyzed the intracellular motion during a 20-second time. The frame intervals which is used for optical flow computation will influence the precision of the optical flow field. Considering that the computation cost will increase if the interframe interval is small; on the contrary, the motion characteristics cannot be captured if the interframe interval is too large, so we set the frame interval as 25 based on a large number of experiments. For example, we clip 500 frames from an original video, then sample the clipped video by 25, so a 20-frame sampled video is obtained, which will be used in the next optical flow implementation.

Afterwards, we extract the intracellular motion feature of the preprocessed data, including the following steps: first, compute the optical flow field from two successive frames of the data (the 20-frame sampled video), then we obtain 19 frame optical flow fields from one video, shown as Figure 5(b). Second, extract HOOF from every optical flow field, then we have 19 frame HOOFs, shown as Figure 5(c). Third, calculate the Euclidean distance of the two successive HOOFs, then we acquire a feature vector of intracellular motion. It is obvious that the smaller the Euclidean distances are, the slighter the intracellular motion is, and vice versa.

In order to validate the effectiveness of feature vector, we also projected the distances of the different feature vector matrix of the 120 data sets onto a two-dimensional plane using multidimensional scaling (MDS), which is a means of visualizing the level of similarity of individual cases of a dataset [23]. The result of MDS is shown in Figure 6.

Figure 6 indicates that the three groups of cell image sequence can be differentiated clearly. To further evaluate

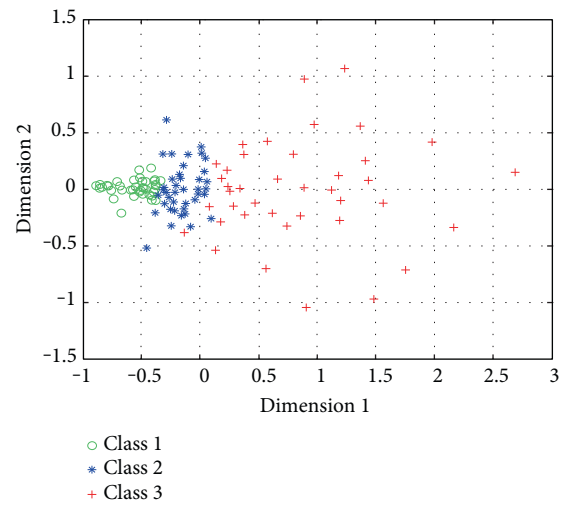


FIGURE 6: MDS projections of feature vector distances between 120 image sequences (40 from each of the three groups); the circle denotes the slight motion group, the star denotes the moderate motion group, and the plus denotes the dramatic motion group.

the quality of the optical feature vector, support vector machine (SVM) is used to classify intracellular motion in the microscopic images. For the data in each group, we randomly choose 20 as train sets, and another 20 for test sets. So there are 60 train sets and 60 test sets totally. The rate of classification accuracy on the test data sets by SVM achieves 91.7%.

5. Discussion

In this article, we proposed a novel scheme for quantitative analysis of intracellular motility based on the variation optical flow model. We applied improved variation optical flow model to visualize the velocity of intracellular motion and further coded the velocity by color, as shown in Figures 1 and 2. Moreover, HOOF was developed to quantify optical flow field of the intracellular motion, as shown in Figures 3 and 5. Lastly, we conducted two experiments to verify the proposed approach. In the first experiment, we verified the proposed approach to the synthesized data, which was obtained by sampling a microscopic cell video with different

intraframe interval. Experimental results were shown in Figure 4. As shown in Figure 4(c), four kinds of velocity can be differentiated clearly based on our proposed optical flow model, while Figures 4(a) and 4(b) show that the instantaneous velocity based on HS model and Brox model cannot be distinguished effectively. The first experiment shows that the instantaneous velocity of the intracellular motion is extracted effectively by our improved optical flow model. In the second experiment, the proposed approach was applied to the microscopic cell video acquired from the clean mice. There are three kinds of cell data, representing different cases (slight intracellular motion, moderate intracellular motion, and dramatic intracellular motion) of different clean mice. Experimental results were shown in Figure 6, and it is obvious that our proposed approach can differentiate the different intracellular motion, and the rate of classification accuracy can achieve more than 90% by SVM.

The contributions of the proposed method are twofold: first, we proposed the energy functional of the optical flow model with adaptive adjustment of $p(x, y)$ which change with the local feature of the image. From (6), it is obvious that $p(x, y) = 1$ near the edge of the cell, which is equivalent to L_1 norm optimization for the computation of the optical flow model; therefore, the proposed model can deal with the border problem of the optical flow computation well. While $p(x, y) = 2$ in the center of the intracellular area, it is equivalent to L_2 norm optimization and beneficial to extract the accurate optical flow field of the intracellular motion. Second, we calculated the HOOFs of all optical flow field extracted from the intracellular motion, and the Euclidean distances of the consecutive HOOFs were used to quantify the cell mobility in vivo.

Finally, it should be pointed out that there are still limitations in our study. First, our study was motivated by clinicians' observation that the specific cells are more active (means more morphological changes and intracellular motion) when the patient, who undergoes organ transplantation, gets the graft rejection. In consideration of security and performance, human beings with organ transplantation were replaced by the mice which undergone skin transplant in our designed scheme. Second, we just analyzed the intracellular motion in 2-dimensional space, and we will extend this study to 3-dimensional space, which agrees with the reality more.

In brief, we proposed an optical flow computation method based on variation model for quantitatively analysis of intracellular motion in microscopic images. And our research will open up new avenues for quantifying intracellular motion and better understanding of the relationship between the

biological processes and the pathological phenomena at the cellular level.

Appendix

Derivations of the Euler-Lagrange Equation

Based on the calculus of variations, minimizing the objective functional (A.1) must satisfy the associated Euler-Lagrange (A.2).

$$J[u(x, y), v(x, y)] = \iint F(x, y, u, v, u_x, u_y, v_x, v_y) dx dy, \quad (\text{A.1})$$

$$\begin{aligned} F_u - \frac{\partial}{\partial x} F_{u_x} - \frac{\partial}{\partial y} F_{u_y} &= 0 \\ F_v - \frac{\partial}{\partial x} F_{v_x} - \frac{\partial}{\partial y} F_{v_y} &= 0. \end{aligned} \quad (\text{A.2})$$

In our proposed energy functional of the adaptive TV optical flow model is as follows:

$$E_{\text{aTV}}(u, v) = \int_{\Omega} \left\{ \frac{1}{2} (I_x u + I_y v + I_t)^2 + \frac{\alpha}{p} (|\nabla u|^p + |\nabla v|^p) \right\} d\Omega. \quad (\text{A.3})$$

We have that

$$F(x, y, u, v, u_x, u_y, v_x, v_y) = \frac{1}{2} (I_x u + I_y v + I_t)^2 + \frac{\alpha}{p} (|\nabla u|^p + |\nabla v|^p). \quad (\text{A.4})$$

So

$$\begin{aligned} F_u &= (I_x u + I_y v + I_t) I_x \\ F_{u_x} &= \alpha (u_x^2 + u_y^2)^{(p-2)/2} u_x \\ F_{u_y} &= \alpha (u_x^2 + u_y^2)^{(p-2)/2} u_y, \end{aligned} \quad (\text{A.5})$$

$$\begin{aligned} F_v &= (I_x u + I_y v + I_t) I_y \\ F_{v_x} &= \alpha (v_x^2 + v_y^2)^{(p-2)/2} v_x \\ F_{v_y} &= \alpha (v_x^2 + v_y^2)^{(p-2)/2} v_y. \end{aligned} \quad (\text{A.6})$$

Substituting (A.5) and (A.6) into (A.2), then we can reach (A.7) as follows:

$$\begin{aligned} F_u - \frac{\partial}{\partial x} F_{u_x} - \frac{\partial}{\partial y} F_{u_y} &= (I_x u + I_y v + I_t) I_x - \frac{\partial}{\partial x} \left[\alpha (u_x^2 + u_y^2)^{(p-2)/2} u_x \right] - \frac{\partial}{\partial y} \left[\alpha (u_x^2 + u_y^2)^{(p-2)/2} u_y \right] \\ F_v - \frac{\partial}{\partial x} F_{v_x} - \frac{\partial}{\partial y} F_{v_y} &= (I_x u + I_y v + I_t) I_y - \frac{\partial}{\partial x} \left[\alpha (v_x^2 + v_y^2)^{(p-2)/2} v_x \right] - \frac{\partial}{\partial y} \left[\alpha (v_x^2 + v_y^2)^{(p-2)/2} v_y \right]. \end{aligned} \quad (\text{A.7})$$

We obtain the Euler-Lagrange (A.8) of the adaptive TV optical flow model after rearranging (A.7).

$$\begin{aligned} (I_x u + I_y v + I_t) I_x - \alpha \cdot \nabla \cdot \frac{\nabla u}{|\nabla u|^{2-p}} &= 0 \\ (I_x u + I_y v + I_t) I_y - \alpha \cdot \nabla \cdot \frac{\nabla v}{|\nabla v|^{2-p}} &= 0. \end{aligned} \quad (\text{A.8})$$

Conflicts of Interest

The authors declare that there is no conflict of interests regarding the publication of this paper.

Acknowledgments

This work was supported by the National Natural Science Foundation of China (no. 61271112) and was also supported by the Youth Foundation from Educational Department of Hebei Province (no. QN2016169). The authors would like to thank the president of Beijing You'an Hospital, Ning Li, for providing the microscopic cell images.

References

- [1] F. Bename, G. Pawlak, P. Roux, and U. Hibner, "What makes cells move: requirements and obstacles for spontaneous cell motility," *Molecular BioSystems*, vol. 6, pp. 648–661, 2010.
- [2] C. Terryn, A. Bonomet, J. Cutrona et al., "Video-microscopic imaging of cell spatio-temporal dispersion and migration," *Critical Reviews in Oncology Hematology*, vol. 69, pp. 144–152, 2009.
- [3] G. Thurston, B. Jaggi, and B. Palcic, "Measurement of cell motility and morphology with an automated microscope system," *Cytometry*, vol. 9, pp. 411–417, 1988.
- [4] F. Siegert, C. J. Weijer, A. Nomura, and H. Miike, "A gradient method for the quantitative analysis of cell movement and tissue flow and its application to the analysis of multicellular dictyostelium development," *Journal of Cell Science*, vol. 107, pp. 97–104, 1994.
- [5] Y. Sato, J. Chen, R. A. Zoroofi, N. Harada, S. Tamura, and T. Shiga, "Automatic extraction and measurement of leukocyte motion in microvessels using spatiotemporal image analysis," *IEEE Transactions on Biomedical Engineering*, vol. 44, pp. 225–236, 1997.
- [6] X. Ronot, A. Doisy, and P. Tracqui, "Quantitative study of dynamic behavior of cell monolayers during in vitro wound healing by optical flow analysis," *Cytometry*, vol. 41, pp. 19–30, 2000.
- [7] Y. Huang, Z. Liu, and Y. Shi, "Quantitative analysis of live lymphocytes morphology and intracellular motion in microscopic images," *Biomedical Signal Processing and Control*, vol. 18, pp. 195–203, 2015.
- [8] B. K. P. Horn and B. G. Schunck, "Determining optical flow," *Artificial Intelligence*, vol. 17, pp. 185–203, 1981.
- [9] B. D. Lucas and T. Kanade, "An iterative image registration technique with an application to stereo vision," in *The 7th International Joint Conference on Artificial Intelligence (IJCAI)*, pp. 674–679, Vancouver, BC, Canada, August 24–28, 1981.
- [10] F. Amat, E. W. Myers, and P. J. Keller, "Fast and robust optical flow for time-lapse microscopy using super-voxels," *Bioinformatics*, vol. 29, pp. 373–380, 2013.
- [11] D. Fortun, P. Boutheymy, P. Paul-Gilloteaux, C. Kervrann, and IEEE, "Aggregation of patch-based estimations for illumination-invariant optical flow in live cell imaging," in *2013 IEEE 10th International Symposium on Biomedical Imaging (ISBI)*, pp. 660–663, San Francisco, CA, USA, April 7–11, 2013.
- [12] E. Parrilla, M. Armengot, M. Mata et al., "Primary ciliary dyskinesia assessment by means of optical flow analysis of phase-contrast microscopy images," *Computerized Medical Imaging and Graphics*, vol. 38, pp. 163–170, 2014.
- [13] D. K. Vig, A. E. Hamby, and C. W. Wolgemuth, "On the quantification of cellular velocity fields," *Biophysical Journal*, vol. 110, pp. 1469–1475, 2016.
- [14] K. Boric, P. Orto, T. Vieville, and K. Whitlock, "Quantitative analysis of cell migration using optical flow," *PLoS One*, vol. 8, pp. 1–11, 2013.
- [15] D. Guo, A. L. Van de Ven, and X. Zhou, "Red blood cell tracking using optical flow methods," *IEEE Journal of Biomedical and Health Informatics*, vol. 18, pp. 991–998, 2014.
- [16] Y. Liu, E. Saber, A. Glading, and M. Helguera, "Measurement of blood flow velocity for in vivo video sequences with motion estimation methods," in *Conference on Medical Imaging - Image Processing*, San Diego, CA, 2014.
- [17] N. Papenberg, A. Bruhn, T. Brox, S. Didas, and J. Weickert, "Highly accurate optic flow computation with theoretically justified warping," *International Journal of Computer Vision*, vol. 67, pp. 141–158, 2006.
- [18] T. Pock, M. Urschler, C. Zach, R. Beichel, and H. Bischof, "A duality based algorithm for TV-L 1-optical-flow image registration," in *Medical Image Computing and Computer-Assisted Intervention (MICCAI)*, pp. 511–518, Brisbane, Australia, 2007.
- [19] B. Song, *Topics in Variational PDE Image Segmentation, Inpainting and Denoising*, University of California Los Angeles, 2003.
- [20] R. Chaudhry, A. Ravichandran, G. Hager, and R. Vidal, "Histograms of oriented optical flow and binet-cauchy kernels on nonlinear dynamical systems for the recognition of human actions," in *IEEE Conference on Computer Vision and Pattern Recognition (CVPR)*, pp. 1932–1939, Piscataway, 2009.
- [21] Y. Huang and Z. Liu, "Segmentation and tracking of lymphocytes based on modified active contour models in phase contrast microscopy images," *Computational and Mathematical Methods in Medicine*, vol. 2015, Article ID 693484, 2015.
- [22] S. Baker, D. Scharstein, J. Lewis, S. Roth, M. J. Black, and R. Szeliski, "A database and evaluation methodology for optical flow," *International Journal of Computer Vision*, vol. 92, pp. 1–31, 2011.
- [23] I. Borg and P. J. Groenen, *Modern Multidimensional Scaling: Theory and Applications*, Springer Series in Statistics, Springer, New York, 2005.

Research Article

A Kalman Filtering and Nonlinear Penalty Regression Approach for Noninvasive Anemia Detection with Palpebral Conjunctiva Images

Yi-Ming Chen¹ and Shaou-Gang Miaou²

¹*Acoustic Science and Technology Laboratory, College of Underwater Acoustic Engineering, Harbin Engineering University, Harbin, China*

²*Department of Electronic Engineering, Chung Yuan Christian University, Taoyuan City, Taiwan*

Correspondence should be addressed to Shaou-Gang Miaou; miaou@cycu.edu.tw

Received 14 February 2017; Revised 4 May 2017; Accepted 1 June 2017; Published 30 July 2017

Academic Editor: João Manuel R.S. Tavares

Copyright © 2017 Yi-Ming Chen and Shaou-Gang Miaou. This is an open access article distributed under the Creative Commons Attribution License, which permits unrestricted use, distribution, and reproduction in any medium, provided the original work is properly cited.

Noninvasive medical procedures are usually preferable to their invasive counterparts in the medical community. Anemia examining through the palpebral conjunctiva is a convenient noninvasive procedure. The procedure can be automated to reduce the medical cost. We propose an anemia examining approach by using a Kalman filter (KF) and a regression method. The traditional KF is often used in time-dependent applications. Here, we modified the traditional KF for the time-independent data in medical applications. We simply compute the mean value of the red component of the palpebral conjunctiva image as our recognition feature and use a penalty regression algorithm to find a nonlinear curve that best fits the data of feature values and the corresponding levels of hemoglobin (Hb) concentration. To evaluate the proposed approach and several relevant approaches, we propose a risk evaluation scheme, where the entire Hb spectrum is divided into high-risk, low-risk, and doubtful intervals for anemia. The doubtful interval contains the Hb threshold, say 11 g/dL, separating anemia and nonanemia. A suspect sample is the sample falling in the doubtful interval. For the anemia screening purpose, we would like to have as less suspect samples as possible. The experimental results show that the modified KF reduces the number of suspect samples significantly for all the approaches considered here.

1. Introduction

According to WHO [1], anemia is a prevalent health problem affecting an estimate of 2 billion people in many parts of the world, especially where dietary iron deficiency, malaria, and hookworm infections are common. Blood test is the most common way for the anemia assessment based on the level of hemoglobin (Hb) concentration. A normal blood test procedure needs drawing blood from a vein or a finger stick, which is all right for most people but not acceptable for those who suffer from blood phobia and fainting during acupuncture. In addition, phlebotomists, laboratory practitioners, and nurses are charged with drawing a patient's blood, and training those people to have enough professional skills is also the hidden cost that cannot be overlooked. Besides, the

entire procedure of blood test may take more than an hour, which limits the number of patients that could be examined in a day and makes the large-scale anemia screening difficult. In summary, the traditional way of drawing blood for anemia assessment is time consuming and costly and not appropriate for everyone. Therefore, an efficient way to screen out anemia patients for essentially anyone is desirable.

In view of the considerations above, a great number of studies on noninvasive approaches for Hb estimate as well as anemia test have been conducted in the recent years [2–14]. One popular solution is to crop a small image within the digital photo of the palpebral conjunctiva area (Figure 1). Physicians can diagnose a patient's anemia condition based on the pale degree observed from the image, such as the nonanemic sample in Figure 2(a) and the anemic

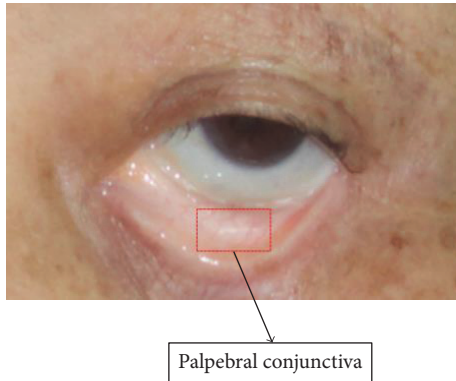


FIGURE 1: The palpebral conjunctiva part of an eye.

sample in Figure 2(b). Sometimes, image samples taken in poor condition are not as good as those presented in Figure 2. The quality of the image is obviously the key to the success of this kind of solution. Hence, some researchers study how to acquire palpebral conjunctiva images more reliably, and this is usually accomplished by reducing its dependency on ambient light condition. These include photo plethysmography [4] and reflectance spectroscopy [5], as well as a head-mounted device with LED array inside to capture conjunctiva images [12]. However, they are not popular or affordable, especially in the rural areas of developing countries where medical resources are often limited. Thus, we get data acquisition back on track by using a more popular and affordable device such as a commercially available digital camera. At the same time, we need to deal with the biggest potential problem of this kind of approach, that is, the threat from noisy sources, including various ambient light conditions and camera settings.

The noise effect results in the interference of extracting color feature and makes the anemia assessment more susceptible to error. Therefore, a preprocessing step before color extraction is desirable. Few preprocessing efforts have been made specifically for noninvasive anemia examining. In [13, 14], a preprocessing algorithm based on k-mean clustering is tailored to remove the bright reflection spot in the image. However, this is just one type of special noises due to camera setting and/or ambient light condition and the k-mean clustering approach is not general enough to deal with all possible noise types. In fact, applying k-mean clustering to the image with no bright reflection may even introduce unwanted man-made noise. Therefore, a more general solution with low probability of adverse effect is considered in this paper.

We treat the bright reflection or any other noise as simply a measurement error. Apparently, if a preprocessing process was not able to eliminate all the noise in the first step, the corresponding measurement error would add difficulty to the next step—feature extraction. Being aware of it, some noninvasive methods for anemia assessment attempt to obtain image samples as clean as possible in the very beginning with various rather sophisticated equipment [4–7]. With no perfect preprocessing method or such special equipment, our prime work is therefore aimed at reducing the overall measurement error. The idea is connected to one of the most

famous algorithms—Kalman filter (KF). Although it is commonly used in the problem of position and orientation tracking, its main function stays unchanged, that is, to optimize each data measurement and estimation. Therefore, we modify the traditional KF such that it can be applied to our current problem. In fact, there have been examples of applying the KF for medical fields, such as those in [15, 16], where Kalman filters were applied to medical image reconstruction and tracking blood vessel, respectively. Another application is in signal filtering, which is more direct and easily understood. Foussier et al. in [17] used KF to reduce the measurement error of cardiorespiratory signal, resulting in improved signal quality for further processing. In spite of different applications above, they share a common characteristic, that is, Kalman filtering is often used to deal with the data with time-dependent nature. In this paper, we apply it to the time-independent data derived from an original medical signal, which is unique to the best of our knowledge. Specifically, a feature sample extracted from a palpebral conjunctiva image is regarded as a dependent variable, while the corresponding Hb level is treated as an independent variable (equivalent to time variable in traditional KF). As discussed above, each computed feature has somehow inherited measurement error from the original data. Therefore, applying KF in such setting is plausible.

Regression analysis is widely used for prediction and forecasting, where its use has substantial overlap with the field of machine learning. Regression analysis is also used to understand which among the independent variables are related to the dependent variable and to explore the forms of these relationships. In restricted circumstances, regression analysis can be used to infer causal relationships between the independent and dependent variables. However, this can lead to illusions or false relationships [18], such as overfitting. In overfitting, a statistical model describes random error or noise instead of the underlying relationship. Overfitting occurs when a model is excessively complex, such as having too many parameters relative to the number of observations. An overfitting model usually has poor predictive performance, as it overreacts to minor fluctuations in training data [19]. For medical applications, physicians often do not know how large a sample measurement error could be. It is expected that the fitting relationship from medical data will appear to perform slightly worse on a new data set than on the data set used for fitting and prediction, which would cause a serious problem for both patients and physicians. Therefore, we add penalty consideration in the regression analysis to avoid the overfitting problem. Penalty methods are a class of algorithms for solving constrained optimization problems [20].

In this paper, we propose a combining algorithm based on a modified Kalman filter and the nonlinear penalty regression for anemia assessment. We simply compute the mean value of the red (R) component of conjunctiva images and consider it as the only recognition feature to simplify the proposed system. Then, given the data of these mean values, we use the combining algorithm to fit a nonlinear curve that presents the relationship between the feature value and the Hb level. With the fitting curve, we then propose a three-level evaluation scheme to determine the anemia status of a given subject as well as the performance of the proposed approach.



FIGURE 2: Cropped palpebral conjunctiva samples. (a) Nonanemic sample; (b) anemic sample.

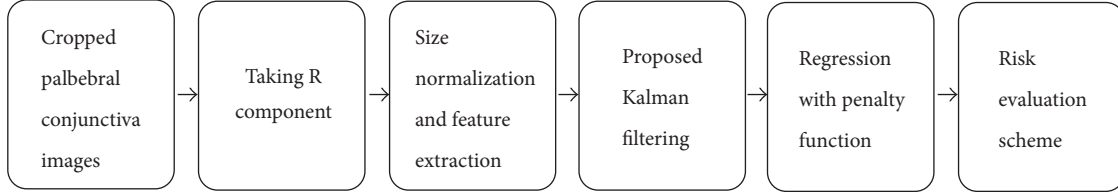


FIGURE 3: A flow chart of the proposed approach.

2. Method

A flow chart of the proposed approach is shown in Figure 3. The original data at hand consist of N palpebral conjunctiva images of unequal sizes, along with N corresponding Hb levels, taken from N subjects, respectively. Firstly, we consider only the R component of each cropped palpebral conjunctiva image. Each image is then normalized to the same size. Next, for each normalized image, we simply take the mean value of R component pixels as the only one recognition feature in our approach to simplify the proposed system. Since we perform 10-fold cross validation in this work, about 90% and 10% of the images and the corresponding features values shall be used in training and testing, respectively. Given the training images and the corresponding Hb levels, we propose and perform a modified version of Kalman filtering. In the next step, regression with penalty function is used to find the relationship between feature values and Hb levels. Finally, a three-level evaluation scheme called risk evaluation scheme (RES) is proposed for the testing images to signify the subject's anemia status and evaluate the performance of the proposed approach as well.

2.1. Traditional Kalman Filter. The Kalman filter (KF) was proposed as a novel approach for the state estimation of dynamic linear state system in [21], and it has been widely implemented in various applications [22–29].

The KF is analogous to the Markov model, where it needs an estimate state from the previous time instant and the current measurement to calculate the estimate for the current state. The KF is usually conceptualized as two distinct phases, time update phase ((1) and (2)) and measurement update phase ((3), (4), and (5)) [30].

$$x_{k|k-1} = F_k x_{k-1|k-1} + B_{k-1} u_{k-1}, \quad (1)$$

$$P_{k|k-1} = F_k P_{k-1|k-1} F_k^T + Q_k, \quad (2)$$

$$K_k = \frac{P_{k|k-1} H_k^T}{H_k P_{k|k-1} H_k^T + R_k}, \quad (3)$$

$$x_{k|k} = x_{k|k-1} + K_k (z_k - H_k x_{k|k-1}), \quad (4)$$

$$P_{k|k} = (I - K_k H_k) F_k P_{k-1|k-1} F_k^T + (I - K_k H_k) Q_k. \quad (5)$$

Here, the KF model computes the estimate state $x_{k|k}$ at time k which is evolved from the previous estimate state $x_{k-1|k-1}$; the F_k is the state transition model which is applied to the previous state; the B_k is the control-input model which is applied to the control vector u_k ; the $P_{k|k}$ is the estimate of error covariance matrix; the K_k is Kalman gain; z_k is the observation value at the current time k . In practice, the process noise covariance matrix Q (must be positive semi-definite in theory) and the measurement noise covariance matrix R (must be positive definite in theory) might change with respect to time change or measurement. They are assumed to be independent (of each other), white, and normally distributed.

The time update phase is responsible for projecting forward the current state (1) and error covariance estimates (2) to obtain the first predicted estimates $x_{k|k-1}$ for the next time step. The aim of this step is to minimize the covariance of the estimation error, which represents a degree of uncertainty of the estimation [30]. The measurement update phase is responsible for updating the Kalman gain in (3), state estimate in (4), and estimate covariance in (5). In (4), $x_{k|k-1}$ is updated to the final estimate state $x_{k|k}$ at time k . Equation (5) for the updated estimate of covariance matrix above is only valid for the optimal Kalman gain.

In most cases, Kalman filtering is widely applicable to the time-dependent field of navigation, radar, computer vision, and so forth, and very few works have applied it to medical data processing. In the next section, we attempt to modify the traditional KF so that it can be connected to the medical data processing task of interest.

2.2. A Proposed Modified Kalman Filter. The original images have various sizes, and they are normalized (enlarged) to a fixed size to avoid possible loss of useful information. Then, we compute the mean value of the R component in the

RGB color space and use it as a recognition feature for anemia assessment, because the reddish and pale conjunctiva may correspond to two opposite extremes of Hb levels.

However, when the variance or standard deviation of feature values is large (due to measurement errors in data acquisition and individual differences in physiology), it is more difficult to figure out the exact relationship between the feature values and the Hb levels. Thus, we use Kalman filtering to make the samples closer to each other so that it will be easier for us to find the fitting curve representing the relationship between these two quantities. Kalman filtering is commonly used in time-dependent cases, as we discussed earlier. We map our time-independent feature Hb problem into a target position-tracking problem, which is a well-known time-dependent problem. In the tracking problem, time is the independent variable and the target position is the dependent variable with some measurement error or uncertainty. The KF is used to reduce the uncertainty. In our problem, the Hb level is regarded as an independent variable and the feature is considered to be a dependent variable, which also suffers from measurement error due to camera setting or ambient light condition. With this mapping, the same principle of KF can be applied to our problem after a proper reformulation of the original KF setting.

Firstly, we sort the measurement data $z_{\text{original}}(k)$ by Hb in an ascending order. We assume that there are enough amounts of measurement data for analysis. We also assume that the interval defined by any pair of two adjacent and sorted Hb values has small enough differences, so that we have essentially the same interval length. Furthermore, one Hb level with finite precision may correspond to multiple feature values in practice. To simplify the problem, we take the average of these feature values in this case and convert a possibly one-to-many mapping function $z_{\text{original}}(k)$ to a one-to-one counterpart $z(k)$. Now, k is no longer limited to a time step; instead, it can be interpreted as a discrete number of cases considered in either ascending or descending order of Hb. We are about ready to apply Kalman filtering to our problem. For the efficient implementation of KF, we simplify the original KF by treating some complicated parameters in KF to be constants and avoiding the required iteration of their estimation as follows.

We firstly assume that the first data in the array $z(k)$ is correct, where we have $P(1) = 0$. And there is no control vector in our case, so u_k is set to be 0. For the one-dimensional data in our case, let $H = 1$ (just a scaler, not a matrix anymore). We also consider the system to be stable and set $F = 1$. Extensive researches have been done to estimate noise covariance matrices Q_k and R_k from the data, such as [31–37]. A practical implementation of getting a good estimate of these covariance matrices is still difficult. Furthermore, KF is sensitive to errors in Q_k and R_k , and its output can be unacceptable if errors are large. Therefore, we usually assume they are small constants within a certain range, say $Q_k = Q = 1 \times 10^{-3} \sim 1 \times 10^{-2}$ and $R_k = R = 1 \times 10^{-3} \sim 1 \times 10^{-2}$. Thus, after a simple derivation, the mathematical formulation of the original KF is reduced to that shown next:

$$K(k) = \frac{P(k-1) + Q}{P(k-1) + Q + R}, \quad (6)$$

$$x(k) = K(k) \cdot z(k) + (1 - K(k)) \cdot x(k-1), \quad (7)$$

$$P(k) = (1 - K(k)) \cdot P(k-1) - 2 \cdot Q \cdot K(k) + 2 \cdot Q, \quad (8)$$

where $K(k)$ is the Kalman gain. Note that (6), (7), and (8) give a simplified version of Kalman filtering according to our current research work. The simplification provides a useful guide for those who want to implement the filtering directly with their own programming languages and techniques. One handy alternative is to use the existing MATLAB function “kalman” with a proper parameter setting. In our implementation, we use the statement $[\text{output}] = \text{kalman}(\text{system_input}, Q, R)$, where system_input is the structure array containing the input signal and the parameters such as H and F , and Q and R correspond to Q_k (or Q here) and R_k (or R here), respectively.

With the modified KF proposed above, a more condensed data $x(k)$ than $z(k)$ can be obtained and then used in the following step.

2.3. Penalty Regression. The anemia examining can be considered as a linear regression problem, since the pale degree of the palpebral conjunctiva is commonly regarded as an obviously visible feature reflecting Hb level. For example, the conjunctiva looks paler when Hb level tends to be low. However, no study has ever shown that the problem considered here can be modeled perfectly by a linear expression between the pale degree and the Hb level. Naturally, we cannot exclude the development of a nonlinear expression for our problem.

Since we take the mean value in R component as the feature, we formulate the anemia-examining problem as a predicting problem based on a fitting curve with an n th order nonlinear polynomial function:

$$f(h_k, a_i) = \sum_{i=0}^n a_i \cdot h_k^i, \quad (9)$$

where h_k represents k th subject’s Hb level in an ascending order after applying the proposed Kalman filtering and $f(h_k, a_i)$ is the corresponding function whose value represents a feature value. The coefficient a_i in (9) is to be determined next.

The coefficient determination problem is basically an optimization problem. An unconstrained optimization problem is formed by adding a term, called penalty function, to the objective function. The penalty function consists of a penalty parameter multiplied by a measure of violation of some constraints. In the case of overfitting problem, we consider a penalty function $S(a_i)$ in terms of penalty coefficient c_i :

$$S(a_i) = \lambda \cdot \sum_{i=1}^n c_i \cdot a_i^2, \quad (10)$$

where λ is a penalty parameter. Similar to solving a normal regression problem, we look for each calculated feature

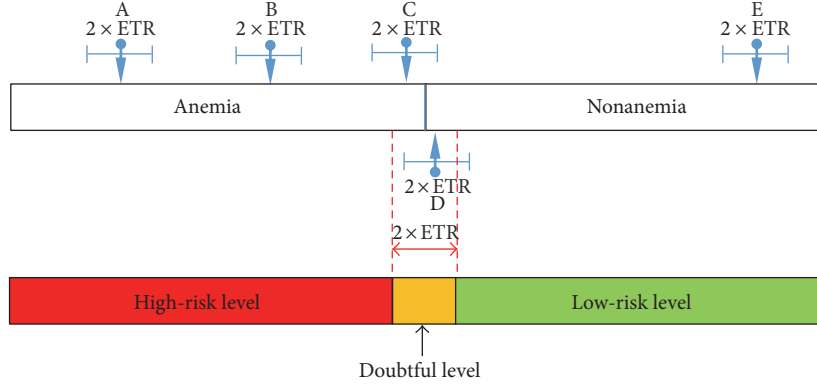


FIGURE 4: Illustration of RES.

$f(h_k, a_i)$ that could be as close to the measurement value $x(k)$ as possible. Do note that $x(k)$ is the value after using the proposed KF. The final penalty regression curve is computed by minimizing the cost function E as follows:

$$E = \alpha \cdot \sum_{k=1}^M (f(h_k, a_i) - x(k))^2 + S(a_i), \quad (11)$$

where α is called learning rate. To find the minimum value of the cost function for the M samples (after applying the proposed KF) in terms of the coefficient a_i , we use the well-known gradient descend algorithm comprising of the following two main equations:

$$\frac{\partial E}{\partial a_0} = 2\alpha \cdot \sum_{k=1}^M (f(h_k, a_i) - x(k)) = 0, \quad (12)$$

$$\frac{\partial E}{\partial a_i} = 2\alpha \cdot \sum_{k=1}^M (f(h_k, a_i) - x(k)) \cdot h_k^i + 2\lambda \cdot c_i \cdot a_i = 0. \quad (13)$$

By assigning appropriate values for the coefficient c_i , we can inhibit the increase for a particular higher-order coefficient a_i to avoid overfitting.

Since there is no closed-form solution for a_i 's based on (12) and (13), an iterative computer procedure is generally required. We use an existing MATLAB function for this problem. When we get all the a_i 's, the relationship between Hb level h_k and the feature value $f(h_k, a_i)$ is established. Once we have extracted the feature value from a new sample image, the corresponding Hb level would be estimated immediately according to this relationship.

2.4. Evaluation Schemes. Here, we proposed a three-level evaluation scheme to examine the performance of the anemia detection methods based on how risky a patient may have anemia. Therefore, it is called risk evaluation scheme (RES). The RES extends the traditional evaluation approach that classifies a sample in two levels, one for anemia and another for nonanemia. The RES considers the uncertainty or possible classification error for the samples located around the borderline separating anemia and nonanemia and adding one more level for those samples.

Specifically, the RES is designed to separate the samples into three different levels, which are high risk, doubtful, and low risk in terms of the chance of having anemia. In RES, we consider an error tolerance range (ETR) for each individual sample because the KF cannot eliminate all the errors completely, especially the variation from individual differences.

The ETR is based on the idea that each sample cannot stay in one position, but within a certain range. Similarly, the threshold borderline for anemia and nonanemia separation cannot stay at a fixed location either. Figure 4 shows two parallel horizontal Hb level bars. In the top bar, an anemic threshold indicated by a vertical line segment is given and the threshold could be 11 g/dL or other choices. Each arrow points to a sample value, say x , and the corresponding horizontal line segment containing the arrow represents an interval of length $2 \times \text{ETR}$. To be more specific, the interval containing x is from $x - \text{ETR}$ to $x + \text{ETR}$. When x happens to be the threshold (say, $x = 11$ g/dL), the corresponding interval defines the doubtful level as indicated in the yellow region of the bottom bar. Similarly, the Hb range from zero to the left boundary of the doubtful interval is defined as the interval having a high-risk level (or the red area in the bottom bar), and the remaining Hb range is defined as the interval having a low-risk level (or the green area in the bottom bar). For the samples whose intervals touch the interval of doubtful levels such as C and D, they have higher chances of being misclassified to the opposite status, that is, from anemia to nonanemia and vice versa. These samples are called suspect samples. The remaining samples are therefore called nonsuspect samples, and they are either in the high-risk level or in the low-risk level. For example, in Figure 4, A and B are in the high-risk level, while E is in the low-risk level.

Since the intervals determined here are based on the choice of ETR and a particular set of training data, they can vary from different training sets even when we set a fixed ETR. In the experiment of Section 3, the ETR is chosen to be the standard deviation of the training data, making the determination of interval depend more on training data. To evaluate the anemia detection methods using testing data, we define an index for each risk level as follows:

$$\text{High-risk index} = \frac{\text{no. of labeled anemic samples in high-risk level}}{\text{total no. of samples in high-risk level}}, \quad (14)$$

$$\text{Low-risk index} = \frac{\text{no. of labeled nonanemic samples in low-risk level}}{\text{total no. of samples in low-risk level}}, \quad (15)$$

$$\text{Doubtful index} = \frac{\text{total no. of nonsuspect samples}}{\text{total no. of samples}}. \quad (16)$$

Since the indices are evaluated in terms of testing data, while the corresponding risk levels are determined by training data, the performance evaluation of the anemia detection methods can be more reliable in this way. The possible values of each index are all in $(0, 1)$ and higher values are preferred. The first two indices indicate how reliable the anemia detection methods can determine anemia and nonanemia cases, respectively, with high confidence. The doubtful index evaluates the screening capability of the methods to differentiate anemia and nonanemia cases. Samples that are predicted to be in the doubtful level (i.e., suspect samples) are more likely to be uncertain. More suspect samples imply poorer screening capability of the anemia detection methods because further examination, including real blood test, is required for the uncertain cases. The doubtful index evaluates the capability of the anemia detection methods to push suspect samples away into the high-risk level or low-risk level. Obviously, an excellent algorithm would have less estimated samples in the doubtful level (contributing to a higher value of the doubtful index), higher value of the high-risk index, and higher value of the low-risk index. Note that the doubtful interval is adjustable in practice by controlling the value of ETR. For example, if a physician requires less doubt or more confidence in anemia diagnosis, the interval can be extended so that more data will fall in this interval and less data will be considered as high risk or low risk. Further discussion and numerical values of these indices are given in Section 3.2.

3. Experimental Results and Discussion

In our experiment, we use the same palpebral conjunctiva images in [13, 14] as our database. There are a total of 100 images in which 40 of them are labeled as anemia samples and 60 of them are labeled as nonanemia samples according to the threshold set at 11 g/dL [13, 14]. In other words, those with an Hb level higher than 11 g/dL are labeled as anemia patients in this paper; otherwise, they would be nonanemic patients. All cases are adult patients and the Hb levels of all of them are examined prior to the treatment. Given the database, we use 10-fold cross validation to evaluate the performance of the proposed approach. In other words, 90 images are used for training and 10 images are used for testing each time and the overall performance is the average result of 10 times (i.e., a total of 100 test data are averaged).

In our previous works ([13, 14]), we enlarged the images to 500×500 pixels in order to observe the image texture better and facilitate the further processing of images (e.g., extract entropy features). The two articles ([13, 14]) use the same

database, where the original images are usually not square and their sizes vary significantly, but all of them are less than 150×150 pixels. All available images are resized (enlarged) to a fixed size of 500×500 pixels using relevant MATLAB functions. To comply with those two works, we also do the same thing here. The resulting images indeed become finer in this way and the image characteristics is more obvious.

To initialize the first estimate value in our modified KF, let $x(1) = z(1)$. For the penalty regression, we let $n = 4$. If we choose a polynomial order higher than 4, the final regression curve stays almost unchanged at the price of additional computing cost. Furthermore, we attempt to avoid the overfitting problem by punishing the higher-order term and inhibiting the growth of its coefficient. The key of choosing penalty parameters c_1 – c_4 and λ is to reduce the contribution from higher-order terms (to avoid overfitting or overtraining), which reduces the curvature of our fitting line and makes it smoother. So, the assignment principle for the parameters is as follows: The parameter values for lower-order terms are set smaller (lower penalty) and those for higher-order terms are set larger (higher penalty). The fitting algorithm is based on gradient descend, which means it would still be capable of finding the fitting line as long as we follow the assignment principle just mentioned. For example, even if the values for c_2 – c_4 are set much greater than c_1 , the final fitting line can be obtained (it would look like the result of linear fitting). Thus, the choice of c_1 – c_4 is customized by the user subject to the assignment rule just discussed. The parameter λ is chosen such that the penalty term would not be too large to make the convergence difficult. In our case, the value assigned to the penalty parameter is smaller than α in order not to make the convergence difficult. For α , it is the step size in the iteration process. Technologically, we should assign α a value that is as small as possible in order not to miss the extremal point in the optimization process. But, the computational cost would be relatively high accordingly. The final results would be the same if α is limited to within a range. For example, through our simulation, if the value range for α is under 9×10^{-11} , the final results remain the same generally.

Thus, we set $c_1 = 1$, $c_2 = 10$, $c_3 = 20$, and $c_4 = 30$ empirically, since we want to keep higher-order coefficients closer to zero. We set a random value from 0 to 1 for the initial value of a_i . Considering the performance and the convergence speed, we let a_0 be the first value of the feature data and set learning rate $\alpha = 1 \times 10^{-11}$ and penalty parameter $\lambda = 1 \times 10^{-12}$. The loop termination condition is met when the two objective cost functions in two successive iterations differ by less than 1×10^{-6} .

3.1. Experimental Results of the Proposed Approach. Comparing Figures 5 and 6, we can see that the data (denoted by asterisks) after applying the proposed Kalman filtering has lower data variation, which facilitates the use of regression analysis in the next step. For the fitting curve without penalty function in Figure 5(a), a serious overfitting problem occurs due to great data fluctuation. We can see that the mean value around 180 has roughly two different corresponding Hb levels, which will have a matching issue during the testing phase. In contrast to the regression curve with penalty

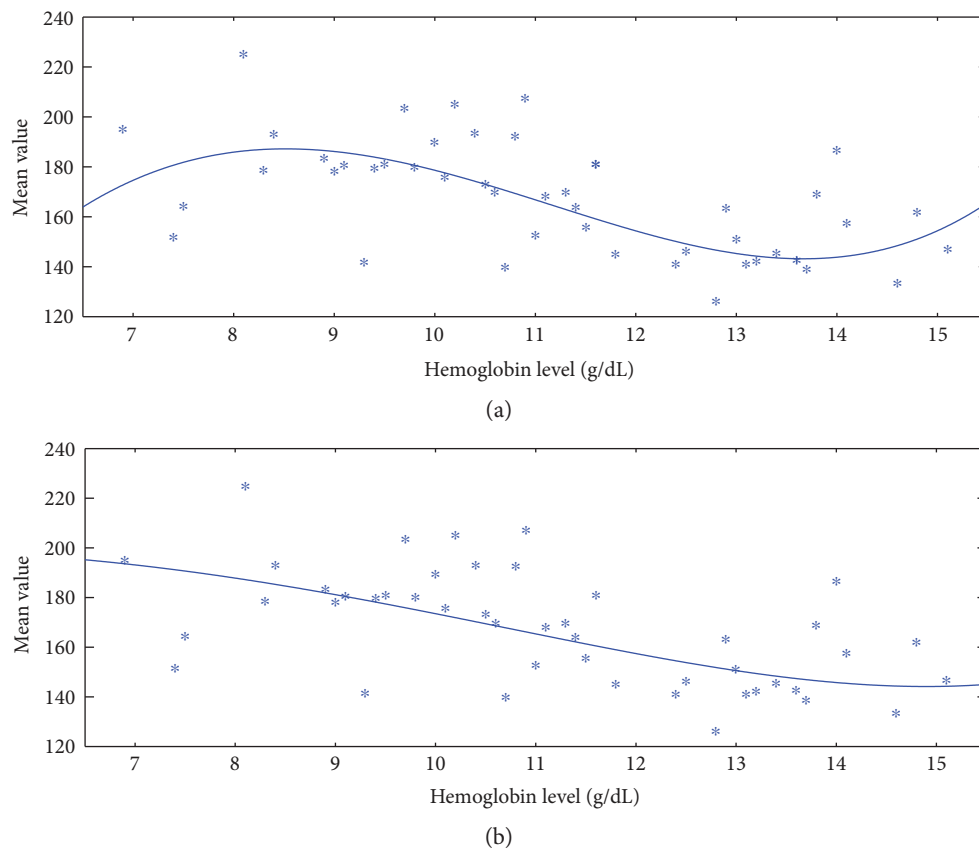


FIGURE 5: A typical result for the training data without proposed Kalman filtering and the fitting curve (a) without and (b) with penalty function.

function in Figure 5(b), it can better present the decreasing trend of the feature. In addition, the regression curve with penalty function is robust that it changes little before and after applying the proposed Kalman filtering. Furthermore, for the no-penalty regression in Figure 6(a), the matching issue still exists even though the data fluctuation is reduced after applying the proposed KF. The fitting curve in Figure 6(b) gets around the problems of both matching issue and great data fluctuation. Therefore, Kalman filtering helps to improve the fitting accuracy and penalty function helps to improve the fitting robustness.

3.2. Applying the Proposed Approach to Selected Methods. In addition to our proposed methods, we also examine several related anemia assessment methods using the RES proposed in Section 2.4. The first one includes the use of a linear regression for R color component only (adopted from [38], where it originally considered all R, G, and B components as a whole for regression). The second one uses the erythema index (defined as the logarithm of the R component value) and linear regression [10]. The third one uses the hue color component in the HSI color model as the recognition feature and perform anemia classification manually [39]. However, for the convenience of comparison, we use our nonlinear penalty regression method to replace the manual classification part. These methods are chosen for comparison because they are related to ours as follows: (1) they all use only one simple

recognition feature, such as R component value, erythema index, and hue component value, to determine the anemia status, and (2) the first two methods also implement a regression approach for Hb level estimation. None of them includes KF or any other filters in their original methods.

In the following, we compare the results of all the methods considered before and after applying the proposed KF. The results are shown in Figure 7 and Table 1. Unlike the samples in low- or high-risk levels, anemic samples in the doubtful level do not appear to have obvious color features. The Hb level threshold of 11 g/dL or any specific threshold value is commonly viewed as a “golden” standard to differentiate anemia and nonanemia. However, it is not a “perfect” one. For example, not every patient with 10.9 g/dL can be diagnosed as anemic with great confidence. In a general medical case, a doctor or a researcher may consider a disease in more than one level. The patients with minor symptom or asymptomatic may fall in level 1 and others in another level, say level 2. The treatment plans for the patients in level 1 are more conservative because the doctor is not sure if the patients really have the disease. Back to our case, the samples in the doubtful level are more likely in the uncertain zone. Reducing the number of such samples becomes our primary task. The results of Figure 7 show that all the methods can reduce the number of suspect samples after applying the modified KF. Especially for [39], it can hardly identify any anemic samples or nonanemic samples with

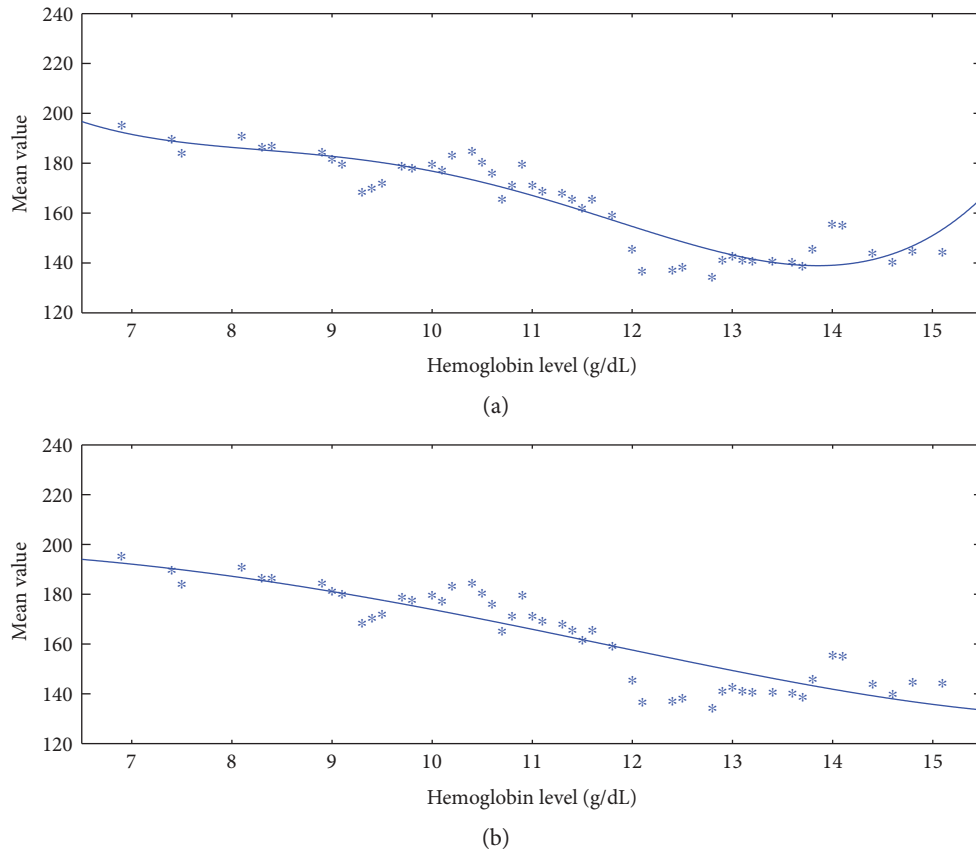


FIGURE 6: A typical result for the training data with proposed Kalman filtering and the fitting curve (a) without and (b) with penalty function.

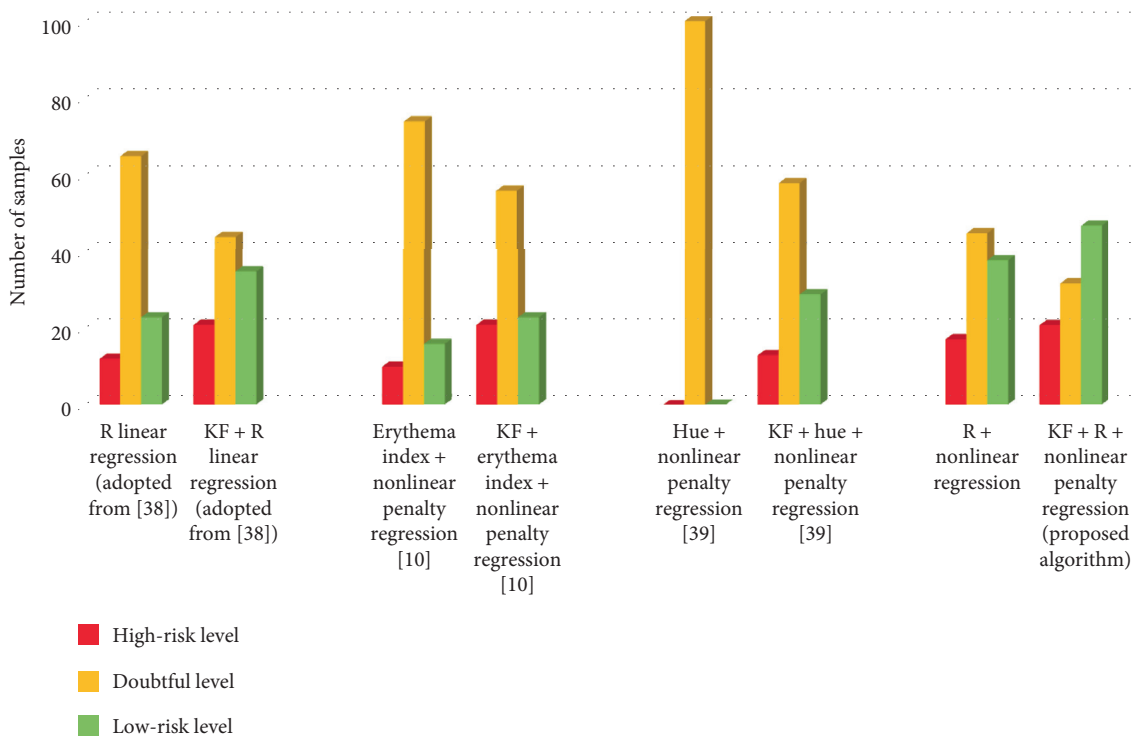


FIGURE 7: Comparison of the results with and without proposed KF for four different methods.

TABLE 1: Performance comparison between the methods with and without KF.

	Sensitivity	Specificity	Number of suspect samples	Sensitivity change	Specificity change	Number of suspect samples change
R + linear regression (adopted from [38])	0.8333	0.8261	65	+2.86%	-6.62%	-32.31%
KF + R + linear regression (adopted from [38])	0.8571	0.7714	44			
Erythema index + linear regression [10]	1.0000	1.0000	74	0%	-4.35%	-24.34%
KF + erythema index + linear regression [10]	1.0000	0.9565	56			
Hue + nonlinear penalty regression [39]	*NAN	*NAN	100	*NAN	*NAN	-42%
KF + hue + nonlinear penalty regression [39]	0.8462	0.5862	58			
R + nonlinear penalty regression	0.7647	0.8158	45			
KF + R + nonlinear penalty regression (proposed algorithm)	0.7619	0.8085	32	-0.36%	-0.89%	-28.89%

*NAN: there is no data, which means all test samples are considered to be suspect samples.

TABLE 2: The index of each level in RES.

	High-risk index	Doubtful index	Low-risk index
KF + R + linear regression (adopted from [38])	0.6923	0.56	0.9000
KF + erythema index + linear regression [10]	0.9545	0.44	1.0000
KF + hue + nonlinear penalty regression [39]	0.4783	0.42	0.8947
KF + R + nonlinear penalty regression (proposed algorithm)	0.6400	0.68	0.8837

confidence before the use of KF, since the data variation is too large for the method. However, it can reduce the number of suspect samples from 100 to 58 after applying KF and regain the capability of identifying anemic samples with confidence.

Table 1 shows the performance comparison using RES, where ETR is selected as the standard deviation of the training data. The sensitivity and specificity criteria follow their well-known definitions except that only the nonsuspect samples are considered. From Table 1, we can see that the sensitivity and specificity performance for some methods have declined slightly after using the proposed KF, but the KF reduces both the standard deviation of feature values and the number of suspect samples. From the aspect of practical medical application, a physician needs to give patients the correct information as much as possible, and thus, an appropriate reduction in the numbers of suspect samples is desirable. Although some methods in Table 1 show very high performance in sensitivity and specificity such as the one in [10], they have too many suspect samples (74 out of 100), which means the corresponding subjects may still need blood test for further verification just in case. Then, the screening purpose of any noninvasive anemia assessment study is hardly met. Therefore, our work is to reduce the occurrence of suspect samples as much as possible, which is equivalent to reducing the number of suspect samples in doubtful level. Although with slight decreasing in sensitivity and specificity, according to the last column, the proposed KF can reduce the number of suspect samples significantly for all the methods considered here.

Of course, we can also change ETR in RES to achieve customized results. The choice of ETR is obviously a trade-off. As discussed in Section 2.4, a larger range would produce more uncertain (suspected) data, while achieving higher

accuracy on certain data and vice versa. Table 2 shows the results of different methods (with the proposed KF) using (14), (15), and (16) in RES. Generally speaking, these methods perform quite well among the nonsuspect samples except [39]. Then, the primary task of noninvasive anemia examining becomes reducing as many suspect samples as possible. The method of KF + hue + nonlinear penalty regression [39] has the worst result with the lowest high-risk, low-risk, and doubtful indices. For the rest of the methods in Table 2, the method of KF + R + linear regression has comparable results with ours. However, it has 0.56 in the doubtful index, which is worse than that of ours. For the method of KF + erythema index + linear regression [10], it has excellent results of 0.9545 and 1.0000 in the high-risk index and low-risk index, respectively, but poor result of 0.44 in doubtful index due to too many suspect samples.

Originally, KF is often used to smooth time-varying data. Now, we apply it to deal with the feature without any time-varying nature, especially in medical applications. It demonstrates how to reduce measurement error. In fact, many medical-related data are time irrelevant, which means our work has the potential use in many other medical applications. Since no research works discuss how a KF can be applied to a time-unrelated medical field to the best of our knowledge, one contribution of our work is to present a new extending application of KF. With the proposed Kalman filtering, physicians and researchers could operate regression algorithms more effectively. Thus, KF may become a useful option for medical applications. Another contribution of our work is to propose a three-level evaluation scheme for anemia detection methods, which is particularly useful if anemia screening is the main objective of the methods.

4. Conclusion

In this paper, we proposed a combining approach consisting of the modified Kalman filtering and penalty regression for noninvasive anemia detection. The KF is reformulated so that it can be applied to time-irrelevant medical data. With our proposed KF, the variance of the data could be reduced which can facilitate the pattern-recognition task at a later stage. The penalty regression reduces the chance of overfitting, resulting in a more robust prediction system. We also propose a risk evaluation scheme and the idea of suspect samples. The suspect samples are those difficult to determine for sure whether we have an anemia case or not. The experimental results show that the proposed KF can effectively reduce the number of suspect samples for our proposed method and other relevant methods. This is a great advantage for the screening purpose of noninvasive anemia detection methods. We have proposed a simple and easy-to-use anemia detection method, which can be transformed into wearable or mobile devices if required. In the future, we would explore the use of the proposed KF for other medical applications.

Conflicts of Interest

The authors declare that they have no financial and personal relationships with other people or organizations that can inappropriately influence this work; there is no professional or other personal interest of any nature or kind in any product, service, and/or company that could be construed as influencing the position presented in, or the review of, the manuscript.

Acknowledgments

The authors would like to thank Professor Hwai-Tsu Hu from the Department of Electronic Engineering, Ilan University, and Doctor Ching-Chao Fan from the Saint Mary's Hospital Luodong, Taiwan, for providing them with the essential research materials of this study.

References

- [1] (January, 2017) <http://www.who.int/nutrition/topics/ida/en/>.
- [2] H. Ranganathan and N. Gunaarsekan, "Simple method for estimation of hemoglobin using color analysis," *IEEE Transactions on Information Technology in Biomedicine*, vol. 10, no. 4, pp. 657–662, 2006.
- [3] R. Kumar, M. Mahadevappa, and D. Goswami, "Low cost point of care estimation of hemoglobin levels," in *2014 International Conference on Medical Imaging, m-Health and Emerging Communication Systems (MedCom)*, pp. 216–221, Greater Noida, India, 2014.
- [4] T. Aldrich, M. Moosikasuwana, S. D. Shah, and K. S. Deshpande, "Length-normalized pulse photoplethysmography: a noninvasive method to measure blood hemoglobin," *Annals of Biomedical Engineering*, vol. 30, no. 10, pp. 1291–1298, 2002.
- [5] O. Kim, J. McMurdy, G. Jay, C. Lines, G. Crawford, and M. Alber, "Combined reflectance spectroscopy and stochastic modeling approach for noninvasive hemoglobin determination via palpebral conjunctiva," *Physiological Reports*, vol. 2, no. 1, article e00192, 2014.
- [6] I. Pavlova, C. R. Weber, R. A. Schwarz, M. D. Williams, A. M. Gillenwater, and R. R. Kortum, "Fluorescence spectroscopy of oral tissue: Monte Carlo modeling with site-specific tissue properties," *Journal of Biomedical Optics*, vol. 14, no. 1, article 014009, 2009.
- [7] G. Mari, R. L. Deter, R. L. Carpenter et al., "Noninvasive diagnosis by Doppler ultrasonography of fetal anemia due to maternal red-cell alloimmunization," *The New England Journal of Medicine*, vol. 342, no. 1, pp. 9–14, 2000.
- [8] R. J. Stoltzfus, A. Edward-Raj, M. L. Dreyfuss et al., "Clinical pallor is useful to detect severe anemia in populations where anemia is prevalent and severe," *The Journal of Nutrition*, vol. 129, pp. 1675–1681, 1999.
- [9] S. Collings, O. Thompson, E. Hirst, L. Goossens, A. George, and R. Weinkove, "Noninvasive detection of anaemia using digital photographs of the conjunctiva," *PloS One*, vol. 11, no. 4, article e0153286, 2016.
- [10] T. Yamamoto, H. Takiwaki, S. Arase, and H. Ohshima, "Derivation and clinical application of special imaging by means of digital cameras and Image J freeware for quantification of erythema and pigmentation," *Skin Research and Technology*, vol. 14, no. 1, pp. 26–34, 2008.
- [11] C. C. Fan, *Application of Artificial Classification Techniques to Assess the Anemia Conditions via Palpebral Conjunctiva Color Component*, [M.S. Thesis], National Ilan University, Taiwan, 2013.
- [12] V. Bevilacqua, G. Dimauro, F. Marino et al., "A novel approach to evaluate blood parameters using computer vision techniques," in *2016 IEEE International Symposium on Medical Measurements and Applications (MeMeA)*, pp. 1–6, Benevento, Italy, 2016.
- [13] Y. M. Chen, S. G. Miaou, and H. Bian, "Examining palpebral conjunctiva for anemia assessment with image processing methods," *Computer Methods and Programs in Biomedicine*, vol. 137, pp. 125–135, 2016.
- [14] Y. M. Chen and S. G. Miaou, "Anemia assessment based on color feature of palpebral conjunctiva," in *Proceedings of the 27th IPPR Conference on Computer Vision, Graphics, and Image Processing*, vol. 27, pp. 177–179, Kenting, Taiwan, 2014.
- [15] S. Goliaei, S. Ghorshi, M. T. Manzuri, and M. Mortazavi, "A Kalman filter technique applied for medical image reconstruction," in *Eighth International Multi-Conference on Systems, Signals and Devices*, pp. 1–5, 2011.
- [16] O. Chutatape, L. Zheng, and S. M. Krishnan, "Retinal blood vessel detection and tracking by matched Gaussian and Kalman filters," in *Proceedings of the 20th Annual International Conference of the IEEE Engineering in Medicine and Biology Society*, vol. 20, pp. 3144–3149, Hong Kong, China, 1998.
- [17] J. Foussier, D. Teichmann, J. Jia, B. Misgeld, and S. Leonhardt, "An adaptive Kalman filter approach for cardiorespiratory signal extraction and fusion of non-contacting sensors," *BMC Medical Informatics and Decision Making*, vol. 14, 2014.
- [18] J. S. Armstrong, "Illusions in regression analysis," *International Journal of Forecasting*, vol. 3, no. 28, pp. 689–694, 2012.
- [19] (January, 2017) https://en.wikipedia.org/wiki/Overfitting#cite_note-1.

- [20] K. Bryan and Y. Shibberu, "Penalty functions and constrained optimization," January 2017, <https://www.rose-hulman.edu/~bryan/lottamath/penalty.pdf>.
- [21] R. E. Kalman, "A new approach to linear filtering and prediction problems," *Journal of basic Engineering*, vol. 82, no. 1, pp. 35–45, 1960.
- [22] A. Carron, M. Todescato, R. Carli, L. Schenato, and G. Pillonetto, "Machine learning meets Kalman filtering," in *2016 IEEE 55th Conference on Decision and Control (CDC)*, pp. 4594–4599, Las Vegas, NV, USA, 2016.
- [23] Z. Wei, K. J. Tseng, N. Wai, T. M. Lim, and M. Skyllas-Kazacos, "Adaptive estimation of state of charge and capacity with online identified battery model for vanadium redox flow battery," *Journal of Power Sources*, vol. 332, pp. 389–398, 2016.
- [24] S. Chen, C. Kang, Z. Zhang, and H. Zhu, "A method for SOC estimation for lead-acid battery based on multi-model adaptive extended Kalman filtering estimation," in *IECON 2016 - 42nd Annual Conference of the IEEE Industrial Electronics Society*, pp. 18–24, Florence, Italy, 2016.
- [25] A. Davoudi, Y. Zou, I. C. Camacho, and X. Hu, "Guest editorial modeling and control of electrified vehicles and transportation systems," *IEEE Transactions on Transportation Electrification*, vol. 2, no. 2, pp. 115–118, 2016.
- [26] R. Olivera, R. Olivera, O. Vite, H. Gamboa, M. A. Navarrete, and C. A. Rivera, "Application of the three state Kalman filtering for moving vehicle tracking," *IEEE Latin America Transactions*, vol. 14, no. 5, pp. 2072–2076, 2016.
- [27] M. G. Ruppert, D. M. Harcombe, and S. O. R. Moheimani, "State estimation for high-speed multifrequency atomic force microscopy," in *2016 American Control Conference (ACC)*, pp. 2617–2622, Boston, MA, USA, 2016.
- [28] A. S. Leong and D. E. Quevedo, "Kalman filtering with relays over wireless fading channels," *IEEE Transactions on Automatic Control*, vol. 61, no. 6, pp. 1643–1648, 2016.
- [29] R. Ananthoju, A. P. Tiwari, and M. N. Belur, "A two-time-scale approach for discrete-time Kalman filter design and application to AHWR flux mapping," *IEEE Transactions on Nuclear Science*, vol. 63, no. 1, pp. 359–370, 2016.
- [30] R. Toscano and P. Lyonnet, "A Kalman optimization approach for solving some industrial electronics problems," *IEEE Transactions on Industrial Electronics*, vol. 59, no. 11, pp. 4456–4464, 2016.
- [31] K. Nam, S. Oh, H. Fujimoto, and Y. Hori, "Estimation of sideslip and roll angles of electric vehicles using lateral tire force sensors through RLS and Kalman filter approaches," *IEEE Transactions on Industrial Electronics*, vol. 60, no. 3, pp. 988–1000, 2013.
- [32] V. Smidl and Z. Peroutka, "Advantages of square-root extended Kalman filter for sensorless control of AC drives," *IEEE Transactions on Industrial Electronics*, vol. 59, no. 11, pp. 4189–4196, 2012.
- [33] J. Lim, M. Shin, and W. Hwang, "Variants of extended Kalman filtering approaches for Bayesian tracking," *International Journal of Robust and Nonlinear Control*, vol. 27, no. 2, pp. 319–346, 2016.
- [34] (January, 2017) https://en.wikipedia.org/wiki/Kalman_filter.
- [35] M. R. Rajamani, *Data-Based Techniques to Improve State Estimation in Model Predictive Control*, [Doctoral Dissertation], pp. 118–120, University of Wisconsin–Madison, USA, 2007.
- [36] M. R. Rajamani and J. B. Rawlings, "Estimation of the disturbance structure from data using semidefinite programming and optimal weighting," *Automatica*, vol. 45, no. 1, pp. 142–148, 2009.
- [37] G. Welch and G. Bishop, "An introduction to the Kalman filter," Tech. Rep. TR95041, Department Computer Science, University of North Carolina, Chapel Hill, 2000.
- [38] S. Suner, G. Crawford, J. McMurdy, and G. Jay, "Non-invasive determination of hemoglobin by digital photography of palpebral conjunctiva," *The Journal of Emergency Medicine*, vol. 33, no. 2, pp. 105–111, 2007.
- [39] C. I. Sanchez-Carrillo, "Bias due to conjunctiva hue and the clinical assessment of anemia," *Journal of Clinical Epidemiology*, vol. 42, no. 8, pp. 751–754, 1989.

Review Article

The Use of Optical Coherence Tomography in Dental Diagnostics: A State-of-the-Art Review

Monika Machoy,¹ Julia Seeliger,² Liliana Szyszka-Sommerfeld,¹ Robert Koprowski,³ Tomasz Gedrange,² and Krzysztof Woźniak¹

¹*Division of Orthodontics, Pomeranian Medical University in Szczecin, Ul. Powstańców Wlkp 72, 70-111 Szczecin, Poland*

²*Division of Orthodontics, Technical University Dresden, Fetscherstrasse 74, 01307 Dresden, Germany*

³*Department of Biomedical Computer Systems, Faculty of Computer Science and Materials Science, Institute of Computer Science, University of Silesia, Ul. Będzińska 39, 41-200 Sosnowiec, Poland*

Correspondence should be addressed to Monika Machoy; m.machoy@gmail.com

Received 17 February 2017; Revised 2 May 2017; Accepted 31 May 2017; Published 16 July 2017

Academic Editor: João Manuel R.S. Tavares

Copyright © 2017 Monika Machoy et al. This is an open access article distributed under the Creative Commons Attribution License, which permits unrestricted use, distribution, and reproduction in any medium, provided the original work is properly cited.

Optical coherence tomography provides sections of tissues in a noncontact and noninvasive manner. The device measures the time delay and intensity of the light scattered or reflected from biological tissues, which results in tomographic imaging of their internal structure. This is achieved by scanning tissues at a resolution ranging from 1 to 15 μm . OCT enables real-time in situ imaging of tissues without the need for biopsy, histological procedures, or the use of X-rays, so it can be used in many fields of medicine. Its properties are not only particularly used in ophthalmology, in the diagnosis of all layers of the retina, but also increasingly in cardiology, gastroenterology, pulmonology, oncology, and dermatology. The basic properties of OCT, that is, noninvasiveness and low wattage of the used light, have also been appreciated in analytical technology by conservators, who use it to identify the quality and age of paintings, ceramics, or glass. Recently, the OCT technique of visualization is being tested in different fields of dentistry, which is depicted in the article.

1. Introduction

Medical imaging is the basis of effective medical diagnosis and is now the mainstream of a dynamically developing branch of science, which is biomedical engineering. Its development started after an accidental discovery of Wilhelm Conrad Roentgen, a professor of physics, who in 1895 observed little fluorescence during his research on electrical discharges and cathode rays. X-radiation turned out to be a fundamental discovery which is still used in medicine today.

Another milestone was the development of the first computed tomography (CT) device by Godfrey Newbold Hounsfield in 1967. The concept of tomography refers to a method that provides images showing sections of the tested structure. The first CT scanner initiated rapid development of medical imaging techniques. A common feature of different types of

CT devices is noninvasive imaging of tissue structures and internal organs, as well as their functional parameters. The desire to minimize invasiveness of methods such as biopsy or exploratory surgery, which are painful and may cause deterioration in the patient's condition, was an impetus for the improvement of computed tomography equipment. As a result, completely new technologies were developed, such as magnetic resonance imaging (MRI), ultrasonography (USG), positron emission tomography (PET), single photon emission computed tomography (SPECT), and the latest and more widely used optical coherence tomography (OCT).

The method of optical coherence tomography using interferometry with partially coherent light was first presented in 1991 at the Institute of Technology of the University of Massachusetts [1]. The first in vivo measurements of the section of the human retina were made two years later

in Vienna [2]. The first commercial optical tomography device was produced in 1996 by Zeiss-Humphrey [3].

The article depicts the types of optical tomographs and the schematic construction based on the academic knowledge and enunciates the up-to-date knowledge concluded in the articles accessible in the US National Library of Medicine National Institutes of Health (PubMed), Dentistry & Oral Sciences Source EBSCO, and the <http://octnews.org> website.

2. Types of Optical Coherence Tomography

Optical coherence tomography (OCT) uses a beam of partially coherent light to create tomographic images. Currently, there are two basic types of optical coherence tomography: time domain optical coherence tomography (TDOCT) and Fourier domain optical coherence tomography (FD-OCT). The former technique was developed in 1991 by the above-mentioned group of researchers from the Massachusetts Institute of Technology in the United States [1] for use in ophthalmic diagnosis. It can produce tomographic images of relatively low quality, resulting from long time of measurement, but it does not allow for three-dimensional imaging of objects [4]. Modern optical tomography with detection in the frequency domain (Fourier domain optical coherence tomography) reduces the capture time by more than a hundred times and creates three-dimensional images of the test object.

Optical coherence tomography enables the study of objects that are partially transparent for light from the near infrared range. In the OCT scanner based on this method, the information about the location of scattering (reflecting) layers along the sample beam is contained in the modulation frequency of the light intensity measured as a function of frequency. The electric signal resulting from detection of spectra of interfering beams is called the signal of spectral bands. Nowadays, two methods of practical realization of this type of detection are used. The first is spectral optical coherence tomography (SOCT). The other method is swept source OCT or optical Fourier domain imaging (OFDI) [4]. The common elements, used in both methods (SOCT and OFDI), are fixed reference mirrors (as opposed to time domain OCT).

This improves mechanical stability of the system. An interference image is obtained by the numerical Fourier transform of registered spectral bands. However, the method of detection of an interference signal is different. In SOCT, the light source generates a broadband light beam. A spectrometer is used to detect signals for individual optical frequencies. In OFDI, an ordinary photodetector is used instead of a spectrometer, because the applied fast tunable laser generates light of a narrow spectral line individually for each wavelength.

The recently introduced SS-OCT uses a short cavity swept laser with a tunable wavelength of operation instead of the diode laser used in spectral-domain OCT [5]. The SS-OCT has improved image penetration using a wavelength of 1050 nm and has an axial resolution of $5.3 \mu\text{m}$ and an axial scan rate of 100,000 scans per second. Prototype models could reach faster scan speed of more than 400,000 scans per second [6, 7]. The $12 \times 9 \text{ mm}$ scan enables simultaneous

imaging of the macula, the peripapillary area, and the optic nerve head and the choroidal thickness. The $12 \times 9 \text{ mm}$ scan comprises 256 B scans each comprising 512 A scans with a total acquisition time of 1.3 s [8]. SS-OCT also provides the capability of a wide field up to $12 \times 12 \text{ mm}$ images [9]. SS-OCT enables clear simultaneous visualization of the vitreous and the posterior precortical vitreous pockets and the choroid and the sclera [10].

3. Operating Principle of Optical Coherence Tomography

OCT is a modular device. It consists of coupled hardware components. It contains the software and five basic modules: a partially coherent light source, an imaging apparatus, a measurement head, a module of data processing, and image generation as well as a computer control system. The light source used in the device determines its axial resolution and penetration depth of the light beam. The OCT imaging apparatus module is the central element of the system. This may be any measuring device capable of measuring the reflected or backscattered light with high sensitivity and resolution. Instruments that enable lossless signal transmission are also indispensable.

Other elements of the described OCT system are the measuring head and the system for bringing the probe beam to the test structure. They take different forms, depending on the field of medicine for which they are intended. Their shape also depends on the structure of the imaging apparatus block. The purpose of this module is to acquire measurement data from the imaging apparatus. Another necessary step is analysis of the obtained values, their processing, and presentation. This is achieved through a variety of techniques in the field of image processing, such as noise reduction algorithms, motion and visualization correction algorithms, segmentation, and image resolution enhancement.

The computer control system controls the entire OCT scanner. It enables to control scanning the reference arm of the interferometer and synchronize the operation of all components. Moreover, it allows for communication between the apparatus and the image processing block as well as the display of measurement results in real time as it is shown in Figure 1 [11].

OCT imaging is possible by measuring the intensity and time delay of the "echo" of the reflected or backscattered light. The method of OCT imaging is analogous to ultrasonography. However, they differ in terms of data measurement techniques. This is due to the fact that the speed of light is almost one million times greater than the speed of sound and, as a result, the distance measured by OCT is characterized by a much higher time resolution than USG. OCT resolution is $10 \mu\text{m}$, and in ultrasonography, it is $150 \mu\text{m}$. OCT, on the other hand, has a more limited tissue penetration ability. A light wave in OCT reaches a depth of 2 mm, whereas a sound wave in USG a depth of 10 cm. In the case of USG, electronic detectors can be used for detection of the returning acoustic wave reflected from an object. The use of such devices for detecting light waves is impossible, because the rate of signal changes is too high. The basis of

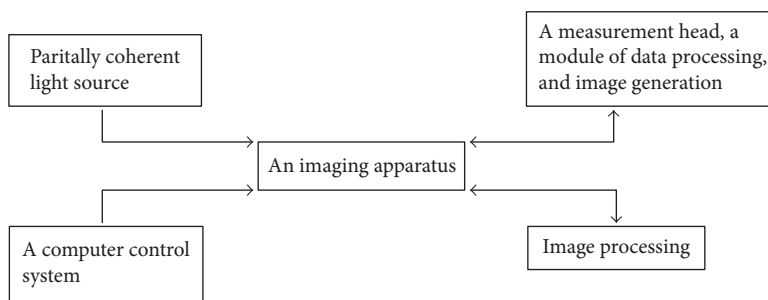


FIGURE 1: Modular diagram showing the operating principle of OCT.

optical tomography is the phenomenon of interference of two partially coherent light beams coming from a single source—the reference beam and the probe beam. Biological objects, such as tissues and organs, are for light waves, the centres with nonuniform distribution of a refractive index. The analysis of interference signal enables to locate the points at which the refractive index changes. These points are situated along the direction of propagation of the probe beam. The graph of reflected wave power density as a function of the position of the reflective point, which is the source of the wave, is called an A-scan. B scans give sagittal scans of the object and C scans—lateral scanning images at a constant depth. Combination of measurement results lying in one plane (numerous parallel directions of the probe beam) creates a two-dimensional image of the section of the test object [12].

The localization of the boundaries of layers with different refractive indices, that is, determination of the waveform of refractive index changes as a function of light beam penetration depth is realized by interferometric distance measurement systems. They use the property of light waves, which is the ability to overlap. This property is dependent on coherence of light. There are two types of light coherence: spatial—defining the phase correlation between wave sequences generated by different points of the light source and time—defining the phase correlation of wave sequences emitted by a single point of the light source at different points in time [13]. The time consistency of light is examined using the Michelson interferometer [14]. The schematic diagram of the operation of the Michelson interferometer is shown in Figure 2.

The light wave incident on the semi-transparent mirror BS (beam splitter) splits into two beams. The light source (LS) changing its direction into perpendicular after passing through BS is reflected by the movable mirror M1, again passes through BS, without changing its direction, and reaches the screen D (detector). The second beam formed by the passage of the primary beam through BS without changing its direction is reflected by the fixed mirror M2, then passes through BS changing the direction into perpendicular, and falls on screen D. The beam incident on the screen forms an interference image.

4. The Short History of OCT in Dentistry

Attempts to use optical coherence tomography in dentistry were first made in 1998 by researchers from the Laboratory

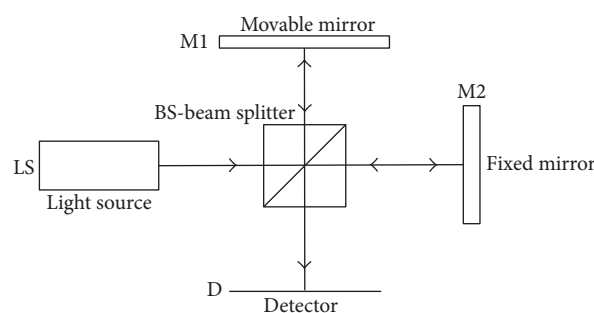


FIGURE 2: Schematic diagram of the operation of the Michelson interferometer.

of Medical Technology of Livermore, California, in collaboration with researchers from the University of Connecticut. In their work, they presented a prototype of dental optical coherence tomography and its in vivo application [15].

The device designed by them scanned hard tissues to a depth of 3 mm and soft tissues to a depth of 1.5 mm, which even now, 14 years after the creation of this sample design, is comparable to the possibilities of the latest generation apparatus. Two years later, the same group of researchers presented the first intraoral scans not only of the hard tissues but also soft tissues of the oral cavity, using another specifically designed CT prototype. In the published work, they demonstrated the possibility of imaging the gum margin, periodontal pockets, and attachments, both epithelial and connective, using an infrared beam of light [16]. The usefulness of optical coherence tomography in the recognition of lesions in the structure of both soft and hard tissues of the oral cavity was also presented in the same year 1998 by experimental and clinical studies conducted by Feldchtein et al. [17], which was actually the first mention of the possibility of OCT examination of hard tissue. In 2000, the same scientific center compared two OCT prototypes having different wavelengths of light: 850 and 1310 nm. Analysis of the quality of scans from individual devices and the evaluation of the possibility of reflecting the anatomical details of the oral cavity showed greater effectiveness of the apparatus using longer wavelengths of light [18]. Five years later, as an experiment, twenty-one dentists were asked to analyze fissure sealants, composite fillings, or tissue enamel based on OCT scans. Despite the lack of knowledge of the techniques of OCT scan interpretation, the dentists who took part in the study

TABLE 1: The OCT facilities and diagnostics in the last 5 years of publications.

Number	Reference number	Author	Title	Significance
(1)	[75]	Shi et al.	Monte Carlo modeling of human tooth optical coherence tomography imaging	This modeling will become a powerful and accurate tool for a preliminary numerical study of the OCT technique on diseases of dental hard tissue in human teeth.
(2)	[76]	Fried et al.	Near-IR imaging of cracks in teeth	Cracks were clearly visible using near-IR imaging at 1300 nm in both in vitro and in vivo images. Cracks and fractures also interfered with light propagation in the tooth aiding in crack identification and assessment of depth and severity.
(3)	[77]	Tom et al.	Near-IR imaging of demineralization under sealants	The wavelength region between 1500–1700 nm yielded the highest contrast of lesions under sealants for near-IR reflectance measurements.
(4)	[78]	Lee et al.	Dental optical coherence tomography: new potential diagnostic system for cracked-tooth syndrome	Crack lines shown in the SS-OCT images had distinct characteristics, and structural crack lines and craze lines could be distinguished in SS-OCT images. Thus, the detection ability of SS-OCT renders it an acceptable diagnostic device for cracked-tooth syndrome.
(5)	[79]	Simon et al.	Near-infrared imaging of secondary caries lesions around composite restorations at wavelengths from 1300–1700 nm	Intensity changes in NIR images at wavelengths ranging from 1300 to 1700 nm correlate with increased mineral loss measured using TMR. NIR reflectance and transillumination at wavelengths coincident with increased water absorption yielded significantly higher ($P < 0.001$) contrast between sound enamel and adjacent demineralized enamel. In addition, NIR reflectance exhibited significantly higher ($P < 0.01$) contrast between sound enamel and adjacent composite restorations than visible reflectance.
(6)	[80]	Chan et al.	Clinical monitoring of smooth surface enamel lesions using CP-OCT during nonsurgical intervention	Even though it appears that most of the lesions manifested little change with fluoride varnish application in the 30 weeks of the study, CP-OCT was able to measure the depth and internal structure of all the lesions including the thickness of the important transparent surface zone located at the surface of the lesions, indicating that CP-OCT is ideally suited for monitoring lesion severity in vivo.
(7)	[81]	Al-Azri et al.	Optical coherence tomography use in the diagnosis of enamel defects	OCT imaging enabled the identification of the type of enamel defect and the determination of the extent of the enamel defects in MIH with the advantage of being a radiation free diagnostic technique.
(8)	[82]	Tezuka et al.	Assessment of cervical demineralization induced by <i>Streptococcus mutans</i> using swept-source optical coherence tomography	The gaps along the dentinoenamel junction were additionally observed in SS-OCT. SS-OCT was capable of monitoring the cervical demineralization induced by a cariogenic biofilm and is considered to be a promising modality for the diagnosis of cervical demineralization.
(9)	[83]	Kang et al.	Enhancement of OCT images with vinyl polysiloxane (VPS)	Vinyl polysiloxane (VPS) impression materials which are routinely used in dentistry can be used to enhance the detection of dental lesions on tooth occlusal surfaces.

TABLE 1: Continued.

Number	Reference number	Author	Title	Significance
(10)	[84]	Damodaran et al.	Optical coherence tomography-based imaging of dental demineralisation and cavity restoration in 840 nm and 1310 nm wavelength regions	Were comparable with that of the widely used 1310 nm OCT system. In the case of restoration with filler material, the 1310 nm OCT imaging displayed better imaging capacity due to lower scattering than 840 nm imaging.
(11)	[85]	Duma et al.	Handheld scanning probes for optical coherence tomography: developments, applications, and perspectives	Two probes are constructed almost entirely from off-the-shelf components, while a third, final variant is constructed with dedicated components, in an ergonomic design. The handheld probes have unidimensional (1D) galvanometer scanners; therefore, they achieve transversal sections through the biological sample investigated—in contrast to handheld probes equipped with bidimensional (2D) scanners that can also achieve volumetric (3D) reconstructions of the samples. These latter handheld probes are therefore also discussed, as well as the possibility to equip them with galvanometer 2D scanners or with Risley prisms. For galvanometer scanners, the optimal scanning functions studied in a series of previous works are pointed out; these functions offer a higher temporal efficiency/duty cycle of the scanning process, as well as artifact-free OCT images.
(12)	[86]	Mahdian et al.	Tissue characterization using optical coherence tomography and cone beam computed tomography: a comparative pilot study	Within the limitations of this ex vivo pilot study, OCT can reliably differentiate between a range of hard and soft tissues.
(13)	[87]	Bakhsh et al.	Ultrastructural features of dentinoenamel junction revealed by focused gallium ion beam milling	The great potential of cryo-FIB in handling different biological tissues having different physical properties, with great precision and accuracy and minimum artefacts.
(14)	[88]	Oguro et al.	The role of enamel thickness and refractive index on human tooth colours	Enamel affected tooth colour, in which n was a statistically significant predictor for tooth colour change.
(15)	[89]	Algarni et al.	Enamel thickness determination by optical coherence tomography: in vitro validation	Human enamel samples were prepared and evaluated with μ -CT and PS-OCT and then sectioned and observed via digital transversal light microscopy. For all methods, a standard transversal section (B-scan) in each sample was selected, and the enamel thickness was measured at three predetermined positions using ImageJ analysis software. The results revealed significant high agreement between all tested methods, indicating the potential of PS-OCT as a clinical tool to effectively measure enamel thickness.
(16)	[90]	Wijesinghe et al.	Bio-photonic detection and quantitative evaluation method for the progression of dental caries using optical frequency domain imaging method	The physicians were able to diagnose the tooth volumetric and thickness changes at an initial stage by considering the obtained results as promising threshold parameters, which will be useful to barricade the progression of caries. To enhance the accuracy of the threshold parameters, quantitative (thickness and volumetric) information of multiple in vivo specimens will be evaluated, averaged, and normalized along with clinical trials in future studies.

TABLE 1: Continued.

Number	Reference number	Author	Title	Significance
(17)	[91]	Watanabe et al.	Resolution characteristics of optical coherence tomography for dental use	This study successfully clarified the resolution characteristics of two types of OCTs. The obtained data may be useful for diagnostic purposes, and the glass chart device used in this study may be useful for OCT quality assurance programmes.
(18)	[92]	Kim et al.	Automatic detection of tooth cracks in optical coherence tomography images	The authors were able to distinguish structural cracks, craze lines, and split lines in tooth cracks using SS-OCT images and to automatically detect the position of various cracks in the OCT images. Therefore, the detection capability of SS-OCT images provides a useful diagnostic tool for cracked tooth syndrome.
(19)	[93]	Segarra et al.	Three-dimensional analysis of enamel crack behavior using optical coherence tomography	Crack pattern, tooth type, and the location of the crack on the tooth exhibited a strong correlation. We show that the use of 3D SS-OCT permits for the nondestructive 3D imaging and analysis of enamel crack behavior in whole human teeth in vitro. 3D SS-OCT possesses potential for use in clinical studies for the analysis of enamel crack behavior.
(20)	[94]	Simon et al.	Near-IR and CP-OCT imaging of suspected occlusal caries lesions	Near-IR imaging methods have great potential for improving the early diagnosis of occlusal lesions.
(21)	[61]	Hariri et al.	Effects of structural orientation of enamel and dentine on light attenuation and local refractive index: an optical coherence tomography study.	Unlike enamel, refractive index and OCT signal patterns in dentine vary according to structural orientation, with dentine tubules playing the role. Attenuation of OCT signal intensity was small in enamel. The findings may contribute to a better understanding of the interactions of light with the dental tissue. Precise records of refractive indices and OCT signal patterns may be important for clinical diagnosis of caries and measurement of structural depth for operative purposes using this technology. Effects of dentine structural orientation on refractive index and scattering pattern must be considered when observing human teeth by OCT cross-sectional imaging.

obtained clinically acceptable results, which proved the potential clinical application of OCT [19]. The possibility of assessing caries developing under fissure sealants, which is difficult to diagnose, was subject to similar verification. After 90-minute training, doctors assessed the correctness of the enamel structure under 5 different types of sealing materials. When analysing OCT scans, the doctors detected caries more frequently compared with clinical or radiological assessment [20].

In the following years, a leading center dealing with optical tomography became the University of California in San Francisco. A series of articles was published, broadening the knowledge on the aspects of OCT application in conservative dentistry. The described issues were related to imaging of caries incipiens, their remineralization, and monitoring of the progressing or stopped demineralization of the enamel surface or tooth structure underneath fillings [21–29]. The issue of enamel remineralization is still continued [12]. In 2010, an innovative work was presented on attempts of

enamel remineralization with chitosan. The penetration depth of chitosan into the enamel structure was evaluated by optical tomography. An attempt of complete enamel remineralization using this method did not prove to be successful, but the exploratory efficiency of the used diagnostic method was once again confirmed [30]. In the same year, the enamel structure of primary teeth was analysed. Since caries is a disease that affects both primary and permanent teeth, the authors verified the effectiveness of the new method of caries diagnosis in the primary dentition. They proved a high potential of optical tomography in paediatric dentistry, as a technique for effective, painless, and noninvasive detection of early tooth decay [31]. The next studies described the effectiveness of optical coherence tomography in monitoring the range and efficiency of infrared and fractional CO₂ lasers in caries removal [32–37]. The effectiveness of a diode laser and Nd-YAG laser in the development of root canals during endodontic treatment was also verified [38]. An attempt was also made to use OCT in endodontic

TABLE 2: OCT in cariology and restorative dentistry in the last 5 years of publications.

Number	Reference number	Author	Title	Significance
(1)	[95]	Shimada et al.	Noninvasive cross-sectional imaging of proximal caries using swept-source optical coherence tomography (SS-OCT) in vivo	SS-OCT appears to be a more reliable and accurate method than bitewing radiographs for the detection and estimation of the depth of proximal lesions in the clinical environment.
(2)	[96]	Van Hilsen and Jones	Comparing potential early caries assessment methods for teledentistry	Although MID and CP-OCT were useful in detecting the presence of demineralization, examiners were not able to utilize these devices to adequately assess the depth of the demineralization. This study found that MID and CPOCT did not have markedly superior diagnostic values from simple CAM assessment for use in teledentistry.
(3)	[97]	Nazari et al.	3D assessment of void and gap formation in flowable resin composites using optical coherence tomography	The flowable composite with SDR (stress-decreasing resin) technology performed better than the conventional composite; however, bulk filling a 4 mm-deep cavity will compromise the sealing of the bonding interface regardless of the type of composite. OCT is a unique method of characterizing materials and their behaviors nondestructively and precisely.
(4)	[98]	Mandurah et al.	Monitoring remineralization of enamel subsurface lesions by optical coherence tomography	OCT signal attenuation demonstrated a capability for monitoring changes of enamel lesions during remineralization.
(5)	[99]	de Oliveira Mota et al.	Optical coherence tomography as an auxiliary tool for the screening of radiation-related caries	The OCT technique was able to characterize radiation-related caries, from a morphological point of view. Also demonstrated was its potential benefit for use in the clinical monitoring of radiation-related carious process.
(6)	[100]	Bista et al.	Nondestructive assessment of current one-step self-etch dental adhesives using optical coherence tomography	OCT is a unique tool to nondestructively evaluate the sealing performance of the restoratives through the cavity, provided that cavity walls have a certain minimum inclination with respect to the beam.
(7)	[101]	Park et al.	Assessment of interfacial defects at composite restorations by swept source optical coherence tomography	OCT imaging has the potential to nondestructively assess the interfacial adaptation of composite restorations and to detect internal defects in the layered composite material.
(8)	[102]	Marcauteanu et al.	Quantitative evaluation of dental abfraction and attrition using a swept-source optical coherence tomography system	A valuable tool in the evaluation of the dynamic evolution of ex vivo artificially induced abfractions and attritions is able to measure minute changes in the tooth morphology, having the potential to be employed as an effective tool for monitoring the temporal evolution of dental wear. OCT can offer the possibility of providing in vivo volumetric measurements and identification of fractural lines in dentine. The 2D and 3D pictures prove the OCT ability in the evaluation of dental abfractions and attritions. The system could measure a minimal volume of $2352 \mu\text{m}$ to $32,352 \mu\text{m}^3$, where each volume is acquired as 25,000 A scans in 2.5 s.

TABLE 2: Continued.

Number	Reference number	Author	Title	Significance
(9)	[103]	Liu and Jones	Evaluating a novel fissure caries model using swept source optical coherence tomography	Despite correctly evaluating the depth, this work showed that the lesion width calculated from SS-OCT reflectivity images did not accurately predict the demineralized width. The relative reflectivity could not accurately determine the mineral density of the demineralized lesions. SS-OCT detected subsurface fissure demineralization and could be used to determine if the decay process was advancing toward the enamel-dentin junction.
(10)	[104]	Chan K. H. et al.	Use of 2D images of depth and integrated reflectivity to represent the severity of demineralization in cross-polarization optical coherence tomography	Calculated lesion depths from OCT were compared with lesion depths measured from histological sections examined using polarized light microscopy. The 2D images of the lesion depth and integrated reflectivity are well suited for visualization of early demineralization.
(11)	[105]	Chew et al.	Measuring initial enamel erosion with quantitative light-induced fluorescence and optical coherence tomography: an in vitro validation study	OCT and QLF were able to detect demineralization after 10 min of erosive challenge and could be used to monitor the progression of demineralization of initial enamel erosion in vitro.
(12)	[106]	Nakajima et al.	Detection of occlusal caries in primary teeth using swept source optical coherence tomography	The results obtained from SS-OCT and conventional visual inspections were compared with those of CLSM. SS-OCT detects both cavitated and noncavitated lesions. The magnitude of sensitivity for SS-OCT was higher than those for visual inspection (sensitivity of visual inspection and SS-OCT, 0.70 versus 0.93 for enamel demineralization, 0.49 versus 0.89 for enamel cavitated caries, and 0.36 versus 0.75 for dentin caries). Occlusal caries of a few clinical cases were observed using SS-OCT in vivo. SS-OCT has a great detecting potential for occlusal caries in primary teeth.
(13)	[107]	Rominu et al.	Zirconia enriched dental adhesive: a solution for OCT contrast enhancement. Demonstrative study by synchrotron radiation microtomography	The present study proved the capability of the OCT method in visualizing the morphology and integrity of zirconia-doped tooth adhesive fillings to be used for a further in vivo tool development.
(14)	[108]	Mandurah et al.	Characterization of transparent dentin in attrited teeth using optical coherence tomography	Physiological changes in transparent dentin that involve deposition of mineral casts in the dentinal tubules lead to lower attenuation of OCT signal. OCT has a potential role to detect transparent dentin on the surface of attrited teeth and can be used in the future as a clinical adjunct tool.
(15)	[109]	Ku et al.	Detection of early changes in caries lesion using QLF-D and OCT	The QLF-D and SS-OCT could detect subtle changes in mineral loss and lesion depth with respect to demineralized time. Furthermore, these devices were useful for monitoring changes in mineral amount and lesion depth.
(16)	[110]	Turkistani et al.	Sealing performance of resin cements before and after thermal cycling: evaluation by optical coherence tomography	OCT could be used for monitoring of composite inlays with several interfacial resin layers. The application of a direct bonding agent in the resin-coating technique improved interfacial sealing and durability of all resin cements.

TABLE 2: Continued.

Number	Reference number	Author	Title	Significance
(17)	[111]	Lee et al.	Automated assessment of the remineralization of artificial enamel lesions with polarization-sensitive optical coherence tomography	PS-OCT can automatically measure the changes in artificial enamel lesion structure and severity upon exposure to remineralization solutions.
(18)	[112]	Chan et al.	A method for monitoring enamel erosion using laser irradiated surfaces and optical coherence tomography	Irradiation of the enamel surface with a pulsed carbon dioxide laser at subablative intensities results in significant inhibition of erosion and demineralization under the acid challenge employed in this study. In addition, these results suggest that it may be feasible to modify regions of the enamel surface using the laser to serve as reference marks to monitor the rate of erosion in vivo.
(19)	[113]	Cara et al.	Evaluation of two quantitative analysis methods of optical coherence tomography for detection of enamel demineralization and comparison with microhardness	Both methods for signal analysis from OCT allowed detection of demineralization with good performance. The AUC-OCT approach enables obtaining a linear relation with the microhardness results, for a quantitative assessment of mineral loss in human teeth.
(20)	[114]	Oancea et al.	Assessment of the sealant/tooth interface using optical coherence tomography	Optical inspection and X-ray investigation revealed no defects, while SS-OCT assesses exactly the position, the nature, and the dimensions of each type of these defects.
(21)	[115]	Damodaran et al.	Development of an electro-optically tuned optical coherence tomography system for imaging dental lesions	The tuning range for LiNbO ₃ and KTP was found to be in the order of few micrometers whereas KTN (potassium tantalate niobate) using the quadratic electro-optic effect is expected to show scanning range of tens of micrometers. KTN based hybrid scanning for dental caries imaging is also planned.
(22)	[116]	Wada et al.	Clinical assessment of non carious cervical lesion using swept-source optical coherence tomography	SS-OCT results confirm that dentin mineral loss and occlusal attrition were associated with larger NCCLs and can be considered as an etiological fact or information and progress of these lesions.
(23)	[117]	Anadioti et al.	Internal fit of pressed and computer-aided design/computer-aided manufacturing ceramic crowns made from digital and conventional impressions	The combination of the digital impression and pressed crown produced the least accurate internal fit.
(24)	[118]	Bortolotto et al.	Failure analysis of adhesive restorations with SEM and OCT: from marginal gaps to restoration loss	When marginal imperfections, or noncontinuous margins, were detected by SEM, also imperfections beneath the surface could be observed at the tooth-restoration interface with OCT. Restoration loss occurred above the borderline of 50% of marginal gaps on enamel and dentin. Marginal discrepancies of adhesive restorations can propagate inside the cavity and lead to restoration loss.
(25)	[119]	Alsayed et al.	Optical coherence tomography for evaluation of enamel and protective coatings	The coatings showed different thicknesses (60–250 micrometers) and various levels of structural and interfacial integrity. OCT could detect a demineralization inhibition zone adjacent to the edge of the fluoride- and calcium-releasing material. Localized demineralization was occasionally observed under thinner coatings. Protection of susceptible enamel surfaces by thin resin-based bioactive coatings provides protection from demineralization. OCT can be used to nondestructively monitor the integrity of such coatings, as well as enamel changes beneath and adjacent to them.

TABLE 2: Continued.

Number	Reference number	Author	Title	Significance
(26)	[120]	Espigares et al.	Assessment of natural enamel lesions with optical coherence tomography in comparison with microfocus X-ray computed tomography	The images obtained clinically in real time using the dental SS-OCT system are suitable for the assessment of natural subsurface lesions and their surface layer, providing comparable images to a laboratory high resolution μ CT without the use of X-ray.
(27)	[121]	Sun et al.	Sensing of tooth microleakage based on dental optical coherence tomography	The results of this study show that microleakage can be detected with oral probing using SS-OCT in vivo. The calculated microleakage length was 401 μ m and the width is 148 μ m, which is consistent with the related histological biopsy measurements. The diagnosis of microleakage in teeth could be useful for prevention of secondary caries in the clinical treatment plans developed in the field of oral medicine.
(28)	[122]	Park et al.	Assessment of defects at tooth/self-adhering flowable composite interface using swept-source optical coherence tomography (SS-OCT)	Given the high proportion of adhesive defects with the experimental self-adhering flowable composite, its use as the definitive restorative material in class-V cavities must be critically scrutinized and clinical indications must be investigated further with in vitro and in vivo trials.
(29)	[123]	Milly et al.	Surface pre-conditioning with bioactive glass air-abrasion can enhance enamel white spot lesion remineralization	Bioactive glass air-abrasion was used to precondition enamel white spot lesion. Preconditioning increased the average surface roughness of the lesion. An ultrathin, clinically insignificant layer was removed from the lesion surface. Preconditioning enhanced subsequent remineralization using bioactive glass.
(30)	[124]	Min et al.	Evaluation of penetration effect of resin infiltrant using optical coherence tomography	The OCT was the promising quantitative evaluation method for RI penetrated into EC. The OCT would be used as a nondestructive and real-time evaluation method for resin infiltrant penetrated into caries lesion on clinical procedure.
(31)	[125]	Sinescu et al.	Noninvasive quantitative evaluation of the dentin layer during dental procedures using optical coherence tomography	The study demonstrates the usefulness of OCT imaging in guiding such evaluations during dental procedures.
(32)	[126]	Majkut et al.	Validation of optical coherence tomography against micro-computed tomography for evaluation of remaining coronal dentin thickness	We used optical coherence tomography (OCT) and microcomputed tomographic (micro-CT) imaging to scan teeth after deep dentin caries removal. The remaining dentin thickness (RDT) at pulpal horns was measured and compared. A strong correlation was found in measurements between OCT and micro-CT imaging. It was possible to clearly visualize pulp horns with RDT up to 1.5 mm in thickness. A refractive index value of 1.54 is valid to convert optical readings of RDT by OC.
(33)	[127]	Turkistani et al.	Microgaps and demineralization progress around composite restorations	Microgaps forming at the margins of restorations depend on adhesives and significantly contribute to the progress of demineralization around the margins, while fluoride release may decrease the rate of progression.

TABLE 2: Continued.

Number	Reference number	Author	Title	Significance
(34)	[128]	Mota et al.	Optical coherence tomography applied to the evaluation of wear of composite resin for posterior teeth	90% of the restorations of both groups had fractures and/or points of stress concentration, considered niches for early dissemination of new fracture lines.
(35)	[129]	Barbosa et al.	Analysis of photodynamic cream effect in dental caries using optical coherence tomography	The OCT technique demonstrated that cream associated with laser showed the lowest quantitative enamel mineral losses after cariogenic challenge.
(36)	[130]	Makishi et al.	Assessment of current adhesives in class I cavity: nondestructive imaging using optical coherence tomography and microtensile bond strength	Sealing performance was measured in five adhesives by optical coherence tomography. Sealing and bond strength performance within individual specimens were correlated. Interfacial defects increased after thermal aging. Increased interfacial defects tended to decrease the bond strength. Two- and three-dimensional images were useful in assessing bonding performance.
(37)	[74]	Ibusuki et al.	Observation of white spot lesions using swept source optical coherence tomography (SS-OCT): in vitro and in vivo study	SS-OCT appears to be an effective tool for observation of the internal structure of WSLs, enabling quantitative assessment of WSL depth. Such data can be considered in the clinical management of white spot lesion.
(38)	[131]	Yoshimine et al.	Interfacial adaptation of composite restorations before and after light curing: effects of adhesive and filling technique	SS-OCT is a unique method to observe the pre-existing interfacial defects and gaps developed during polymerization, which were found to depend on both placement technique and applied adhesive.
(39)	[132]	Sampaio et al.	Effect of restorative system and thermal cycling on the tooth restoration interface—OCT evaluation	The self-etching adhesive system (CSE) showed better dentin marginal integrity after thermal cycling, compared with the etch-and-rinse (SB2), regardless of the type of resin composite used. Enamel was not affected even after thermal cycling.
(40)	[130]	Makishi et al.	Assessment of current adhesives in class I cavity: nondestructive imaging using optical coherence tomography and microtensile bond strength	Sealing performance was measured in five adhesives by optical coherence tomography. Sealing and bond strength performance within individual specimens were correlated. Interfacial defects increased after thermal aging. Increased interfacial defects tended to decrease the bond strength. Two- and three-dimensional images were useful in assessing bonding performance.
(41)	[133]	Borges et al.	Marginal and internal analysis of preheated dental fissure-sealing materials using optical coherence tomography	Preheated flowable composite provided the best marginal sealing of fissures and internal homogeneity of the material.
(42)	[134]	Dsouza et al.	Assessment of curing behavior of light-activated dental composites using intensity correlation based multiple reference optical coherence tomography	These results show that MR-OCT has the potential to measure the curing time and monitor the curing process as a function of depth. Moreover, MR-OCT as a product has potential to be compact, low-cost, and to fit into a smartphone. Using such a device for monitoring the curing of the resin will be suitable for dentists in stationary and mobile clinical settings.

TABLE 2: Continued.

Number	Reference number	Author	Title	Significance
(43)	[135]	Han et al.	Non-destructive evaluation of an internal adaptation of resin composite restoration with swept-source optical coherence tomography and micro-CT	Micro-CT and SS-OCT may be useful nondestructive methods for evaluating internal adaptation. The microleakage measured by micro-CT was lower than that of SS-OCT; however, the two measurements were relatively high-correlated. When adhesion depends mostly on the dentin surface, a two-step self-etch adhesive system should be considered for long-term longevity.
(44)	[137]	Tom et al.	Near-IR image-guided laser ablation of demineralization on tooth occlusal surfaces	Sequential near-IR reflectance images at 1500–1700 nm can be used to guide a 9.3 μm CO ₂ laser for the selective ablation of early demineralization on tooth occlusal surfaces.
(45)	[138]	Cassimiro-Silva et al.	Mitigation of enamel erosion using commercial toothpastes evaluated with optical coherence tomography	A significant increase in the mean roughness values was observed on eroded surface and also on treated surface as revealed by scanning electron microscopy. The use of SnF ₂ /NaF toothpaste was the most effective method for reducing mineral loss. As quantitative methods, OCT and contact profilometry showed no statistical differences. OCT, which was used for this purpose for the first time, has the advantage of being noninvasive and therefore has the potential for clinical application.
(46)	[139]	Dao Luong et al.	Fractography of interface after microtensile bond strength test using swept-source optical coherence tomography	Testing MTBS samples at higher crosshead speeds induced more cracks in dentin. Lining with a flowable composite improved the bonding quality and increased the bond strength. SS-OCT can visualize interfacial cracks after restoration debonding.
(47)	[140]	Ito et al.	Assessment of occlusal fissure depth and sealant penetration using optical coherence tomography	The diagnostic power of SS-OCT was higher than that of visual inspection for fissure depth. Additionally, clear cross-sectional images of sealant penetration into fissures were observed with SS-OCT. SS-OCT can be used to evaluate fissure depth and monitor sealant penetration.
(48)	[141]	Han et al.	Internal adaptation of resin composites at two configurations: influence of polymerization shrinkage and stress	Internal adaptation in a high C-factor cavity was inferior to that in a low C-factor cavity for both conventional and bulk-filled composites. Internal adaptation, polymerization shrinkage, and stress were different among composite materials. Polymerization stress under the compliance-allowed condition showed significant correlations with internal adaptations in high and low C-factor cavities.
(49)	[142]	Horie et al.	Monitoring of cariogenic demineralization at the enamel–composite interface using swept-source optical coherence tomography	The carious demineralization around composite restorations was observed as a bright zone in SS-OCT during the process of bacterial demineralization. SS-OCT appears to be a promising modality for the detection of caries adjacent to an existing restoration.

TABLE 2: Continued.

Number	Reference number	Author	Title	Significance
(50)	[143]	Zhou et al.	Assessment of bacterial demineralization around composite restorations using swept-source optical coherence tomography (SS-OCT)	SS-OCT nondestructively detected demineralization around composite restorations and interfacial gaps created by <i>S. mutans</i> biofilm in this in vitro model.
(51)	[144]	de Moraes et al.	Progression of erosive lesions after Nd:YAG laser and fluoride using optical coherence tomography	The OCT technique is promising for diagnosing and monitoring erosive lesion damage; however, further in vitro and in vivo research is needed to improve its use.
(52)	[145]	Ueno et al.	Optical analysis of enamel and dentin caries in relation to mineral density using swept-source optical coherence tomography	Both enamel and dentin demineralization showed significantly higher IS200 and $\mu\mu$ than the sound tooth substrate from the sagittal scan. Enamel demineralization showed significantly higher IS200 than sound enamel, even with low levels of demineralization. In demineralized dentin, the $\mu\mu$ from the horizontal scan consistently trended downward compared to the sound dentin.
(53)	[146]	Sugita et al.	A pilot study to assess the morphology and progression of non-carious cervical lesions	The dimensional analysis demonstrated notable progression with large variations. The wedge-shaped lesions appeared to show greater D_{\max} values compared to the saucer-shaped lesions.
(54)	[147]	Schneider et al.	Imaging resin infiltration into non-cavitated carious lesions by optical coherence tomography	Resin infiltration can be increased by optimizing the etching process. Optical coherence tomography provides information about the process and degree of resin infiltration.
(55)	[20]	Holtzman et al.	Ability of optical coherence tomography to detect caries beneath commonly used dental sealants	Dentists were able to detect tooth decay beneath four commonly used dental sealants based on OCT images. Clinical investigations are now underway to determine the usefulness of this approach in vivo.
(56)	[12]	Kang et al.	Nondestructive monitoring of the repair of enamel artificial lesions by an acidic remineralization model using polarization-sensitive optical coherence tomography	This study demonstrated that PS-OCT can be used to nondestructively measure changes in lesion structure and severity upon exposure to an acidic remineralization model. This study also demonstrated that automated algorithms can be used to assess the lesion severity even with the presence of a weakly reflective surface zone.
(57)	[28]	Kang et al.	Nondestructive assessment of early tooth demineralization using cross-polarization optical coherence tomography	Cross-polarization OCT is ideally suited for the nondestructive assessment of early demineralization.
(58)	[58]	Nazari et al.	Effect of hydration on assessment of early enamel lesion using swept-source optical coherence tomography	In summary, the strong relationship found between DH and lesion extent indicates the potential of this method for assessment of early enamel lesion using SS-OCT. However, further studies on DH for evaluation of a wider range of demineralized lesions as well as remineralization, accompanied by a clinically relevant drying method are necessary to optimize the suggested methodology.
(59)	[60]	Shimada et al.	3D evaluation of composite resin restoration at practical training using swept-source optical coherence tomography (SS-OCT)	SS-OCT could detect the internal gaps and voids within the restorations in tomography images synthesized based on the backscatter signal from within the restoration. It is suggested that the SS-OCT is promising diagnostic modality, as well as educational imaging device for the detection of internal gaps in adhesive restorations.

TABLE 2: Continued.

Number	Reference number	Author	Title	Significance
(60)	[62]	Nakajima et al.	Noninvasive cross-sectional imaging of incomplete crown fractures (cracks) using swept-source optical coherence tomography	SS-OCT can clearly discriminate cracks, which appear as highlighted lines due to the scattering of light. The results obtained from the three scanning directions were correlated well with those of the histological sections.
(61)	[63]	Braz et al.	In situ gold nanoparticles formation: contrast agent for dental optical coherence tomography	The results show that the OCT technique, using in situ formed gold nanoparticles as contrast enhancers, can be used to visualize dentin structures in a noninvasive and nondestructive way.
(62)	[67]	Holtzman et al.	Assessment of early occlusal caries pre- and post-sealant application—an imaging approach	This study found that OCT-based imaging combined with a simple diagnostic algorithm accurately assessed the severity of natural early caries on occlusal surfaces in extracted teeth both in the absence and presence of dental sealant. The findings of this study support the clinical use of OCT imaging for assessment and monitoring progression of early noncavitated caries lesions on occlusal surfaces including areas under dental sealants.
(63)	[69]	Sugita et al.	A pilot study to assess the morphology and progression of non-carious cervical lesions	The dimensional analysis demonstrated notable progression with large variations. The wedge-shaped lesions appeared to show greater maximal values compared to the saucer-shaped lesions. With respect to the depth, the wedge-shaped lesions may progress at a greater rate compared to the saucer-shaped lesions.
(64)	[70]	Zhou et al.	Assessment of bacterial demineralization around composite restorations using swept-source optical coherence tomography (SS-OCT)	SS-OCT nondestructively detected demineralization around composite restorations and interfacial gaps created by <i>S. mutans</i> biofilm in this in vitro model.
(65)	[71]	Maia et al.	Evaluation of dental enamel caries assessment using quantitative light induced fluorescence and optical coherence tomography	Comparison of the percentage of alteration between optical properties of sound and artificial enamel caries regions showed that OCT processed images through the attenuation of light enhanced the tooth optical alterations more than fluorescence detected by QLF system. QLF versus OCT imaging of enamel caries: a photonics assessment.
(66)	[72]	Horie et al.	Monitoring of cariogenic demineralization at the enamel–composite interface using swept-source optical coherence tomography	The carious demineralization around composite restorations was observed as a bright zone in SS-OCT during the process of bacterial demineralization. SS-OCT appears to be a promising modality for the detection of caries adjacent to an existing restoration.
(67)	[73]	Damodaran et al.	Optical coherence tomography based imaging of dental demineralization and cavity restoration in 840 nm and 1310 nm wavelength regions	Results were comparable with that of the widely used 1310 nm OCT system. In the case of restoration with filler material, the 1310 nm OCT imaging displayed better imaging capacity due to lower scattering than 840 nm imaging.

TABLE 3: OCT in endodontics in the last 5 years of publications.

Number	Reference number	Author	Title	Significance
(1)	[148]	de Oliveira et al.	Detection of apical root cracks using spectral domain and swept-source optical coherence tomography	The detection ability verified for both OCT systems renders them promising tools for the diagnosis of apical microcracks.
(2)	[149]	Brady et al.	A comparison of cone beam computed tomography and periapical radiography for the detection of vertical root fractures in nonendodontically treated teeth	Under the conditions of this ex vivo study, periapical radiographs and CBCT were unreliable for the detection of simulated incomplete VRFs. The widths of the fractures appeared to have an impact on the diagnostic accuracy of CBCT as the detection of VRFs of $\geq 50 \mu\text{m}$ was significantly higher than those of $< 50 \mu\text{m}$. The detection of complete fractures was significantly higher for all systems than that of incomplete fractures.
(3)	[150]	Minamino et al.	Nondestructive observation of teeth post core space using optical coherence tomography: a pilot study	In the cementum absent group, the internal structure of the root could be visualized clearly compared with the cementum present group. The root internal structure could be observed by OCT and the image became clearer when cementum was removed.
(4)	[151]	Ding et al.	Application of optical coherence tomography to identify pulp exposure during access cavity preparation using an Er:YAG laser	Swept-source OCT is a useful tool for identifying pulp exposure during access opening with the Er: YAG laser.
(5)	[152]	Chavda R. et al.	Comparing in vivo diagnostic accuracy of digital periapical radiography with cone-beam computed tomography for the detection of vertical root fracture	Both DR and CBCT imaging have significant limitations when detecting vertical root fractures.
(6)	[153]	Iino et al.	Detection of a second mesiobuccal canal in maxillary molars by swept-source optical coherence tomography	SS-OCT imaging is noninvasive, involves no ionizing radiation, and is accurate for the detection of MB2 canals.
(7)	[154]	Majkut et al.	Validation of optical coherence tomography against micro-computed tomography for evaluation of remaining coronal dentin thickness	Further analysis indicated linear regression with a slope of 1.54 and no intercept, closely matching the bulk refractive index of dentin. OCT enables visualization of anatomic structures during deep caries excavation. Exposure of the vital dental pulp because of the removal of very thin remaining coronal dentin can be avoided with this novel noninvasive technique.
(8)	[155]	Minamino et al.	Nondestructive observation of teeth post core-space using optical coherence tomography: comparison with microcomputed tomography and live images	The resulting OCT images were superior for identifying gap formation at the interface, while μCT images were better to grasp the tooth form. Continuous tomographic images from real-time OCT observation allowed successful construction of a video of the resin core build-up procedure.
(9)	[156]	Scotti et al.	Evaluation of composite adaptation to pulpal chamber floor using optical coherence tomography	Composite adaptation to the pulp chamber floor is fundamental for endodontic treatment outcome. Optical coherence tomography is the most noninvasive method to assess interfaces. Less interfacial gaps were observed when flowable resins were used. Any differences between conventional flow and bulk fill composite were shown.

TABLE 3: Continued.

Number	Reference number	Author	Title	Significance
(10)	[157]	Lee et al.	Activity assessment of root caries lesions with thermal and near-IR imaging methods	The PS-OCT algorithm for the automated assessment of remineralization successfully detected the highly mineralized surface layer on both natural and simulated lesions. Thermal imaging provided the most accurate diagnosis of root caries lesion activity. These results demonstrate that thermal imaging and PS-OCT may be ideally suited for the nondestructive root caries lesion activity during a clinical examination.
(11)	[39]	Shemesh et al.	Diagnosis of vertical root fractures with optical coherence tomography	OCT is a promising nondestructive imaging method for the diagnosis of VRFs.
(12)	[56]	Natsume et al.	Estimation of lesion progress in artificial root caries by swept source optical coherence tomography in comparison to transverse microradiography	The OCT showed a potential for quantitative estimation of lesion depth and mineral loss with cavitated dentin lesions in vitro.

TABLE 4: OCT in pedodontics in the last 5 years of publications.

Number	Reference number	Author	Title	Significance
(1)	[159]	Lenton et al.	Clinical cross-polarization optical coherence tomography assessment of subsurface enamel below dental resin composite restorations	CP-OCT imaging may be used to confirm the subsurface marginal integrity below resin composite restorations but with careful consideration of limitations of the imaging modality. CP-OCT imaging may be a useful adjunct to clinical visual investigation to confirm that a composite margin has a sound and well-adapted interface.

in vitro studies [39]. The results of studies evaluating the errors in prosthetic treatment were also published: defects in the structure of the materials used in prosthetic restoration and microleakage at the contact surface of the reconstruction and the tooth as well as the appropriateness of using OCT to control the internal structure of the prosthetic restoration without the need for its removal [34, 40].

Attempts were also made to visualize and measure the length of periodontal ligaments before and during orthodontic tooth movement. Incisors of rats were moved by applying successively varying sizes of forces and then the teeth were removed. The condition of the ligaments was imaged using optical coherence tomography and X-rays. OCT scans showed differences in periodontal ligament arrangement depending on the size of the applied force and their significant twist when using the greatest forces [41]. In subsequent studies, scans of the periodontium were performed and the lengths of both stretched and relaxed ligaments were measured. These structures were imaged using standard radio visual graphic intraoral images. However, they did not prove useful in the evaluation of periodontal elements obstructed in the image by tooth tissues. OCT enabled three-dimensional measurement and multilateral imaging of ligaments. The results obtained when using a CT scanner were different from those obtained by means of standard two-dimensional

imaging. Periodontal fibres measured in X-ray images appeared to be much thinner than in reality [42].

Another application of OCT was an attempt to evaluate the salivary pellicle. In order to compare the results and to improve the resolution and specificity of images, an optical coherence microscope (OCM) was used. Salivary pellicle islands were visible in the samples incubated in saliva, which grow into complexes completely covering the enamel surface [43]. The aim of the next study was to evaluate the retention of the biofilm around orthodontic hooks depending on the ligaturing method using OCT and microbiological samples. Both microbiological and optical (OCT) analysis showed a significant difference in biofilm formation depending on the ligaturing method. The hooks ligatured with elastic elements showed a greater amount of cariogenic *Streptococcus mutans*, whereas metal ligatures showed much less biofilm retention. The study found that optical coherence tomography may also be treated as a full-fledged quantitative indicator of bacterial plaque, which can be quickly and reliably visualized around orthodontic hooks [44]. Similar problems were presented in an ex vivo models. They proved the possibility of calculating the biofilm mass by measuring the distribution of light intensity scattering to a depth of the biofilm. An indirect possibility of characterizing the examined ecosystem on the surface of various types of composite

TABLE 5: OCT in prosthetics in the last 5 years of publications.

Number	Reference number	Author	Title	Significance
(1)	[158]	Park et al.	Digital technique for in vivo assessment of internal and marginal fit of fixed dental prostheses	Digital approaches to assess the misfit of fixed dental prostheses have been limited to in vitro evaluation. The present article describes a fully digital technique for the in vivo assessment of the fit of fixed dental prostheses by means of a chairside optical scanner and software for three-dimensional (3D) analysis. The 3D digital capture is performed in 3 steps: an extraoral scan of the restoration, an intraoral scan of the abutment tooth, and an intraoral registration scan of the restoration positioned on the abutment tooth.
(2)	[160]	Lin et al.	Examination of ceramic restorative material interfacial debonding using acoustic emission and optical coherence tomography	Sustainable cyclic load stresses in ceramic/dentin-bonded specimens were substantially lower than the measured SBS. Predicted S–N curve showed that the maximum endured load was 4.18 MPa passing 10^6 fatigue cyclic.
(3)	[161]	Lin et al.	Examination of ceramic/enamel interfacial debonding using acoustic emission and optical coherence tomography	The acoustic emission technique combined with OCT MPa images as a preclinical assessment tool to determine the integrity of cemented load bearing restored ceramic material. Sustainable cyclic load stresses in ceramic/enamel-bonded specimens were substantially lower than the measured SBS. Predicted S–N curve showed that the maximum endured load was 10.98 (about 34.48 N) passing 10^6 fatigue cyclic.
(4)	[162]	Madaras et al.	Material defects in ceramic crowns identification by optical coherence tomography and microCT	OCT technology can be considered an early diagnosis method of faults contained in the table structure of the ceramic crowns before inserting them in the oral cavity, by reducing the risks of a prosthetic treatment.
(5)	[163]	Fernandes et al.	Optical coherence tomography investigations of ceramic lumineers	The OCT is an effective and promising method to clinical evaluation of the cementing line in lumineers.
(6)	[164]	Gabor et al.	OCT evaluation of single ceramic crowns: comparison between conventional and chair-side CAD/CAM technologies	The marginal accuracy of all ceramic crowns fabricated with digital impression and the CAD/CAM technique is superior to the conventional impression technique.
(7)	[165]	Türk et al.	Comparison of the marginal adaptation of direct and indirect composite inlay restorations with optical coherence tomography	Within the limitations of this in vitro study, marginal discrepancies of inlay restorations were quantitatively and noninvasively evaluated by the OCT system. The following conclusions may be drawn: direct inlays presented smaller marginal gap values than indirect inlays. The marginal gap values were increased for all restorations after cementation.

materials was also demonstrated [45]. The study on biofilm imaging, describing the impact of dental calculus, enamel decalcification, and plaque, was an attempt to use optical coherence tomography not only in dentistry but also clinical periodontics. These studies confirmed the possibility of detecting enamel decalcification despite the presence of dental calculus or plaque and their diversification in the scans [46].

Another direction of research using the OCT technique has become the assessment of restorations with composite fillings in conservative dentistry. The study demonstrated, based on analysis of OCT scans, the leakage of composite restorations of enamel defects. The fissures were on average $50\ \mu\text{m}$. The results were confirmed by X-ray images and

optical microscopy. The study resulted in the development of their own spectral CT scanner, which was based on the Michelson interferometer. The created device, as well as the modern optical tomography instrument, divides monochromatic light into two beams, allowing for the reflection of the beams from semi-transparent mirrors and their subsequent interference. Using such a device, the researchers revealed the errors of composite reconstruction in the form of visible pits and fissures at the border between the filling and the cavity wall [47]. Enamel cracks at the border between the enamel and the composite filling reinforced with glass fibre were evaluated in a similar manner [48]. The subject of evaluation was also the tightness of three selected composite fillings, cracks of composite reconstruction reinforced with

TABLE 6: OCT in periodontology and diagnostics of oral tissues and implantology in the last 5 years of publications.

Number	Reference number	Author	Title	Significance
(1)	[166]	Gladkova et al.	Evaluation of oral mucosa collagen condition with cross-polarization optical coherence tomography	The OCT signal SD in cross-polarized images reflects two boundary conditions of collagen disorganization, namely, loss of fibre properties at active inflammation which attenuates the signal and fibrosis that occurs due to synthesis of a new remodeled collagen which amplifies the OCT signal.
(2)	[167]	Weber et al.	Towards a bimodal proximity sensor for in situ neurovascular bundle detection during dental implant surgery	The proximity to the neurovascular bundle can be tracked in real time in the range of a few millimeters with NIR signals, after which higher resolution imaging OCT to provide finer ranging in the submillimeter distances.
(3)	[168]	Kikuchi et al.	Evaluation of the marginal fit at implant-abutment interface by optical coherence tomography	OCT appeared as an effective tool for evaluating the misfit of implant-abutment under thin layers of soft tissue.
(4)	[169]	Mota et al.	Non-invasive periodontal probing through Fourier-domain optical coherence tomography	Regarding the ability of the two OCT systems to visualize periodontal structures, the system operating at 1325 nm shows a better performance, owing to a longer central wavelength that allows deeper tissue penetration. The results with the system at 930 nm can also be used, but some features could not be observed due to its lower penetration depth in the tissue.
(5)	[170]	Boadi et al.	Imaging of 3D tissue-engineered models of oral cancer using 890 and 1300 nm optical coherence tomography	890 nm OCT retains some of its known advantages of higher contrast between anatomical tissue layers when used to observe dysplastic and malignant 3D oral mucosa constructs. However, 1300 nm OCT is confirmed to possess a greater ability to image the full thickness of the model epithelia, and in particular, it is more suited to imaging through the keratinized layer.
(6)	[171]	Sanda et al.	The effectiveness of optical coherence tomography for evaluating peri-implant tissue: a pilot study	Cement remnants at the submucosal area can be detected in some cases, which can be helpful in preventing peri-implant diseases. Still, though there are some restrictions to its application, OCT could have potential as an effective diagnostic instrument in the field of implant dentistry as well.
(7)	[172]	Damodaran et al.	Non-invasive detection of periodontal loss of attachment using optical coherence tomography	The conventional time domain OCT system acquisition speed is limited by the speed of the mechanical scanning system. In order to overcome this issue, a novel electro-optic-based scanning system is proposed and demonstrated.
(8)	[173]	Fernandes et al.	Monitoring the gingival regeneration after aesthetic surgery with optical coherence tomography	OCT is an efficient method in the evaluation of regeneration gingival.
(9)	[174]	Augustine et al.	Optical coherence tomography in oral cancer detection	OCT can pinpoint epithelial changes; this imaging tool has sought potential broad applications in other mucosal lesions such as vesiculobullous and vascular lesions. The possibility of this application for bone-related disease imaging is an interesting research prospect. Future research should focus on the suitable wavelength of the light source of OCT for better observation of oral diseases. Faster and

TABLE 6: Continued.

Number	Reference number	Author	Title	Significance
				higher resolution OCT systems may replace the need for biopsies in many situations in the near future.
(10)	[175]	Negrutiu et al.	Assessment of dental plaque by optoelectronic methods	The biofilm network was dramatically destroyed after the professional dental cleaning. OCT noninvasive methods can act as a valuable tool for the 3D characterization of dental biofilms.
(11)	[176]	Fernandes et al.	In vivo assessment of periodontal structures and measurement of gingival sulcus with optical coherence tomography: a pilot study	OCT has the potential to be a reliable tool for in vivo periodontal tissues evaluation and for reproducible sulcus depth measurements in healthy sites. Further technological advances are required to reduce the procedure time and promote evaluation of posterior oral regions.
(12)	[177]	Salehi et al.	Characterization of human oral tissues based on quantitative analysis of optical coherence tomography images	These OCT features can reliably differentiate between a range of hard and soft tissues and could be extremely valuable in assisting dentists for in vivo evaluation of oral tissues and early detection of pathologic changes in the tissues.
(13)	[178]	Englund et al.	Assessing the dynamic biofilm removal of sulfonated phenolics using CP-OCT	This novel CP-OCT flow cell assay has the potential to examine rapid interactions between antibiofilm agents and tooth like surfaces.
(14)	[179]	Bordin et al.	Optical coherence technology detects early signs of peri-implant mucositis in the minipig model	Development of clinical applications of OCT imaging for early diagnosis of mucositis could lead to therapeutic interventions to reduce one of the causes of implant failure.
(15)	[180]	Kim et al.	Improved accuracy in periodontal pocket depth measurement using optical coherence tomography	OCT was able to visualize periodontal pockets and show attachment loss. By calculating the calibration factor to determine the accurate axial resolution, quantitative standards for measuring periodontal pocket depth can be established regardless of the position of periodontal pocket in the OCT image.
(16)	[45]	Chen et al.	Quantifying dental biofilm growth using cross-polarization optical coherence tomography	CP-OCT has the ability to nondestructively monitor biofilm growth and elucidate the growth characteristics of these microcosms on different dental material compositions. CP-OCT was able to quantify the mass of the biofilm by measuring the overall depth-resolved scattering of the biofilm.
(17)	[65]	Adegun et al.	Quantitative analysis of optical coherence tomography and histopathology images of normal and dysplastic oral mucosal tissues	Quantitative differentiation of normal and dysplastic lesions using OCT offers a noninvasive objective approach for localizing the most representative site to biopsy, particularly in oral lesions with similar clinical features.
(18)	[66]	Adegun et al.	Quantitative optical coherence tomography of fluid-filled oral mucosal lesions	The differentiation of normal and fluid-filled areas using individual SID values yielded both a sensitivity and specificity of approximately 80%. OCT complemented by SID analysis provides a potential in vivo clinical tool that would enable noninvasive objective visualization of the oral mucosa.

TABLE 7: OCT in orthodontics in the last 5 years of publications.

Number	Reference number	Author	Title	Significance
(1)	[181]	Koprowski et al.	Automatic method of analysis of OCT images in the assessment of the tooth enamel surface after orthodontic treatment with fixed braces	This paper presents an automatic quantitative method for the assessment of tooth enamel thickness captured on the OCT scans. This method has proven to be an effective diagnostic tool that allows evaluation of the surface and cross section of tooth enamel after orthodontic treatment with fixed thin-arched braces and proper selection of the methodology and course of treatment.
(2)	[182]	Seeliger et al.	Enamel thickness before and after orthodontic treatment analysed in optical coherence tomography	The range of variations in the enamel thickness after treatment with fixed thin-arched braces is not subjected to modification of a factor such as the type of adhesive system. The OCT is an effective diagnostic tool to evaluate the thickness of the enamel tissue before and after the completed orthodontic treatment.
(3)	[183]	Pithon et al.	Effectiveness of fluoride sealant in the prevention of carious lesions around orthodontic brackets: an OCT evaluation	Pro Seal sealant alone or combined with brushing and/or brushing and the use of a mouthwash with fluoride was more effective in protecting enamel, in comparison to brushing alone.
(4)	[184]	Leão Filho et al.	Enamel quality after debonding: evaluation by optical coherence tomography	The results demonstrated that enamel fractures were observed only in the samples bonded with ceramic brackets, and the type of pliers did not influence the incidence and extent of enamel damage. Moreover, the type of debonding technique (with side-cutting pliers or anterior bracket removal pliers) and the type of bracket did not influence the amount of adhesive remaining after debonding. The burs at low speed removed the remaining adhesive more effectively during cleanup procedures.
(5)	[185]	Pithon et al.	Effectiveness of varnish with CPP-ACP in prevention of caries lesions around orthodontic brackets: an OCT evaluation	The major limitation of this study is that it is a study in which demineralization was obtained with the use of chemical products and did not occur due to the presence of <i>Streptococcus mutans</i> and its acid byproducts. Application of CPP-ACP-containing varnish irrespective of being associated with brushing and mouthwash, or not, reduced depth of caries lesions around orthodontic brackets.
(6)	[186]	Nee et al.	Longitudinal monitoring of demineralization peripheral to orthodontic brackets using cross polarization optical coherence tomography	CP-OCT was able to measure a significant increase in demineralization ($P < 0.0001$) at the base of orthodontic brackets over a period of 12 months.
(7)	[187]	Isfeld et al.	Assessing near infrared optical properties of ceramic orthodontic brackets using cross-polarization optical coherence tomography	Noninvasive, near infrared (NIR) cross-polarization optical coherence tomography (CP-OCT) has potential to effectively image through portions of ceramic brackets; however, further investigation into the optical effects of resin integration in the base portion of the brackets is warranted.

TABLE 7: Continued.

Number	Reference number	Author	Title	Significance
(8)	[188]	Leão Filho et al.	Optical coherence tomography for debonding evaluation: an in-vitro qualitative study	The analysis of the two-dimensional and three-dimensional images allows observation and evaluation of adhesive remnants, enamel damage, and superficial aspects of enamel from different methods of adhesive remnant removal. The 2D optical coherence tomography analysis allows in-depth observation of the adhesive remnant layer. Optical coherence tomography can be a powerful tool for academic and clinical applications for the evaluation of debonding procedures.

glass fibre, which were imaged using optical coherence tomography (OCT), scanning electron microscopy (SEM), and optical microscopy (OM) [49]. The results enabled to describe the internal cracks of composites, which were not accessible during SEM or OM imaging. It was also observed that the assessment by means of optical coherent tomography required no special sample preparation, making it less expensive compared with the assessment in the scanning electron microscope [50]. In a further step, the efficiency of optical coherence tomography and confocal microscope in the evaluation of composite materials was compared [51].

There are also publications extending the above issue and evaluating marginal adaptation, porosity, and internal integrity of composite fillings. The potential of OCT and high resolution scans, allowing for critical assessment of the structure of fillings, previously inaccessible using common diagnostic methods, has thus been proven [52]. Similar studies evaluating polymerization shrinkage showed significant differences in its size depending on the tested materials [53]. Composite fillings restoring bovine enamel defects and their marginal adaptation with the use of self-etching techniques were also studied. The findings confirmed the thesis that optical coherence tomography is an effective tool in the accurate assessment of tightness of composite fillings [54]. The study of Senawongse et al. [55] made it possible to visualize the adhesive connection between the bonding system and the dentin, analyse carious lesions within the crown and root of the tooth, and assess secondary caries [56, 57]. From a clinical point of view, the studies identifying the relationship between the quality of OCT scans and the level of tooth hydration are very important [58, 59]. It directly affects the strength of the enamel prisms to injuries and the colour of the tissue, which is to be reproduced during conservative or prosthetic restorations. The use of OCT for educational purposes was also presented. The mistakes in the fillings made by dental students were discussed based on performed scans [60].

A further development of work on using an optical scanner and analysis of images was the research which used the potential of OCT to evaluate light scatter and the magnitude of the local refractive index depending on the state of the enamel and dentin. Optical properties of the prisms of the human enamel and dentin tubules were imaged [61].

OCT was also used to evaluate enamel cracks. The results were verified using a stereomicroscope and histological

samples of individual enamel layers. Enamel cracks were identified by CT as intensified signals appearing in exactly the same places where damage to the histological samples and stereomicroscopic images was visible. The results showed that OCT very accurately identified cracks and their size, so measurements of the scanned teeth yielded results that were equally reliable to those obtained from stereomicroscopy and histological examination of subsequent enamel layers [62].

In order to improve the quality of OCT scans and facilitate their interpretation, gold nanoparticles were applied. They are normally used as contrast in SEM imaging to visualize the hybrid layer and dentin tubules [63]. This was a significant advancement in dentin imaging because until then only a qualitative and quantitative evaluation of tooth decay had been possible, without distinguishing histological structures [64].

Attempts were also made to use optical coherence tomography in maxillofacial surgery for separating normal and dysplastic fragments of oral epithelium and distinguishing between solid and bullous lesions [65, 66].

The latest studies continue to focus primarily on early diagnosis of caries, assessment of the quality and thickness of dentin, and assessment of dental fillings [67–74]. The precise topics and conclusions of the articles from the last 5 years, according to field of dentistry are summarized in Tables 1, 2, 3, 4, 5, 6, 7, and 8. In the first table, there is set of publications [61, 75–94] that are exposing the facilities of OCT and the possibility of diagnostics in dentistry.

Table 2 collects publications [12, 19, 28, 58, 60, 62, 63, 67, 69–74, 95–148] which show the advancement in cariology and restorative dentistry that has taken place by using the OCT. Publications [39, 56, 149–158] presented in Table 3 are hastening the experiments and the results that were taken in endodontics. The publication [159] contained in Table 4 is the only recent publication connected directly with the pedodontics. Table 5 present the articles in the field of prosthetics [160–165]. Table 6 collects the articles [45, 65, 66, 166–180] about OCT in periodontology and diagnostics of oral tissues and implantology. The articles about diagnostics in orthodontics are presented in Table 7 [181–188]. Table 8 is collecting the other review articles that can be useful in extending the knowledge about OCT in dentistry.

TABLE 8: OCT in dentistry review articles in the last 5 years.

Number	Reference number	Author	Title	Significance
(1)	[189]	Clarkson et al.	Optical technology: an update on optical coherence tomography in dentistry	The technique of optical coherence tomography is considered to be significant since the technology involved allows imaging using light to around 2-3 mm in the teeth and can, for example, allow the extent and progression of carious lesions to be determined.
(2)	[190]	Gupta et al.	Optical coherence tomography: a new era in dentistry	It can be used for noninvasive investigations for both in vivo and in vitro structural imaging within the oral cavity.
(3)	[191]	Canjau et al.	Optical coherence tomography for non-invasive ex vivo investigations in dental medicine—a joint group experience	Complementary studies are possible embracing OCT with more traditional methods, such as confocal microscopy and micro-CT. Combination of principles is expected to evolve due to their limitations when considered separately.
(4)	[192]	Benic et al.	Novel digital imaging techniques to assess the outcome in oral rehabilitation with dental implants: a narrative review	New optical imaging techniques may be considered possible approaches for monitoring peri-implant soft tissue health. MRI and ultrasonography appear promising non-ionizing radiation-imaging modalities for the assessment of soft tissue and bone defect morphologies. Optical scanners and OCT may represent efficient clinical methods for accurate assessment of the misfit between the reconstructions and the implants.
(5)	[193]	Singh M. et al.	Optical coherence tomography—a imaging modality in dentistry beyond X-rays	OCT offers noninvasive, noncontact, in vivo, and real-time subsurface images with high-depth resolution. OCT represents a valuable method for investigation and assessment of the health status of soft oral tissues and of hard dental structures. OCT can be used for evaluation of dental treatments reducing their failure rate and saving time and resources, by eliminating incorrect restorations before their insertion in the oral cavity.
(6)	[194]	Hsieh et al.	Dental optical coherence tomography	Dental OCT demonstrates broad applications in soft and hard tissue imaging and early detection of caries, periodontal disease, and oral cancer. OCT can be used for gingiva, periodontal, and mucosa imaging. OCT may also apply in bone-related disease imaging. OCT and PS-OCT represent powerful ability for early diagnosis of caries. Mineral changes at early demineralization stages can be distinguished by PS-OCT. Subgingival calculus can also be detected by OCT. OCT provides images of dental tissue in situ and real-time and allows early detection of many oral diseases, including caries, periodontal disease, and oral cancer.
(7)	[195]	Shimada et al.	Application of optical coherence tomography (OCT) for diagnosis of caries, cracks, and defects of restorations	Describes the use of OCT for detecting dental caries, tooth fractures, and interfacial gaps in intraoral restorations. OCT can be a reliable and accurate method and a safer alternative to X-ray radiography.
(8)	[196]	Benic et al.	Novel digital imaging techniques to assess the outcome in oral rehabilitation with dental implants: a narrative review	Optical scanners and OCT may represent efficient clinical methods for accurate assessment of the misfit between the reconstructions and the implants.

TABLE 8: Continued.

Number	Reference number	Author	Title	Significance
(9)	[197]	Colston et al.	Imaging of the oral cavity using optical coherence tomography	The intensity of backscattered light is measured as a function of depth in the tissue. Low coherence interferometry is used to selectively remove the component of backscattered signal that has undergone multiple scattering events, resulting in very high resolution images (<15 microns). Lateral scanning of the probe beam across the biological tissue is then used to generate a 2D intensity plot, similar to ultrasound images. This imaging method provides information that is currently unobtainable by any other means, making possible such diverse applications as diagnosis of periodontal disease, caries detection, and evaluation of restoration integrity.
(10)	[198]	Se-Wook et al.	Study on application to the field of dentistry using optical coherence tomography (OCT)	This review discusses not only the basic principles of operation, types, advantages, and disadvantages of OCT but also the future applications of OCT technology and their potential in the field of dental diagnosis.

5. Discussion

The common objectives of the discussed studies were increased diagnostic capabilities in the oral cavity, more accurate understanding of physiological and pathophysiological processes related to soft and hard tissues of the oral cavity, and monitoring the effects of treatment.

OCT capabilities commonly applied in many fields of medicine (such as ophthalmology) are not yet fully used in dentistry, mainly due to the low availability of customized intraoral equipment and insufficient range of OCT rays, which penetrate into the tissue to a depth of only a few millimeters depending on the apparatus type. Lesions within the tooth tissue usually reach deeper and are often measured in centimeters, which makes it necessary to perform hundreds or even thousands of scans to illustrate the entire lesion. Latest studies [56, 168, 169] are using the intraoral probes, which show that this obstacle is being slowly eliminated in the intraoral diagnostics.

To maximize the efficiency of the dental diagnostic OCT, the wavelengths of light responsible for generating the image should be subjected to testing. In the near infrared light range, the central wavelength determines the maximum depth of penetration into the tissue due to scattering and absorption properties [71]. A wavelength below 1000 nm provides the greatest imaging efficiency because light scattering properties are similar to the size of tissue particles. Hydrated tissues dissipate much more energy than hard tissues containing a small percentage of water. For this reason, universal dental OCT should offer the possibility of controlling the wavelength depending on the type of the tested tissues. A different wavelength must be used for imaging the periodontal and tooth tissue per se.

However, the technical limitation of the dental OCT is not the only problem. A very important issue is the golden

standard that lacks the methodology in many publications. Only few experiments design the study in a manner that compares the obtained results to other more or less conventional methods. There are studies that practice the golden standard by comparing it, for example, to the transverse microradiography [52], microscope [58], standard histopathology [61], confocal laser scanning microscope and light microscopy [70], micro-OCT [74], cone beam computed tomography [82], synchrotron radiation microtomography [103], laser [108], SEM [114], and microfocus X-ray computed tomography [116]. It is important to focus on this topic during analyzing and citing the published results.

Another problem arising in dental diagnosis is the quality of individual teeth. The enamel can vary in its structure in a single subject. Likewise, dental fillings or prosthetic materials having a different composition reflect or absorb light at varying degrees, which has a decisive effect on the image quality and the possibility of its correct interpretation. Materials whose reflectance index is similar to that of the background will give a similar image. In addition to image quality, the possibility of performing objective measurements of the obtained scans is very important. To date, publications have been mainly focused on the possibility of obtaining images of individual structures and their acquisition rate, which is especially important in *in vivo* studies. The authors of the present paper attempted to develop an algorithm for rapid and accurate measurements of tooth tissues. This algorithm works fully automatically, without any operator intervention, enables to quantify the changes in the structure of enamel, allows for quantitative assessment of the effectiveness of cleaning the tooth surface and the effectiveness of the use of selected methods of enamel development. The analysis time of a sequence of 2D images does not exceed 5 seconds when using the Core i5 CPU M460 @ 2.5 GHz 4 GB RAM. The results of the mean thickness of the tooth enamel and

minimum and maximum values as well as standard deviation are analysed automatically and saved to text files *.txt and Excel *.xls. Automatic analysis of tooth enamel thickness provides a number of further possibilities. These include area analysis of enamel thickness (for each individual tooth area separately) and enamel texture analysis. Imaging and quantitative measurement of the enamel structure before installation of braces and after their removal enables to expose the tooth tissue damage extent depending on the used brackets and method of attachment. This makes it possible to deduce which brackets and what technique of their installation is the safest for tooth enamel. This solution has been published in work [72]. There are also a few other possibilities for using the quantitative analysis of the intraoral structures and tissue conditions such as dental enamel and dental caries [86], dental abfraction and attrition [98], enamel erosion [101], enamel demineralization [109], thickness of dentin layer [121], and soft tissues [173].

6. Conclusions

OCT is a very important tool for the study of various tissues in vivo and in vitro. Despite problems with equipment, the possibility of early diagnosis of caries in conservative dentistry in adults and children has already been proven. It is a unique improvement in relation to X-ray diagnostics exposing patients to X-ray radiation, which is often unable to visualize the early stages of caries.

OCT allows for soft-tissue imaging, which is important in the treatment of periodontal diseases, inaccessible to direct clinical assessment, and offers great perspectives for early diagnosis of lesions in the oral mucosa. Early differentiation of the observed lesion is of great importance in the treatment of a patient due to the frequent occurrence of tumours in the oral cavity. The use of long light waves will also enable the early diagnosis of tumours of the jaw bones.

OCT provides tissue sections in a noncontact and noninvasive manner and allows for real time tissue imaging in situ, without the need for biopsy, histological procedures, or the use of X-rays, so after solving the problems related to the availability and quality of equipment, it will be the method of choice in modern dental diagnostics.

Conflicts of Interest

The authors declare that there is no conflict of interest regarding the publication of this paper.

References

- [1] D. Huang, E. A. Swanson, C. P. Lin et al., "Optical coherence tomography," *Science*, vol. 254, pp. 1178–1181, 1991.
- [2] A. F. Fercher, C. K. Hitzenberger, W. Drexler, G. Kamp, and H. Sattmann, "In vivo optical coherence tomography," *American Journal of Ophthalmology*, vol. 116, no. 1, pp. 113–114, 1993.
- [3] A. F. Fercher, C. K. Hitzenberger, G. Kamp, and S. Y. El-Zaiat, "Measurement of intraocular distances by back-scattering spectral interferometry," *Optics Communication*, vol. 117, pp. 30–43, 1995.
- [4] M. Wojtkowski, "Obrazowanie za pomocą tomografii optycznej OCT z detekcją fourierowską," in *Wydawnictwo Naukowe Uniwersytetu Mikołaja Kopernika*, 16–58, Toruń, 2009.
- [5] Z. Yang, A. J. Tatham, L. M. Zangwill, R. N. Weinreb, C. Zhang, and F. A. Medeiros, "Diagnostic ability of retinal nerve fibre layer imaging by swept-source optical coherence tomography in glaucoma," *American Journal of Ophthalmology*, vol. 159, pp. 193–201, 2015.
- [6] B. Postaid, B. Baumann, D. Huang et al., "Ultrahigh speed 1050 nm swept source/Fourier domain OCT retinal and anterior segment imaging at 100,000 to 400,000 axial scans per second," *Optics Express*, vol. 18, pp. 200029–200048, 2010.
- [7] K. J. Mohler, W. Draxinger, T. Klein et al., "Combined 60° wide-field choroidal thickness maps and high-definition en face vasculature visualization using swept-source megahertz OCT at 1050 nm," *Investigative Ophthalmology & Visual Science*, vol. 55, pp. 6284–6293, 2015.
- [8] C. Zhang, A. J. Tatham, F. A. Medeiros, L. M. Zangwill, Z. Yang, and R. N. Weinreb, "Assessment of choroidal thickness in healthy and glaucomatous eyes using swept source optical coherence tomography," *PLoS One*, vol. 9, article e109683, 2014.
- [9] T. E. De Carlo, A. Romano, N. K. Waheed, and J. S. Duker, "A review of optical coherence tomography angiography," *International Journal of Retina and Vitreous*, vol. 1, p. 5, 2015.
- [10] H. Itakura, S. Kishi, D. Li, and H. Akiyama, "Observation of posterior precortical vitreous pocket using swept-source optical coherence tomography," *Investigative Ophthalmology & Visual Science*, vol. 54, pp. 3102–3107, 2013.
- [11] B. E. Bouma and G. J. Tearney, "Handbook of optical coherence tomography," *Information CRC Press*, 2001.
- [12] H. Kang, C. L. Darling, and D. Fried, "Nondestructive monitoring of the repair of enamel artificial lesions by an acidic remineralization model using polarization-sensitive optical coherence tomography," *Dental Materials*, vol. 28, no. 5, pp. 488–494, 2012.
- [13] H. Klejman, "Lasery. Państwowe Wydawnictwo Naukowe," Warszawa, 1979.
- [14] P. Miszta, "Interferometr Michelsona - zasada i zastosowanie. Zakład Dydaktyki Instytutu Fizyki UMK," *artykuł Dostępny na Stronie*, <http://dydaktyka.fizyka.umk.pl/Michelson/Michelson.pdf>.
- [15] B. W. Colston, U. S. Sathyam, L. B. DaSilva, and M. J. Everett, "6, 230–8," *Dental OCT Optical Express*, p. 3, 1998.
- [16] L. L. Otis, M. J. Everett, U. S. Sathyam, and B. W. Colston Jr, "Optical coherence tomography: a new imaging technology for dentistry," *Journal of the American Dental Association (1939)*, vol. 131, no. u, pp. 11–14, 2000.
- [17] F. Feldchtein, V. Gelikonov, R. Iksanov et al., "In vivo OCT imaging of hard and soft tissue of the oral cavity," *Optics Express*, vol. 14, pp. 239–250, 1998.
- [18] L. L. Otis, B. W. Colston Jr., M. J. Everett, and H. Nathel, "Dental optical coherence tomography: a comparison of two in vitro systems," *Dento Maxillo Facial Radiology*, vol. 29, no. 2, pp. 85–89, 2000.
- [19] L. L. Otis, R. I. Al-Sadhan, J. Meiers, and R. Badwa, "Identification of occlusal sealants using optical coherence tomography," *The Journal of Clinical Dentistry*, vol. 14, no. 1, pp. 7–10, 2003.

- [20] J. S. Holtzman, K. Osann, J. Pharar et al., "Ability of optical coherence tomography to detect caries beneath commonly used dental sealants," *Lasers in Surgery and Medicine*, vol. 42, pp. 752–759, 2010.
- [21] D. Fried, J. Xie, S. Shafi, J. D. Featherstone, T. M. Breunig, and C. Le, "Imaging caries lesions and lesion progression with polarization sensitive optical coherence tomography," *Journal of Biomedical Optics*, vol. 7, pp. 618–627, 2002.
- [22] R. S. Jones, M. Staninec, and D. J. Fried, "Imaging artificial caries under composite sealants and restorations," *Journal of Biomedical Optics*, vol. 9, pp. 1297–1304, 2004.
- [23] R. S. Jones and D. J. Fried, "Remineralization of enamel caries can decrease optical reflectivity," *Journal of Dental Research*, vol. 85, pp. 804–808, 2006.
- [24] S. K. Manesh, C. L. Darling, and D. Fried, "Polarization-sensitive optical coherence tomography for the nondestructive assessment of the remineralization of dentin," *Journal of Biomedical Optics*, vol. 14, article 044002, 2009.
- [25] C. Lee, C. L. Darling, and D. Fried, "Polarization-sensitive optical coherence tomographic imaging of artificial demineralization on exposed surfaces of tooth roots," *Dental Materials*, vol. 25, pp. 721–728, 2009.
- [26] S. K. Manesh, C. L. Darling, and D. Fried, "Nondestructive assessment of dentin demineralization using polarization-sensitive optical coherence tomography after exposure to fluoride and laser irradiation," *Journal of Biomedical Materials Research. Part B, Applied Biomaterials*, vol. 90, pp. 802–812, 2009.
- [27] J. Wu and D. Fried, "High contrast near-infrared polarized reflectance images of demineralization on tooth buccal and occlusal surfaces at $\lambda = 1310$ nm," *Lasers in Surgery and Medicine*, vol. 41, pp. 208–213, 2009.
- [28] H. Kang, J. J. Jiao, C. Lee, M. H. Le, C. L. Darling, and D. J. Fried, "Nondestructive assessment of early tooth demineralization using cross-polarization optical coherence tomography," *Journal of Selected Topics in Quantum Electronics*, vol. 16, pp. 870–876, 2010.
- [29] R. S. Jones, C. L. Darling, J. D. Featherstone, and D. J. Fried, "Remineralization of in vitro dental caries assessed with polarization-sensitive optical coherence tomography," *Journal of Biomedical Optics*, vol. 11, pp. 014–016, 2006.
- [30] T. M. Arnaud, B. de Barros Neto, and F. B. Diniz, "Chitosan effect on dental enamel remineralization: an in vitro evaluation," *Journal of Dentistry*, vol. 38, pp. 848–852, 2010.
- [31] A. M. Maia, D. D. Fonsêca, B. B. Kyotoku, and A. S. Gomes, "Characterization of enamel in primary teeth by optical coherence tomography for assessment of dental caries," *International Journal of Paediatric Dentistry*, vol. 20, pp. 158–164, 2010.
- [32] Y. C. Tao and D. J. Fried, "Near-infrared image-guided laser ablation of dental decay," *Biomedical Optics Express*, vol. 14, article 054045, 2009.
- [33] Y. C. Tao and D. Fried, "Selective removal of natural occlusal caries by coupling near infrared imaging with a CO(2) laser," *Biomedical Optics (BiOS)*, vol. 6843, pp. 68430I–68430I8, 2008.
- [34] Y. Sumi, N. Ozawa, S. Nagaosa, S. Minakuchi, and O. Umemura, "Application of optical coherence tomography (OCT) to nondestructive inspection of dentures," *Archives of Gerontology and Geriatrics*, vol. 53, pp. 237–241, 2011.
- [35] H. Natsume, G. van Soest, M. K. Wu, L. W. van der Sluis, and P. R. Wesselink, "The ability of optical coherence tomography to characterize the root canal walls," *Journal of Endodontia*, vol. 33, pp. 1369–1373, 2007.
- [36] D. J. Hsu, C. L. Darling, M. M. Lachica, and D. Fried, "Nondestructive assessment of the inhibition of enamel demineralization by CO2 laser treatment using polarization sensitive optical coherence tomography," *Journal of Biomedical Optics*, vol. 13, article 054027, 2008.
- [37] A. M. Can, C. L. Darling, C. Ho, and D. Fried, "Non-destructive assessment of inhibition of demineralization in dental enamel irradiated by a $\lambda = 9.3$ microm CO2 laser at ablative irradiation intensities with PS-OCT," *Lasers in Surgery and Medicine*, vol. 40, pp. 342–349, 2008.
- [38] C. Todea, C. Balabuc, C. Sinescu et al., "En face optical coherence tomography investigation of apical microleakage after laser-assisted endodontic treatment," *Lasers in Medical Science*, vol. 25, pp. 629–639, 2010.
- [39] H. Shemesh, G. van Soest, M. K. Wu, and P. R. Wesselink, "Diagnosis of vertical root fractures with optical coherence tomography," *Journal of Endodontia*, vol. 34, pp. 739–742, 2008.
- [40] C. Sinescu, M. L. Negrutiu, C. Todea et al., "Quality assessment of dental treatments using en-face optical coherence tomography," *Journal of Biomedical Optics*, vol. 13, article 054065, 2008.
- [41] J. Na, B. H. Lee, J. H. Baek, and E. S. Choi, "Optical approach for monitoring the periodontal ligament changes induced by orthodontic forces around maxillary anterior teeth of white rats," *Medical & Biological Engineering & Computing*, vol. 46, pp. 597–603, 2008.
- [42] J. H. Baek, J. Na, B. H. Lee, E. Choi, and W. S. Son, "Optical approach to the periodontal ligament under orthodontic tooth movement: a preliminary study with optical coherence tomography," *American Journal of Orthodontics and Dentofacial Orthopedics*, vol. 135, pp. 252–259, 2009.
- [43] J. H. Baek, T. Krasieva, S. Tang et al., "Optical approach to the salivary pellicle," *Journal of Biomedical Optics*, 2009.
- [44] A. S. Gracez, S. S. Suzuki, M. S. Ribeiro, E. Y. Mada, A. Z. Freitas, and H. Suzuki, "Biofilm retention by 3 methods of ligation on orthodontic brackets: a microbiologic and optical coherence tomography analysis," *American Journal of Orthodontics and Dentofacial Orthopedics*, vol. 140, pp. 193–198, 2011.
- [45] R. Chen, J. Rudney, C. Aparicio, A. Fok, and R. S. Jones, "Quantifying dental biofilm growth using cross-polarization optical coherence tomography," *Letters in Applied Microbiology*, vol. 54, no. 6, pp. 537–542, 2012.
- [46] A. Humnicki, C. Dong, B. Cleghorn, M. Sowa, M. Hewko, and L. P. Choo-Smith, "Determining the effect of calculus, hypocalcification, and stain on using optical coherence tomography and polarized Raman spectroscopy for detecting white spot lesions," *International Journal of Dentistry*, vol. 879252, 2010.
- [47] A. K. Braz, C. M. Aguiar, and A. S. Gomes, "Evaluation of the integrity of dental sealants by optical coherence tomography," *Dental Materials*, vol. 27, no. 4, pp. 60–64, 2011.
- [48] A. K. Braz, B. B. Kyotokub, R. Brazc, and A. S. Gomes, "Evaluation of crack propagation in dental composites by optical coherence tomography," *Dental Materials*, vol. 25, pp. 74–79, 2009.
- [49] G. Q. Monteiro, M. A. Montes, A. S. Gomes, C. C. Mota, S. L. Campello, and A. Z. Freitas, "Marginal analysis of resin

- composite restorative systems using optical coherence tomography,” *Dental Materials*, vol. 27, pp. 213–223, 2011.
- [50] T. C. Matheus, C. M. Kauffman, A. K. Braz, C. C. Mota, and A. S. Gomes, “Fracture process characterization of fiber-reinforced dental composites evaluated by optical coherence tomography, SEM and optical microscopy,” *Brazilian Dental Journal*, vol. 21, pp. 420–427, 2010.
- [51] T. A. Bakhsh, A. Sadr, Z. Shimada, J. Tagami, and Y. Sumi, “Non-invasive quantification of resin-dentin interfacial gaps using optical coherence tomography: validation against confocal microscopy,” *Dental Materials*, vol. 27, pp. 915–925, 2011.
- [52] K. Ishibashi, N. Ozawa, J. Tagami, and Y. Sumi, “Swept-source optical coherence tomography as a new tool to evaluate defects of resin-based composite restorations,” *Journal of Dentistry*, vol. 39, pp. 543–548, 2011.
- [53] G. Q. de Melo Monteiro, M. A. Montes, T. V. Rolim et al., “Alternative methods for determining shrinkage in restorative resin composites,” *Dental Materials*, vol. 27, pp. 176–185, 2011.
- [54] P. Makishi, Y. Shimada, A. Sadr, J. Tagami, and Y. Sumi, “Non-destructive 3D imaging of composite restorations using optical coherence tomography: marginal adaptation of self-etch adhesives,” *Journal of Dentistry*, vol. 39, pp. 316–325, 2011.
- [55] P. Senawongse, P. Pongprueksa, C. Harnirattisai et al., “Non-destructive assessment of cavity wall adaptation of class V composite restoration using swept-source optical coherence tomography,” *Dental Materials Journal*, vol. 30, pp. 517–522, 2011.
- [56] Y. Natsume, S. Nakashima, A. Sadr, Y. Shimada, J. Tagami, and Y. Sumi, “Estimation of lesion progress in artificial root caries by swept source optical coherence tomography in comparison to transverse microradiography,” *Journal of Biomedical Optics*, vol. 16, article 071408, 2011.
- [57] Y. Shimada, A. Sadr, M. F. Burrow, J. Tagami, N. Ozawa, and Y. Sumi, “Validation of swept-source optical coherence tomography (SS-OCT) for the diagnosis of occlusal caries,” *Journal of Dentistry*, vol. 38, pp. 655–665, 2010.
- [58] A. Nazari, A. Sadr, M. Campillo-Funollet et al., “Effect of hydration on assessment of early enamel lesion using swept-source optical coherence tomography,” *Journal of Biophotonics*, 2012.
- [59] Y. Shimamura, R. Murayama, H. Kurokawa, M. Miyazaki, Y. Mihata, and S. Kmaguchi, “Influence of tooth-surface hydration conditions on optical coherence tomography imaging,” *Journal of Dentistry*, vol. 39, pp. 572–577, 2011.
- [60] Y. Shimada, A. Sadr, A. Nazari et al., “3D evaluation of composite resin restoration at practical training using swept-source optical coherence tomography (SS-OCT),” *Dental Materials Journal*, vol. 31, pp. 409–417, 2012.
- [61] I. Hariri, A. Sadr, Y. Shimada, J. Tagami, and Y. Sumi, “Effects of structural orientation of enamel and dentine on light attenuation and local refractive index: an optical coherence tomography study,” *Journal of Dentistry*, vol. 40, pp. 387–396, 2012.
- [62] Y. Nakajima, Y. Shimada, M. Miyashin, Y. Takagi, J. Tagami, and Y. Sumi, “Noninvasive cross-sectional imaging of incomplete crown fractures (cracks) using swept-source optical coherence tomography,” *International Endodontic Journal*, 2012.
- [63] A. K. Braz, R. E. de Araujo, T. Y. Ohulchanskyy et al., “In situ gold nanoparticles formation: contrast agent for dental optical coherence tomography,” *Journal of Biomedical Optics*, vol. 17, article 066003, 2012.
- [64] C. S. Azevedo, L. C. Trung, M. R. Simionato, A. Z. Freitas, and A. B. Matos, “Evaluation of caries-affected dentin with optical coherence tomography,” *Brazilian Oral Research*, vol. 25, pp. 407–413, 2011.
- [65] O. K. Adegun, P. H. Tomlins, E. Hagi-Pavli et al., “Quantitative analysis of optical coherence tomography and histopathology images of normal and dysplastic oral mucosal tissues,” *Lasers in Medical Science*, vol. 27, pp. 795–804, 2012.
- [66] O. K. Adegun, P. H. Tomlins, E. Hagi-Pavli, D. L. Bader, and F. Fortune, “Quantitative optical coherence tomography of fluid-filled oral mucosal lesions,” *Lasers in Medical Science*, vol. 28, pp. 1249–1255, 2013.
- [67] J. S. Holtzman, J. Ballantine, M. Fontana et al., “Assessment of early occlusal caries pre- and post-sealant application – an imaging approach,” *Lasers in Surgery and Medicine*, vol. 46, pp. 499–507, 2014.
- [68] J. Jan, W. Z. Wan Bakar, S. M. Mathews et al., “Proximal caries lesion detection using the canary caries detection system: an in vitro study,” *Journal of Investigative and Clinical Dentistry*, vol. 7, pp. 383–390, 2016.
- [69] I. Sugita, S. Nakashima, A. Ikeda et al., “A pilot study to assess the morphology and progression of noncarious cervical lesions,” *Journal of Dentistry*, vol. 57, pp. 51–56, 2017.
- [70] Y. Zhou, Y. Shimada, K. Matin, A. Sadr, Y. Sumi, and J. Tagami, “Assessment of bacterial demineralization around composite restorations using swept-source optical coherence tomography (SS-OCT),” *Dental Materials Journal*, vol. 9, p. 1177, 2016.
- [71] A. M. Maia, A. Z. de Freitas, S. de L Campello, A. S. Gomes, and L. Karlsson, “Evaluation of dental enamel caries assessment using quantitative light induced fluorescence and optical coherence tomography,” *Journal of Biophotonics*, vol. 6, pp. 596–602, 2016.
- [72] K. Horie, Y. Shimada, K. Matin et al., “Monitoring of cariogenic demineralization at the enamel–composite interface using swept-source optical coherence tomography,” *Dental Materials Journal*, vol. 9, p. 1103, 2016.
- [73] V. Damodaran, R. S. Ranga, and N. J. Vasa, “Optical coherence tomography based imaging of dental demineralisation and cavity restoration in 840 nm and 1310 nm wavelength regions,” *Optics and Lasers in Engineering*, vol. 59, p. 14, 2016.
- [74] T. Ibusuki, Y. Kitasako, A. Sadr, Y. Shimada, Y. Sumi, and J. Tagami, “Observation of white spot lesions using swept source optical coherence tomography (SS-OCT): in vitro and in vivo study,” *Dental Materials Journal*, vol. 34, pp. 545–552, 2015.
- [75] B. Shi, M. Zhuo, W. Longzhi, and L. Tiegen, “Monte Carlo modeling of human tooth optical coherence tomography imaging,” *Journal of Optics*, vol. 15, p. 7, 2013.
- [76] W. A. Fried, J. C. Simon, S. Lucas et al., “Near-IR imaging of cracks in teeth,” *Proceedings of SPIE the International Society for Optical Engineering*, vol. 18, pp. 8929–89290Q, 2014.
- [77] H. Tom, K. H. Chan, C. L. Darling, and D. Fried, “Near-IR imaging of demineralization under sealants,” *Proceedings of SPIE the International Society for Optical Engineering*, vol. 18, pp. 8929–89290S, 2014.

- [78] S. H. Lee, J. J. Lee, H. J. Chung, J. T. Park, and H. J. Kim, "Dental optical coherence tomography: new potential diagnostic system for cracked-tooth syndrome," *Surgical and Radiologic Anatomy*, vol. 38, pp. 49–54, 2016.
- [79] J. C. Simon, S. Lucas, R. C. Lee et al., "Near-infrared imaging of secondary caries lesions around composite restorations at wavelengths from 1300–1700-nm," *Dental Materials*, vol. 32, pp. 587–595, 2016.
- [80] K. H. Chan, H. Tom, R. C. Lee et al., "Clinical monitoring of smooth surface enamel lesions using CP-OCT during non-surgical intervention," *Lasers in Surgery and Medicine*, vol. 8, pp. 915–923, 2016.
- [81] K. Al-Azri, L. N. Melita, A. P. Strange et al., "Optical coherence tomography use in the diagnosis of enamel defects," *Journal of Biomedical Optics*, vol. 21, article 36004, 2016.
- [82] H. Tezuka, Y. Shimada, K. Matin et al., "Assessment of cervical demineralization induced by *Streptococcus mutans* using swept-source optical coherence tomography," *Journal of Medical Imaging*, vol. 3, article 014504, 2016.
- [83] H. Kang, C. L. Darling, and D. Fried, "Enhancement of OCT images with vinyl polysiloxane (VPS)," *Proceedings of SPIE the International Society for Optical Engineering*, vol. 13, p. 9692, 2016.
- [84] V. Damodaran, R. R. Suresh, and J. V. Nilesh, "Optical coherence tomography based imaging of dental demineralization and cavity restoration in 840 nm and 1310 nm wavelength," *Optics and Lasers in Engineering*, vol. 83, pp. 59–65, 2016.
- [85] V. F. Duma, D. Demian, C. Sinescu. et al., "Handheld scanning probes for optical coherence tomography: developments, applications, and perspectives," *Proc. SPIE 9670, Sixth International Conference on Lasers in Medicine*, vol. 22, article 96700V, 2016.
- [86] M. Mahdian, H. S. Salehi, A. G. Lurie, S. Yadav, and A. Tadinada, "Tissue characterization using optical coherence tomography and cone beam computed tomography: a comparative pilot study," *Oral Surgery, Oral Medicine, Oral Pathology, Oral Radiology*, vol. 122, no. 1, pp. 98–103, 2016.
- [87] T. A. Bakhsh, "Ultrastructural features of dentinoenamel junction revealed by focused gallium ion beam milling," *Journal of Microscopy*, vol. 264, no. 1, pp. 14–21, 2016.
- [88] R. Oguro, M. Nakajima, N. Seki, A. Sadr, J. Tagami, and Y. Sumi, "The role of enamel thickness and refractive index on human tooth colour," *Journal of Dentistry*, vol. 51, pp. 36–44, 2016.
- [89] A. Algarni, H. Kang, D. Fried, G. J. Eckert, and A. T. Hara, "Enamel thickness determination by optical coherence tomography: in vitro validation," *Caries research*, vol. 50, no. 4, pp. 400–406, 2016.
- [90] R. E. Wijesinghe, N. H. Cho, K. Park, M. Jeon, and J. Kim, "Bio-photon detection and quantitative evaluation method for the progression of dental caries using optical frequency-domain imaging method," *Sensors (Basel)*, vol. 6, pp. 16–12, 2016.
- [91] H. Watanabe, A. Kuribayashi, Y. Sumi, and T. Kurabayashi, "Resolution characteristics of optical coherence tomography for dental use," *Dento Maxillo Facial Radiology*, vol. 46, no. 3, article 20160358, 2017.
- [92] J. M. Kim, S. R. Kang, and W. J. Yi, "Automatic detection of tooth cracks in optical coherence tomography images," *J. Period, Implementation Science*, vol. 47, no. 1, pp. 41–50, 2017.
- [93] M. S. Segarra, Y. Shimada, A. Sadr, Y. Sumi, and J. Tagami, "Three dimensional analysis of enamel crack behavior using optical coherence tomography," *Journal of Dental Research*, vol. 96, no. 3, pp. 308–314, 2017.
- [94] J. C. Simon, H. Kang, M. Staninec et al., "Near IR and CP-OCT imaging of suspected occlusal caries lesions," *Lasers in surgery and medicine*, vol. 49, no. 3, pp. 215–224, 2017.
- [95] Y. Shimada, H. Nakagawa, A. Sadr et al., "Noninvasive cross-sectional imaging of proximal caries using swept-source optical coherence tomography (SS-OCT) in vivo," *Journal of Biophotonics*, vol. 7, pp. 506–513, 2014.
- [96] Z. Van Hilsen and R. S. Jones, "Comparing potential early caries assessment methods for teledentistry," *BMC Oral Health*, vol. 28, pp. 13–16, 2013.
- [97] A. Nazari, A. Sadr, Y. Shimada, J. Tagami, and Y. Sumi, "3D assessment of void and gap formation in flowable resin composites using optical coherence tomography," *The Journal of Adhesive Dentistry*, vol. 15, no. 3, pp. 237–243, 2013.
- [98] M. M. Mandurah, A. Sadr, Y. Shimada et al., "Monitoring remineralization of enamel subsurface lesions by optical coherence tomography OCT signal attenuation demonstrated a capability for monitoring changes of enamel lesions during remineralization," *Journal of Biomedical Optics*, vol. 18, no. 4, article 046006, 2013.
- [99] M. C. C. de Oliveira, L. A. Gueiros, A. M. Maia et al., "Optical coherence tomography as an auxiliary tool for the screening of radiation-related caries," *Photomedicine and Laser Surgery*, vol. 31, pp. 301–306, 2013.
- [100] B. Bista, A. Sadr, A. Nazari, Y. Shimada, Y. Sumi, and J. Tagami, "Nondestructive assessment of current one-step self-etch dental adhesives using optical coherence tomography," *Journal of Biomedical Optics*, vol. 18, article 76020, 2013.
- [101] K. J. Park, H. Schneider, and R. Haak, "Assessment of interfacial defects at composite restorations by swept source optical coherence tomography," *Dental Materials*, vol. 31, pp. 534–541, 2015.
- [102] C. Marcauteanu, A. Bradu, C. Sinescu, F. Topala, M. L. Negrutiu, and A. G. Podoleanu, "Quantitative evaluation of dental abfraction and attrition using a swept-source optical coherence tomography system," *Journal of Biomedical Optics*, vol. 19, article 21108, 2014.
- [103] X. Liu and R. S. Jones, "Evaluating a novel fissure caries model using swept source optical coherence tomography," *Dental Materials Journal*, vol. 32, pp. 906–912, 2013.
- [104] K. H. Chan, A. C. Chan, W. A. Fried, J. C. Simon, and C. L. Darling, "Use of 2D images of depth and integrated reflectivity to represent the severity of demineralization in cross-polarization optical coherence tomography," *Journal of Biophotonics*, vol. 8, pp. 36–45, 2015.
- [105] H. P. Chew, C. M. Zakian, I. A. Pretty, and R. P. Ellwood, "Measuring initial enamel erosion with quantitative light-Induced fluorescence and optical coherence tomography: an in vitro validation study," *Caries*, vol. 48, pp. 254–262, 2014.
- [106] Y. Nakajima, Y. Shimada, A. Sadr et al., "Detection of occlusal caries in primary teeth using swept source optical coherence tomography," *Journal of Biomedical Optics*, vol. 19, article 16020, 2014.

- [107] M. Rominu, A. Manescu, C. Sinescu et al., "Zirconia enriched dental adhesive: a solution for OCT contrast enhancement. Demonstrative study by synchrotron radiation microtomography," *Dental Materials*, vol. 30, pp. 417–423, 2014.
- [108] M. M. Mandurah, A. Sadr, T. A. Bakhsh, Y. Shimada, Y. Sumi, and J. Tagami, "Characterization of transparent dentin in attrited teeth using optical coherence tomography," *Lasers in surgery and medicine*, vol. 30, pp. 1189–1196, 2015.
- [109] H. M. Ku, B. R. Kim, S. M. Kang, J. H. Chung, H. K. Kwon, and B. I. Kim, "Detection of early changes in caries lesion using QLF-D and OCT," *Journal of Korean Academy of Oral Health*, vol. 38, pp. 10–16, 2014.
- [110] A. Turkistani, A. Sadr, Y. Shimada, T. Nikaido, Y. Sumi, and J. Tagami, "Sealing performance of resin cements before and after thermal cycling: evaluation by optical coherence tomography," *Dental Materials*, vol. 30, pp. 993–1004, 2014.
- [111] R. C. Lee, H. Kang, C. L. Darling, and D. Fried, "Automated assessment of the remineralization of artificial enamel lesions with polarization-sensitive optical coherence tomography," *IEEE Journal of Selected Topics in Quantum Electronics*, vol. 22, p. 3, 2016.
- [112] K. H. Chan, H. Tom, C. L. Darling, and D. Fried, "A method for monitoring enamel erosion using laser irradiated surfaces and optical coherence tomography," *Lasers in surgery and medicine*, vol. 46, pp. 672–678, 2014.
- [113] A. C. Cara, D. M. Zezell, P. A. Ana, E. P. Maldonado, and A. Z. Freitas, "Evaluation of two quantitative analysis methods of optical coherence tomography for detection of enamel demineralization and comparison with microhardness," *Lasers in surgery and medicine*, vol. 46, pp. 666–671, 2014.
- [114] R. Oancea, A. Bradu, C. Sinescu et al., "Assessment of the sealant/tooth interface using optical coherence tomography," *Journal of Adhesion Science and Technology*, vol. 29, p. 1, 2015.
- [115] V. Damodaran and N. J. Vasa, "Development of an electro-optically tuned optical coherence tomography system for imaging dental lesions," *Conference Proceedings: Annual International Conference of the IEEE Engineering in Medicine and Biology Society*, pp. 170–173, 2014.
- [116] I. Wada, Y. Shimada, M. Ikeda et al., "Clinical assessment of non carious cervical lesion using swept-source optical coherence tomography," *Journal of Biophotonics*, vol. 8, pp. 846–854, 2015.
- [117] E. Anadioti, S. A. Aquilino, D. G. Gratton et al., "Internal fit of pressed and computer-aided design/computer-aided manufacturing ceramic crowns made from digital and conventional impressions," *The Journal of Prosthetic Dentistry*, vol. 113, no. 4, pp. 304–309, 2015.
- [118] T. Bortolotto, J. Bahillo, O. Richoz, F. Hafezi, and I. Krejci, "Failure analysis of adhesive restorations with SEM and OCT: from marginal gaps to restoration loss," *Clinical Oral Investigations*, vol. 19, pp. 1881–1890, 2015.
- [119] E. Z. Alsayed, I. Hariri, A. Sadr et al., "Optical coherence tomography for evaluation of enamel and protective coatings," *Dental Materials Journal*, vol. 34, pp. 98–107, 2015.
- [120] J. Espigares, A. Sadr, H. Hamba et al., "Assessment of natural enamel lesions with optical coherence tomography in comparison with microfocus X-ray computed tomography," *Journal of Medical Imaging*, vol. 2, article 014001, 2015.
- [121] C. W. Sun, Y. C. Ho, and S. Y. Lee, "Sensing of tooth microleakage based on dental optical coherence tomography," *Journal of Sensors*, vol. 984627, 2015.
- [122] K. J. Park, H. Schneider, and R. Haak, "Assessment of defects at tooth/self-adhering flowable composite interface using swept-source optical coherence tomography (SS-OCT)," *Dental Materials*, vol. 31, pp. 534–541, 2015.
- [123] H. Milly, F. Festy, M. Andiappan, T. F. Watson, I. Thompson, and A. Banerjee, "Surface pre-conditioning with bioactive glass air-abrasion can enhance enamel white spot lesion remineralization," *Dental Materials*, vol. 31, pp. 522–533, 2015.
- [124] J. H. Min, D. Inaba, H. K. Kwon, J. H. Chung, and B. I. Kim, "Evaluation of penetration effect of resin infiltrant using optical coherence tomography," *Journal of Dentistry*, vol. 43, pp. 720–725, 2015.
- [125] C. Sinescu, M. L. Negrutiu, A. Bradu, V. F. Duma, and A. G. Podoleanu, "Noninvasive quantitative evaluation of the dentin layer during dental procedures using optical coherence tomography," *Computational and Mathematical Methods in Medicine*, vol. 709076, 2015.
- [126] P. Majkut, A. Sadr, Y. Shimada, Y. Sumi, and J. Tagami, "Validation of optical coherence tomography against micro-computed tomography for evaluation of remaining coronal dentin thickness," *Journal of Endodontia*, vol. 41, pp. 1349–1352, 2015.
- [127] A. Turkistani, S. Nakashima, Y. Shimada, J. Tagami, and A. Sadr, "Microgaps and demineralization progress around composite restorations," *Journal of Dental Research*, vol. 94, pp. 1070–1077, 2015.
- [128] C. C. Mota, B. A. Guerra, B. S. Machado, A. J. Cabral, and A. S. Gomes, "Optical coherence tomography applied to the evaluation of wear of composite resin for posterior teeth," *Proceedings of SPIE Biophysics Symposium America*, vol. 9531, article 95313I.
- [129] P. S. Barbosa, A. Z. Freitas, and G. R. de Sant'Anna, "Analysis of photodynamic cream effect in dental caries using optical coherence tomography," *Proceedings of SPIE Biophysics Symposium America*, article 95313A, 2015.
- [130] P. Makishi, S. Thitthaweerat, A. Sadr et al., "Assessment of current adhesives in class I cavity: nondestructive imaging using optical coherence tomography and microtensile bond strength," *Dental Materials*, vol. 31, pp. e190–e200, 2015.
- [131] N. Yoshimine, Y. Shimada, J. Tagami, and A. Sadr, "Interfacial adaptation of composite restorations before and after light curing: effects of adhesive and filling technique," *The Journal of Adhesive Dentistry*, vol. 17, pp. 329–336, 2015.
- [132] C. S. Sampaio, R. V. Rodrigues, E. J. Souza-Junior et al., "Effect of restorative system and thermal cycling on the tooth-restoration interface—OCT evaluation," *Operative Dentistry*, vol. 41, pp. 162–170, 2016.
- [133] B. C. Borges, I. V. de Assunção, C. A. de Aquino, M. G. Q. de Melo, and A. S. Gomes, "Marginal and internal analysis of preheated dental fissure-sealing materials using optical coherence tomography," *International Dental Journal*, vol. 66, pp. 23–28, 2016.
- [134] R. Dsouza, H. Subhash, K. Neuhaus, R. Kantamneni, and P. M. McNamara, "Assessment of curing behavior of light-activated dental composites using intensity correlation based multiple reference optical coherence tomography," *Lasers in surgery and medicine*, vol. 48, pp. 77–82, 2016.
- [135] S. H. Han, A. Sadr, J. Tagami, and S. H. Park, "Non-destructive evaluation of an internal adaptation of resin composite restoration with swept-source optical coherence

- tomography and micro-CT,” *Dental Materials*, vol. 32, pp. e1–e7, 2016.
- [136] P. Makishi, R. R. Pacheco, A. Sadr, Y. Shimada, and Y. Sumi, “Assessment of self-adhesive resin composites: nondestructive imaging of resin–dentin interfacial adaptation and shear bond strength,” *Microscopy and Microanalysis*, vol. 21, pp. 1523–1529, 2015.
- [137] H. Tom, K. H. Chan, C. L. Darling, and D. Fried, “Near-IR image-guided laser ablation of demineralization on tooth occlusal surfaces,” *Lasers in surgery and medicine*, vol. 48, pp. 52–61, 2016.
- [138] S. F. Cassimiro-Silva, A. M. Araújo Maia, G. Q. de Melo Monteiro, and A. S. Gomes, “Mitigation of enamel erosion using commercial toothpastes evaluated with optical coherence tomography,” *Proceedings of SPIE 9670, Sixth International Conference Lasers in Medicine*, article 96700Y, 2016.
- [139] M. N. Dao Luong, Y. Shimada, A. Turkistani, J. Tagami, and Y. Sumi, “Fractography of interface after microtensile bond strength test using swept-source optical coherence tomography,” *Dental Materials*, vol. 32, pp. 862–869, 2016.
- [140] S. Ito, Y. Shimada, A. Sadr et al., “Assessment of occlusal fissure depth and sealant penetration using optical coherence tomography,” *Dental Materials Journal*, vol. 35, pp. 432–439, 2016.
- [141] S. H. Han, A. Sadr, J. Tagami, and S. H. Park, “Internal adaptation of resin composites at two configurations: influence of polymerization shrinkage and stress,” *Dental Materials*, vol. 32, pp. 1085–1094, 2016.
- [142] K. Horie, Y. Shimada, K. Matin et al., “Monitoring of cariogenic demineralization at the enamel–composite interface using swept-source optical coherence tomography,” *Dental Materials*, vol. 32, pp. 1103–1112, 2016.
- [143] Y. Zhou, Y. Shimada, K. Matin, A. Sadr, and Y. Sumi, “Assessment of bacterial demineralization around composite restorations using swept-source optical coherence tomography (SS-OCT),” *Dental Materials*, vol. 32, pp. 1177–1188, 2016.
- [144] M. C. de Moraes, A. Z. Freitas, and A. C. Aranha, “Progression of erosive lesions after Nd:YAG laser and fluoride using optical coherence tomography,” *Lasers in Medical Science*, vol. 32, pp. 1–8, 2017.
- [145] T. Ueno, Y. Shimada, K. Matin et al., “Optical analysis of enamel and dentin caries in relation to mineral density using swept-source optical coherence tomography,” *Journal of Medical Imaging (Bellingham)*, vol. 3, article 035507, 2016.
- [146] I. Sugita, S. Nakashima, A. Ikeda et al., “A pilot study to assess the morphology and progression of non-cariious cervical lesions,” *Journal of Dentistry*, vol. 57, pp. 51–56, 2017.
- [147] H. Schneider, K. J. Park, C. Rueger, D. Ziebolz, F. Krause, and R. Haak, “Imaging resin infiltration into non-cavitated carious lesions by optical coherence tomography,” *Journal of Dentistry*, vol. 10, no. 17, pp. 30061–30061, 2017.
- [148] B. P. de Oliveira, A. C. Câmara, D. A. Duarte et al., “Detection of apical root cracks using spectral domain and swept-source optical coherence tomography,” *Journal of Endodontia*, vol. 14, no. 17, pp. 30068–30067, 2017.
- [149] E. Brady, F. Mannocci, J. Brown, R. Wilson, and S. Patel, “A comparison of cone beam computed tomography and periapical radiography for the detection of vertical root fractures in nonendodontically treated teeth,” *International Endodontic Journal*, vol. 47, pp. 735–746, 2014.
- [150] T. Minamino, A. Mine, K. Omiya et al., “Nondestructive observation of teeth post core space using optical coherence tomography: a pilot study,” *Journal of Biomedical Optics*, vol. 19, article 046004, 2014.
- [151] J. Ding, A. Ebihara, S. Watanabe et al., “Application of optical coherence tomography to identify pulp exposure during access cavity preparation using an Er:YAG laser,” *Photomedicine and Laser Surgery*, vol. 32, pp. 356–359, 2014.
- [152] R. Chavda, F. Mannocci, M. Andiappan, and S. Patel, “Comparing the in vivo diagnostic accuracy of digital periapical radiography with cone-beam computed tomography for the detection of vertical root fracture,” *Journal of Endodontia*, vol. 40, pp. 1524–1529, 2014.
- [153] Y. Iino, A. Ebihara, T. Yoshioka et al., “Detection of a second mesiobuccal canal in maxillary molars by swept-source optical coherence tomography,” *Journal of Endodontia*, vol. 40, pp. 1865–1868, 2014.
- [154] P. Majkut, A. Sadr, Y. Shimada, Y. Sumi, and J. Tagami, “Validation of optical coherence tomography against micro-computed tomography for evaluation of remaining coronal dentin thickness,” *Journal of Endodontia*, vol. 41, pp. 1349–1352, 2015.
- [155] T. Minamino, A. Mine, M. Matsumoto et al., “Nondestructive observation of teeth post core-space using optical coherence tomography: comparison with microcomputed tomography and live images,” *Journal of Biomedical Optics*, vol. 20, article 107001, 2015.
- [156] N. Scotti, C. Alovisi, A. Comba et al., “Evaluation of composite adaptation to pulpal chamber floor using optical coherence tomography,” *Journal of Endodontia*, vol. 42, pp. 160–163, 2016.
- [157] R. C. Lee, C. L. Darling, M. Staninec, A. Ragadio, and D. Fried, “Activity assessment of root caries lesions with thermal and near-IR imaging methods,” *Journal of Biophotonics*, vol. 10, pp. 433–445, 2017.
- [158] J. M. Park, C. H. Hämmerle, and G. I. Benic, “Digital technique for in vivo assessment of internal and marginal fit of fixed dental prostheses,” *The Journal of Prosthetic Dentistry*, no. 17, pp. 30008–30002, 2017.
- [159] P. Lenton, J. Rudney, A. Fok, and R. S. Jones, “Clinical cross-polarization optical coherence tomography assessment of subsurface enamel below dental resin composite restorations,” *Journal of Medical Imaging (Bellingham)*, vol. 1, no. 1, article 016001, 2014.
- [160] C. L. Lin, W. C. Kuo, J. J. Yu, and S. F. Huang, “Examination of ceramic restorative material interfacial debonding using acoustic emission and optical coherence tomography,” *Dental Materials*, vol. 29, pp. 382–388, 2013.
- [161] C. L. Lin, W. C. Kuo, Y. H. Chang, J. J. Yu, and Y. C. Lin, “Examination of ceramic/enamel interfacial debonding using acoustic emission and optical coherence tomography,” *Dental Materials*, vol. 30, pp. 910–916, 2014.
- [162] C. A. Madaras, C. Sinescu, M. L. Negrutiu et al., “Material defects in ceramic crowns identification by optical coherence tomography and microCT,” *Key Engineering Materials*, vol. 614, pp. 124–133, 2014.
- [163] L. O. Fernandes, N. D. Graça, L. S. Melo, C. H. Silva, and A. S. Gomes, “Optical coherence tomography investigations of

- ceramic lumineers,” *Proceedings of SPIE, Lasers in Dentistry*, article 96920P, 2016.
- [164] A. Gabor, A. Jivanescu, C. Zaharia, S. Hategan, and F. I. Topala, “OCT evaluation of single ceramic crowns: comparison between conventional and chair-side CAD/CAM technologies,” *Proceedings of SPIE 9670, Sixth International Conference Lasers in Medicine*, article 96700Z, 2016.
- [165] A. G. Türk, M. Sabuncu, S. Ünal, B. Önal, and M. Ulusoy, “Comparison of the marginal adaptation of direct and indirect composite inlay restorations with optical coherence tomography,” *Journal of Applied Oral Science*, vol. 24, pp. 383–390, 2016.
- [166] N. Gladkova, E. Kiseleva, N. Robakidze et al., “Evaluation of oral mucosa collagen condition with cross-polarization optical coherence tomography,” *Journal of Biophotonics*, vol. 6, pp. 321–329, 2013.
- [167] J. R. Weber, F. Baribeau, P. Grenier et al., “Towards a bimodal proximity sensor for in situ neurovascular bundle detection during dental implant surgery,” *Biomedical Optics Express*, vol. 5, pp. 16–30, 2013.
- [168] K. Kikuchi, N. Akiba, A. Sadr, Y. Sumi, J. Tagami, and S. Minakuchi, “Evaluation of the marginal fit at implant-abutment interface by optical coherence tomography,” *Journal of Biomedical Optics*, vol. 19, article 055002, 2014.
- [169] C. C. Mota, L. O. Fernandes, R. Cimões, and A. S. Gomes, “Non-invasive periodontal probing through Fourier-domain optical coherence tomography,” *Journal of Periodontology*, vol. 86, pp. 1087–1094, 2015.
- [170] J. Boadi, J. Fernandes, S. Mittar et al., “Imaging of 3D tissue-engineered models of oral cancer using 890 and 1300 nm optical coherence tomography,” *Sovremennye Tehnologii v Medicine*, vol. 7, pp. 60–67, 2015.
- [171] M. Sanda, M. Shiota, C. Imakita, A. Sakuyama, S. Kasugai, and Y. Sumi, “The effectiveness of optical coherence tomography for evaluating peri-implant tissue: a pilot study,” *Imaging Science in Dentistry*, vol. 46, pp. 173–178, 2016.
- [172] V. Damodaran, N. J. Vasa, R. Sarathi, and S. R. Rao, “Non-invasive detection of periodontal loss of attachment using optical coherence tomography,” *Proceedings of SPIE, International Conference of Optics and Photonics*, article 96540Q, 2015.
- [173] L. O. Fernandes, N. D. Graça, L. S. Melo, C. H. Silva, and A. S. Gomes, “Monitoring the gingival regeneration after aesthetic surgery with optical coherence tomography,” *Proceedings of SPIE, Lasers in Dentistry*, article 96920Q, 2016.
- [174] D. Augustine, R. S. Rao, and S. Patil, “Optical coherence tomography in oral cancer detection,” *International Journal of Contemporary Dental and Medical Reviews*, article 010316, 2016.
- [175] M. L. Negrutiu, C. Sinescu, C. M. Bortun et al., “Assessment of dental plaque by optoelectronic methods,” *Proceedings of SPIE 9670, Sixth International Conference Lasers in Medicine*, article 96700W, 2016.
- [176] L. O. Fernandes, C. C. Mota, L. S. de Melo, S. M. U. da Costa, D. da Silva Feitosa, and A. S. Gomes, “In vivo assessment of periodontal structures and measurement of gingival sulcus with optical coherence tomography: a pilot study,” *Journal of Biophotonics*, 2016.
- [177] H. S. Salehi, A. Kosa, M. Mahdian, S. Moslehpour, H. Alnajjar, and A. Tadinada, “Characterization of human oral tissues based on quantitative analysis of optical coherence tomography images,” *Proceedings of SPIE, Lasers in Dentistry*, article 1004406, 2017.
- [178] K. Englund, J. Nikrad, and R. Jones, “Assessing the dynamic biofilm removal of sulfonated phenolics using CP-OCT,” *Proceedings of SPIE, Lasers in Dentistry*, article 1004409, 2017.
- [179] S. Bordin, C. M. Pino, J. Mavadia-Shukla, and X. Li, “Optical coherence technology detects early signs of peri-implant mucositis in the minipig model,” *International Journal of Dentistry and Oral Science*, vol. 3, pp. 375–379, 2017.
- [180] S. H. Kim, S. R. Kang, H. J. Park, J. M. Kim, W. Yi, and T. I. Kim, “Improved accuracy in periodontal pocket depth measurement using optical coherence tomography,” *Journal of Periodontal & Implant Science*, vol. 47, pp. 13–19, 2017.
- [181] R. Koprowski, M. Machoy, K. Woźniak, and Z. Wróbel, “Automatic method of analysis of OCT images in the assessment of the tooth enamel surface after orthodontic treatment with fixed braces,” *Biomedical Engineering Online*, vol. 13, p. 48, 2014.
- [182] J. Seeliger, M. Machoy, R. Koprowski, K. Safranow, T. Gedrange, and K. Woźniak, “Enamel thickness before and after orthodontic treatment analysed in optical coherence tomography,” *BioMed Research International*, vol. 8390575, 2017.
- [183] M. M. Pithon, M. D. Santos, C. A. Souza et al., “Effectiveness of fluoride sealant in the prevention of carious lesions around orthodontic brackets: an OCT evaluation,” *Dental press journal of orthodontics*, vol. 20, pp. 37–42, 2015.
- [184] J. C. Leão Filho, A. K. Braz, R. E. de Araujo, O. M. Tanaka, and M. M. Pithon, “Enamel quality after debonding: evaluation by optical coherence tomography,” *Brazilian Dental Journal*, vol. 26, pp. 384–389, 2015.
- [185] M. M. Pithon, M. J. Dos Santos, C. S. Andrade et al., “Effectiveness of varnish with CPP-ACP in prevention of caries lesions around orthodontic brackets: an OCT evaluation,” *European Journal of Orthodontics*, vol. 37, pp. 177–182, 2015.
- [186] A. Nee, K. Chan, H. Kang, M. Staninec, C. L. Darling, and D. Fried, “Longitudinal monitoring of demineralization peripheral to orthodontic brackets using cross polarization optical coherence tomography,” *Journal of Dentistry*, vol. 42, pp. 547–555, 2014.
- [187] D. M. Isfeld, C. Aparicio, and R. S. Jones, “Assessing near infrared optical properties of ceramic orthodontic brackets using cross-polarization optical coherence tomography,” *Journal of Biomedical Materials Research. Part B, Applied Biomaterials*, vol. 102, pp. 516–523, 2014.
- [188] J. C. Leão Filho, A. K. Braz, T. R. de Souza, R. E. de Araujo, M. M. Pithon, and O. M. Tanaka, “Optical coherence tomography for debonding evaluation: an in-vitro qualitative study,” *American Journal of Orthodontics and Dentofacial Orthopedics*, vol. 143, pp. 61–68, 2013.
- [189] D. M. Clarkson, “Optical technology: an update on optical coherence tomography in dentistry,” *Dental Update*, vol. 41, pp. 174–176, 2014, 179 – 80.
- [190] G. Gupta, S. Dhaded, and B. N. Shalini, “Optical coherence tomography: a new era in dentistry,” *Bangladesh Journal of Medical Science*, vol. 13, pp. 388–390, 2014.
- [191] S. Canjau, C. Todea, M. L. Negrutiu, C. Sinescu, and F. I. Topala, “Optical coherence tomography for non-invasive ex vivo investigations in dental medicine – a joint group experience,” *Sovremennye Tehnologii v Medicine*, vol. 7, pp. 97–114, 2015.

- [192] G. I. Benic, M. Elmasry, and C. H. Hämmerle, "Novel digital imaging techniques to assess the outcome in oral rehabilitation with dental implants: a narrative review," *Clinical oral implants research*, vol. 26, pp. 86–96, 2015.
- [193] M. Singh, S. Singh, A. Nagpal, and S. Laller, "Optical coherence tomography- a imaging modality in dentistry beyond X-rays," *Int. J. Oral Maxillofac. Res.*, vol. 1, pp. 22–25, 2015.
- [194] Y. S. Hsieh, Y. C. Ho, S. Y. Lee et al., "Dental optical coherence tomography," *Sensors (Basel)*, vol. 13, pp. 8928–8949, 2013.
- [195] Y. Shimada, A. Sadr, Y. Sumi, and J. Tagami, "Application of optical coherence tomography (OCT) for diagnosis of caries, cracks, and defects of restorations," *Current Oral Health Reports*, vol. 2, pp. 73–80, 2015.
- [196] G. Benic, M. Elmasry, and C. H. Hämmerle, "Novel digital imaging techniques to assess the outcome in oral rehabilitation with dental implants: a narrative review," *Clinical oral implants research*, vol. 11, pp. 86–96, 2015.
- [197] B. W. Colston Jr., M. J. Everett, U. S. Sathyam, L. B. DaSilva, and L. L. Otis, "Imaging of the oral cavity using optical coherence tomography," *Monographs in Oral Science*, vol. 17, pp. 32–55, 2000.
- [198] P. Se-Wook, L. Young-Joon, L. Won-Jin, and L. Jun-Jae, "Study on application to the field of dentistry using optical coherence tomography (OCT)," *The Journal of Korean Academy of Prosthodontics*, vol. 55, pp. 100–110, 2017.